

ATMOSPHERIC NLTE-MODELS FOR THE
SPECTROSCOPIC ANALYSIS OF MASSIVE STARS:
NEW METHODS AND FIRST RESULTS FOR DERIVING
CNO SURFACE ABUNDANCES



Luiz P. Carneiro

ATMOSPHERIC NLTE-MODELS FOR THE
SPECTROSCOPIC ANALYSIS OF MASSIVE STARS:
NEW METHODS AND FIRST RESULTS FOR DERIVING
CNO SURFACE ABUNDANCES

Dissertation

an der
Ludwig–Maximilians–Universität (LMU) München

Ph.D. Thesis

at the
Ludwig–Maximilians–University (LMU) Munich

submitted by

Luiz Paulo Carneiro Gama

born on 23st March 1989 in Rio de Janeiro, Brazil

Munich, August 22th 2018

1st Evaluator: Priv. Doz. Dr. Joachim Puls

2nd Evaluator: Prof. Dr. Barbara Ercolano

Date of the oral exam: 10th October, 2018

*In memory of my cousins Denis Rosman and Daniel Schwin
that could not wait for me to come back home and nowadays
watch and protect my steps.*

Contents

Contents	v
List of Figures	x
List of Tables	xi
Zusammenfassung	xiii
Abstract	xv
1 Introduction	1
1.1 Massive star evolution	2
1.1.1 Phases of evolution	3
1.2 Mass loss through stellar winds	6
1.3 CNO evolution and internal mixing	9
1.4 Motivation of this thesis	12
1.5 Outline of this thesis	13
2 Atmospheric NLTE models for the spectroscopic analysis of blue stars with winds: X-ray emission from winds	
2.1 Introduction	15
2.2 Implementation of X-ray emission and absorption in FASTWIND	17
2.2.1 X-ray emission	17
2.2.2 X-ray absorption and Auger ionization	20
2.2.3 Radiative and adiabatic cooling	20
2.3 Model grid	21
2.4 Tests	23
2.4.1 Impact of various parameters	24
2.4.2 Scaling relations for L_x	28
2.4.3 Comparison with WM-BASIC models	30
2.5 Results	34
2.5.1 Ionization fractions	35
2.5.2 Impact of Auger ionization	46
2.5.3 Dielectronic recombination of O v	47

2.5.4	Mass absorption coefficient	50
2.6	Summary and conclusions	58
2.A	Appendix A: Ionization fractions of selected ions: Dependence on X-ray filling factor and shock temperature	67
2.B	Appendix B: Comparison with WM-BASIC: Ionization fractions and UV line profiles	67
2.C	Appendix C: Averaged mass absorption coefficients: Clumped winds and dependence on averaging interval	67
3	Carbon line formation and spectroscopy in O-type stars	71
3.1	Introduction	72
3.2	Prerequisites for a carbon diagnostics	74
3.2.1	The code	74
3.2.2	The carbon model atom	75
3.2.3	Diagnostic optical carbon lines	78
3.2.4	Model grid	78
3.2.5	Observational data	80
3.3	Testing the atomic model	80
3.3.1	Dielectronic recombination	82
3.3.2	Further comparison with WM-BASIC	86
3.3.3	Optical carbon lines – dependence on stellar parameters	88
3.4	First comparison with observed carbon spectra	91
3.4.1	Basic considerations	91
3.4.2	Details on individual spectra	94
3.4.3	Which lines to use?	96
3.4.4	Impact of X-rays	102
3.5	Summary and conclusions	103
3.A	Appendix A: Electronic states of each carbon ion	107
3.B	Appendix B: Dependence on stellar parameters	110
4	Surface abundances of CNO in Galactic O-stars:A pilot study with FASTWIND	114
4.1	Introduction	115
4.2	Observations and target selection	117
4.3	Abundance analysis: strategy	118
4.3.1	Basic considerations	118
4.3.2	Stellar parameters and model grids	120
4.3.3	Diagnostic lines in the optical	122
4.4	Analysis of CNO abundances	124
4.4.1	Equivalent width measurements	124
4.4.2	Which lines to use?	125
4.4.3	χ^2 -minimization and error estimates	125
4.5	Results	128
4.5.1	Basic considerations	128
4.5.2	General comments	130
4.5.3	Microturbulence	131

4.5.4	Stellar evolutionary models	131
4.5.5	A consistency check – mixing-sensitive ratios	133
4.5.6	Comparison with previous studies	135
4.6	Comparison with evolutionary calculations	137
4.6.1	Evolutionary stages	138
4.6.2	CNO evolution	140
4.7	Summary, conclusions, and future work	147
4.A	Appendix A: Equivalent width measurements – three typical examples	150
4.B	Appendix B: χ^2 minimization – exemplary cases	150
4.C	Appendix C: Line profiles	152
5	Summary and Conclusions	160
	Bibliography	163
	Acknowledgements	183

List of Figures

1.1	Schematic picture of the CNO cycle	10
2.1	Emergent Eddington fluxes for model S30 and for a model with an unshocked wind	25
2.2	Ratio of shock emissivity to total emissivity for model S30 from Fig. 2.1 with $R_{\min} = 1.2 R_*$	26
2.3	Emergent Eddington fluxes for model S30, with $T_s^\infty = 3 \cdot 10^6$ K and $R_{\min}^{\text{input}} = 1.5 R_*$, for different values of f_X	
2.4	Emergent Eddington fluxes for model S30	28
2.5	Emergent X-ray luminosities (in erg s^{-1}) as a function of \dot{M}/v_∞	29
2.6	Logarithmic, scaled Eddington flux (in units of $\text{erg cm}^{-2} \text{s}^{-1} \text{Hz}^{-1}$) as a function of wavelength/energy	31
2.7	Logarithmic Eddington fluxes as a function of wavelength for supergiant models	33
2.8	Ionization fractions of important ions at $v(r) = 0.5 v_\infty$, as a function of T_{eff} , for models with typical X-ray emission parameters	
2.9	Helium ionization fractions as a function of local velocity	37
2.10	Helium ionization fractions as a function of τ_{Ross} , for S30 models calculated by FASTWIND and WM-BASIC	
2.11	Synthetic He II 1640 and He II 4686 profiles for our S30 model	40
2.12	Ionization fractions of selected ions as a function of T_{eff} , for 14 O-star models	42
2.13	Radial stratification of phosphorus ionization fractions, as a function of τ_{Ross}	43
2.14	Ionization fractions of P IV and P V as a function of normalized velocity for an S35 and S40 model	44
2.15	Ionization fractions of ions most affected by Auger ionization, at different depth points	45
2.16	Radial stratification of oxygen ionization fractions, as a function of τ_{Ross} , for an S40 model	48
2.17	Ionization fractions of oxygen, as a function of τ_{Ross} , for a D45 model	49
2.18	Contour plots illustrating the radial dependence of the mass absorption coefficient, $\kappa_\nu(r)$, as a function of wavelength and velocity	
2.19	Radial variation of the mass absorption coefficient in dwarf and supergiant models for specific values of wavelength and velocity	
2.20	Density-weighted mean of the mass absorption coefficient, $\bar{\kappa}_\nu$, for the interval between 1.2 and 110 R_* , as a function of wavelength and velocity	
2.21	Ionization fractions of C IV (at $v(r) = 0.5v_\infty$), as a function of T_{eff} , and for different X-ray emission parameters	
2.22	As above (C IV at $v(r) = 0.5v_\infty$), but now for dwarf and supergiant models, for all X-ray emission parameters	
2.23	As Fig. 2.21, but for N V at $v(r) = 0.6v_\infty$	63
2.24	As Fig. 2.22, but for N V ($v(r) = 0.6v_\infty$)	63
2.25	As Fig. 2.21, but for O V at $v(r) = 0.6v_\infty$	64
2.26	As Fig. 2.22, but for O V ($v(r) = 0.6v_\infty$)	64
2.27	As Fig. 2.21, but for O VI at $v(r) = 0.6v_\infty$	65
2.28	As Fig. 2.22, but for O VI ($v(r) = 0.6v_\infty$)	65
2.29	As Fig. 2.21, but for P V at $v(r) = 0.5v_\infty$	66
2.30	As Fig. 2.22, but for P V ($v(r) = 0.5v_\infty$)	66

2.31	Ionization fractions of specific ions, as calculated by FASTWIND (black) and WM-BASIC (magenta) for dwarf models	
2.32	As Fig. 2.31, but for supergiant models.	68
2.33	Emergent line profiles for strategic UV lines as calculated by WM-BASIC and FASTWIND	69
2.34	As Fig. 2.20, but for clumped models	70
2.35	As Fig. 2.20, but averaged over the interval between 10 and 110 R_*	70
3.1	Ratios of ionization fractions resulting from our former and our new model atom, as a function of τ_{Ross} , for model D35	
3.2	Bound-free cross-section of the C III ground state including resonances and the resonance-free data	83
3.3	Ionization fractions of carbon ions, as a function of τ_{Ross} , for model D45	84
3.4	Impact of dielectronic recombination on C II/III lines, for the D35 model	85
3.5	Ionization fraction of carbon ions, as a function of τ_{Ross} , for the S45 model, as calculated by WM-BASIC and FASTWIND	
3.6	C II 5145, C III 5696, and C IV 5801 line profiles for model D35 and similar models with relatively small changes in parameters	
3.7	As Fig. 3.6, but for model S35	89
3.8	Fine-tuning of stellar parameters (here, T_{eff}), for the case of HD 36512 (O9.7V)	92
3.9	Observed carbon spectrum of HD 36512 (O9.7V), and synthetic lines, calculated with carbon abundance of 8.33 dex	
3.10	As Fig. 3.9, but for HD 303311 (O6V), and a carbon abundance of 8.33 dex	99
3.11	As Fig. 3.10, but for HD 93128 (O3.5V), and a carbon abundance of 8.23 dex	99
3.12	As Fig. 3.9, but for HD 188209 (O9.5Iab), and a carbon abundance of 8.23 dex	100
3.13	As Fig. 3.10, but for HD 169582 (O6Ia), and carbon abundance of 8.53 dex	101
3.14	As Fig. 3.10, but for CygOB2-7 (O3I), and a carbon abundance of 8.03 dex	101
3.15	Impact of X-ray radiation on the C IV 5801-12 lines, for a supergiant model with $T_{\text{eff}} = 40$ kK (S40)	104
3.16	C II 5145, C III 5696, and C IV 5801 line profiles for model D30 and similar models with relatively small changes in parameters	
3.17	As Fig. 3.6, but for model D40, and C III 4068-70, instead of C II 5145	111
3.18	As Fig. 3.16, but for model S30, and $\Delta \log g = 0.1$	112
3.19	As Fig. 3.17, but for model S40	112
3.20	Carbon line profiles for model D35, and dependence on stellar parameters, for our complete set of lines	113
4.1	The relation between nitrogen-to-carbon and nitrogen-to-oxygen ratios	132
4.2	Differences between the logarithmic chemical abundances obtained in the present work and the recent literature	
4.3	Kiel diagram ($\log g$ vs. T_{eff}) for our sample stars	138
4.4	Modified sHRD, with abscissa $\log g$ (instead of T_{eff}), providing a clearer separation between the tracks	139
4.5	The relation ϵ_{C} vs. ϵ_{N} in the light of evolutionary tracks	141
4.6	Evolution of C/N/O abundances for different masses as a function of T_{eff} , as predicted by the rotating Geneva models	
4.7	Nitrogen-to-carbon ratio vs. $v \sin i$ for our sample stars	146
4.8	Examples for equivalent width measurements via Gaussian fits and direct integration	151
4.9	Oxygen analysis for HD 36512 (O9.7 V)	153
4.10	As Fig. 4.9, but for nitrogen in HD12993 (O6.5 V((f)) Nstr)	154
4.11	As Fig. 4.9, but for carbon in HD151515 (O7 II(f)).	155
4.12	HD 36512 (O9.7 V). Comparison of observed and synthetic line profiles	157
4.13	As Fig. 4.12, but for HD 12993 (O6.5 V((f)) Nstr)	158
4.14	As Fig. 4.12, but for HD 151515 (O7 II(f))	159

List of Tables

1.1	The different phases of evolution during the lifetime of massive stars	5
2.1	Stellar and wind parameters of our grid models	22
2.2	X-ray emission parameters used to compare FASTWIND and WM-BASIC models . . .	32
3.1	Diagnostic carbon lines in the optical spectra of early B- and O-type stars, together with potential blends	77
3.2	Stellar and wind parameters of our grid models with homogeneous winds	79
3.3	Stellar and wind parameters adopted for and derived from fitting the H/He plus carbon lines displayed in Fig.	
3.4	C II levels: label, electronic configuration, and term designation	107
3.5	As Table 3.4, but for C III	108
3.6	As Table 3.4, but for C IV	109
4.1	Stellar, wind, and line-broadening parameters for the 18 sample stars	119
4.2	Diagnostic carbon, nitrogen, and oxygen lines in the optical spectrum, used to derive corresponding abundances	
4.3	Carbon, nitrogen and oxygen abundances obtained from our analysis, and the best fitting v_{mic} for the CNO lines	
4.4	Initial values of CNO abundances adopted in the evolutionary grids referred to in this chapter, and corresponding	
4.5	Ranges in initial evolutionary mass and initial masses for the objects analyzed in this chapter	143

Zusammenfassung

Das Ziel vorliegender Dissertation ist es, geeignete Werkzeuge für die quantitative Spektroskopie von O-Sternen im optischen Spektralbereich bereitzustellen, um deren Kohlenstoff-, Stickstoff- und Sauerstoffhäufigkeiten zu bestimmen, und zwar mittels automatisierter Methoden, die auch auf große Stichproben anwendbar sind. Solche Häufigkeiten erlauben uns dabei, Vorhersagen aktueller Sternentwicklungsmodelle massereicher Sterne zu überprüfen, und insbesondere den Einfluss von Rotationsmischung und verwandter Prozesse einzugrenzen. Bereits auf der Hauptreihe können massereiche Sterne chemische Häufigkeitsvariationen auf kurzen Zeitskalen aufweisen, wobei der CNO-Zyklus Stickstoff auf Kosten von Kohlenstoff und - später - Sauerstoff produziert. Diese Variationen stellen ein Schlüsselmerkmal dar, um die Zuverlässigkeit entsprechender theoretischer Modelle zu bewerten, und sind eines der Hauptthemen vorliegender Arbeit.

Zur Durchführung dieser Studie benötigen wir einen Code, der es uns erlaubt, Spektren heißer Sterne zu synthetisieren. Zu diesem Zweck verwendeten (und erweiterten) wir den NLTE (nicht lokales thermodynamisches Gleichgewicht) Atmosphären- und Windcode FASTWIND, vor allem wegen seiner geringen Rechenzeiten, verglichen mit anderen Codes, die für den gleichen Zweck entwickelt wurden. Bevor wir unser eigentliches Ziel angehen konnten, mussten wir zunächst jedoch (i) die Röntgenemission von Shockregionen im Wind implementieren, und (ii) ein zuverlässiges Kohlenstoffmodellatom entwickeln, das für die Analyse von O-Sternen geeignet ist.

(i) Extrem ultraviolette (EUV) und Röntgenstrahlung von Shockregionen in den Winden heißer, massereicher Sterne kann das Ionisationsgleichgewicht in deren äußeren Atmosphären beeinflussen, und kann für die Erzeugung hochionisierter Elemente verantwortlich sein, die vor allem in den windbeeinflussten UV-Spektren sichtbar sind. Um diese Prozesse zu simulieren und zu untersuchen, haben wir die entsprechende Shockemission in den FASTWIND-Code implementiert. Anschließend studierten wir die Bedingungen, unter denen sich solche Shockemission als wesentlich für die Beschreibung von Ionen wie z.B. C v, N v und O vi erweist. In fast allen betrachteten Fällen hat dabei die direkte Ionisation (d.h., die Abtrennung des Valenzelektrons) aufgrund der verstärkten kurzwelligeren Strahlung den größten Einfluss auf die Ionisationsraten von niedrig ionisierten Stufen (z.B. C II, N III und O III), wohingegen die Augerionisation N vi und O vi signifikant beeinflusst. Zusätzlich untersuchten wir die Frequenzabhängigkeit und das radiale Verhalten des Massenabsorptionskoeffizienten ($\kappa_\nu(r)$, wichtig im Zusammenhang mit der Röntgenlinienentstehung in den Winden massereicher Sterne), und fanden, dass zumindest für $r \gtrsim 1.2R_*$ und $\lambda \lesssim 18 \text{ \AA}$ die Näherung eines radial konstanten κ_ν gerechtfertigt ist.

(ii) Unter NLTE-Bedingungen erfordert die Bestimmung chemischer Häufigkeiten eine detail-

lierte Beschreibung aller Strahlungs- und Stoßprozesse, die die Ionisation und Anregung der untersuchten Elemente bestimmen. Dazu entwickelten wir ein neues Kohlenstoffmodellatom (für die Ionen C II/III/IV/V) und überprüften, in wie weit beobachtete Spektren reproduziert werden können. Mit unserem neuen Modellatom konnten wir tatsächlich die meisten der beobachteten (optischen) Linien einer kleinen, aber repräsentativen Stichprobe reproduzieren, und diejenigen Kohlenstoffhäufigkeiten ableiten, die die Linien verschiedener Kohlenstoffionen in Übereinstimmung bringen. Ein wichtiges Resultat unserer Tests betrifft den Einfluss von Röntgenstrahlen, vor allem auf C IV Linien: Die Auswirkung (starker) Shockemission ist ähnlich wie die einer hohen Kohlenstoffhäufigkeit, und kann daher die Kohlenstoffhäufigkeitsbestimmung affektieren.

Nach diesen Schritten war es dann möglich, CNO-Oberflächenhäufigkeiten in O-Sternen mittels FASTWIND zu bestimmen (Modellatome für N und O waren bereits verfügbar). Da schon gegenwärtige Stichproben äußerst umfangreich sind, entwickelten wir eine automatisierte Pipeline für die Analyse der strategischen optischen C-, N- und O-Linien verschiedener Ionen. Besonderes Augenmerk wurde dabei auf die (signifikanten) Fehlerintervalle gelegt, die durch die typischen Unsicherheiten in den stellaren Parametern resultieren. Wir studierten das Leistungsvermögen unserer neu entwickelten Werkzeuge anhand hochqualitativer Spektren einer Probe von achtzehn (vermutlich einzelnen) galaktischen O-Sternen mit niedriger projizierter Rotationsgeschwindigkeit. Die meisten unserer Ergebnisse für Kohlenstoff und Stickstoff stimmen innerhalb der Fehler sowohl mit Literaturwerten (soweit vorhanden) überein, als auch mit theoretischen Vorhersagen massereicher Sternentwicklung einschließlich Rotationsmischung. Dasselbe gilt für die Sauerstoffhäufigkeit in frühen O-Überriesen. Besonders bei späten O-Zwergen sind die abgeleiteten Sauerstoffhäufigkeiten jedoch unerwartet niedrig, was vermutlich auf Defizite im verwendeten Sauerstoffmodellatom hinweist, das in zukünftigen Studien überprüft und verbessert werden muss.

Zusammenfassend stellt die hier beschriebene Arbeit eine Methode zur Verfügung, die prinzipiell für die CNO-Häufigkeitsanalyse großer O-Stern Stichproben verwendet werden kann, und die sicherlich dazu beitragen wird, unser Wissen über massereiche Sterne und deren Entwicklung zu erweitern.

Abstract

This work aims at advancing current tools for the quantitative optical spectroscopy of O-stars, in order to derive carbon, nitrogen and oxygen abundances using an automatized method applicable also to large samples of spectra. These abundances allow us to check current predictions on massive star evolution, and to establish tighter constraints on the impact of rotational mixing and other processes. Already on the Main Sequence, massive stars might display chemical abundance variations on short time-scales, where the CNO cycle produces nitrogen at the expense of carbon and - later on - oxygen. These variations represent a key feature to evaluate the reliability of corresponding theoretical models, and are one of the main topics investigated in the present thesis.

To accomplish this study, we need a code that allows us to synthesize hot star spectra. To this end, we used (and extended) the NLTE (non local thermodynamic equilibrium) atmosphere and wind code FASTWIND, mainly because of its low turn-around times compared to other codes developed for the same purpose. Before tackling our immediate objective, however, we needed to implement (i) the X-ray emission from wind-embedded shocks, and (ii) a reliable carbon model suited for the analysis of O-stars:

(i) Extreme ultraviolet (EUV) and X-ray radiation from wind-embedded shocks in hot, massive stars can affect the ionization balance in their outer atmospheres, and can be responsible for producing highly ionized atomic species in the stellar wind UV spectra. To simulate and investigate these processes, we implemented such emission into the FASTWIND code. Subsequently, we estimated the conditions under which the inclusion of these shocks turned out to be essential for the description of ions as C v, N v, and O vi in the UV spectra of massive stars. In almost all considered cases, direct ionization (i.e., the strip of the valence electron) by the enhanced short-wavelength radiation field has the major influence in the ionization rates of low ionized stages (e.g., C II, N III, and O III), whereas Auger ionization affects N VI and O VI significantly. Additionally, we investigated the frequency dependence and radial behavior of the mass absorption coefficient ($\kappa_\nu(r)$, important in the context of X-ray line formation in the winds of massive stars), and concluded that at least for $r \gtrsim 1.2R_*$ and $\lambda \lesssim 18 \text{ \AA}$, the approximation of a radially constant κ_ν is justified.

(ii) Under NLTE conditions, chemical abundance determinations require a detailed description of all radiative and collisional processes that determine the ionization and excitation of the analyzed element(s). We developed a new carbon model atom including C II/III/IV/V, and verified to which extent observational constraints can be reproduced. We were able to reproduce most of the observed lines from a small but representative stellar sample, and to estimate the carbon abundances required to bring the lines from different carbon ions into agreement. Another important finding concerns the impact of

X-rays particularly on C IV lines. The presence of (strong) shock radiation may mimic the effects of a high carbon abundance, and therefore potentially affects the carbon abundance determination.

After these steps, CNO surface abundance determinations in O-type stars by means of FAST-WIND became possible (model atoms for N and O were already available). However, with the advent of large samples of spectra, we needed to set up an automatized pipeline for the analysis of strategic optical C, N and O lines from different ions. We paid special attention to the (significant) errors introduced by typical uncertainties in stellar parameters. We investigated the performance of our newly developed tools using a set of high-quality spectra of a sample of eighteen presumably single Galactic O-type stars with low projected rotational velocities. Most of our results for carbon and nitrogen agree, within the errors, both with literature values (where available), and with theoretical expectations of massive star evolution including rotational mixing. The same is true for oxygen abundances in early-O supergiants. Particularly in late-O dwarfs, however, the derived oxygen abundances are unexpectedly low, presumably indicating deficiencies in the adopted oxygen model atom, which needs to be checked and improved in future studies.

In summary, the work described in this thesis provides us with a method basically ready to be applied to the CNO abundance analysis of much larger O-star samples, and will certainly help to expand our knowledge about massive stars and their evolution.

Chapter 1

Introduction

Massive stars are physically defined as stars which finally end their lives as core collapse supernovae, and have masses roughly larger than eight solar masses (M_{\odot}) at the beginning of their lives, i.e., at the start of their regular main sequence¹ (MS). The highest mass of a star remains an open question, but initial masses of a few hundred M_{\odot} were already suggested (e.g., Crowther et al. 2016 who found masses of $315M_{\odot}$ and $230M_{\odot}$ for R136a1 and R136c, respectively, both stars in the Large Magellanic Cloud (LMC)). The higher the mass, the shorter the lifetime: high-mass stars complete their evolution in a few million years, while low- and intermediate-mass stars ($M_{ZAMS} < 8M_{\odot}$; zero-age main sequence, ZAMS) may live for hundred of millions to billions of years. Although completing their evolution faster, massive stars can easily be observed, since stellar luminosity scales with initial mass as $L \sim M^{\alpha}$, where $2.3 \lesssim \alpha \lesssim 4.0$ depending on stellar mass (see Kuiper 1938, Duric 2003), and thus, the rare stars born with masses above $\sim 15M_{\odot}$ outshine the larger number of stars with lower masses.

From their birth to their death, high-mass stars have a fundamental influence on different aspects of the Cosmos. Massive stars on the main sequence are characterized by high temperatures and radiative intensities that drive a stellar wind, thus impacting their surroundings in form of radiative and mechanical energy feedback via UV radiation and stellar winds. Additionally, supernova² (SN) explosions mix the interstellar gas, which drives turbulences and possibly triggers the formation of new generations of stars (Bresolin et al. 2008). Thus, the deaths of massive stars in form of supernovae represent both the end and the beginning of new stellar evolution.

Furthermore, the collapse of a rapidly rotating high-mass star yields the most energetic explosions so far observed in the Universe, known as (long duration) gamma-ray bursts (GRBs, Woosley 1993). After an initial flash of gamma rays, a longer-lived “afterglow” is usually emitted at longer wavelengths (X-rays, ultraviolet, optical, infrared, microwave and radio). These afterglows are thought to be the best probes for the metallicity³ and ionization state of the intergalactic medium during the reionization epoch (Bromm et al. 2001, Matteucci & Calura 2005, Morales & Wyithe 2010).

¹ The main sequence (MS) is the longest and the most stable phase in the life of a star. During this time, the fusion of hydrogen forms helium in the stellar core and produces an outward pressure (provided by the nuclear fusion) that balances the inward gravitational force. This equilibrium will last until the H-core is exhausted.

² Regarding the last phase in the life of a massive star, we refer to supernovae after the collapse of the iron core. But supernovae can also result from pair instabilities or electron capture for stars with lower masses ($8-10M_{\odot}$).

³ The abundances of elements heavier than He.

The epoch of reionization refers to a period in the history of the Universe when most of the neutral hydrogen (that had formed shortly ($\sim 380,000$ years) after the Big Bang and that filled the Universe) was ionized by UV radiation. Massive stars may have played an important role in producing these UV photons.

The above mentioned points illustrate some of the ways how advances in our knowledge of massive stars will also lead to a better understanding of the Universe as a whole. The present work has exactly this objective. By improving how we can extract the information about massive stars encoded in their spectra, we take one step further to a better description of these objects. Our innovative method that automatizes spectral analysis brings more consistency and scalability to future works with large samples of stellar spectra.

This introduction briefly describes the key topics of this work. We mostly describe and discuss the evolution of single (isolated) stars⁴.

1.1 Massive star evolution

The initial mass of a star basically determines how the object will evolve. After hydrogen and helium in the stellar core is exhausted, the evolution of massive stars differs significantly from those with lower masses. In massive stars, the weight of the outer layers compresses the carbon-oxygen core until it becomes hot enough to fuse carbon and oxygen into heavier nuclei. This cycle of contraction and heating repeats, successively producing heavier elements like neon, magnesium, silicon, sulfur, argon, calcium and, finally, iron. An “onion-like” structure develops, where each layer is composed by a different chemical element. The last fusion processes happen extremely fast (years) compared to the million years a massive star spends in its main-sequence phase.

The limit for the fusion of elements is iron; after that, stellar collapse is inevitable, since iron is the most tightly bound nucleus, and no further energy can be extracted by fusing to even heavier nuclei (in fact, fusing to heavier nuclei takes energy). The synthesis of iron is the last step in the sequence of element production. Until that, every fusion reaction produces energy since each product of the process is more stable than the atom(s) that formed it. In other words, a light nuclei gives up some of its energy in the fusion process to form stronger bound, heavier nuclei. This release of energy counteracts the inward pushing gravity. This balance of forces is named hydrostatic equilibrium. When the nuclear reactions cease, the core is supported by the outward pressure originating from the compressed electrons, similar to the physics seen in white dwarfs⁵. In case of stars with initial mass higher than $10M_{\odot}$, this core is mainly made of iron⁶. At some point the iron core becomes too heavy (hundred billion times the density of water) and it forces the remaining electrons to combine with protons, forming neutrons and neutrinos. Depending on the stellar mass at this point, the neutron core can stop the infalling nuclei with an outward pressure even stronger than that from the compressed

⁴ Due to interaction with their companion, (close) binaries may evolve differently (e.g. Vanbeveren et al. (1998), Langer et al. (2008), de Mink et al. (2013)).

⁵ These are the final evolutionary stages of stars without enough mass to form a neutron star. They are very dense with a mass comparable to the Sun, however, compressed to an Earth-like volume.

⁶ Low mass stars never become hot enough to form iron, and their core is likely formed by oxygen, neon and magnesium.

electrons. Then a relatively stable state, called a neutron star (this is not valid for stars with initial mass higher than $40M_{\odot}$, see below), is reached.

The core of the star remains stable when the collapse is stopped by the process forming neutrons, while the outer layers of the star are repelled. During the formation of the neutron core, each time an electron and a proton merge to make a neutron, energy is released by neutrino particles. The neutrinos interact only weakly with matter. However, the matter in the collapsing star envelope is so dense, that neutrinos can interact with it and input their energy in the layers of the star near the core. This energy, again produced in the stellar core, stops the infall of the external layers and may actually reverse it outwards. Apart from the mass concentrated in the neutron core, all the rest is blown away in a core collapse supernova. This is one of the basic mechanisms through which massive stars influence chemically the Universe, and how these stars (in their late evolutionary phases) may trigger star formation through the shock wave turbulence caused in the nearby molecular clouds. The Universe is also enriched due to nuclear reactions produced in the shock wave. But even more, the supernovae eject energy, and particles that combined with heavy elements (iron for example) produce heavier elements like gold, silver and uranium. The chemical enrichment of the interstellar medium (ISM) plays also a role in the formation of Earth-like planets.

What if the neutron formation energy is not strong enough to stop the infalling star envelope? For very massive stars not even the newly formed neutrons can stop the collapse of the core. In this case the stellar core collapses to a black hole. The recently created black hole swallows the outer envelopes of its progenitor star. Theoretically, mass and energy may be released along the rotation axis of the black hole when the matter of the just-extinguished star is gravitationally attracted to the center of the singularity, yielding then a gamma-ray burst.

1.1.1 Phases of evolution

The term “high-mass stars” comprises different types of stars. Stellar evolution theory uses the Hertzsprung-Russell diagram (HRD, Hertzsprung 1911, Russell 1913) to compare evolutionary predictions with observed quantities of actual stars. The main idea is to study the relation between absolute magnitude or luminosity and stellar spectral type or effective temperature (T_{eff}). There are also alternative diagrams that follow the method of the HRD, but use different quantities as for example the spectroscopic HR diagram (sHRD, see Langer & Kudritzki 2014). These diagrams can be used for characterizing the evolutionary stage of an object, since the stars follow an unique track through these diagrams mostly depending on their initial masses, and also significantly influenced by their mass-loss and rotation (further details in Chapter 4). We quickly review the different phases in the life of the massive stars before describing the physics along their evolution.

OB stars are hot massive main-sequence stars with O or (early) B spectral type⁷. O stars have masses above $15M_{\odot}$, and effective temperature between 30 to 55kK. Their spectra display mostly absorption lines of H/He and different stages of ionization for different metals (C II/III/IV, N II/III/IV/V, O II/III). Giants and supergiants may also display emission by the so-called the P-Cygni lines, whose

⁷ Based on their spectral features, stars are divided into different spectral types. These types indicate the temperature of the star and form the sequence OBAFGKM running from the hottest to the coolest.

characteristic profiles are shaped by a stellar wind. On the other hand, early B dwarfs (B0-B2) have lower temperature (from 22kK to 30kK) and are less massive (between 8 and $15M_{\odot}$). For these stars the higher ionization stages of metals are rarely seen, but it is still possible to identify different ionization stages of one atomic species. Recently, Smith (2014) published a complete review of the evolution and fate of these objects. Example for an O-type supergiant: ζ Puppis.

Blue Supergiants (BSG) are evolved stages from the previously described (O and early B) stars, when those finish their H-burning phase and begin to process helium in their cores. For stars with initial mass between 10 and $40M_{\odot}$, BSG form a transitional phase before the red supergiants (see below). Otherwise, in case of very massive stars ($>40M_{\odot}$), a BSG episode may not happen (Maeder 1999 and references therein) and the star evolves directly to a Wolf-Rayet star (described below). Their spectral type are late B and early A. Example: Rigel.

Yellow Supergiants (YSG) is a short and transitional phase for binaries and single-stars also during the helium burning. When a blue supergiant expands, its temperature decreases and the star becomes redder passing then briefly to a yellower color along this transition, which repeats when a RSG evolves back to BSG. These are rare objects and appear in the “middle” of the HR diagram, possibly as post-RSG stars and usually with strong mass loss (see next section). These stars are normally classified spectroscopically as F0-G9. Our present knowledge of these objects was recently summarized by Drout et al. (2012). Example: α Leporis.

Red supergiants (RSG) are also in a He-burning stage of their evolution that has begun as an intermediate-mass OB-star. RSGs have the largest radii among the phases here described (although, they are far from being the most massive), and are of spectral type K to M with a spectrum dominated by molecular absorption lines. They are the coolest evolved massive stars. In the lower mass regime ($10M_{\odot} \leq M < 25M_{\odot}$), this is the last phase before a supernova. On the other hand, for initial stellar masses $\sim 40M_{\odot}$, the RSG phase is brief, and evolves back to the BSG or a Wolf-Rayet phase (see below). Levesque (2010) summarized recently the latest advances in our understanding of these objects. Example: Betelgeuse.

Luminous Blue Variable (LBV) is also a transitional phase, in this case from O-type to Wolf-Rayet stars (see Vink 2009 for a concise review). With large masses and high luminosity, their lifetime is short (only a few million years), mostly with strong winds and an emission-line spectrum. This evolutionary phase takes place in the latest phases of core hydrogen burning (LBV with high T_{eff}), hydrogen shell burning (LBV with low T_{eff}) and the earliest part of He-burning (LBV with high T_{eff}), again before transitioning to Wolf-Rayet stars. These objects evolve in observable timescales and have been observed as the progenitor stage of massive stars supernovae, at least for stars with initial masses between 20 to $25M_{\odot}$. Example: η Carinae.

Wolf-Rayet (WR) stars are the cores of a progenitor that lost its envelope by a strong stellar wind ($\dot{M} \sim 5 \cdot 10^{-6}$ to a few $10^{-5}M_{\odot}\text{yr}^{-1}$). WR-stars themselves have the strongest winds. Their spectrum

Table 1.1: The different phases of evolution during the lifetime of massive stars, depending mainly on their initial masses, but also on initial rotational speed (as summarized by Maeder & Meynet 2010).

Initial Mass (M_{\odot})	Finish its evolution as a	Stages of evolution
10 - 25	Supernova that leaves a neutron star	O-RSG-SN
25 - 30	Supernova that leaves a black hole	O-BSG-RSG \leftrightarrow BSG(blue loop)-RSG-SN
30 - 40	”	O-BSG-RSG \leftrightarrow WN-WC-SN
40 - 60	”	O-BSG-LBV \leftrightarrow WN-WC-SN
60 - 90	”	O-WN \leftrightarrow LBV-WC-SN
> 90	”	O-WN-WC-SN

is dominated by emission lines partly from an optically thick stellar wind. Depending on the strength of these lines, the WR-stars have different classifications, basically separated into carbon (WC) or nitrogen (WN) rich⁸. In the case of WR stars, the nitrogen enrichment is a product of the H-burning while the C is a sign of He-burning, and therefore WC stars are believed to be more evolved than WNs. Crowther (2007) summarized our modern knowledge about these objects. Example: WR 22

Table 1.1 details which of these evolutionary stages (described above) a star will most probably pass, depending on its initial mass. The objects analyzed throughout this work (with minimum mass $\sim 20M_{\odot}$) will most probably finish their life the same way, as core-collapse SNe. Maeder & Meynet (2010) detail the fate of massive stars.

In contrast to low-mass stars (Shu et al. 1987), there is no well established evolutionary sequence to describe the formation of massive stars. A key difference between the formation of low and high mass stars is the radiation field, which plays a remarkable role in hot stars since it heats and eventually ionizes the gas and dust of the protostellar envelope. This surrounding shell of heated dust is observable in the infrared, but makes the direct observation of the proto-massive embryo difficult. Indeed, high-mass prestellar cores have still to be observed. Thus, in the case of hot stars, the term “protostar” refers not only to the very young massive star but also to its birth cocoon. The massive star becomes finally observable only when its radiation field is strong enough to dissipate its surrounding dust. A potential consequence of that point is the lack of present observation of hot stars close to the ZAMS (we return to this discussion in Chapter 4).

The evolutionary paths described so far consider the scenario of single stars. However multiple factors can influence the evolution of a star besides its initial mass, as for example the presence of one (or more) companion(s) forming a binary (or multiple) system, strong stellar winds and rotational velocity (inherited from the molecular cloud that formed the star). We concentrate on the study of presumably single stars along this work.

The population III stars, also called “first stars”, are worth to be noted in the discussion of massive

⁸ there are also WO stars and WNh-stars.

star evolution. These ancient objects are theoretically born out of primordial material from the Big Bang with virtually no metals, maybe except for some trace of nearby (previous) population III supernovae products. Their existence is inferred theoretically, but they have not been observed directly. However, indirect evidences of these objects have been found in gravitationally lensed distant galaxies (see Fosbury et al. 2003). Obviously, many points differ in the physical description of the population III and population I objects (that we study in this work). Still, the first stars are believed to also have been massive and played a crucial role in the formation of the Universe as we presently observe, in particular regarding reionization and first chemical enrichment.

1.2 Mass loss through stellar winds

All hot stars expel part of their mass through radiatively driven winds. Massive stars of spectral type O, B and A with luminosity higher than $10^4 L_{\odot}$ show spectroscopic evidences of winds throughout their lifetime (Abbott 1980). The radiative output of high-mass stars is so intense that photon momentum transfer can drive a strong wind via spectral line scattering and absorption. The wind features are observable over the whole wavelength range, from X-rays to the radio. These spectral features can be analysed in medium or high resolution spectra of blue supergiants out to ~ 20 Mpc (Kudritzki & Puls 2000) as well as in starburst regions of distant galaxies (out to redshifts $z \sim 4$, Steidel et al. 1996). In extreme cases, massive stars can lose 90% of their mass through winds, which obviously influences the structure and evolution of those stars considerably. This last part calls the attention to the importance of understanding such winds and the impact on stellar evolution, in order to enable also the interpretation of these winds in more complex cases and for distant objects. Stellar winds can provide outstanding information about different objects, and deserve a quick overview before we proceed further.

Line scattering is the main contributor to the overall radiative acceleration. In the wind of a massive star, momentum is transferred from the photospheric radiation to the gas through absorption and scattering by UV metal lines (Lucy & Solomon 1970, Castor et al. 1975). Therefore, the rate of mass lost by the star through this mechanism (radiative acceleration) should in principle scale with luminosity, temperature (i.e. ionization stages) and metallicity (Puls et al. 2008). The main concept in momentum transfer by line scattering is that the incoming photons move in a particular direction (roughly radial), while the subsequent re-emission is nearly isotropic. The angle formed by these two directions leads to a transfer of momentum (detailed by Puls 1987),

$$\Delta P = \frac{h}{c}(v_{in} \cos \theta_{in} - v_{out} \cos \theta_{out}) \quad (1.1)$$

and is the key for radiative line acceleration. Integrating this momentum change over all scattering events, the losses and gains due to re-emission cancel (almost⁹) because of symmetry, and it results in a total (radial) acceleration (Puls et al. 2008 present a concise description of the physics involved).

The hot star winds are mainly characterized by two parameters: the terminal velocity (v_{∞}) and the mass-loss rate (\dot{M}). Since these winds are initiated and then continuously accelerated by spectral line

⁹ there is only partial cancellation when lines overlap

absorption and scattering of photons, the velocity reached at large distances from the star corresponds to the maximum velocity of the stellar wind (v_∞). Afterwards the radiative acceleration should tend to zero due to geometrical dilution of the radiation field. Assuming that winds are stationary and spherically symmetric (within the so-called standard model), the continuity equation reads:

$$\dot{M} = 4\pi r^2 \rho(r) V(r), \quad (1.2)$$

where $\rho(r)$ and $V(r)$ are the average mass density and the velocity at a particular radius, respectively. The high mass loss imprints a characteristic signature on the spectral energy distribution (SED) and spectral lines of these objects. To obtain the wind parameters from observations is non-trivial, and requires detailed models including realistic opacities.

Stellar wind parameters are no direct observables. Their determination relies on stellar atmosphere models including the effects of winds. Therefore any “observed wind property” is based on comparing observed spectra with synthetic spectra from theoretical models, and the reliability of results strongly depends on the wavelength regime used and on the reliability of the adopted code. The theoretical reproduction of some parts of the observed spectra (quantitative spectroscopy) provides a good illustration for such discussions. Recombination lines like H_α and He II 4686, for example, may be used as indicator of wind density, as well as the strength of blueshifted P-Cygni absorption features in UV resonance lines (e.g, Puls et al. 2008). However quantitative spectroscopy has its own difficulties, e.g.: rotation and atmospheric turbulent motions act as broadening mechanisms for the shape of a spectral line; radial motions of the star in relation to the observer (Earth) shift the observed wavelengths as a whole; the quality of the observing equipment itself reflects in the resolution of the spectra. Finally, the wind parameter diagnostics have also their own challenges, e.g, due to wind instabilities induced by the line acceleration itself.

Because of these instabilities, winds may be inhomogeneous and deviate from spherical symmetry (see Owocki et al. 1988, Owocki & Puls 1999, Hillier 1991). H_α , He I, and He II emission lines are (mostly) formed from recombination processes, such that their emissivity varies with ρ^2 , while the P-Cygni absorption though depends linearly on ρ . This raises a problem. If only small-scale inhomogeneities (known as “clumps”) are considered, then recombination emission arising in dense clumps is stronger than if the same mass was distributed homogeneously through the wind (mathematically, $\langle \rho^2 \rangle > \langle \rho \rangle^2$). In other words, many diagnostic methods of the wind features may rely on processes with opacities proportional to ρ , but the determination of \dot{M} , for example, is usually done through ρ^2 dependencies (H_α , IR or radio).

Nowadays it is generally accepted that hot star winds have a time-dependent and inhomogeneous structure consisting of shocks and clumps. Thus, if determined by H_α and assuming a smooth wind, the mass-loss rate is overestimated by a factor of $\sqrt{f_{cl}}$, which is typically defined as $f_{cl} = \langle \rho^2 \rangle / \langle \rho \rangle^2$ and called the “clumping factor” (always greater or equal than 1, see Puls et al. 1996, Kudritzki & Puls 2000 for further discussion). In this case, the analysis of the UV part of the spectrum may be of great help since it is less affected by clumps. Fullerton et al. (2006) proposed a reduction by a factor of 10 or more from previous \dot{M} determinations using the optical wavelength regime (adopting f_{cl} values of ~ 100), while Bouret et al. (2005) estimated reductions by factor of ~ 3 also analyzing the optical. Additionally, microclumping assumes that the structures are optically thin. However, there are also processes which become optically thick (e.g., UV lines) in these clumps, leading to so-called

porosity effects (e.g., Oskinova et al. 2007, Sundqvist et al. 2011, Šurlan et al. 2013, Sundqvist et al. 2014, Sundqvist & Puls 2018).

Sophisticated model atoms become imperative for a better description of ionization and excitation stratification in the stellar atmosphere. Recently, much work has been invested in the description of radiative and collisional transitions in order to properly reproduce the observations (Pauldrach et al. 2001, Nieva & Przybilla 2008, Rivero González et al. 2012a, Carneiro et al. 2018). In this respect, the precision of the data plays a main role in the quality of the results. A sequence of choices have to be made before and during the development of model atoms, mainly regarding the temperature range of the stars that will be analyzed, as for example, the number of energy levels that will be accounted for (we discuss this topic further in Chapter 3). The reproduction of P-Cygni profiles formed by the so-called super-ionized ions (e.g., O VI) challenges the completeness of atomic models as well.

Stellar winds are X-ray emitters. O stars as soft X-ray emitters were among the first detections from the EINSTEIN observatory (Harnden et al. 1979, Seward et al. 1979). Subsequently, it was found that the X-ray luminosity is closely correlated with stellar luminosity by $L_x/L_{\text{bol}} \approx 10^{-7}$ in O stars (Chlebowski et al. 1989, Sana et al. 2006, Nazé et al. 2011). Stellar wind embedded shocks are thought to be responsible for this X-ray emission (Lucy & White 1980, Lucy 1982, Cassinelli & Swank 1983), and result from the strong hydrodynamic instability of radiation driven winds (see above). Hillier et al. (1993) determined shock temperatures, filling factors¹⁰ and onset of X-ray emission, assuming randomly distributed isothermal¹¹ shocks in the stellar wind, where the hot shocked gas is collisionally ionized and excited, and the emitted photons might then be absorbed by the cooler wind material (in Chapter 2, we explore the description of emission from such embedded shocks). This first model was able to reproduce the soft X-ray emission, but not the hard X-ray tail. Feldmeier (1995) relaxed the assumption of isothermal shocks and extended these models accounting for a structured wind with radiative and adiabatic cooling parts. Feldmeier et al. (1997a,b) stratified the shocks including post-shock cooling zones for radiative and adiabatic shocks and concluded that cloud collisions produce a significant part of the X-ray emission. These models retain the possibility of reproducing the previous stationary models, while also solving known problems as for example the reproduction of hard X-rays plus the superionization. The inclusion of X-rays in the atmospheric models affect the ionization balance of many atoms (Pauldrach et al. 1994, Krtička & Kubát 2009, Bouret et al. 2012, Carneiro et al. 2016), therefore its effect, even if indirect, becomes significant.

In our case, the ionization energy of the ions we will study is basically what guides the necessity of including wind embedded shocks or not. When analyzing the first to the third ionization stage of any atom, the splitting of the outermost (valence) electron plays the main role in the description of the ionization fraction. However, to interact with electrons closer to the atomic nuclei, higher energies are required for the ionization process, and might be provided by X-ray photons. Nevertheless, for many early-B and late-O stars, the fraction of high ionization stages (e.g., C V, N V, O VI) is almost negligible, and the inclusion of X-ray emission may be relaxed in the analysis. In other words, the necessity of including shock radiation in the chemical abundance determination is basically set by the temperature range of the studied object, and the considered atoms.

¹⁰(Volume) Fraction of X-ray emitting material.

¹¹These shocks are named isothermal due to their almost immediate cooling in the post-shock region.

The reproduction of two or more ions of the same atomic species in a chemical abundance analysis increases considerably the reliability of the obtained results. As written previously, a precise description of X-rays in the atmospheric models impacts the ionization balance of mainly higher ionized atoms, and the simultaneous reproduction of lines of multiple ions is only possible with a plausible description of the stellar and wind parameters. Additionally, the combination of UV and optical analysis gives a very strong evidence about the consistency of the results, where the UV analysis particularly demands the inclusion of shock radiation and clumps in the atmospheric models since strong UV-lines are formed in the wind.

Due to the (often) large mass-loss rates, the inclusion of stellar winds turns out to be essential for the understanding of stellar evolution. Thus a big effort was made in the end of the last century to include the mass-loss in stellar evolutionary models (Schaller et al. 1992, Bressan et al. 1993, Meynet et al. 1994, Fagotto et al. 1994a,b,c, Girardi et al. 1996, are some examples from different groups), and some problems have been solved, e.g., the better agreement with the observed number ratio of WR-stars to O stars at different metallicities (Maeder & Meynet 1994). On the other hand, other problems were still not solved, as for example the observed abundance anomalies in several OB-stars, mostly referring to a nitrogen enrichment (Herrero et al. 1992, 2000). With the inclusion of rotation, the ambiguous abundances as observed in O-type stars have been better understood.

1.3 CNO evolution and internal mixing

Indeed, rotation plays a key role in the determination of stellar lifetimes, evolutionary tracks in the HRD, chemical yields, final stellar masses, etc. Usually, hot massive stars are fast rotators (e.g., Simón-Díaz & Herrero 2014), even though rotation was considered a second-order effect for a long time. New evolutionary models including mass-loss and rotation (Meynet & Maeder 2000, Heger & Langer 2000, Heger et al. 2000, Maeder & Meynet 2001) were calculated and could solve, at least basically, the problem of atypical abundances. Rotationally induced chemical mixing then became a key feature to understand stellar chemical evolution.

Rotation modifies the evolution of stars through different physical effects: it lowers the effective gravity (due to centrifugal acceleration), it flattens the chemical gradient in the stellar interior, enhances the mass-loss rates, and distorts the stellar photosphere, since it induces deviations from spherical symmetry. Direct consequences are, e.g.:

- Rotational mixing transports fresh hydrogen from the stellar envelope into the core, resulting in a more massive He-core at the end of the MS and producing evolutionary tracks that extend to lower T_{eff} .
- As hydrogen is transported to the stellar interior, rotating stars have a (~40%) longer MS life compared to non-rotating models.
- At the same time rotational mixing transports H-burning products to the stellar envelope and photosphere. In particular He decreases the opacity and leads to an increase in luminosity.

- Compared to non-rotating models, the mass loss of rotating stars is increased, mainly due to the higher luminosity, which in combination with the longer MS phase produces smaller final masses.

The effects of rotation on the stellar models were detailed by Heger & Langer (2000), Maeder & Meynet (2000b), and Meynet & Maeder (2000).

Rotational induced mixing is one of the major consequences of including rotation in the calculation of atmospheric models, and plays a key role in our study. Due to mixing, CNO-cycle processed material produced in the stellar interior may reach the stellar surface at early evolutionary stages and consequently modify the observed photospheric abundances.

The CNO-cycle is one of the two processes by which stars convert hydrogen to helium; the other is called the proton-proton chain. The first is present in high (and intermediate) mass stars, and is a catalytic process, i.e., the total number of C, N, and O nuclei is not changed, but the different isotope concentrations are modified. This leads to an increase of nitrogen in parallel with a depletion of carbon and oxygen, the latter to a lesser extent and mainly at later phases.

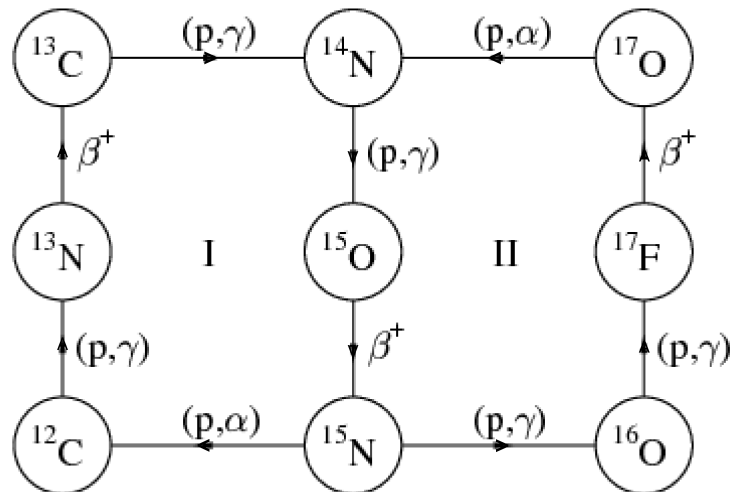


Figure 1.1: Schematic picture of the CNO cycle. The left rectangle (I) represents the CN-cycle while the right rectangle (II) stands for the NO cycle. The notation between the atoms in the form of $X(a,b)Y$ means that the nucleus X captures the particle “ a ” and emits “ b ”, resulting in Y . β^+ indicates a beta plus decay (positron emission). Arrows indicate the nuclear reactions sequence for both cycles. Figure adapted from Maeder (2009).

Figure 1.1 displays a scheme of the CNO-cycle which is the combination of two (almost) independent cycles: the CN-cycle represented in the left rectangle (I) of the figure and the NO-loop displayed by the right rectangle (II). The first cycle converts the initial carbon nucleus into ^{14}N which becomes the most abundant isotope. Within the first reactions, $^{14}\text{N} + ^1\text{H} \rightarrow ^{15}\text{O} + \gamma$ is the slowest one, and

while the abundant ^{14}N ‘waits’ to be transformed into ^{15}O , it can be mixed from the upper core into the stellar surface. Therefore during the CN-cycle, the nitrogen is enriched at the expense of carbon, while oxygen remains constant. As the conversion of ^{14}N to ^{15}O is the slowest reaction, it acts as a “bottleneck” and:

- some of the “fresh” nitrogen may reach the stellar surface due to rotational mixing;
- some of the nitrogen will form ^{15}N and eventually, the nitrogen-15 nucleus captures a fast-moving proton and breaks down into a carbon-12 nucleus plus a helium nucleus (alpha particle);
- a small fraction of ^{15}N triggers the formation of ^{16}O , and the NO-cycle starts.

The amount of ^{16}O produced after the proton capture by ^{15}N is low. Approximately 10^3 cycles are required before a significant number of CN nuclei are transferred to the NO-loop. Consequently, the CN-cycle reaches equilibrium before the ON-cycle reactions become efficient and both are largely decoupled. Overall, the final surface abundance of carbon decreases, the same is valid for oxygen however less efficiently, whereas nitrogen becomes enhanced. Finally, the ratio of abundances may then be used to trace stellar evolution and rotational mixing efficiency (e.g., Langer et al. 1997, Meynet & Maeder 2000, Heger et al. 2000, Paxton et al. 2013).

As the CN-cycle is considerably faster compared to the ON-loop, the N/C abundance ratio changes already in the initial phase of the MS. The O/N ratio is also affected during the MS, but its variation from ZAMS is flatter than N/C. In the case of non-rotating stellar models, on the other hand, surface chemical abundances remain unchanged throughout most of the stellar lifetime (Brott et al. 2011, Ekström et al. 2012).

Theoretically then, we should see distinct values of N/C and O/N ratios when studying a set of dwarfs and supergiant stars (tested in Chapter 4). It is worth noting, though, that after observational campaigns as the VLT-FLAMES Survey of Massive Stars (Evans et al. 2005, 2006, hereafter FLAMES-I), the OWN survey (Barbá et al. 2010) and the IACOB survey (Simón-Díaz et al. 2011a), there are still problems to reproduce the observational findings with theoretical models even when stellar winds and rotation effects are included. Most likely, the deviations are due to other effects such as *binarity* (e.g., Langer et al. 2008, Sana et al. 2009, 2011) and *magnetic fields* (e.g., Maeder & Meynet 2003, 2004, 2005, Morel et al. 2008, Maeder et al. 2009).

Recent studies pointed out that a significant fraction of massive stars are part of binary systems (e.g., Sana et al. 2008, 2009, 2011, Mason et al. 2009). In the case of close binaries, the primary star (the one with higher mass) may fill the Roche lobe¹² during its MS and transfer mass from its envelope to the companion. Due to this process, the surface nitrogen abundance of the companion may become enriched by a factor of 3 to 5 independent of rotational mixing (Langer et al. 2008).

Magnetic fields may be responsible for the existence of slowly rotating and highly enriched stars. Martins et al. (2012) found evidences for nitrogen enrichments in magnetic slowly rotating Galactic O-stars, and magnetic braking is a potential mechanism to explain such populations (Townsend et al. 2010).

¹²Roche lobe (or Roche limit) is the region around a star in a binary system within which the orbiting material is gravitationally bound to that star. Any material outside this approximately teardrop-shaped region may, depending on its initial location, energy and momentum, either escape the system completely, orbit both stars, or fall onto the binary companion.

1.4 Motivation of this thesis

Taking the previous sections into account, it becomes apparent that quantitative spectroscopy inherits multiple challenges, particularly in the case of massive stars. Modeling their atmospheres (a prerequisite for quantitative spectroscopy) is especially complex due to the strong radiative field emitted by these objects, which leads to departures from local thermodynamic equilibrium (so-called non-LTE or NLTE, which means that the atomic level population no longer follows a Saha-Boltzmann distribution as in cool stars, but must instead be computed explicitly from individual populating and depopulating rates), and the presence of strong, radiation-driven winds (see above). Precise atomic data turn out to be mandatory for a realistic estimate of the ionization stratification throughout the star's atmosphere, which might demand the inclusion of X-ray emission from wind embedded shocks. This chain of dependencies must be split into the specific processes, and each of them investigated separately in order to reach a sufficiently precise model.

One of the major objectives of our research group (namely the Munich massive star group) is the derivation of stellar and wind parameters (particularly, chemical abundances in this thesis) for statistically complete samples, to check and provide constraints for stellar evolutionary models. This thesis gives a first step in this direction, since it extends the present capabilities of our fast performance model atmosphere/spectrum synthesis code `FASTWIND`.

`FASTWIND` was developed in close collaboration between the Munich and the Tenerife hot-star groups (see Santolaya-Rey et al. 1997, Puls et al. 2005, and Rivero González et al. 2012a). One of the reasons for doing so is that the alternative atmosphere code `CMFGEN` (Hillier & Miller 1998) is roughly a factor of 10 slower, which prohibits the analysis of larger samples as planned for the current and future projects. We accounted for high quality observations described later in this work.

The present thesis is a first step towards our goal to analyze large samples of massive stars and constrain evolutionary models. This is done by means of quantitative spectroscopy, particularly regarding CNO abundances. Throughout this work, we improve the tools developed by our working group, test our new implementations and derive state-of-the-art surface chemical abundances.

Once we are in a position to obtain reliable values for carbon, nitrogen and oxygen abundances, we investigate the theoretical predictions with respect to the N/C and N/O abundance ratios within stellar evolution models. This kind of analysis reveals certain problems of our methodology that are still fragile and require further developments. Regarding the analysis, we have a multitude of input parameters for the calculation of atmospheric models, and also large samples to be analyzed. Thus it becomes essential to invest time in automatizing a pipeline for the sake of scalability, efficiency and consistency of our methodology.

Besides a newly developed methodology and the produced results, this work should deliver the tools for eventual future works to explore other complex topics, as for example, quantitative spectroscopy in the ultraviolet range and the consistency of chemical abundances obtained from the optical and the UV.

1.5 Outline of this thesis

In the following, we give an outline of the studies presented within the framework of this thesis. The next three chapters are copies of publications produced within this thesis, which is closed by summarizing the major findings and the possibilities for future investigations.

Chapter 2: Atmospheric NLTE models for the spectroscopic analysis of blue stars with winds: X-ray emission from wind-embedded shocks

The ionization balance in the atmospheres of hot massive stars may be affected by extreme ultraviolet and X-ray radiation. To understand these processes, we included the emission from wind embedded shocks in the `FASTWIND` code. We tested exhaustively our implementation and compared it to similar results published recently. We investigate under which conditions the effects of X-rays are more extreme. In the end, we provide an extensive discussion regarding the use of a constant mass absorption coefficient that may simplify the analysis of the soft X-ray regime.

Chapter 3: Carbon line formation and spectroscopy in O-type stars

Chemical abundance plays a key role in the description of stellar evolution. Mainly in high-mass stars, the CNO abundances are of main importance, because of the CNO-cycle and rotational mixing. We present a detailed description of the carbon atom developed in this chapter, and discuss specific problems related to carbon spectroscopy in O-type stars. We test the sensibility of carbon lines to the variation of different parameters, and demonstrate our capability of reproducing prototypical observations.

Chapter 4: Surface abundances of CNO in Galactic O-stars: A pilot study with FASTWIND

Rotational mixing is a key feature of rotating star models, and there are a variety of theoretical predictions for the chemical evolution of hot-stars. In this chapter, we present a set of semi-automatic tools for measuring and analyzing the observed equivalent widths of strategic optical C, N, O lines from different ionization stages. We compare our results with different theoretical predictions, and provide a pipeline that automatizes many steps of the chemical abundance analysis based on the equivalent width of the observed lines.

Chapter 5: Summary and Conclusions

To close this work, we summarize our main findings and describe the open questions that may be the subject of future investigations thanks to the improvements made in this work.

Chapter 2

Atmospheric NLTE models for the spectroscopic analysis of blue stars with winds: X-ray emission from wind-embedded shocks

This chapter is a copy of Carneiro, Puls, Sundqvist, & Hoffmann (2016), *Astronomy & Astrophysics*, 590, A88, 2016.

Abstract Extreme ultraviolet (EUV) and X-ray radiation emitted from wind-embedded shocks in hot, massive stars can affect the ionization balance in their outer atmospheres and can be the mechanism responsible for producing highly ionized atomic species detected in stellar wind UV spectra.

To allow for these processes in the context of spectral analysis, we have implemented the emission from wind-embedded shocks and related physics into our unified, NLTE model atmosphere/spectrum synthesis code FASTWIND.

The shock structure and corresponding emission is calculated as a function of user-supplied parameters (volume filling factor, radial stratification of shock strength, and radial onset of emission). We account for a temperature and density stratification inside the postshock cooling zones, calculated for radiative and adiabatic cooling in the inner and outer wind, respectively. The high-energy absorption of the cool wind is considered by adding important K-shell opacities, and corresponding Auger ionization rates have been included in the NLTE network. To test our implementation and to check the resulting effects, we calculated a comprehensive model grid with a variety of X-ray emission parameters.

We tested and verified our implementation carefully against corresponding results from various alternative model atmosphere codes, and studied the effects from shock emission for important ions from He, C, N, O, Si, and P. Surprisingly, dielectronic recombination turned out to play an essential role for the ionization balance of O IV/O V (particularly in dwarfs with $T_{\text{eff}} \sim 45,000$ K). Finally, we investigated the frequency dependence and radial behavior of the mass absorption coefficient, $\kappa_{\nu}(r)$,

which is important in the context of X-ray line formation in massive star winds.

In almost all of the cases considered, direct ionization is of major influence because of the enhanced EUV radiation field, and Auger ionization only affects N VI and O VI significantly. The approximation of a radially constant κ_ν is justified for $r \gtrsim 1.2R_*$ and $\lambda \lesssim 18 \text{ \AA}$ and also for many models at longer wavelengths. To estimate the actual value of this quantity, however, the He II opacities need to be calculated from detailed NLTE modeling, at least for wavelengths longer than 18 to 20 \AA , and information on the individual CNO abundances has to be present.

2.1 Introduction

Most of our knowledge about the physical parameters of hot stars has been inferred by means of quantitative spectroscopy, i.e., the analysis of stellar spectra based on atmospheric models. The computation of such models is very challenging, mostly because of the intense radiation fields of hot stars leading to various effects that are absent in the atmospheres of cooler stars, such as the requirement for a kinetic equilibrium description (also simply called NLTE = non-LTE) and the presence of strong, radiation-driven winds.

In recent decades, a number of numerical codes have been developed that enable the calculation of synthetic profiles/spectral energy distributions (SEDs) from such hot stars. Apart from plane-parallel, hydrostatic codes, which can be used to analyze those atmospheres that are less affected by the wind (e.g., TLUSTY, Hubeny 1998; DETAIL/SURFACE, Giddings 1981, Butler & Giddings 1985), all of these codes apply the concept of unified (or global) model atmospheres (Gabler et al. 1989), which aims at a consistent treatment of both photosphere and wind, i.e., including (steady-state) mass loss and velocity fields. Examples of such codes are CMFGEN (Hillier & Miller 1998), PHOENIX (Hauschildt 1992), PoWR (Gräfener et al. 2002), WM-BASIC (Pauldrach et al. 2001), and FASTWIND (Puls et al. 2005, Rivero González et al. 2012a).¹ A brief comparison of these different codes can be found in Puls (2009).

In the present paper, we report on recent progress to improve the capabilities of FASTWIND, which is widely used to analyze the optical spectra of hot massive stars (e.g., in the context of the VLT-FLAMES survey of massive stars, Evans et al. 2008; and the VLT-FLAMES Tarantula Survey, Evans et al. 2011). One of the most challenging aspects of these surveys was the analysis of the atmospheric nitrogen content, which is processed in the stellar core by the CNO cycle and transported to the outer layers by rotational mixing, to derive stringent constraints for up-to-date evolutionary calculations. Though the optical nitrogen analysis of B-stars (dwarfs and supergiants with not too dense winds) could still be performed by a hydrostatic code (in this case TLUSTY, e.g., Hunter et al. 2007, 2008), a similar analysis of hotter stars with denser winds required the application of unified model atmospheres, due to the wind impact on the strategic nitrogen lines (Rivero González et al. 2011, 2012a, Martins et al. 2012). Moreover, because of the complexity of the involved processes, the precision of the derived nitrogen abundances² is still questionable. To independently check this precision and to obtain fur-

¹ The multicomponent code developed by Krtićka & Kubát (2001) that is referred later, was designed to calculate the wind properties and has not been used for diagnostic purposes so far.

² For early-type O stars, this suggests very efficient mixing processes at quite early stages (Rivero González et al. 2012b)

ther constraints, a parallel investigation of the carbon (and oxygen) abundances is urgently needed, since at least the N/C abundance ratio as a function of N/O might be predicted almost independently from the specific evolutionary scenario (Przybilla et al. 2010), and thus allows individually derived spectroscopic abundances to be tested (see also Martins et al. 2015a).

As shown by Martins & Hillier (2012), however, the optical diagnostics of carbon in O stars is even more complex than the nitrogen analysis, since specific, important levels are pumped by a variety of UV resonance lines. Thus, an adequate treatment of UV lines is inevitable, both for the optical diagnostics and to constrain the results by an additional analysis of carbon lines located in the UV. If at least part of these lines are formed in the wind, the inclusion of X-ray and EUV emission from wind-embedded shocks turns out to be essential (see below); this is the main reason (though not the only one) for our current update of FASTWIND. Other codes such as CMFGEN, PoWR, and WMBASIC already include these processes, thus enabling the modeling of the UV (e.g., Pauldrach et al. 2001, Crowther et al. 2002, Hamann & Oskinova 2012) and the analysis of carbon (plus nitrogen and oxygen, e.g., Bouret et al. 2012, Martins et al. 2015a,b for the case of Galactic O stars).

X-ray emission from hot stars has been measured at soft (0.1 to $\gtrsim 2$ keV) and harder energies, either at low resolution in the form of a quasi-continuum, or at high resolution allowing the investigation of individual lines (e.g., Oskinova et al. 2006, Owocki & Cohen 2006, Hervé et al. 2013, Leutenegger et al. 2013b, Cohen et al. 2014b, Rauw et al. 2015). The first X-ray satellite observatory, EINSTEIN, has already revealed that O stars are soft X-ray sources (Harnden et al. 1979, Seward et al. 1979), and Cassinelli & Swank (1983) were the first to show that the observed X-ray emission is due to thermal emission, dominated by lines. Follow-up investigations, particularly by ROSAT, have subsequently allowed us to quantify X-ray properties for many OB stars (see Kudritzki & Puls 2000 and references therein). Accounting also for more recent work based on CHANDRA and XMM-NEWTON, it was found that the intrinsic X-ray emission of “normal” O stars is highly constant w.r.t. time (e.g., Nazé et al. 2013), and that the level of X-ray emission is strictly related to basic stellar and wind parameters, e.g., $L_x/L_{\text{bol}} \approx 10^{-7}$ for O stars (Chlebowski et al. 1989, Sana et al. 2006, Nazé et al. 2011).

Such X-ray emission is widely believed to originate from wind-embedded shocks, and to be related to the line-driven instability (LDI; e.g., Lucy & Solomon 1970, Owocki & Rybicki 1984, Owocki et al. 1988, Owocki 1994, Feldmeier 1995). In terms of a stationary description, a simple model (e.g., Hillier et al. 1993, Cassinelli et al. 1994) assumes randomly distributed shocks above a minimum radius, $R_{\text{min}} \approx 1.5 R_*$. This is consistent with X-ray line diagnostics (e.g., Leutenegger et al. 2013b; see also Rauw et al. 2015) in which the hot shocked gas (with temperatures of a few million Kelvin and a volume filling factor on the order of 10^{-3} to a few 10^{-2}) is collisionally ionized/excited and emits X-ray/EUV photons due to spontaneous decay, radiative recombinations, and bremsstrahlung. The ambient, cool wind then reabsorbs part of the emission, mostly via K-shell processes. The strength of this wind absorption has a strong frequency dependence. For energies beyond 0.5 keV (e.g., the CHANDRA bandpass), the absorption is very modest (e.g., Cohen et al. 2011), whilst for softer X-rays and the EUV regime the absorption is significant, even for winds with low mass-loss rates (e.g., Cohen et al. 1996). In the latter case, only a small fraction of the produced radiation actually leaves the wind.

This simple model, sometimes extended to account for the post-shock cooling zones of radiative and adiabatic shocks (see Feldmeier et al. 1997a, but also Owocki et al. 2013), is used in the previ-

ously mentioned NLTE codes, particularly to account for the influence of X-ray/EUV emission on the photoionization rates.

Since the detection of high ionization stages in stellar wind UV spectra, such as O VI, S VI, and N V (Snow & Morton 1976, Lamers & Morton 1976, Lamers & Rogerson 1978), that cannot be produced in a cool wind (thus, denoted “superionization”), the responsible mechanism was, and partly still is, subject to debate. Because the X-ray and associated EUV luminosity emitted by the shocks is quite strong, it can severely affect the degree of ionization of highly ionized species by Auger ionization (Macfarlane et al. 1993) and even more by direct ionization in the EUV (Pauldrach et al. 1994, 2001). A first systematic investigation of these effects on the complete FUV spectrum, as a function of stellar parameters, mass loss, and X-ray luminosity was performed by Garcia (2005).

In this paper, we present our approach for implementing wind-embedded shocks into FASTWIND to allow for further progress as outlined above, and report on corresponding tests and first results. In Sect. 2.2, our model for the X-ray emission and cool-wind absorption is described along with coupling to the equations of statistical equilibrium. In Sect. 2.3 we present our model grid, which constitutes the basis of our further discussion. Sect. 2.4 provides some basic tests and Sect. 2.5 presents first results. In particular, we discuss how the ionization fractions of specific, important ions are affected by X-ray emission, and how these fractions change when the description of the emission (filling factors and shock temperatures) is varied (Sect. 2.5.1). We compare with results from other studies (Sect. 2.5.1) and investigate the impact of Auger compared to direct ionization (Sect. 2.5.2). We discuss the impact of dielectronic recombination in O V in Sect. 2.5.3, and comment on the radial behavior of the mass absorption coefficient (as a function of wavelength), which is an important issue for X-ray line diagnostics (Sect. 2.5.4). Finally, we present our summary and conclusions in Sect. 2.6.

2.2 Implementation of X-ray emission and absorption in FASTWIND

Our implementation of the X-ray emission and absorption from wind-embedded shocks closely follows the implementation by Pauldrach et al. (2001) for WM-BASIC (see also Pauldrach et al. 1994), which in turn is based on the model for shock cooling zones developed by Feldmeier et al. (1997a, see Sect.2.1). Except for the description of the cooling zones, this implementation is similar to the approaches by Hillier & Miller (1998, CMFGEN, but using a different definition of the filling factor, see below), Oskinova et al. (2006, POWR), and Krtićka & Kubát (2009, hereafter KK09). In the following, we summarize our approach.

2.2.1 X-ray emission

Following Feldmeier et al. (1997a), the energy (per unit of volume, time, and frequency), emitted by the hot gas into the full solid angle 4π can be written as³

$$\epsilon_v = f_X(r)n_p(r)n_e(r)\Lambda_v(n_e(r), T_s(r)), \quad (2.1)$$

where $n_p(r)$ and $n_e(r)$ are the proton and electron density of the (quasi-)stationary, cool (pre-shock) wind, $T_s(r)$ is the shock temperature, and $f_X(r)$ the filling factor related to the (volume) fraction

³ The corresponding emissivity is lower by a factor $1/4\pi$.

of the X-ray emitting material.⁴ Indeed, this definition differs from the formulation suggested by Hillier et al. (1993, their Eq. 2), since we include here their factor 16 into f_X (accounting for the density jump in a strong adiabatic shock). This definition is then identical with that used in WM-BASIC, POWR (presumably⁵), and by KK09, whilst the relation to the filling factor used in CMFGEN, e_s , is given by

$$f_X = 16 e_s^2. \quad (2.2)$$

In principle, Λ_ν is the frequency-dependent volume emission coefficient (“cooling function”) per proton and electron, calculated here using the Raymond-Smith code (Raymond & Smith 1977, see also Smith et al. 2001), with abundances from the FASTWIND input, and neglecting the weak dependence on n_e . We evaluate the cooling function at a fixed electron density, $n_e = 10^{10} \text{ cm}^{-3}$ (as also done, e.g., by Hillier et al. 1993 and Feldmeier et al. 1997a), and have convinced ourselves of the validity of this approximation. We note here that the only spectral features with a significant dependence on electron density are the forbidden and intercombination lines of He-like emission complexes, and even there (i) the density dependence is swamped by the dependence on UV photoexcitation, and (ii) in any case the flux of the forbidden plus intercombination line complex (f+i lines are very closely spaced) is conserved.

In contrast with the assumption of a hot plasma with a fixed postshock temperature and density (as adopted in some of the above codes), in our implementation we account for a temperature and density stratification in the postshock cooling zones, and we note that the decreasing temperature and increasing density should significantly contribute to the shape of the emitted X-ray spectrum (Krolik & Raymond 1985). To this end, we adopt the structure provided by Feldmeier et al. (1997a), and integrate the emitted energy (Eq. 2.1) over the cooling zone,

$$\bar{\epsilon}_\nu = f_X(r) n_p(r) n_e(r) \overline{\Lambda_\nu}(10^{10} \text{ cm}^{-3}, T_s(r)), \quad (2.3)$$

with

$$\overline{\Lambda_\nu}(T_s(r)) = \pm \frac{1}{L_c} \int_r^{r \pm L_c} f^2(r') \Lambda_\nu(T_s(r) \cdot g(r')) dr', \quad (2.4)$$

where r is the position of the shock front and L_c the spatial extent of the cooling zone. In this formulation, the ‘+’ sign corresponds to a reverse shock, and the ‘−’ sign to a forward shock. The functions f and g provide the normalized density and temperature stratification inside the cooling zone, and are calculated following Feldmeier et al. (1997a), accounting for radiative and adiabatic cooling in the inner and outer wind, respectively (see Sect. 2.2.3). We integrate over 1,000 subgrid points within L_c , finding identical results for both $f(r)$ and $g(r)$ as well as for $\overline{\Lambda_\nu}$, compared to the original work (Figs. 1 and 7; 2 and 8 in Feldmeier et al. 1997a). By setting $f = g = 1$, we are able to return to nonstratified, isothermal shocks.

In our implementation, the (integrated) cooling function and, thus, the emissivity is evaluated in the interval between 1 eV and 2.5 keV for a bin-size of 2.5 eV. These emissivities are then resampled

⁴ The actual, local preshock density may be different from its quasi-stationary equivalent, but this difference gets absorbed in the f_X -factor.

⁵ We were not able to find a definite statement, but Oskinova et al. (2006) also refer to Feldmeier et al. (1997a).

onto our coarser frequency grid as used in FASTWIND in such a way as to preserve $\int \varepsilon_\nu d\nu$ in each of the coarser subintervals, thus enabling correct photo integrals for the rate equations.

The immediate postshock temperature, $T_s(r)$, entering Eq. 2.4, follows from the Rankine-Hugoniot equations

$$T_s(r) = \frac{3}{16} \frac{\mu m_H}{k_B} \left(u^2 + \left[\frac{14}{5} a_s^2 \left(1 - \frac{3}{14} \frac{a_s^2}{u^2} \right) \right] \right), \quad (2.5)$$

where u is the jump velocity, μ the mean atomic weight, and a_s the adiabatic upstream sound speed. For simplicity, we calculate the shock temperature from a more approximate expression, neglecting the term in the square bracket, i.e., assuming the strong shock scenario ($u^2 \gg a_s^2$),

$$T_s(r) = \frac{3}{16} \frac{\mu m_H}{k_B} u^2. \quad (2.6)$$

To derive T_s , we thus need to specify the jump velocity u , adopted in accordance with Pauldrach et al. (1994, their Eq. 3) as

$$u(r) = u_\infty \left[\frac{v(r)}{v_\infty} \right]^{\gamma_x}, \quad (2.7)$$

where u_∞ is the maximum jump speed, which in our implementation is an input parameter (on the order of 300 to 600 km s⁻¹, corresponding to a maximum shock temperature, $T_s^\infty \approx 10^6$ to $5 \cdot 10^6$ K for O stars), together with the exponent γ_x (in the typical range 0.5 . . . 2) that couples the jump velocity with the outflow velocity, controlling the shock strength. A parameterization such as Eq. 2.7 is motivated primarily by the observed so-called ‘‘black troughs’’ in UV P-Cygni profiles. Namely, when modeled using a steady-state wind⁶, such black troughs can only be reproduced when assuming a velocity dispersion that increases in parallel with the outflow velocity, which is interpreted as a typical signature of wind structure (e.g., Groenewegen & Lamers 1989, Haser 1995). However, Eq. 2.7 only represents one possible implementation of the radial distribution of wind-shock strengths, and ultimately the user is responsible for her/his choice of parameterization (see also discussion in Sect. 2.6).

The last required parameter is the onset radius of the X-ray emission, R_{\min} . This value is controlled by two input parameters, R_{\min}^{input} and a factor m_x (the latter in accordance with Pauldrach et al. 1994). From these values, R_{\min} is calculated via

$$R_{\min} = \min(R_{\min}^{\text{input}}, r(v_{\min})) \quad \text{with} \quad v_{\min} = m_x a_s. \quad (2.8)$$

For all radii $r > R_{\min}$, the X-ray emission is switched on. R_{\min} values from 1.1 to 1.5 R_* are, e.g., supported by Pauldrach et al. (1994) from their analysis of the O VI resonance lines. Hillier et al. (1993) analyzed the sensitivity to R_{\min} , pointing to indistinguishable X-ray flux differences when the onset is varied between 1.5 and 2 R_* . Recent analyses of X-ray line emission from hot star winds also point to values around 1.5 R_* (e.g., Leutenegger et al. 2006, Oskinova et al. 2006, Hervé et al. 2013, Cohen et al. 2014b), although Rauw et al. (2015) derived a value of 1.2 R_* for the wind of λ Cep.

⁶ See Lucy (1982), Puls et al. (1993) and Sundqvist et al. (2012b) for the case of time-dependent, nonmonotonic velocity fields.

2.2.2 X-ray absorption and Auger ionization

Besides the X-ray emission, we need to compute the absorption by the cold background wind; the optical depths inside the shocked plasma are so low that absorption can be neglected there.

In FASTWIND, the cool wind opacity is computed in NLTE. To include X-ray absorption requires that we (i) extend the frequency grid and coupled quantities (standard⁷ opacities and emissivities, radiative transfer) into the X-ray domain (up to 2.5 keV \approx 5 Å), and (ii) compute the additional absorption by inner shell electrons, leading to, for example, Auger ionization. So far, we included only K-shell absorption for light elements using data from Daltabuit & Cox (1972). L- and M-shell processes for heavy elements, which are also present in the considered energy range, have not been incorporated until now, but would only lead to marginal effects, as test calculations by means of WM-BASIC have shown.

We checked that the K-shell opacities by Daltabuit & Cox (1972) are very similar (with typical differences less than 5%) to the alternative and more modern dataset from Verner & Yakovlev (1995), at least in the considered energy range (actually, even until 3.1 keV).⁸

While the provided dataset includes K-shell opacities from the elements C, N, O, Ne, Mg, Si, and S, the last element (S) has threshold energies beyond our maximum energy, 2.5 keV; hence, K-shell absorption and Auger ionization for this element is not considered in our model.

After calculating the radiative transfer in the X-ray regime, accounting for standard and K-shell opacities and standard and X-ray emissivities, we are able to calculate the corresponding photo rates required to consider Auger ionization in our NLTE treatment. Here, we do not only include the transition between ions separated by a charge difference of two (such as, e.g., the ionization from O IV to O VI), but we follow Kaastra & Mewe (1993) who stressed the importance of cascade ionization processes, enabling a sometimes quite extended range of final ionization stages. For example, the branching ratio for O IV to O V vs. O IV to O VI is quoted as 96:9904, whilst the branching ratios for Si III to Si IV/Si V/Si VI are 3:775:9222; i.e., here the major Auger-ionization occurs for the process III to VI. In our implementation of Auger ionization, we accounted for all possible branching ratios following the data provided by Kaastra & Mewe.

Finally, we reiterate that in addition to such inner shell absorption/Auger ionization processes, direct ionization due to X-rays/enhanced EUV radiation (e.g., of O V and O VI) is essential and automatically included in our FASTWIND modeling. The impact of direct vs. Auger ionization is compared in Sect. 2.5.2.

2.2.3 Radiative and adiabatic cooling

As pointed out in Sect. 2.2.1, the shock cooling zones are considered to be dominated by either radiative or adiabatic cooling, depending on the location of the shock front. More specifically, the transition between the two cooling regimes is obtained from the ratio between the radiative cooling time, t_c , i.e., the time required by the shocked matter to return to the ambient wind temperature, and

⁷ = outer electron shell

⁸ We used data from Daltabuit & Cox (1972) to ensure compatibility with results from WM-BASIC to allow for meaningful comparisons. In the near future, we update our data following Verner & Yakovlev (1995).

the flow time, t_f , the time for the material to cross L_c (expressions for these quantities can be found in Feldmeier et al. 1997a; but see also Hillier et al. 1993). In the inner part of the wind, the cooling time is shorter than the flow time and the shocks are approximated as radiative. Further out in the wind, at low densities, $t_c \gg t_f$, and the cooling is dominated by adiabatic expansion (see also Simon & Axford 1966). In our approach, we switch from one treatment to the other when a unity ratio is reached, where $t_c/t_f \propto T_s(r)^{1.5} r v^2(r)/\dot{M}$. For typical O supergiants and shock temperatures, the transition occurs in the outermost wind beyond $r > 50 R_*$, whilst for O dwarfs the transition can occur at much lower radii, $r > 2.5 R_*$ or even lower for weak-winded stars.

Basically, each cooling zone is bounded by a reverse shock at the starward side and a forward shock at the outer side. Time-dependent wind simulations (e.g., Feldmeier 1995) show that in the radiative case the forward shock is much weaker than the reverse shock and, thus, is neglected in our model. In the adiabatic case, we keep both the reverse and forward shock and, for lack of better knowledge, assume equal T_s for both components ($\Theta = 1$ in the nomenclature by Feldmeier et al. 1997a), and an equal contribution of 50% to the total emission.

2.3 Model grid

In this section, we describe the model grid used in most of the following work. To allow for a grid of theoretical models that enables us to investigate different regimes of X-ray emission for different stellar types and to perform meaningful tests, we use the same grid as presented by (Pauldrach et al. 2001, their Table 5) for discussing the predictions of their (improved) WM-BASIC code.⁹ Moreover, this grid has already been used by Puls et al. (2005) to compare the results from an earlier version of FASTWIND with the WM-BASIC code.

For convenience, we present the stellar and wind parameters of this grid in Table 2.1. For all models, the velocity field exponent has been set to $\beta = 0.9$. The FASTWIND and WM-BASIC models display a certain difference in the velocity field¹⁰.

All entries shown in Table 2.1 refer to homogeneous winds, however, for specific tests (detailed when required) we have calculated microclumped models as well (i.e., assuming optically thin clumps). Although clumping is not considered in our standard model grid, a (micro-)clumped wind could be roughly compared to our unclumped models as long as the mass-loss rate of the clumped model corresponds to the mass-loss rate of the unclumped model divided by the square root of the clumping factor. We note, however, that the K-shell opacities scale linearly with density, i.e., $\propto \dot{M}$, and as such are not affected by microclumping.

All models in the present work were calculated by means of the most recent version (as described in Rivero González et al. 2012a) of the NLTE atmosphere/spectrum synthesis code FASTWIND, including the X-ray emission from wind-embedded shocks as outlined in Sect. 2.2. We further point out that FASTWIND calculates the temperature structure of the photosphere and cold wind from the electron thermal balance (Kubát et al. 1999), and its major influence in the wind is via recombination

⁹ This grid, in turn, is based on observational results from Puls et al. (1996), which at that time did not include the effects of wind inhomogeneities, so that the adopted mass-loss rates might be too large by factors from $\sim 3 \dots 6$.

¹⁰ WM-BASIC calculates the velocity field from a consistent hydrodynamic approach.

Table 2.1: Stellar and wind parameters of our grid models with homogeneous winds, following Pauldrach et al. (2001). For X-ray emission parameters, see text.

Model	T_{eff} (kK)	$\log g$ (cm s^{-2})	R_* (R_{\odot})	v_{∞} (km s^{-1})	\dot{M} ($10^{-6} M_{\odot} \text{yr}^{-1}$)	R_{min} (R_*)
Dwarfs						
D30	30	3.85	12	1800	0.008	1.24
D35	35	3.80	11	2100	0.05	1.29
D40	40	3.75	10	2400	0.24	1.20
D45	45	3.90	12	3000	1.3	1.20
D50	50	4.00	12	3200	5.6	1.23
D55	55	4.10	15	3300	20	1.21
Supergiants						
S30	30	3.00	27	1500	5.0	1.51
S35	35	3.30	21	1900	8.0	1.43
S40	40	3.60	19	2200	10	1.33
S45	45	3.80	20	2500	15	1.25
S50	50	3.90	20	3200	24	1.25

rates. In most cases, this temperature structure is only slightly or moderately affected by X-ray/EUV emission, since the overall ionization balance with respect to main ionization stages¹¹ remains rather unaffected (see Sect. 2.5), except for extreme X-ray emission parameters. In any case, the change of the net ionization rates for ions with edges in the soft X-ray/EUV regime is dominated by modified photo rates (direct and Auger ionization), whilst the changes of recombination rates (due to a modified temperature) are of second order.

In FASTWIND, we used detailed model atoms for H, He, and N (described by Puls et al. 2005, Rivero González et al. 2012a) together with C, O, P (from the WM-BASIC data base, see Pauldrach et al. 2001) and Si (see Trundle et al. 2004) as “explicit” elements. Most of the other elements up to Zn are treated as background elements. For a description of FASTWIND and the philosophy of explicit and background elements, see Puls et al. (2005) and Rivero González et al. (2012a).

In brief, explicit elements are those used as diagnostic tools and treated with high precision by detailed atomic models and by means of comoving frame transport for all line transitions. The background elements (i.e., the rest) are needed only for the line-blocking/blanketing calculations, and are treated in a more approximate way, using parameterized ionization cross sections following Seaton

¹¹These stages dominate the heating/cooling of the cold wind plasma via corresponding free-free, bound-free, and collisional (de-)excitation processes.

(1958) and a comoving frame transfer only for the most important lines, whilst the weaker ones are calculated by means of the Sobolev approximation. We employed solar abundances from Asplund et al. (2009), together with a helium abundance, by number, $N_{\text{He}}/N_{\text{H}} = 0.1$.

Besides the atmospheric and wind parameters shown in Table 2.1, our model of X-ray emission requires the following additional input parameters: f_{X} , u_{∞} , γ_x , m_x , and $R_{\text{min}}^{\text{input}}$, as described in the previous section.

For most of the models discussed in Sect. 2.5, we calculated, per entry in Table 2.1, 9 different sets of X-ray emission: f_{X} (adopted as spatially constant) was set to 0.01, 0.03, and 0.05, whilst the maximum shock velocity, u_{∞} , was independently set to 265, 460, and 590 kms^{-1} , corresponding to maximum shock temperatures of 1, 3, and $5 \cdot 10^6$ K.

For all models, we used $\gamma_x = 1.0$, $R_{\text{min}}^{\text{input}} = 1.5 R_*$, and $m_x = 20$. This corresponds to an effective onset of X-rays, R_{min} , between 1.2 and 1.5 R_* , or 0.1 and 0.2 v_{∞} , respectively (see Table 2.1, last column). Thus, our current grid comprises 9 times 11 = 99 models, and has enough resolution to compare this grid with previous results from other codes and to understand the impact of the X-ray radiation onto the ionization fractions of various elements.

2.4 Tests

In this section, we describe some important tests of our implementation, including a brief parameter study. A comparison to similar studies with respect to ionization fractions (also regarding the impact of Auger ionization) is provided in Sect. 2.5. Of course, we tested much more than described in the following sections. For example, we also tested the following:

(i) The impact of γ_x (see also Pauldrach et al. 2001), particularly when setting γ_x to zero and consequently forcing all shocks, independent of their position, to emit at the maximum shock temperature, T_s^{∞} . In this case and compared to our standard grid with $\gamma_x = 1$, the dwarf models that are cooler than 50 kK display a flux increase of 2 dex shortward of 100 Å (this increase is barely noticeable already for D50), whilst the supergiant models display a similar increase for wavelengths around 10 Å and below. In terms of ionization fractions, setting γ_x to zero results in an increase of highly ionized species (e.g., O VI and N VI) by roughly one dex from the onset of X-ray emission throughout the wind. For all other dwarf models, this increase appears only out to $\sim 4.0 R_*$. The same effect is present in the supergiant models, except for a smaller radial extent.

(ii) We compared the ionization fractions of important atoms when they are either treated as explicit (i.e., “exact”) or as background (i.e., approximate) elements (cf. Sect. 2.3), and we mostly found an excellent agreement (in all cases, the agreement was at least satisfactory) between both approaches for the complete model grid.

(iii) During our study on the variations of the mass absorption coefficient with T_{eff} and r in the X-ray regime (see Sect. 2.5.4), we also compared our opacities with those predicted by KK09 (their Fig. 15, showing mass absorption coefficient versus wavelength), and we were able to closely reproduce their results at least shortward of 21 Å (including the dominating O IV/O V K-shell edge). Our model, however, produces lower opacities on the longward side, thus indicating a different He ionization balance (see Sect. 2.5.4). When comparing the averaged (between 1.5 and 5 R_*) absorption

coefficients in the wavelength regime shortward of 30 Å, KK09 found a slight decrease of 8% after including X-rays in their models because of the induced ionization shift. This is consistent with our findings, which indicate, for the same range of r and λ , a decrease by 9%.

2.4.1 Impact of various parameters

First, we study the impact of various parameters on the emergent (soft) X-ray fluxes, in particular R_{\min} , f_X , and T_s^∞ . For these tests, we used the model S30 (see Table 2.1, similar to the parameters of α Cam (HD 30614, O9.5Ia)) since this object has been carefully investigated by Pauldrach et al. (2001, their Table 9) as well.

Before going into further details, we would like to clarify that the soft X-ray and EUV shock emission are composed almost entirely of narrow lines and that the binning and blending make the spectral features look more like a pseudo-continuum, which is clearly visible in the following figures (though most of them display the emergent fluxes and not the emissivities themselves).¹²

Impact of R_{\min} . The sensitivity of the X-ray fluxes on R_{\min} is shown in Fig. 2.1, where the other parameters were fixed at their center values within our small X-ray grid (i.e., $f_X = 0.03$ and $T_s^\infty = 3 \cdot 10^6$ K). In particular, the shock temperature is quite high for such a stellar model, but was chosen deliberately to allow for somewhat extreme effects.

Indeed, the only visible differences are present in the range between the He II edge and roughly 330 Å. Shortward of the He II edge, all fluxes are identical (though only shown down to 100 Å to allow for a better resolution), since the (cool) wind already becomes optically thick far out in the wind at these wavelengths (He II, O IV, etc. continua, and K-shell processes). For $\lambda \gtrsim 350$ Å, on the other hand, the shock emissivity becomes too low to be of significant impact.

In this context, it is interesting to note that in ϵ CMa (B2II, the only massive hot star with EUVE data) the observed EUV emission lines in the range between 228 to 350 Å *each* have a luminosity comparable to the total X-ray luminosity in the ROSAT bandpass (Cassinelli et al. 1995), which also stresses the importance of this wavelength region from the observational side.

In Fig. 2.2, we show the ratio of the shock emissivity to the total emissivity (including averaged line processes and Thomson scattering), evaluated at the outer boundary of the wind (solid) and at $1.2 R_*$ (dash-dotted), corresponding to the onset of X-ray emission in this model. A number of interesting features are visible:

(i) The total emissivity in the outer wind is dominated by shock emission from just shortward of the He II edge until 2.5 keV (the highest energy we consider in our models). The emissivity in the lower wind, however, is dominated by shock emission only until 200 eV, whilst for larger energies the (local) shock contribution decreases drastically because the assumed shock temperatures ($\propto (v(r)/v_\infty)^2$) are rather low here ($\lesssim 100$ kK). The question is then: Which process dominates the *total* emissivity at high energies in the lower wind? Indeed, this process is the re-emission from electron scattering because it is proportional to the mean intensity and quite high owing to the large number of incoming photons

¹²As shown by Pauldrach et al. (1994), the total shock emissivity is roughly a factor of 50 larger than the corresponding hot plasma free-free emission from hydrogen and helium.

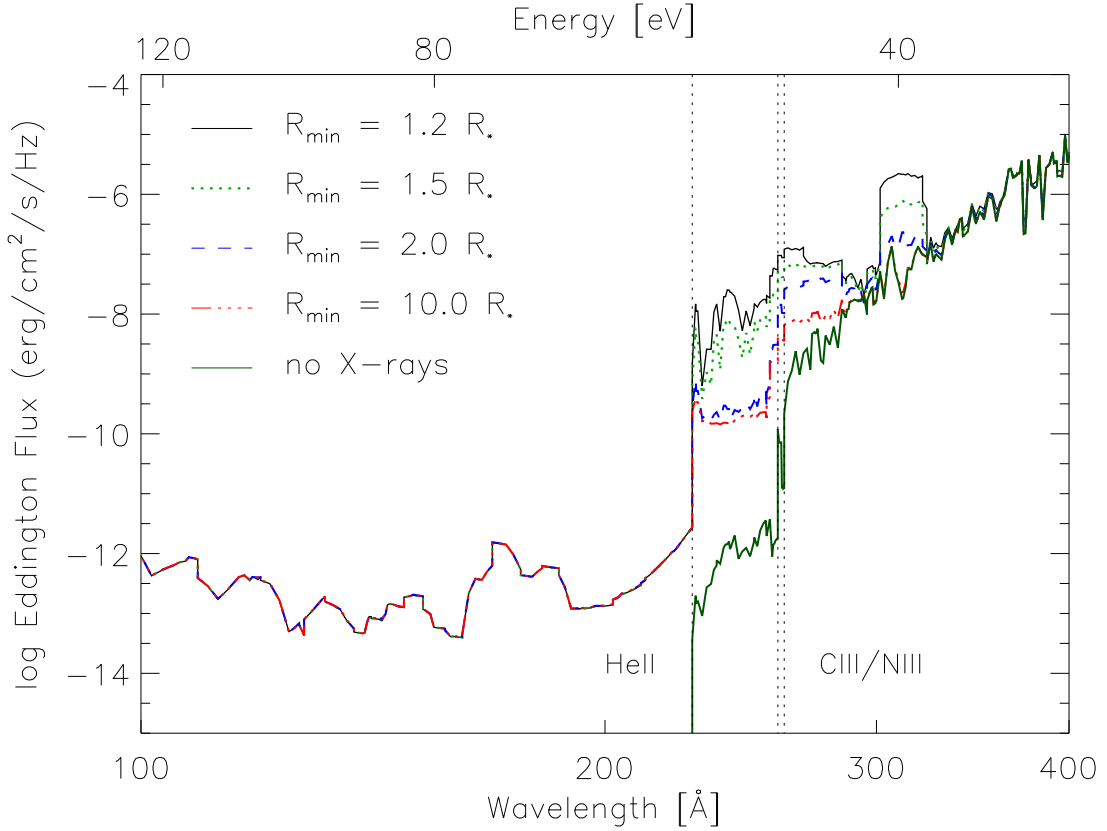


Figure 2.1: Emergent Eddington fluxes for model S30, with $T_s^\infty = 3 \cdot 10^6$ K and $f_X = 0.03$, for different onset radii of X-ray emission, R_{\min} , and for a model with an unshocked wind. The vertical dotted lines refer to the He II, C III, and N III ionization edges, respectively.

from above, i.e., from regions where the shock temperatures are high. This effect becomes also visible in the local radiative fluxes at these frequencies, which are negative, i.e., directed inward.

(ii) Both in the outer and inner wind, the shock emission is also significant longward from the He II edge, until $\lambda \approx 350$ Å, thus influencing the ionization balance of important ions. Whilst the fluxes of models without shock emission and those with $R_{\min} \gtrsim 2R_*$ display a significant absorption edge for C III and N III (see Fig. 2.1), these edges have almost vanished in the models with $R_{\min} = 1.2 \dots 1.5 R_*$ because of the dominant shock emissivity increasing the degree of ionization. Even more, all models display fluxes in this region that lie well above those from models without shock emission because of the higher radiation temperatures compared to the cool wind alone.

(iii) Beyond 350 Å, the shock emissivity becomes almost irrelevant (below 10%), so that the corresponding fluxes are barely affected.

(iv) For the two models in which $R_{\min} = 1.2$ and $1.5 R_*$, a prominent emission feature between roughly 300 and 320 Å is visible in Fig. 2.1. A comparison with Fig. 2.2 (note the box) shows that this emission is due to the dominating shock emission of the lower wind, increasing the temperatures of the radiation field beyond those of the unshocked wind.

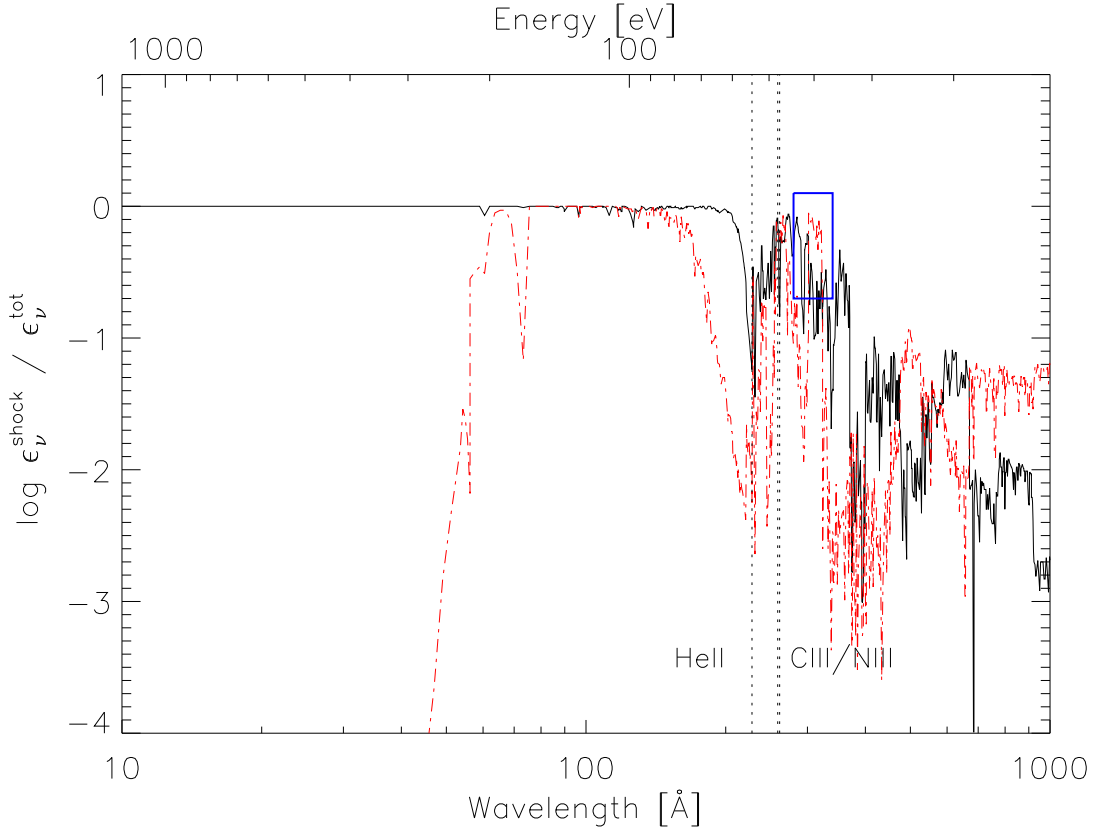


Figure 2.2: Ratio of shock emissivity to total emissivity for model S30 from Fig. 2.1 with $R_{\min} = 1.2 R_*$. Solid line: emissivity ratio at the outer boundary, $r \approx 130 R_*$; dash-dotted line: emissivity ratio at the lower boundary of X-ray emission, $r \approx 1.2 R_*$. The box located between 300 and 320 Å highlights the strong shock emissivity leading to the corresponding emission feature present in Fig. 2.1.

Coming back to Fig. 2.1, significant flux differences between the shocked and unshocked models are visible for all values of R_{\min} (even for $R_{\min} = 2$ or $10 R_*$) below $\lambda \lesssim 350$ Å, particularly below the N III and C III edges as a result of higher ionization.

On the other hand, the models with $R_{\min} = 1.2$ and $1.5 R_*$ are almost indistinguishable, at least regarding the pseudo-continuum fluxes. This turns out to be true also for He II 1640 and He II 4686, although these lines become sensitive to the choice of R_{\min} if we change R_{\min} from 1.5 to $2 R_*$ because of the different intensities around the He II edge and around He II 303 (Lyman-alpha) in the line-forming region. We come back to this point in Sect. 2.5.1.

Impact of f_X . In Fig. 2.3, we investigate the impact of f_X , which has a most direct influence on the strength of the X-ray emission (cf. Eqs. 2.1 and 2.3). Having more X-ray photons leads to higher X-ray fluxes/luminosities and to less XUV/EUV-absorption from the cool wind because of higher ionization stages. The latter effect becomes particularly visible for the model with $f_X = 0.1$, which was used to check at which level of X-ray emission we start to change the overall ionization stratification.

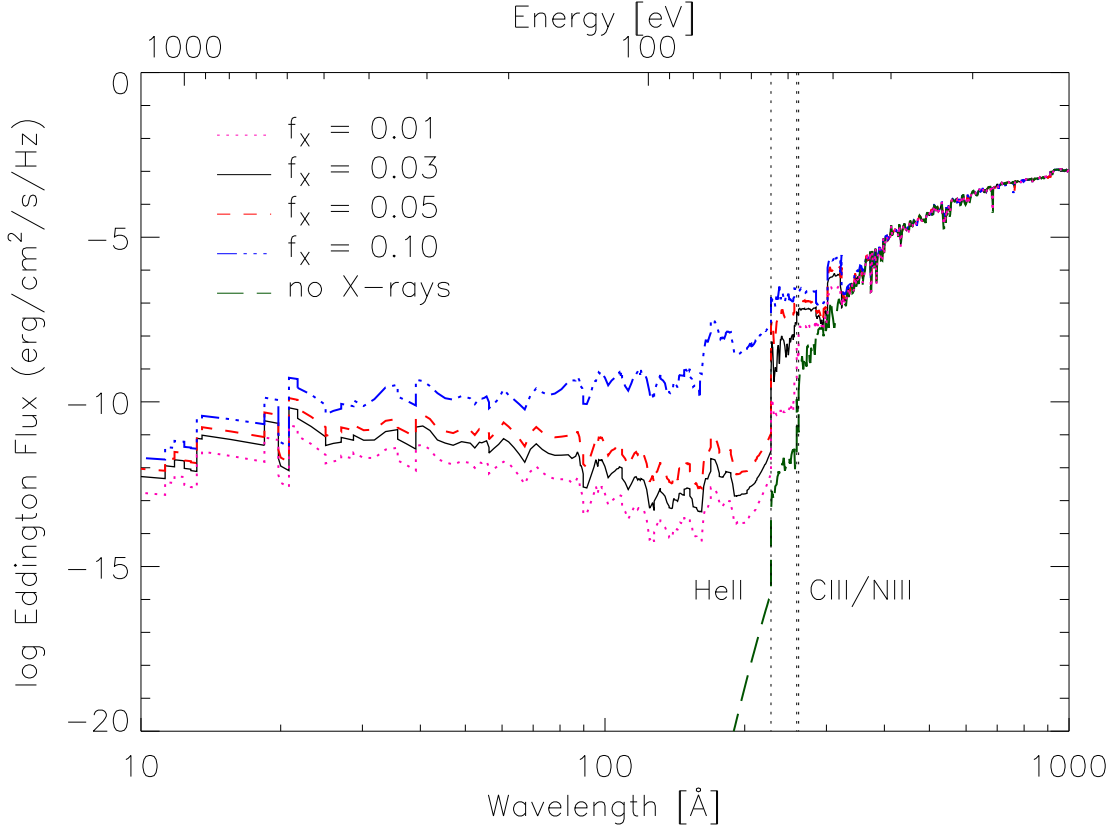


Figure 2.3: Emergent Eddington fluxes for model S30, with $T_s^\infty = 3 \cdot 10^6$ K and $R_{\min}^{\text{input}} = 1.5 R_*$, for different values of f_X , and for a model with an unshocked wind. The histogram-like flux distribution at highest energies results from our resampling of X-ray emissivities (see Sect. 2.2.1).

Most importantly, helium (with He II as the main ion beyond $1.2 R_*$ for S30 models with typical values $0.03 \lesssim f_X \lesssim 0.05$) becomes more ionized, reaching similar fractions of He II and He III between $2.2 R_*$ ($\sim 0.5 v_\infty$) and $8.7 R_*$ ($\sim 0.8 v_\infty$). Also, the main ionization stage of oxygen, which is O IV in S30 models with typical X-ray emission parameters, switches to O V between $1.8 R_*$ ($\sim 0.4 v_\infty$) and $4.0 R_*$ ($\sim 0.7 v_\infty$) when f_X is set to 0.1. The change in the ionization of helium (and oxygen) becomes clearly visible in the much weaker He II edge and much higher fluxes in the wavelength range below 228 \AA , compared to models with lower f_X .

Impact of T_s^∞ . As shown in Fig. 2.4 (see also Pauldrach et al. 2001), the change in the maximum shock temperature, T_s^∞ , becomes mostly visible for the fluxes shortward of $\approx 60 \text{ \AA}$ (of course, the hard X-ray band is even more affected, but not considered in our models). While for the highest maximum shock temperature considered here, $T_s^\infty = 5 \cdot 10^6$ K (corresponding to $u_\infty \approx 590 \text{ km s}^{-1}$), we significantly increase the population of the higher ionized atomic species, this temperature is still not sufficient to change the main ionization stages present in the wind.

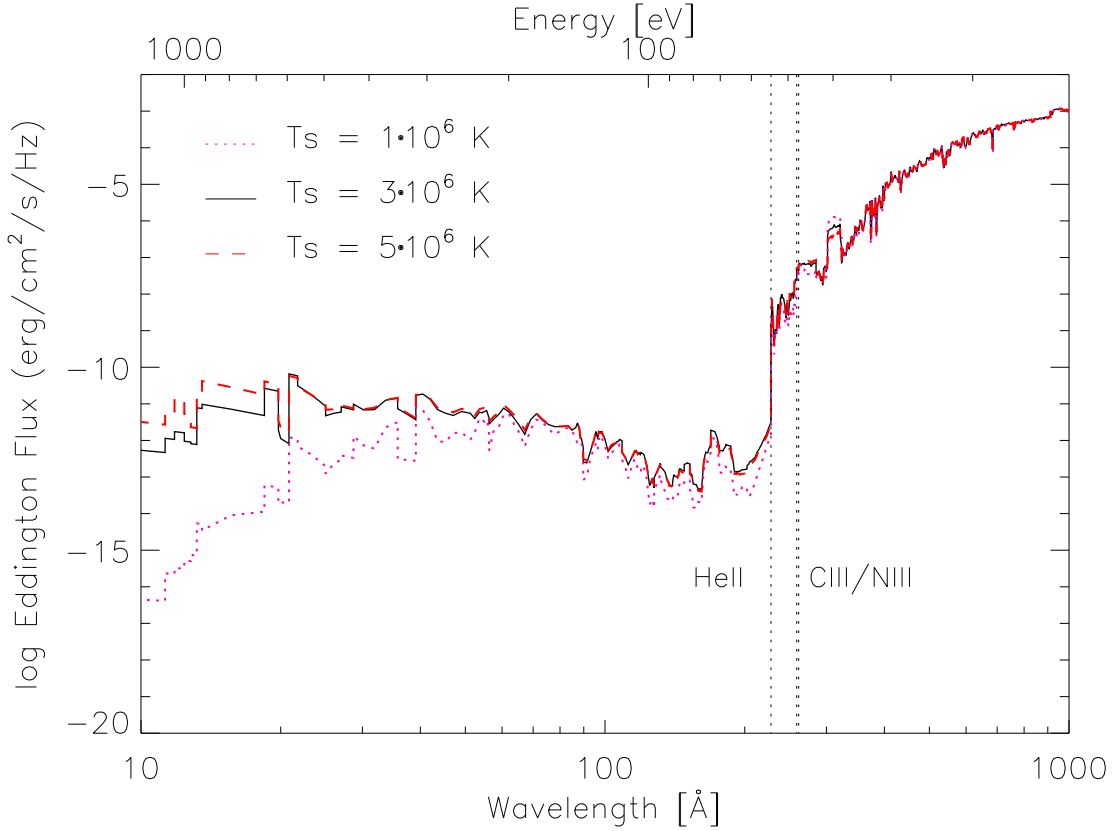


Figure 2.4: Emergent Eddington fluxes for model S30, with $f_X = 0.03$ and $R_{\min}^{\text{input}} = 1.5 R_*$, for different values of maximum shock temperature, T_s^∞

2.4.2 Scaling relations for L_X

From an analytical point of view, Owocki & Cohen (1999) showed that for a constant volume filling factor and, neglecting the effects of radiative cooling (see below), the optically thin (with respect to the cool wind absorption) wind X-ray luminosity depends on the square of the mass-loss rate, $L_X \propto (\dot{M}/v_\infty)^2$, whilst the X-ray luminosity of optically thick winds scales linearly with the mass-loss rate, $L_X \propto \dot{M}/v_\infty$. This is the case provided that one compares models with the same shock temperatures and assumes a spatially constant X-ray filling factor. These relations become somewhat modified if there is a dependence of T_s on the wind terminal velocity, as adopted in our standard X-ray description (see also KK09).

However, in a more recent study Owocki et al. (2013) derived, again from an analytic perspective, scaling relations for L_X for radiative and adiabatic shocks embedded in a cool wind. At first glance, their assumptions seem quite similar to those adopted by Feldmeier et al. (1997a), which is the basis of our treatment, but in the end Owocki et al. predict different scaling relations for *radiative* shocks than those resulting from our modeling. This discrepancy might lead to somewhat different scaling relations for L_X , and needs to be investigated in forthcoming work; for now, we simply compare our

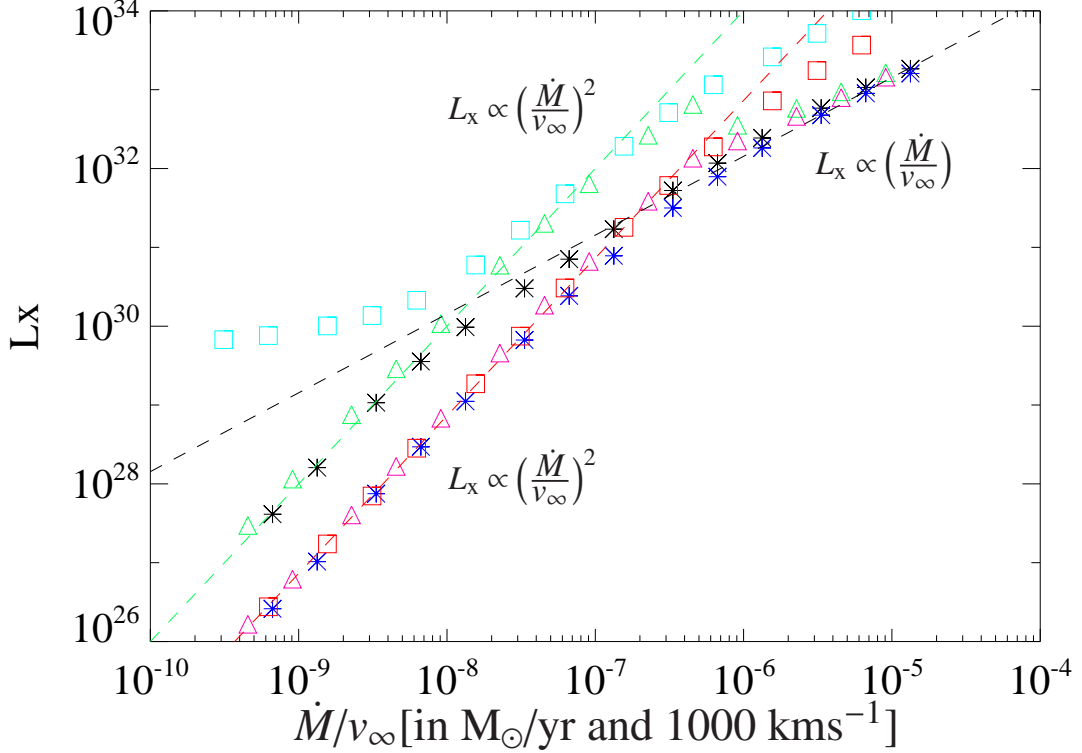


Figure 2.5: Emergent X-ray luminosities (in erg s^{-1}) as a function of \dot{M}/v_∞ . Supergiant models S30 (asterisks), S40 (triangles) and S50 (squares) with $T_{\text{eff}} = 30, 40$ and 50 kK, respectively, and mass-loss rates between 10^{-9} and $2 \cdot 10^{-5} M_\odot/\text{yr}$. All models have the same X-ray properties, $f_x = 0.025$, $\gamma_x = 0.5$, $m_x = 20$, and a maximum jump-velocity, $u_\infty = 400 \text{ km s}^{-1}$, corresponding to maximum shock temperatures of $2.3 \cdot 10^6 \text{ K}$. We calculated the X-ray luminosities in the range $0.1 - 2.5 \text{ keV}$ (black, green, and turquoise) and in the range 0.35 to 2.5 keV (blue, red, and magenta). The dashed lines (no fits) serve as guidelines to check the predicted behavior for optically thin (red and green) and optically thick (black) conditions. (See text.)

models to the earlier results by Owocki & Cohen (1999). A similar test was carried out by KK09.

To this end, we calculated S30, S40, and S50 wind models with a fixed X-ray description: $f_x = 0.025$, $m_x = 20$, and $\gamma_x = 0.5$. For our tests, we used a constant maximum jump velocity, $u_\infty = 400 \text{ km s}^{-1}$ (corresponding to maximum shock temperatures of $2.3 \cdot 10^6 \text{ K}$) for all models to be consistent with the above assumptions.

For these models (with parameters, except for \dot{M} , provided in Table 2.1), we varied the mass-loss rates in an interval between 10^{-9} and $2 \cdot 10^{-5} M_\odot/\text{yr}$. and integrated the resulting (soft) X-ray luminosities in two different ranges: 0.1 to 2.5 keV and 0.35 to 2.5 keV .

From $\dot{M} \gtrsim 10^{-7} M_\odot \text{ yr}^{-1}$ on, the wind becomes successively optically thick at higher and higher energies, although, for example, for $\dot{M} = 10^{-6} M_\odot \text{ yr}^{-1}$ the wind is still optically thin below $\sim 10 \text{ \AA}$, i.e.,

above 1.24 keV. Indeed, the X-ray luminosities of our corresponding models are linearly dependent on (\dot{M}/v_∞) , as can be seen in Fig. 2.5 by comparing them with the black dashed line. For lower \dot{M} , the wind is optically thin at most high energy frequencies and also our results closely follow the predictions ($L_x \propto (\dot{M}/v_\infty)^2$), when comparing the corresponding X-ray luminosities with the red or green dashed lines.

A second finding of Fig. 2.5 relates to the optically thin scaling for model S50, when either starting the integration at 100 eV (turquoise squares) or at 350 eV (red squares). Whilst for S30 (asterisks) and S40 (triangles) the X-ray luminosities just increase by roughly one dex when including the range from 100 to 350 eV but still follow the predicted scaling relation, the S50 models show an increase of four orders of magnitude for the lowest \dot{M}/v_∞ values in this situation (and do not follow the predictions).

To clarify this effect, Fig. 2.6 shows the scaled (scaling proportional to R_*^2 and v_∞^2) Eddington flux as a function of wavelength and energy for supergiant models S30 (black), S40 (green), and S50 (turquoise) with identical, low mass-loss rates, $10^{-8} M_\odot/\text{yr}$. Additionally, energies of 100, 150, and 350 eV are indicated with dotted vertical lines. Beyond 150 eV, all models, independent of their specific parameters, display the same scaled fluxes, thus verifying the optically thin scaling of X-ray luminosities (in this case, only with respect to v_∞). For the S50 model, however, the energy range below 150 eV is contaminated by “normal” stellar/wind radiation, which increases as a function of T_{eff} (see also Macfarlane et al. 1994; their Fig. 5), leading to the strong deviation from the optically thin X-ray scaling law as visible in Fig. 2.5. The same contamination already appears for energies higher than 150 eV for other X-ray parameter sets. Thus, the total X-ray luminosity (regarding the wind emission) of hotter objects might be overestimated when integrating until 100 eV.

In summary, we conclude that our implementation follows the predicted scaling relations, but we also suggest choosing a lower (in energy) integration limit of 0.15 keV (or even 0.3 keV, to be on the safe side) when comparing the X-ray luminosities of different stars (both with respect to models and observations).

In this context, we note that there is a clear distinction between the observable soft X-ray and the longer-wavelength, soft X-ray, and XUV/EUV emission that is almost never directly observed, but, as already outlined, is very important for photoionizing relevant ions. Modern X-ray observatories, such as XMM-NEWTON/RGS and CHANDRA/HETG, do not have a response below 0.35 keV and 0.4 keV, respectively; even a modest ISM column makes it functionally impossible to see X-ray emission below 0.5 keV. We note, however, that ROSAT observed down to 0.1 keV, and EUVE also made a few important measurements relevant for massive stars, in particular, for ϵ CMa (B2II), e.g., Cassinelli et al. (1995).

2.4.3 Comparison with WM-BASIC models

Finally, we also checked the quantitative aspect of our results, by comparing with analogous WM-BASIC models (we note the difference in the velocity fields). As already pointed out, the X-ray description in both codes is quite similar, and there is only one major difference. In WM-BASIC, the user has to specify a certain value for L_x/L_{Bol} (e.g., 10^{-7} as a prototypical value) and the code iteratively determines the corresponding f_x , which is a direct input parameter in the updated version of FASTWIND. In both cases, we used a frequency range between 0.1 to 2.5 keV.

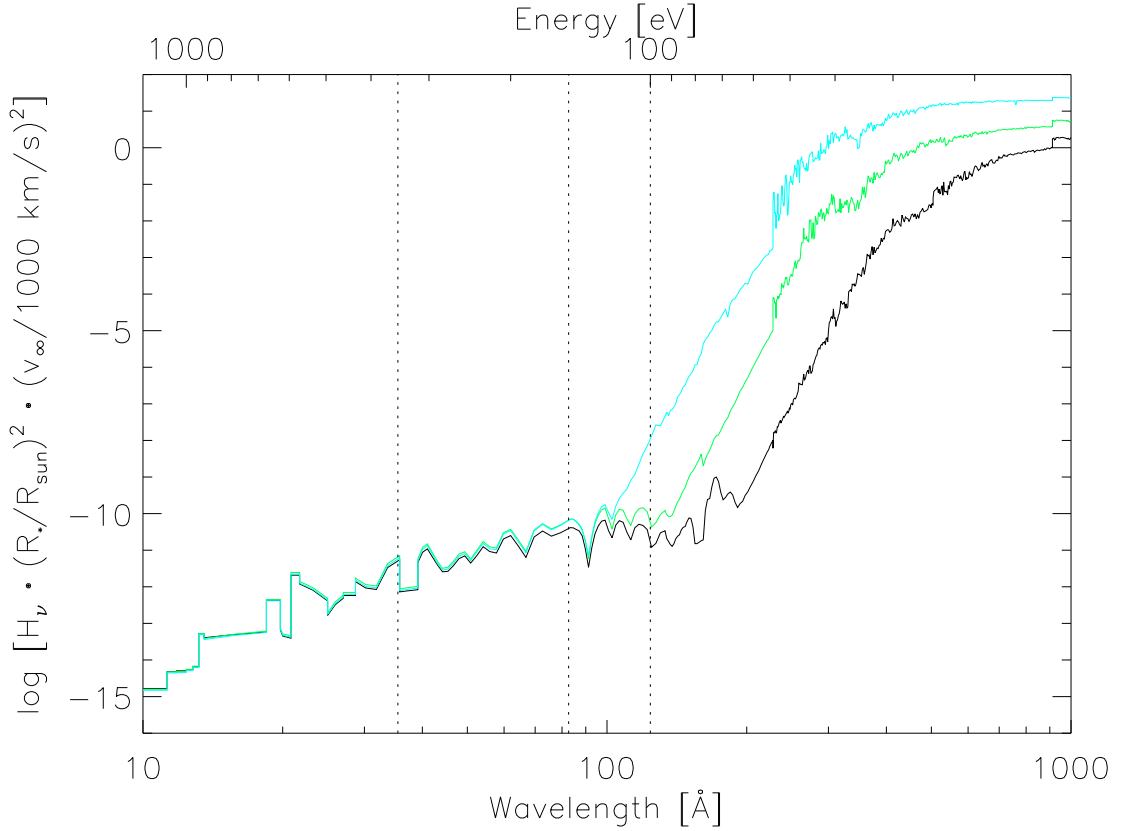


Figure 2.6: Logarithmic, scaled Eddington flux (in units of $\text{erg cm}^{-2} \text{s}^{-1} \text{Hz}^{-1}$) as a function of wavelength/energy, for the supergiant models S30 (black), S40 (green), and S50 (turquoise) with identical mass-loss rates, $10^{-8} M_{\odot}/\text{yr}$. All models have the same X-ray properties, as denoted in Fig. 2.5. The Eddington fluxes have been scaled by $(R_*/R_{\odot})^2$ and $(v_{\infty}/1000 \text{ km s}^{-1})^2$ to ensure theoretically similar values of optically thin X-ray emission. The dotted lines denote energies of 350, 150, and 100 eV, corresponding to 35, 83, and 124 Å. (See text.)

Thus, we first calculated WM-BASIC models with stellar/wind parameters from Table 2.1 and X-ray emission parameters from Table 2.2. For the maximum jump velocity we assumed, as an extreme value, $u_{\infty}/v_{\infty} = 0.3$, together with X-ray luminosities as shown in the sixth column of Table 2.2. These values then correspond to the f_X values provided in the second column of the same table, which are acquired from the WM-BASIC output. We note here that the input values of L_X/L_{Bol} (to WM-BASIC) were not chosen on physical grounds, but were estimated in such a way as to result in roughly similar values for f_X (in the range between 0.01 to 0.03).

To check the overall consistency, we calculated a similar set of FASTWIND models, now using the f_X values from Table 2.2 as *input*. In case of consistent models, the resulting L_X values (from the output) should be the same as the corresponding input values used for WM-BASIC. Both these values are compared in the last two columns of Table 2.2. Obviously, the agreement is quite good, with differences ranging from 0.0 to 0.2 dex and an average deviation of 0.12 dex.

Table 2.2: Left side: X-ray emission parameters used to compare FASTWIND and WM-BASIC models ($u_\infty/v_\infty = 0.3$ and $\gamma_x = 1.0$). For stellar and wind parameters, see Table 2.1. Right side: L_x/L_{bol} (logarithmic) provided as input for WM-BASIC (WMB), compared with the corresponding output value from FASTWIND (FW), integrated in the frequency range between 0.1 to 2.5 keV. See Sect. 2.4.3.

Model	f_X (%)	R_{min} (R_*)	u_∞ (km s^{-1})	T_s^∞ (10^6 K)	L_x/L_{bol} (WMB)	L_x/L_{bol} (FW)
Dwarfs						
D30	2.00	1.24	532	3.90	-9.4	-9.4
D35	0.96	1.29	622	5.27	-8.3	-8.5
D40	1.44	1.21	715	6.98	-7.0	-7.0
D45	1.38	1.20	894	10.9	-6.4	-6.5
D50	2.11	1.22	950	12.4	-5.6	-5.8
Supergiants						
S30	1.99	1.50	453	2.93	-6.3	-6.4
S35	1.24	1.43	577	4.54	-6.2	-6.3
S40	0.80	1.33	663	6.00	-6.3	-6.5
S45	0.93	1.25	754	7.76	-6.2	-6.3
S50	3.13	1.26	941	12.1	-5.2	-5.4

In a second step, we compared the supergiant fluxes resulting from this procedure in Fig. 2.7. For clarity, the fluxes were shifted by -3 , -6 , -9 , and -18 dex (S35, S40, S45, S50), where the solid lines correspond to the FASTWIND and the dashed lines to the WM-BASIC results.

The comparison shows a remarkably good agreement with no striking differences. Smaller differences in the lower wavelength range ($\lambda < 100$ Å) are related to a different frequency sampling (without an effect on the total X-ray luminosity). At longer wavelengths, these differences are related to the fact that WM-BASIC provides high-resolution fluxes, whilst FASTWIND calculates fluxes using averaged line opacities. For details, see Puls et al. (2005). Most important, however, is our finding that the fluxes are not only similar at high frequencies (indicating similar emissivities and cool-wind opacities), but also longward from the He II edge, indicating a similar ionization equilibrium (modified in the same way by the emission from shocked material).

At this stage, we conclude that our implementation provides results that are in excellent agreement with the alternative code WM-BASIC, both with respect to integrated fluxes as well as frequency edges, which moreover follow the predicted scaling relations. Having thus verified our implementation, we now examine important effects of the X-ray radiation within the stellar wind.

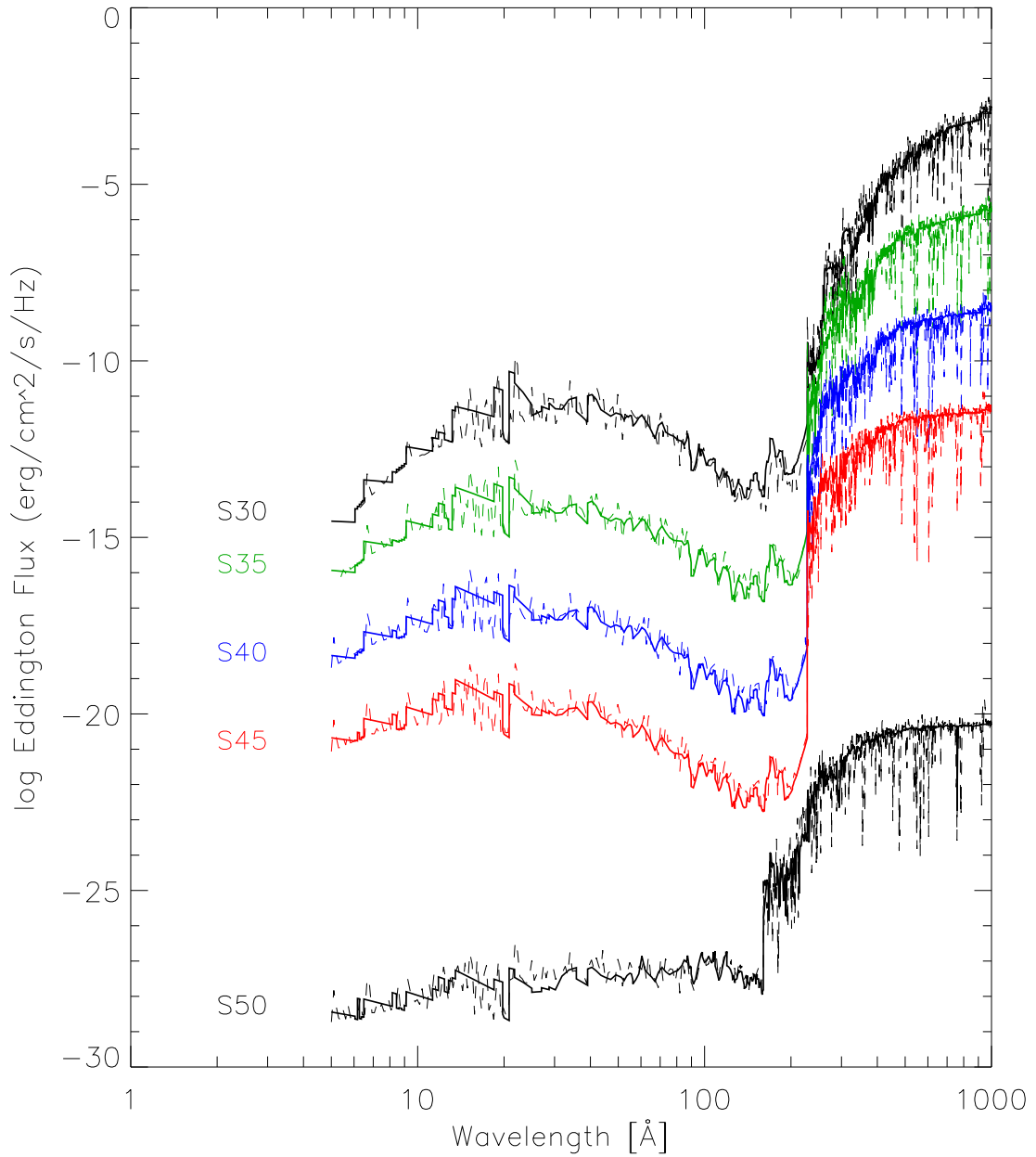


Figure 2.7: Logarithmic Eddington fluxes as a function of wavelength for supergiant models (see Table 2.1 and Table 2.2). The solid lines refer to results from our updated version of FASTWIND and the dashed lines to WM-BASIC results (Pauldrach et al. 1994, 2001). For clarity, the S35, S40, S45, and S50 model fluxes have been shifted by -3 , -6 , -9 , and -18 dex, respectively.

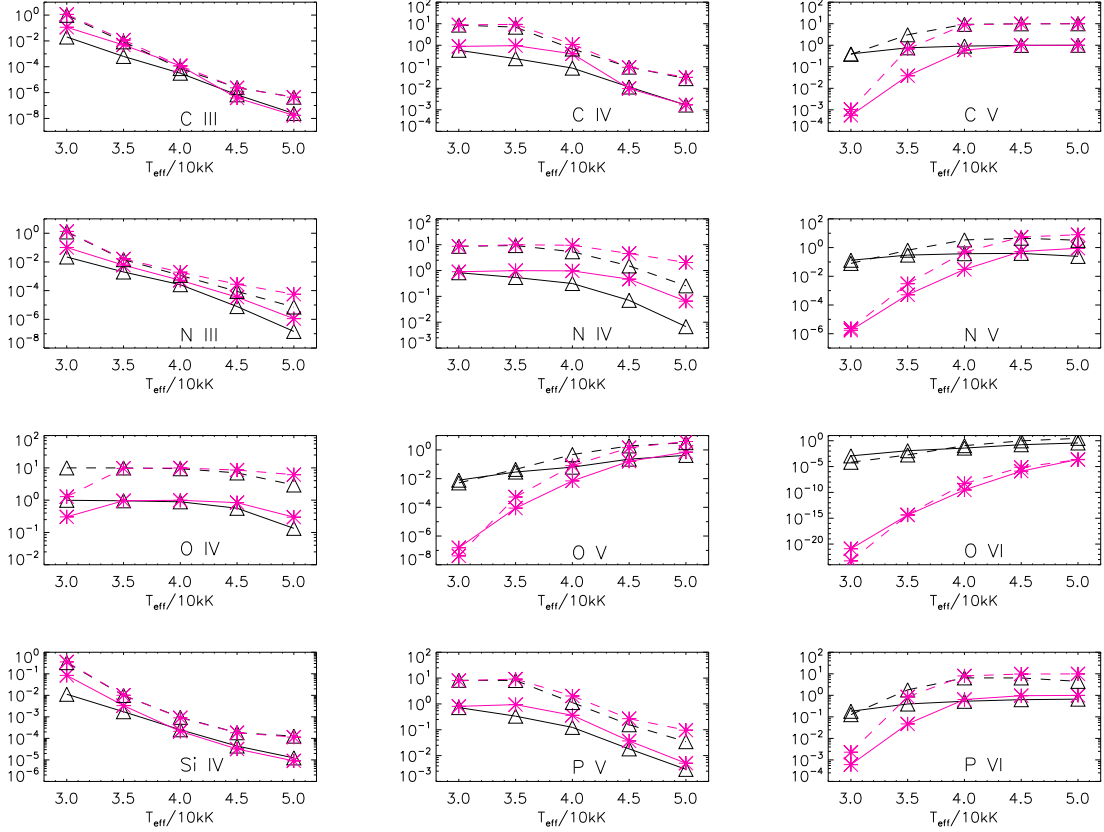


Figure 2.8: Ionization fractions of important ions at $\nu(r) = 0.5 \nu_\infty$, as a function of T_{eff} , for models with typical X-ray emission (triangles, $f_X = 0.03$, $T_s^\infty = 3 \cdot 10^6$ K, corresponding to $u_\infty = 460$ km s $^{-1}$), and without X-rays (asterisks). The solid lines refer to supergiant models, and the dashed lines to dwarf models. For clarity, the ionization fractions of dwarf models were shifted by one dex. For stellar parameters and onset radius, R_{min} , see Table 2.1.

2.5 Results

In this section, we discuss the major results of our model calculations. In particular, we study the impact of X-ray emission on the ionization balance of important elements, both with respect to direct (i.e., affecting the valence electrons) and Auger ionization. We also discuss the impact of dielectronic recombination and investigate the radial behavior of the high-energy mass absorption coefficient, which is an essential issue with respect to the analysis of X-ray line emission.

All of the following results refer to our specific choice of the run of shock temperature (see Eqs. 2.6 and 2.7), which, in combination with our grid-parameter $\gamma_x = 1$, leads to shock temperatures of $T_s(\nu_\infty/2) = 0.25 T_s^\infty$ in the intermediate wind at $\nu(r) = 0.5 \nu_\infty$.

2.5.1 Ionization fractions

General effects

Even though they are only indirectly observable (particularly via UV resonance lines), ionization fractions provide useful insight into the various radiative processes in the atmosphere. In the following, we compare, for important ions (i.e., for ions with meaningful wind lines), the changes due to the combined effects of direct and Auger ionization, whilst the specific effects of Auger ionization are discussed in Sect. 2.5.2. We perform these comparisons for our supergiant (solid) and dwarf models (dashed) from Table 2.1 and for the center values of our X-ray emission parameter grid (Sect. 2.3), $f_X = 0.03$, $T_s^\infty = 3 \cdot 10^6$ K, which are prototypical in many cases. Such maximum shock temperatures might be too high for models around $T_{\text{eff}} = 30$ kK, and certain effects (as discussed in the following) might thus be overestimated in this temperature range. We discuss the reaction from different parameters in the next section. We evaluated all of the ionization fractions at a representative velocity, $v(r) = 0.5 v_\infty$, and these are shown in Fig. 2.8. To check the influence of X-ray emission, one simply needs to compare the triangles (with) and asterisks (without X-ray emission).

Carbon. Our model atom for carbon will be improved soon, but the present one (from the WM-BASIC data base) is already sufficient to study the impact of shock radiation. The upper panels of Fig. 2.8 show the results, which indicate an effect only for cooler supergiant models with $T_{\text{eff}} < 40$ kK. For these objects, C III and C IV become somewhat depleted (less than a factor of ten), whilst C V (which is, without X-ray emission, a trace ion at 30 kK) becomes significantly enhanced. For dwarfs in this temperature range, only C V is increased, since the emission (scaling with ρ^2) is still too weak to affect the major ions. However, the actual filling factor in dwarfs might be much larger than 0.03; see, for example, Cassinelli et al. (1994), Cohen et al. (1997, 2008) and Huenemoerder et al. (2012). For models with $T_{\text{eff}} > 40$ kK, on the other hand, the temperature is already hot enough that the ionization balance is dominated by the normal stellar radiation field and no effect from the X-ray emission is visible.

Nitrogen (2nd row) and oxygen (third row of Fig. 2.8) suffer most from the inclusion of shock radiation. In the following, we concentrate on the differences produced by X-ray ionization in general, whilst in subsequent sections we consider specific effects.

Nitrogen. In the cool range, the behavior of N III, N IV and N V is very similar to the corresponding carbon ions (i.e., a moderate depletion of N III and N IV, and a significant increase of N V, particularly at T_{eff} between 30 and 35 K), whereas in the hot range it is different. Here, N III and N IV continue to become depleted, but N V increases only as long as $T_{\text{eff}} < 45$ kK and decreases again at 45 and 50 kK. In other words, when N V is already the main ion for non-X-ray models, it becomes (slightly) depleted when the X-rays are switched on, in contrast to C V which remains unmodified beyond 40 kK. This difference, of course, relates to the fact that C V has a stable noble-gas (He-) configuration with a high-lying ionization edge (31.6 Å) compared to the N V edge at roughly 126 Å, which allows for a more efficient, direct ionization by emission from the shock-heated plasma.

Oxygen. For almost every temperature considered in our grid, the inclusion of X-rays has a dramatic effect on the ionization of oxygen. At 30 kK, O IV becomes the dominant ion¹³, when for non-X-ray

¹³This is also true for models with different X-ray emission parameters.

models the main ionization stage is still O III, whereas at the hot end O IV becomes somewhat depleted. The behavior of O V is similar to N V (although the final depletion is marginal), and O VI displays the largest effect at all temperatures. At cool temperatures, the ionization fraction changes by 15 orders of magnitude, but there is still an increase by three to four dex even at the hottest T_{eff} . As is well known, this has a dramatic impact on the corresponding resonance doublet.

Silicon. In almost all hot stars, the dominant ion of silicon is Si V (again a noble-gas configuration), and Si IV forms by recombination, giving rise to the well-known Si IV luminosity/mass-loss effect (Walborn & Panek 1984, Pauldrach et al. 1990). The bottom left panel of Fig. 2.8 shows an analogous dependence. Whilst for dwarfs (low ρ^2) no X-ray effects are visible for Si IV, this ion becomes depleted for cool supergiants ($T_{\text{eff}} \lesssim 35$ kK) at most by a factor of ten.

Phosphorus. In recent years, the observed P V doublet at λ 1118,1128 has been important¹⁴ for deriving mass-loss rates from hot star winds in parallel with constraining their inhomogeneous structure (Fullerton et al. 2006, Oskinova et al. 2007, Sundqvist et al. 2011, Šurlan et al. 2013, Sundqvist et al. 2014). Thus, it is of prime importance to investigate the dependence of phosphorus on X-rays, since a strong dependence would contaminate any quantitative result by an additional ambiguity.

As already found in previous studies (e.g., KK09; Bouret et al. 2012), our results also indicate that P V is not strongly modified by X-ray emission (middle and right lower panels of Fig. 2.8). However, more extreme X-ray emission parameters, for example, $f_X = 0.05$ and/or $T_s^\infty = 5 \cdot 10^6$ K, can change the situation (see section 2.5.1). Furthermore, the apparently small change in the ionization fraction of P V at typical X-ray emission parameters (decrease by a factor of two to three) can still be of significance, given the present discussion on the precision of derived mass-loss rates (with similar uncertainties).

Regarding the ionization of P VI, cold models (30 and 35 kK) change drastically when X-ray emission is included, both for supergiants and dwarfs. Since we find less P VI in hot models with shocks (compared to models without), this indicates that the ionization balance is shifted toward even higher stages (P VII).

In this context, we note that Krtićka & Kubát (2012) investigated the reaction of P V when incorporating additional, strong XUV emissivity (between 100 and 228 Å) and microclumping into their models. The former test was driven by a previous study by Waldron & Cassinelli (2010) who argued that specific, strong emission lines in this wavelength range could have a significant impact. Indeed, Krtićka & Kubát (2012) were able to confirm that under such conditions¹⁵ P V becomes strongly depleted in parallel with changes in the ionization fractions of, for example, C IV, N IV, and O IV (see also Sect. 2.5.1). Further work is certainly required to identify the source of such additional emissivity, and, if necessary, to incorporate this mechanism into our FASTWIND models.

¹⁴This is because it is the only UV resonance line(-complex) that basically never saturates owing to the low phosphorus abundance.

¹⁵Enhanced emissivity in the XUV range; however, the lines referred to by Waldron & Cassinelli (2010) are included in standard plasma emission codes.

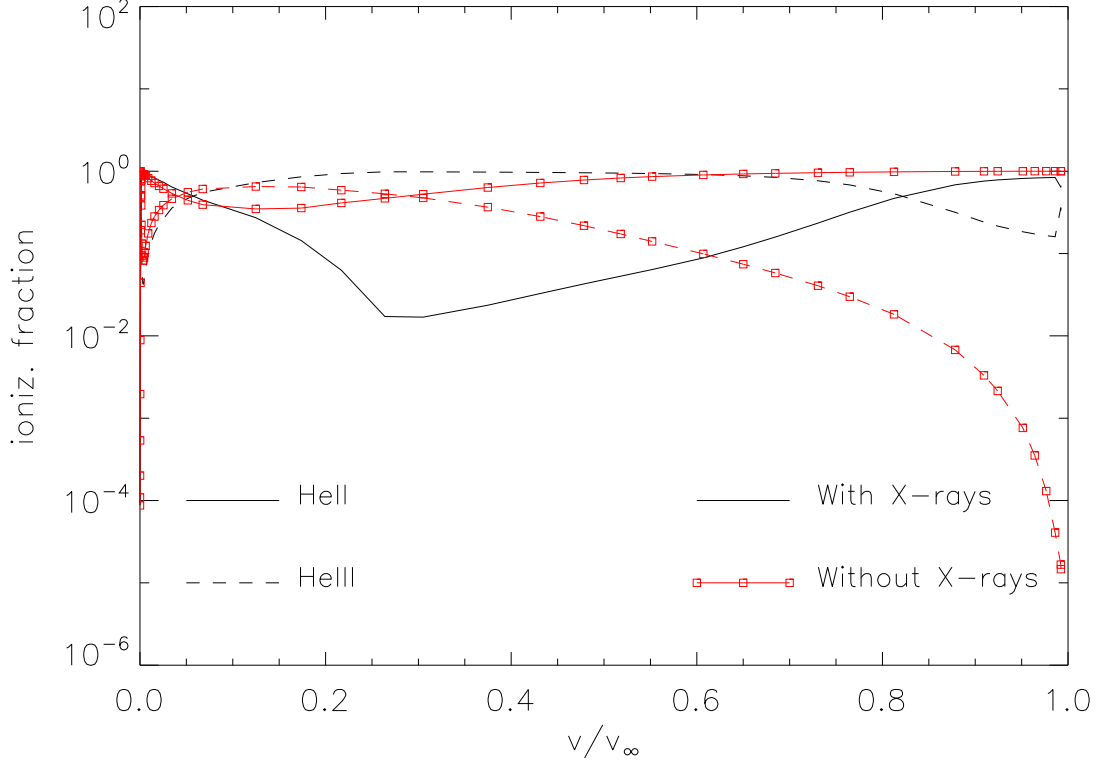


Figure 2.9: Helium ionization fractions as a function of local velocity, for an S30 model with ($f_X = 0.03$ and $T_s^\infty = 3 \cdot 10^6$ K) and without X-rays; see text.

Impact on helium

During our analysis, we noted that helium can also be affected by shock emission (see also Sect. 2.4.1), a finding that has been rarely discussed in related literature. In particular, He II (and He I) can become depleted in the intermediate wind; however, this is only the case for our cooler supergiant models with $30 \text{ kK} \lesssim T_{\text{eff}} \lesssim 40 \text{ kK}$. The effect is strongest for S30 models, but it is barely noticeable even at S40, independent of the specific X-ray emission parameters. For all our dwarf models, no changes are visible at all.

Figure 2.9 shows the helium ionization fractions for an S30 model with typical X-ray emission parameters as a function of local velocity. The depletion of He II (and, in parallel, of He I that is not displayed) is significant in the region between $0.2v_\infty \lesssim v(r) \lesssim 0.8v_\infty$, and results from the increased ionization due to the increased radiation field (in the He II Lyman continuum) in models with shocks (note also the corresponding increase of He III).

In Fig. 2.10, we compare the helium ionization fractions from our solution and a corresponding WM-BASIC S30 model, but now with X-ray emission parameters as tabulated in Table 2.2 (the major difference is a filling factor of 0.02 instead of 0.03). Here, we show the fractions as a function of

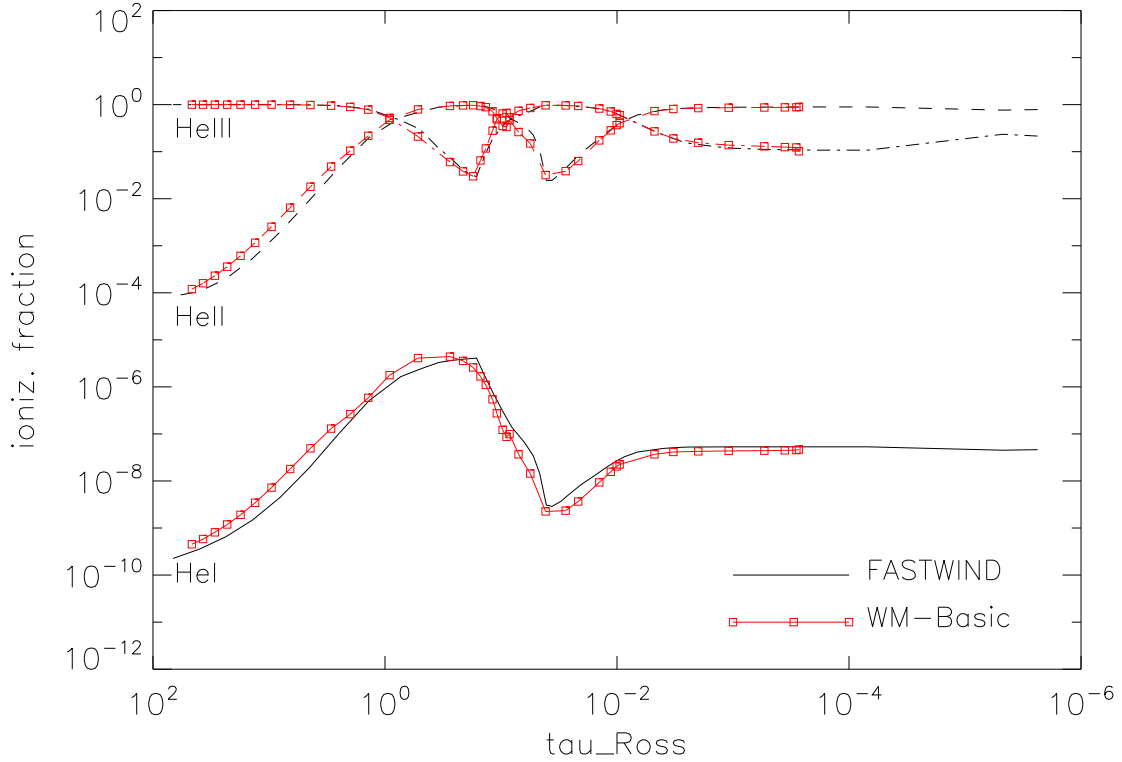


Figure 2.10: Helium ionization fractions as a function of τ_{Ross} , for S30 models calculated by FASTWIND and WM-BASIC, both with X-ray emission parameters from Table 2.2. The agreement is excellent.

τ_{Ross} to enable a comparison of the photospheric regions as well. Again, the depletion of He II (now located between $\tau_{\text{Ross}} \approx 0.1 \dots 0.01$) is visible, and our results coincide perfectly with those predicted by WM-BASIC.

Since the ionization balance already changes at very low velocities, this might affect at least two important strategic lines: He II 1640 and He II 4686. Most other He II and He I lines are formed in the photosphere and remain undisturbed. From Fig. 2.11, we see that He II 4686 shows stronger emission, whilst He II 1640 shows a stronger emission in parallel with absorption at higher velocities compared to the non-X-ray model (dotted). This is readily understood since He II 4686 is predominantly a recombination line, such that the increase in He III leads to more emission; this is also true for He II 1640 to a lesser extent. The lower level of this line, $n = 2$ (responsible for the absorption), is primarily fed by pumping from the ground-state via He II 303. We convinced ourselves that the increased pumping because of the strong EUV radiation field leads to a stronger population of the $n = 2$ state (even if He II itself is depleted), so that also the increased absorption is explained.

As already pointed out in Sect. 2.4.1, changing R_{min} from 1.5 to 1.2 R_* does not make a big difference. Increasing R_{min} to 2 R_* , however, changes a lot, as visible from the dash-dotted profiles

in Fig. 2.11. Except for slightly more emission (again because of increased He III in regions with $r > 2R_*$), the difference to profiles from models without shock emission becomes insignificant, simply because both lines predominantly form below the onset radius.

Dependence on filling factor and shock temperature

As we have already seen above, each ion reacts somewhat differently to the imposed shock radiation. In this section we describe how a change of important X-ray characteristics affects important ions. The figures related to this section are enclosed in Appendix 2.A. The top figure on each page shows specific ionization fractions with and without X-rays, as a function of T_{eff} , for our supergiant and dwarf models (S30 to S50 and D30 to D50, respectively). We evaluated the ionization fractions at the location where the impact of shock radiation is most evident for the considered ion. Each of these figures contains nine panels, in which both the filling factor and maximum shock temperature are varied according to our grid, i.e., $f_X = 0.1, 0.3, 0.5$ and $T_s^\infty = 1, 3, 5 \cdot 10^6$ K. The onset radius, R_{min} , was set to its default value for all models. The lower two figures on each page display the ionization fractions for our dwarf (left) and supergiant models (right), evaluated at the same location as above, but now overplotted for all values of f_X (different colors) and T_s^∞ (different symbols), and without a comparison to the non-X-ray case. Thus, the top figure allows us to evaluate the X-ray effects in comparison to models without shock emission, whilst the bottom two figures provide an impression on the differential effect, i.e., the range of variation.

Carbon. C III and C IV are significantly affected in supergiant models with $30 \text{ kK} \lesssim T_{\text{eff}} \lesssim 40 \text{ kK}$ for intermediate to large values of f_X and T_s^∞ . The depletion of C III and C IV reaches a factor of 10 (or even more) in cooler supergiant models when the highest values of X-ray emission parameters are adopted, which is reflected in a corresponding increase of C V. On the other hand, C III and C IV are barely modified in supergiant models with the lowest values of f_X or T_s^∞ , which is also true for dwarf models with any value of our parameter grid (see Figs. 2.21/2.22). The ionization fraction of C V also increases for the lowest values of X-ray emission parameters, again for cooler supergiant (and dwarf) models. C V remains unmodified beyond 40 kK due to its stable noble-gas configuration, as previously noted.

Nitrogen. The behavior of N III, N IV, and N V in the colder models is similar to the corresponding carbon ions for all different X-ray descriptions. For higher T_{eff} , increasing f_X enhances the depletion of N III and N IV in both supergiants and dwarfs, whilst the impact of T_s^∞ is rather weak. At the largest values of X-ray emission parameters, both stages become highly depleted (one to two orders of magnitude) for all models but D30 and D35.

Shock radiation is essential for the description of N V at almost any temperature, particularly for models with $T_{\text{eff}} < 45 \text{ kK}$ (Figs. 2.23/2.24). Here, the increase of N V (compared to non-X-ray models) can reach 4 to 5 dex at the lowest temperatures. At 45 kK, only a weak impact of shock radiation can be noted, whilst for 50 kK a high depletion of N V for extreme parameters values becomes obvious. Once more, the impact of f_X is more prominent than of T_s^∞ , mainly for the coldest models where N V becomes enhanced by one order of magnitude when increasing f_X from 0.01 to 0.05 and keeping T_s^∞ constant. The hottest models with moderate to high parameters ($f_X \gtrsim 0.02$ and $T_s^\infty \gtrsim 2 \cdot 10^6$ K) indicate that N VI also becomes strongly affected by changes in the X-ray ionization.

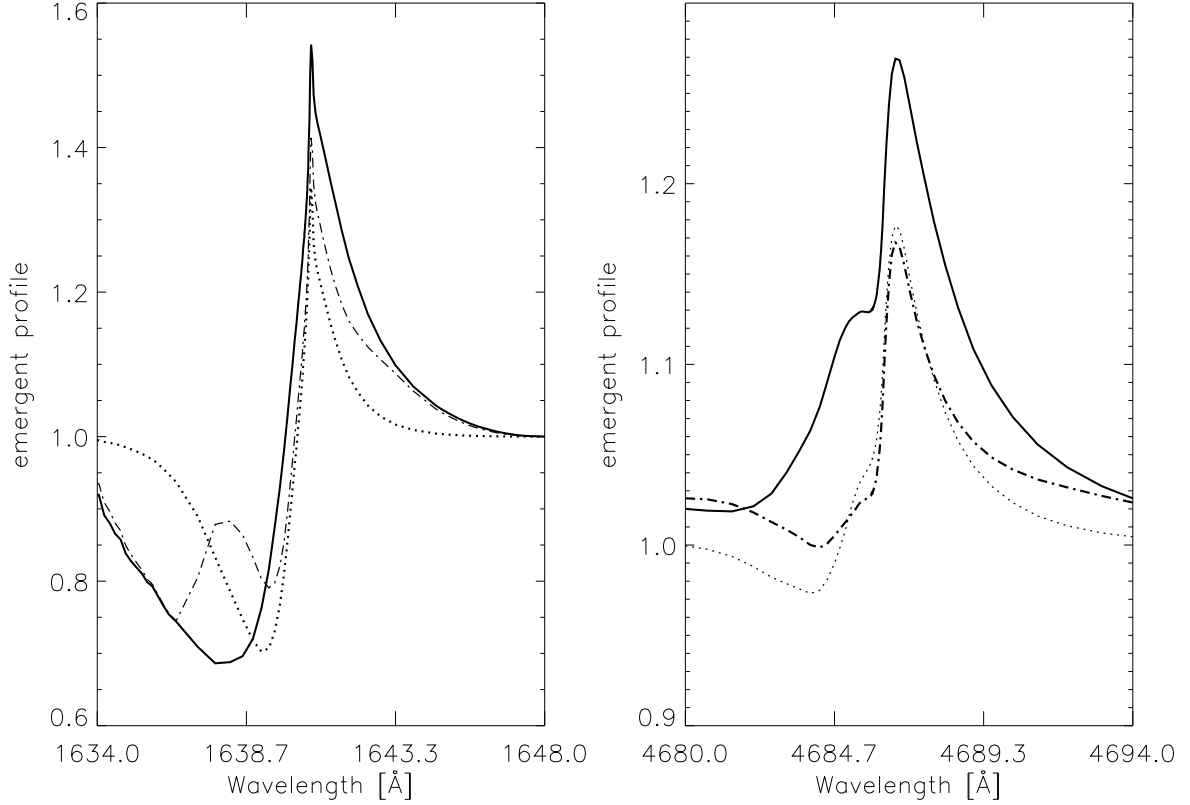


Figure 2.11: Synthetic He II 1640 and He II 4686 profiles for our S30 model. Each profile corresponds to a different X-ray description. Solid: $f_X = 0.03$, $T_s^\infty = 3 \cdot 10^6$ K, $R_{\min} = 1.5 R_*$; dash-dotted: as solid, but with $R_{\min} = 2 R_*$; dotted: no shock emission.

Oxygen. Independent of the X-rays description, the depletion of O IV for hot models happens only in a specific range of the wind, between 0.4 to 0.8 v_∞ (similar to the case of He II discussed in the previous section). Also for X-ray emission parameters different from the central value of the grid, the behavior of O V is still very similar to N V, where mainly the cold models are quite sensitive to variations of f_X (Figs. 2.25/2.26). The shock radiation increases the ionization fraction of O V by 5 to 6 dex (when f_X varies between 0.01 and 0.05, independent of T_s^∞) for the coolest models, whilst these factors decrease as T_{eff} approaches 40 to 45 kK. Models with $T_{\text{eff}} = 45$ kK are barely affected, independent of the specific X-ray emission parameters. Similar to the case for N V at highest values of f_X , T_s^∞ , and T_{eff} , the corresponding depletion of O V points to the presence of a significant fraction of higher ionization stages.

As already pointed out in Sect. 2.5.1 (see also Sect. 2.5.2), the X-ray radiation is essential for the description of O VI, which shows, particularly in the cold models, a high sensitivity to both f_X and T_s^∞ (Figs. 2.27/2.28).

Silicon. Also when varying the X-rays description, Si IV still remains unaffected from shock emission

in dwarf models. On the other hand, for cool supergiants ($T_{\text{eff}} \lesssim 35$ kK), Si iv becomes even more depleted when f_X increases (though T_s^∞ has a negligible influence). No variation is seen in Si v, as expected because of its noble-gas configuration.

Phosphorus. P v shows a sensitivity to both f_X and T_s^∞ , but in this case T_s^∞ is more relevant. Although no difference between models with and without shocks is seen for the lowest values of T_s^∞ , particularly the supergiant models develop a depletion with increasing shock temperature, even at lowest f_X . As noted already in Sect. 2.5.1, for extreme X-ray emission parameters the depletion of P v is significant for all models (both supergiants and dwarfs), except for D30 (Figs. 2.29/2.30). Finally, even P vi becomes highly depleted for hot models ($T_{\text{eff}} \gtrsim 40$ kK) at intermediate and high values of T_s^∞ , which indicates the presence of even higher ionization stages.

To summarize our findings: When increasing the values for f_X and T_s^∞ , the effects already seen in Fig. 2.8 become even more pronounced, as to be expected. For most ions, the impact of f_X appears to be stronger than the choice of a specific T_s^∞ provided the latter is still in the range considered here. However, P v and O vi (for the cooler models) show a strong reaction to variations of T_s^∞ . Overall, the maximum variation of the ionization fractions within our grid reaches a factor of 10 to 100 (dependent on the specific ion), where lower stages (e.g., C iv, N iv, O iv, and P v) become decreased when f_X and T_s^∞ are increased, whilst the higher stages (e.g., N v, O v, O vi) increase in parallel with the X-ray emission parameters. For Si iv alone, the impact of X-rays remains negligible in all models except for S30 and S35.

Comparison with other studies

Since the most important indirect effect of shock emission is the change in the occupation numbers of the cool wind, it is worthwhile and necessary to compare the ionization fractions resulting from our implementation with those presented in similar studies.

To this end, (i) we recalculated the models described in KK09 (ii) compared with two models (for HD 16691 and HD 163758) presented in Bouret et al. (2012), who used CMFGEN and SEI (Sobolev with exact integration, Lamers et al. 1987) fitting to calculate and derive the ionization fractions of phosphorus, and (iii) compared our results with the ionization fractions predicted by WM-BASIC.

Regarding the first point, we recalculated the 14 O-star models (in the temperature range between 30 and 40 kK) presented by KK09, using parameters from their Tables 2 and 3, both without and with shock emission ($f_X = 0.02$ and $u_\infty/v_\infty = 0.3$), by means of FASTWIND using H, He, C, N, O, Si, and P as explicit ions. Figure 2.12 shows our results for the ionization fractions of selected ions, as a function of T_{eff} , and evaluated at $v(r) = 0.5v_\infty$. The layout of this figure is similar to Figure 8 in KK09, and has been augmented by O vi evaluated at $v(r) = 0.05v_\infty$ and N v evaluated at $v(r) = 0.8v_\infty$, corresponding to their Figures 9 and 10.

Indeed, there are only a few ions that display similar fractions over the *complete* temperature range of the O-star models considered by KK09 (which still omits the hotter O stars beyond 40 kK). For C iv, an agreement is only present for the coolest regime ($T_{\text{eff}} \leq 32$ kK) where both studies predict C iv as the main ion, independent of whether X-rays are present or not. Whilst the fractions for non-X-ray models are also comparable for hotter temperatures, the X-ray models by KK09 show a much larger depletion of C iv (fractions of 10^{-2} to 10^{-3} for $T_{\text{eff}} > 34$ kK) than our models reveal (still above 10^{-1}).

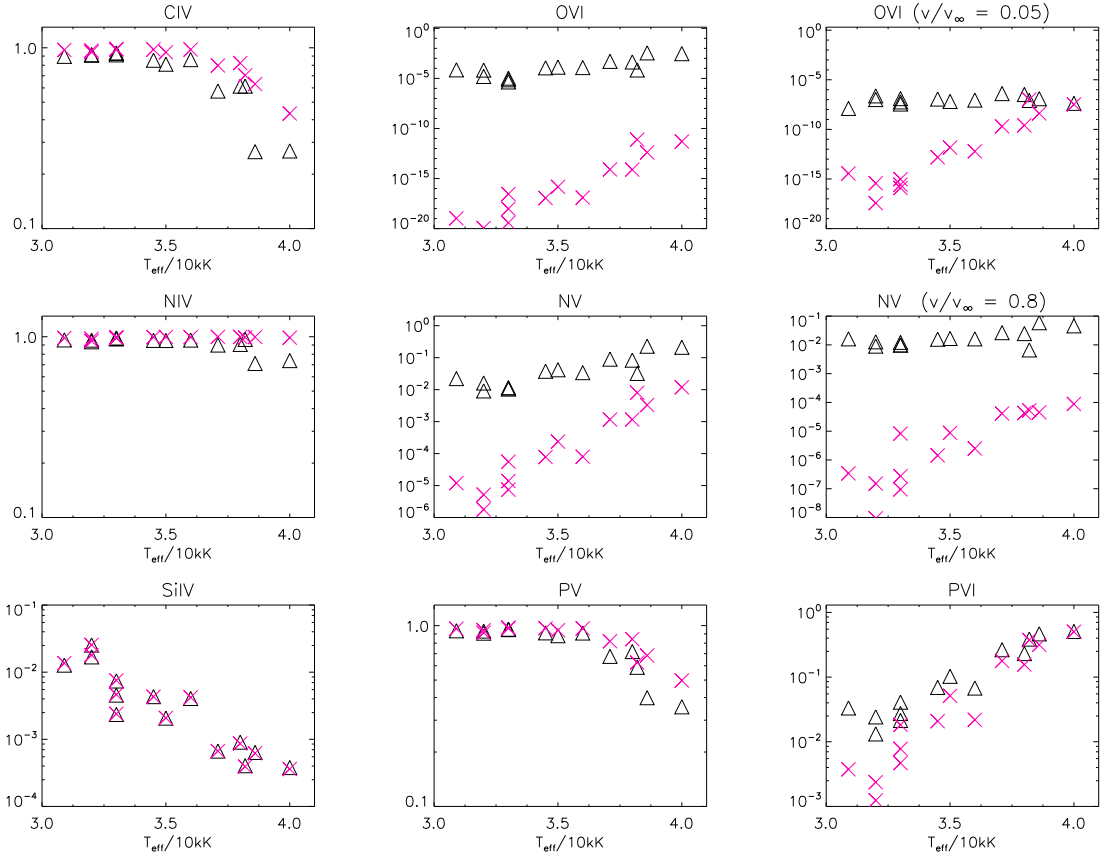


Figure 2.12: Ionization fractions of selected ions as a function of T_{eff} , for 14 O-star models, as detailed in Krtićka & Kubát (2009, KK09); we recalculated these models here using FASTWIND. If not indicated otherwise, fractions are shown at $v(r) = 0.5v_{\infty}$. As in previous figures, triangles represent models with shocks and crosses indicate those without shocks. This figure largely reproduces the layout of Figure 8 from KK09, such that differences and similarities between our and their results can be easily recognized. For details, see text.

For O VI, agreement between both results is present only at the hottest temperatures, whilst between $30 \text{ kK} < T_{\text{eff}} \lesssim 37 \text{ kK}$ our models display a factor of ~ 100 lower fractions for both the non-X-ray models and the models with shock emission. The same factor is visible in the lower wind ($v(r) = 0.05v_{\infty}$) for the X-ray models, but the non-X-ray models are similar here.

For nitrogen (N IV and N V), on the other hand, the results are quite similar in most cases. The exception is N V for models without shocks, where our results are lower (by ~ 1 dex) in the intermediate and outer wind ($v(r) = 0.8v_{\infty}$).

For Si IV, both results fairly agree for the X-rays models, though we do not see a significant effect from including the shock emission in our calculations; in other words, X-ray and non-X-ray models yield more or less identical results. In contrast, the models by KK09 indicate a small depletion of Si IV, by a factor of roughly 2 to 3, when including the shock emission. Thus, our non-X-ray models

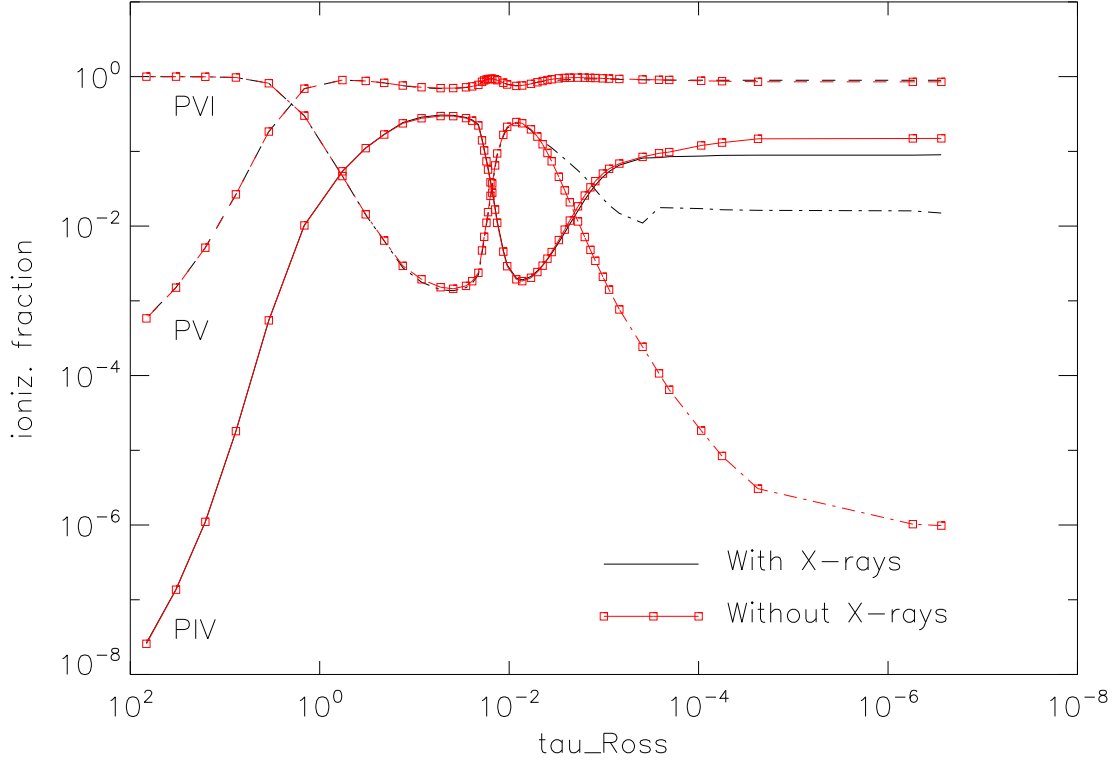


Figure 2.13: Radial stratification of phosphorus ionization fractions, as a function of τ_{Ross} , for our model of HD 203064 at $T_{\text{eff}} = 34.5$ kK (see KK09 for stellar, wind, and X-ray emission parameters). In our implementation, P v is barely modified by the X-ray radiation field, whilst a considerable impact is seen for P vi.

have less Si iv than those by KK09.

Again, phosphorus (in particular, P v) has to be analyzed in more detail. Comparing the last two panels of Fig. 2.12 with Fig. 8 from KK09, we see that our ionization fractions for P v agree with KK09 in the coolest models and in the hottest models regarding P vi. In the other temperature ranges, however, differences by a typical factor of 2 (regarding P v) and 2 to 5 (regarding P vi) are present. In their Fig. 12, KK09 show the radial stratification of the phosphorus ionization fractions for their model of HD 203064, whilst the corresponding results from our implementation are shown in Fig. 2.13. Both codes yield quite similar fractions for P iv and P v (with and without X-rays) in the external wind. The same is true for P vi in the model with X-rays, but we have considerably less P vi for the non-X-ray model. Prominent differences are visible in the lower wind and close to the lower boundary. We attribute this difference to a boundary condition (in the models by KK09) at very low optical depths, where the electron temperature is still close to the effective temperature. (Indeed, we were not able to find statements or figures related to the photospheric structure of the models in papers by Krtićka and coworkers, so our argument is somewhat speculative.) Thus far, it is conceivable that a low ionization

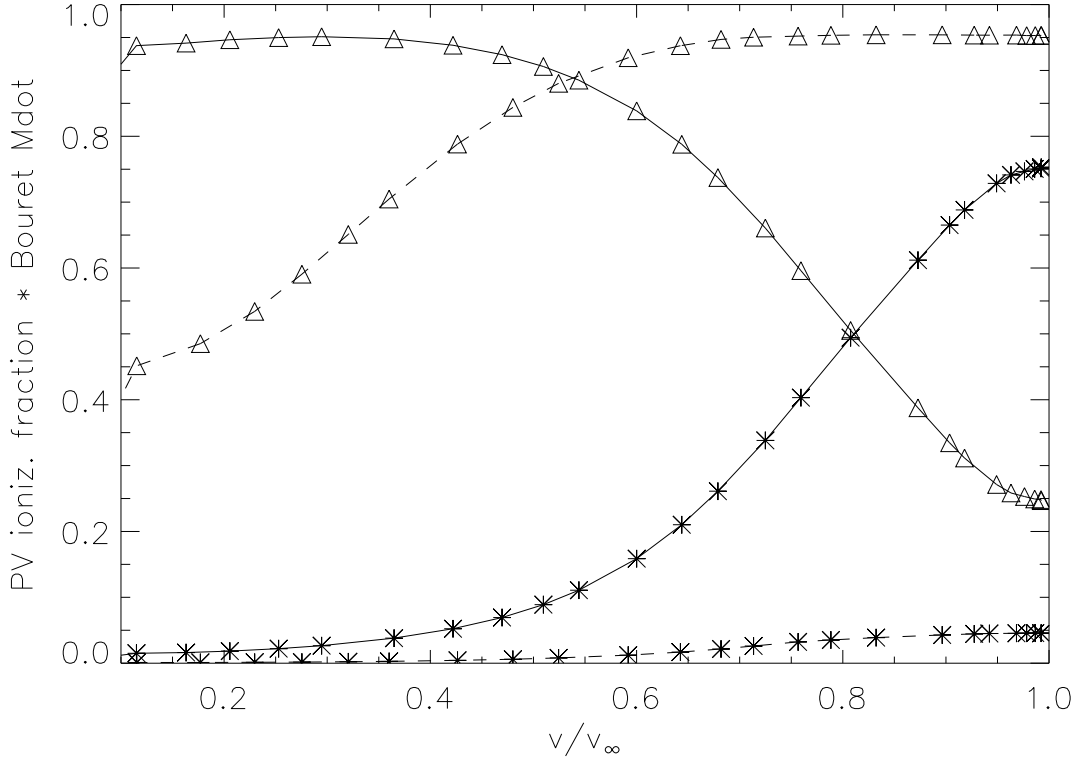


Figure 2.14: Ionization fractions of P IV (asterisks) and P V (triangles) as a function of normalized velocity for an S35 (solid) and S40 (dashed) model. Both models were calculated with a clumping factor $f_{cl} = 20$, and a mass-loss rate reduced by a factor of ~ 4 compared to the values provided in Table 2.1. Compare with Fig. 10 in Bouret et al. (2012).

stage (P IV) dominates their internal atmosphere (followed by P V and negligible P VI), whilst in our case it is the reverse, and P VI dominates owing to much higher temperatures.

To check these discrepancies further, we also compared our results with calculations performed with CMFGEN. In particular, we concentrated on two supergiant models at roughly 35 kK and 40 kK (HD 163758 and HD 16691, respectively), as described by Bouret et al. (2012). These models used an X-ray emitting plasma with constant shock temperature, $T_s(r) = 3 \cdot 10^6$ K, a filling factor corresponding to $L_x/L_{bol} = 10^{-7}$, and an onset radius corresponding to 200 to 300 km s^{-1} (J.-C. Bouret, priv. comm.). In Fig. 14, we present our results for P IV and P V; these can be compared with Fig. 10 of Bouret et al., showing P V alone. Though our models S35 and S40 (here we use a clumped wind with reduced mass-loss rates to ensure comparable wind structures) do not have identical parameters, and in particular, our shock temperatures increase with velocity, the ionization fractions behave similarly. In the cooler model (solid), the ionization of P V decreases with velocity and in the hotter model (dashed), this ionization increases outward. This is because in the cooler model, P V is the dominant ion at low velocities, recombining to P IV, whilst in the hotter model P VI dominates at low velocities,

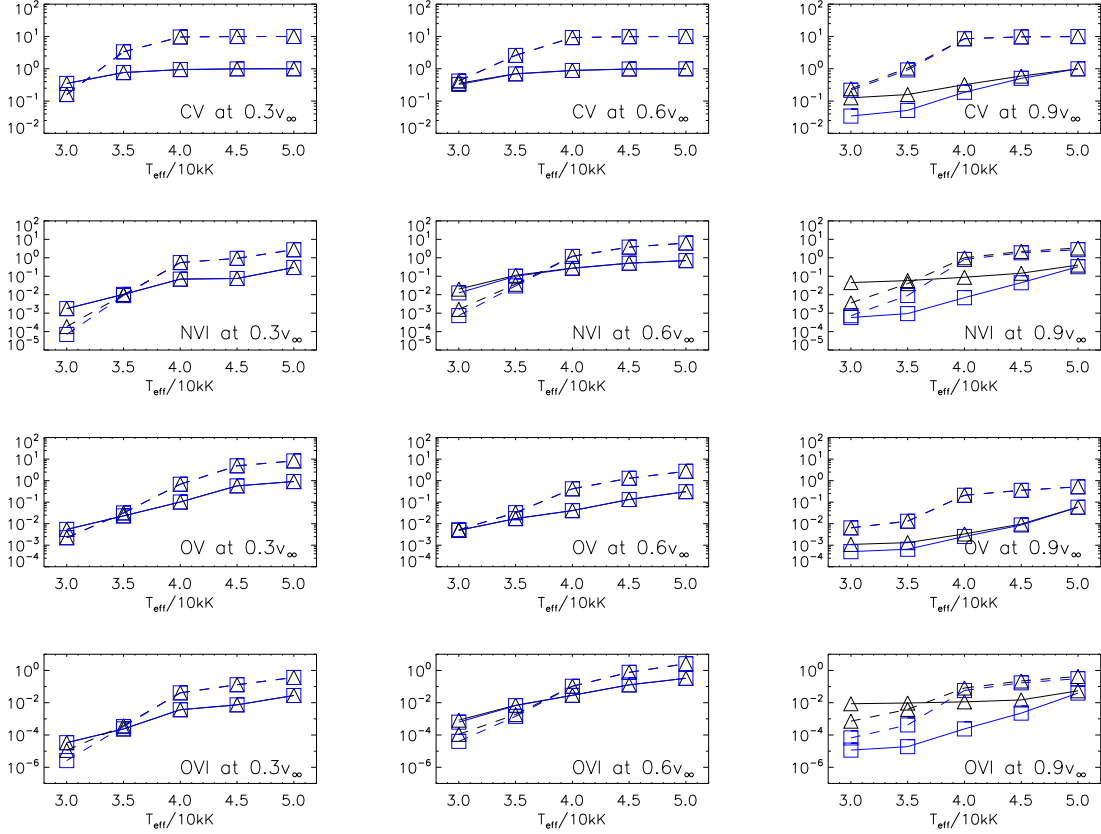


Figure 2.15: Ionization fractions of ions most affected by Auger ionization, at different depth points. All models have typical X-ray emission parameters ($f_X = 0.03$ and $T_s^\infty = 3 \cdot 10^6$ K). The triangles represent models including Auger ionization (standard approach, similar to Fig. 2.8), and squares models without (i.e., only direct ionization has been considered). Solid lines refer to supergiant models, and dashed ones to dwarf models. For clarity, the ionization fractions of dwarf models have been shifted by one dex.

recombining to P v in the run of the wind. Of course, there are some quantitative differences, particularly in the intermediate wind¹⁶, but we attribute these to a different stratification of the clumping factor, f_{cl} , and to a different description of the X-ray emitting plasma; concerning the reaction of P v on various X-ray emission parameters, see Fig. 2.30.

As a final test, we compared our solutions to the predictions by WM-BASIC, using our dwarf and supergiant models (Table 2.1 and X-ray emission parameters from Table 2.2). The results are shown in Figs. 2.31 and 2.32 (Appendix 2.B). The range of comparison extends from 30 to 50 kK, i.e., to much hotter temperatures than in the comparison with KK09.

Overall, the agreement between FASTWIND and WM-BASIC is satisfactory and all trends are reproduced. However, we also find discrepancies amounting to a factor of 10 in specific cases, particu-

¹⁶J.-C. Bouret provided us with an output of the ionization fractions for P iv and P v.

larly for Si iv. Typical differences, however, are on the order of a factor of two or less. We attribute these discrepancies to differences in the atomic models, radiative transfer, and the hydrodynamical structure, but conclude that both codes yield rather similar results with the possible exception of Si iv, which needs to be reinvestigated in future studies.

In Fig. 2.33 we see how some of the encountered differences (compared at only one depth point, $\nu(r) = 0.5\nu_\infty$, except for N v) translate to differences in the emergent profiles. As prototypical and important examples, we calculated line profiles for N iv 1720, N v 1238,1242, O v 1371, O vi 1031,1037, and P v 1117,1128 and compare them with corresponding WM-BASIC solutions for models S30, D40, S40, D50, and S50 (for model D30, all these lines are purely photospheric and thus were not part of this comparison). Both the WM-BASIC and FASTWIND profiles were calculated with a radially increasing microturbulence with maximum value $\nu_{\text{turb}}(\text{max}) = 0.1\nu_\infty$, which allows for reproducing the blue absorption edge and black trough (see Sect. 2.2.1) in the case of saturated P-Cygni profiles.

This comparison clearly shows that in almost all considered cases the agreement is satisfactory; WM-BASIC includes the photospheric background, whilst FASTWIND only accounts for the considered line(s). Larger differences are present only (i) for N iv and O v in the outer wind, where FASTWIND produces more (N iv) and less (O v) absorption, respectively, and (ii) for strong P v lines, where FASTWIND predicts higher emission.

2.5.2 Impact of Auger ionization

All X-ray models discussed so far include the effects from direct and Auger ionization, which was shown to play an important role for the ionization balance in stellar winds (e.g., Cassinelli & Olson 1979, Olson & Castor 1981, Macfarlane et al. 1994, Pauldrach et al. 1994). In the following, we investigate the contribution of Auger ionization to the total ionization in more detail, particularly since this question is still under debate.

Figure 2.15 shows how specific ions are affected throughout the wind for dwarf and supergiant models with different T_{eff} and typical X-ray emission parameters ($f_X = 0.03$ and $T_s^\infty = 3 \cdot 10^6$ K). Each ion is shown at three different locations: $\nu(r) = 0.3 \nu_\infty$ (close to the onset of the shock emission), $\nu(r) = 0.6 \nu_\infty$ (intermediate wind), and $\nu(r) = 0.9 \nu_\infty$ (outer wind).

Two general comments: (i) Significant effects are to be expected only for very high ionization stages, since in the majority of cases Auger ionization couples ions with a charge difference of two (but see Sect. 2.2.2). For example, C iv should remain (almost) unmodified, since C ii is absent in O and, at least, early B stars. In addition, the K-shell absorption of C iv (with a threshold at 35.7 Å), resulting in the formation of C v (with a charge difference of one), is in most cases (but see below) negligible compared to the direct ionization of C iv (with a threshold of ~ 192 Å for the ground-state ionization). Given the radiation field is stronger at longer wavelengths, this favors direct versus Auger ionization. In contrast, O vi should become significantly affected, since O iv is strongly populated in O stars, and the transition threshold for the direct ionization from O v (at ~ 109 Å) is now closer to the K-shell edge. Consequently, the transition rates (depending on the corresponding radiation field) are more similar than in the case of C iv.

(ii) In the same spirit, Auger ionization should become negligible, at least in most cases, for the hotter O stars (see also Sect. 2.4). Once T_{eff} is high, more direct ionization is present because of the

stronger radiation field at the corresponding, lower frequency edges, and consequently the impact of Auger ionization should decrease. This argumentation is basically correct, but the actual results also depend on the wind-strength, since higher densities lead to more X-ray emission (for identical f_X), which increases the impact of Auger ionization. For example, if we check for the behavior of N VI at $0.9 v_\infty$ in Fig. 2.15, we see that for D40, D45, and D50 there is indeed no effect, whilst for S40 and S45 Auger ionization still has a certain influence.

We now examine Auger ionization in greater detail. First, we note that all ions from C, N, O, Si, and P that are *not* shown in Fig. 2.15 are barely changed by Auger ionization with a maximum difference of ± 0.08 dex (corresponding to factors of 0.8 to 1.2) in the fractions calculated with and without Auger.

For carbon, C V is the only ion that under specific conditions becomes affected by Auger ionization. As visible in the first line of Fig. 2.15, cold supergiant models show an increase of C V in the outer wind when Auger is included, since in this case the radiation field at the corresponding K-shell edge becomes very strong, compared to the radiation field around 192 \AA (see Fig. 2.7). This increase is compensated by a similar decrease of C IV, which, in absolute numbers, is quite small.

N VI (second line in Fig. 2.15) is the only nitrogen ion where larger changes are noted. In cool dwarfs, it already becomes influenced at $0.3 v_\infty$, and also in the intermediate wind, which is also true for model S30. In the outer wind, differences appear clearly for all models, except for dwarfs with $T_{\text{eff}} \gtrsim 40 \text{ kK}$. The corresponding change in N IV, on the other hand, is marginal, again because N VI itself has a low population, even when Auger is included.

O V behaves similar to N V (mostly no changes), but now a weak effect appears in the outer wind of cool supergiants (third line of Fig. 2.15), and even for O VI (compare to the reasoning above), changes in the lower and intermediate wind are barely visible (if at all, then only for the S30 model; see last line of Fig. 2.15). In the outer wind, however, considerable differences in O VI (up to three orders of magnitude) can be clearly spotted for all supergiants and cooler dwarf models, similar to the case of N VI. The effect only becomes weak for the hottest models. Fig. 2.16 shows an example for an S40 model where the second-most populated oxygen ion (O V) changes to O VI after the inclusion of Auger ionization.

Finally, the K-shell edges for phosphorus (not implemented so far) and silicon (with quite low cross sections) are located at such high energies ($> 2 \text{ keV}$ or $> 6 \text{ \AA}$) that the corresponding Auger rates become too low to be of importance, at least for the considered parameter range.

To conclude, in most cases the effects of Auger ionization are only significant in the outer wind (for a different run of shock temperatures, they might become decisive already in the lower or intermediate wind), and for highly ionized species. The effect is essential for the description of N VI and O VI, particularly in the outer wind. Thus, and with respect to strategic UV resonance lines, it plays a decisive role only in the formation of O VI 1031,1037 (but see also Zsargó et al. 2008).

2.5.3 Dielectronic recombination of O V

After comparing the results from our first models accounting for shock emission with corresponding WM-BASIC results, we found that in a specific parameter range (for dwarfs around 45 kK) both codes delivered largely different fluxes around the O IV edge at $\sim 160 \text{ \AA}$; these different fluxes could

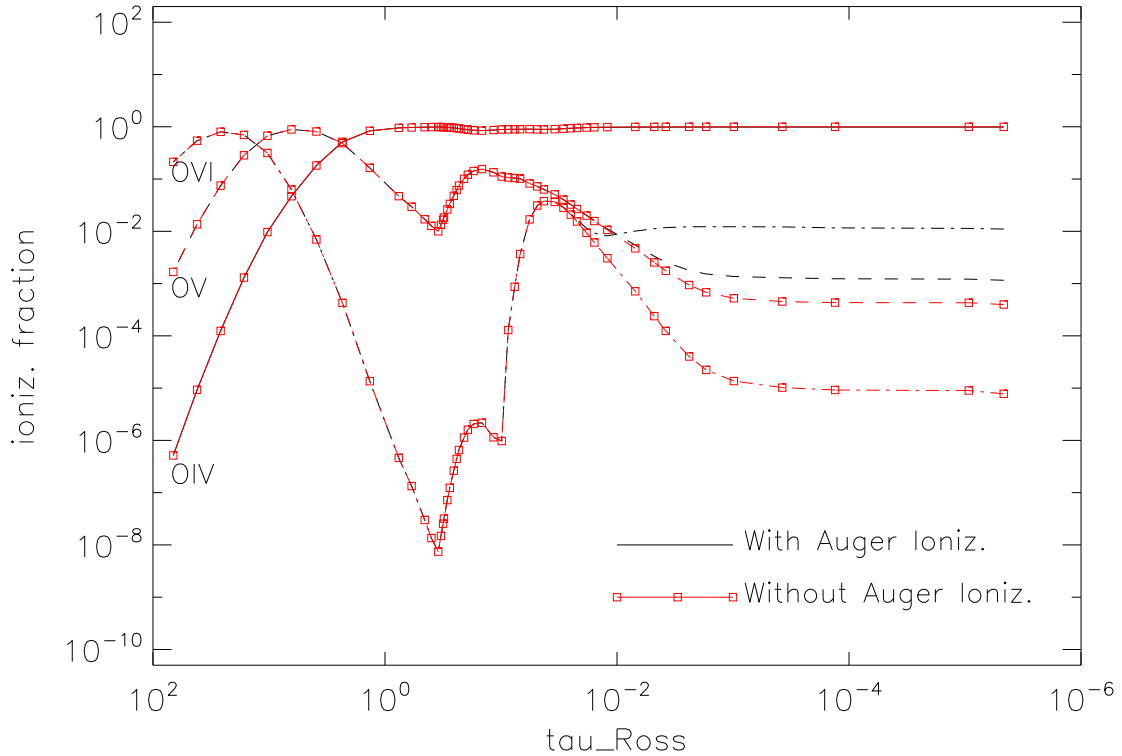


Figure 2.16: Radial stratification of oxygen ionization fractions, as a function of τ_{Ross} , for an S40 model with $f_X = 0.03$ and $T_s^\infty = 3 \cdot 10^6$ K. Auger ionization notably affects the presence of O VI in the outer wind ($\tau_{\text{Ross}} \leq 10^{-2}$ corresponding to $r \geq 4 R_*$ or $v(r) \geq 0.7 v_\infty$). The model without Auger ionization has more O V than O VI and vice versa when the effect is included.

be tracked down to completely different ionization fractions of oxygen. In particular, our models displayed more O V and less O IV than calculated by WM-BASIC.

After investigating the origin of this discrepancy, we found that we had inadvertently not included the data for dielectronic recombination¹⁷ (hereafter DR) in our oxygen atomic model. Thus, DR processes had not been considered for oxygen. (For Si, P, and C v, corresponding data are still missing in our database.)

A series of studies had recently reconsidered the effects of DR with respect to nitrogen (Rivero González et al. 2011, 2012a,b), however no significant effects were found, particularly concerning the formation of the prominent N III $\lambda\lambda$ 4634-4640-4642 emission lines that were previously attributed to DR processes (Brucato & Mihalas 1971, Mihalas & Hummer 1973).

Nevertheless, we subsequently included DR in our oxygen atomic model and were surprised by the consequences. In a large region of our model grid, we found the changes to be negligible for the

¹⁷This process can be summarized as “the capture of an electron by the target leading to an intermediate doubly excited state that stabilizes by emitting a photon rather than an electron” (Rivero González et al. 2012a).

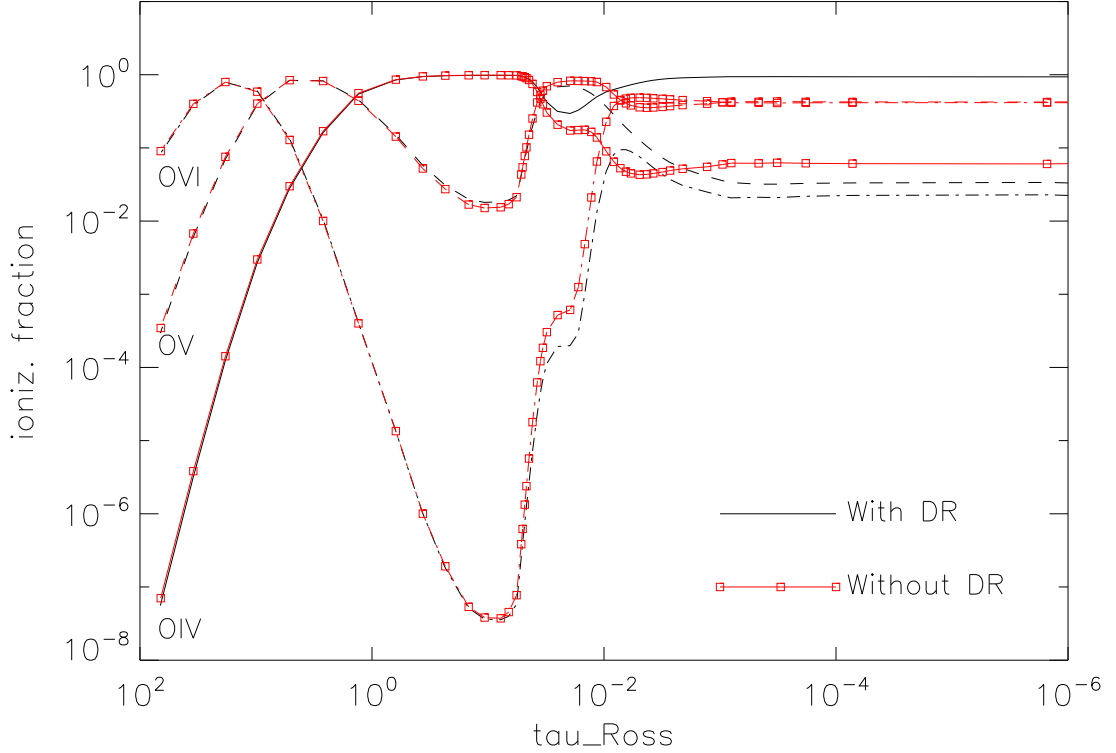


Figure 2.17: Ionization fractions of oxygen, as a function of τ_{Ross} , for a D45 model with $f_X = 0.03$ and $T_s^\infty = 3 \cdot 10^6$ K, with and without dielectronic recombination (DR). We note the large differences for all the stages when $\tau_{\text{Ross}} \leq 10^{-2}$ ($v(r) \geq 0.05v_\infty$), particularly the change in the main ionization stage (from O v/O vi to O iv) when DR is included.

fluxes. However, in all of the supergiant models and in the dwarf models around 45 kK, the ionization fractions were strongly affected, which led to a decrease of O v, typically by a factor of 10 to 50.

For our most problematic D45 model, DR proved to be essential even to predict the correct main ion throughout the wind and to produce a reliable SED around the O iv edge. Fig. 2.17 shows the impact of DR for this model. Indeed, the population of every ionization stage becomes modified in the wind, but for O iv this difference is large enough to change it to the main stage of the model. The reason for such drastic impact in the region around D45 is based on the fact that only here the X-ray ionization is potentially able to allow for the dominance of O v (see Fig. 2.8), which then can be compensated by quite strong dielectronic recombination rates.¹⁸

Nevertheless, since in the majority of models O v becomes severely depleted (see above), independent of whether it is a main ion or not, and because also O vi is affected, this leads to considerable changes in the corresponding UV lines. Thus, we conclude that DR is inevitable for a correct treat-

¹⁸As an independent check of our findings, we also calculated WM-BASIC models without DR and these turned out to be consistent with our non-DR models.

ment of oxygen. Moreover, because of this strong impact, the precision of corresponding data needs to be rechecked. As a final remark, we note that the inclusion of DR also has an impact on non-X-ray models, but to a much lower extent.

2.5.4 Mass absorption coefficient

As already mentioned in Sect. 2.1, in recent years the X-ray line emission (observed by means of CHANDRA and XMM-NEWTON) has also been modeled and analyzed by various groups. Such analysis particularly allows us to obtain constraints on the presence, structure, and degree of wind inhomogeneities at X-ray wavelengths (e.g., Oskinova et al. 2006, Sundqvist et al. 2012a, Leutenegger et al. 2013b). These models also allow us to independently “measure” the mass-loss rates of O-star winds (e.g., Hervé et al. 2013, Cohen et al. 2014b, Rauw et al. 2015) and even to derive nitrogen and oxygen abundances (Oskinova et al. 2006, Zhekov & Palla 2007, Nazé et al. 2012, Leutenegger et al. 2013a; primarily, these abundance determinations involve measuring the strengths of corresponding emission lines in the soft X-ray regime, and possibly correcting them for absorption. However, these diagnostics are not wind absorption diagnostics, but absorption is only a correction needed to derive line luminosities).

One of the assumptions made by various authors is to consider the mass absorption coefficient of the cool wind material, $\kappa_\nu(r)$, as spatially constant, which simplifies the analysis (Owocki & Cohen 2006, Leutenegger et al. 2013b, Cohen et al. 2014b). Other groups include detailed predictions for the spatial and frequency dependence of $\kappa_\nu(r)$, calculated by means of POWR (e.g., Oskinova et al. 2006) or CMFGEN (e.g., Hervé et al. 2013, Rauw et al. 2015), and there is an ongoing discussion about whether the assumption of a spatially constant κ_ν is justified and how far it affects the precision of the deduced mass-loss rates. Though Cohen et al. (2010, 2014b) investigated the variation of $\kappa_\nu(r)$ and its influence on the derived parameters based on selected CMFGEN models (also accounting for variations in the CNO-abundances), a systematic study has not been performed so far; in this section we carry out this study.

At first, we consider why and under which conditions κ_ν should become more or less spatially constant. The prime reason for this expectation is the fact that the K-shell cross sections (at threshold and with respect to wavelength dependence) of the various ions of a specific atom are quite similar, and that the corresponding edges (for these ions) lie close together. Provided now that (i) all ions that are present in the wind are actually able to absorb via K-shell processes, and (ii) that there are no background opacities from other elements, $\kappa_\nu(r)$ indeed becomes (almost) spatially constant, since the total opacity is then the simple sum over the K-shell opacities from all contributing atoms,

$$\begin{aligned}
 \kappa_\nu(r) &\approx \sum_k \left(\sum_j \frac{n_{k,j}(r)}{\rho(r)} \sigma_{k,j}(\nu) \right) \approx \\
 &\approx \sum_k \left(\sum_j \frac{n_{k,j}(r)}{\rho(r)} \right) \sigma_k(\nu) \approx \\
 &\approx \sum_k \frac{n_k(r)}{\rho(r)} \sigma_k(\nu) \approx \frac{\sum_k \alpha_k \sigma_k(\nu)}{m_{\text{H}}(1 + 4Y_{\text{He}})} := \kappa_\nu^{\text{appr}}, \tag{2.9}
 \end{aligned}$$

where α_k is the elemental abundance, Y_{He} the helium abundance (both quantities normalized to hydrogen), and m_{H} the hydrogen mass. The parameter k denotes the atomic species, j is the ion, $n_{k,j}$ is the occupation number of ion (k,j) , and $\sigma_{k,j} \approx \sigma_k$ is the K-shell cross section because it is almost independent of j . In the last step of the above derivation, we assumed that the atmosphere consists mostly of hydrogen and helium.

Thus, we have to check under which conditions restrictions (i) and (ii) might no longer be valid. For the light and abundant elements CNO, K-shell absorption is no longer possible for C v, N vi, and O vii. For these ions, only ordinary, outer-shell ionization is present, but also here the cross sections are not too different from the K-shell processes (both with respect to strength and location of edge). Thus, even for highly ionized winds (hot or with strong X-ray emission), where C v, N vi, and O vii are actually present somewhere, the above approximation is still justified. In so far, restriction (i) should play no role, since even higher ionization stages are not too be expected to be significantly populated.

Regarding restriction (ii), the situation is different. The prime background is given by the He ii bound-free opacity, which becomes strong in cool and/or helium-recombined winds¹⁹, where in the following we always refer to the recombination of He iii to He ii. Hillier et al. (1993) already showed the importance of outer-wind helium recombination on wind opacity and emergent soft X-ray emission.

We now check the maximum influence of the He ii bound-free opacity at important K-shell edges. For a crude estimate, we approximate its frequency dependence by $(\nu_0/\nu)^3 = (\lambda/\lambda_0)^3$, and assume the worst case that He ii is the only He ion present in the wind. Then, a lower limit for the opacity ratio at specific K-shell edges can be approximated by

$$\begin{aligned} \frac{\kappa_k}{\kappa_{\text{HeII}}}(\lambda_0(k)) &\approx \frac{n_k}{n_{\text{HeII}}} \frac{\sigma_0(k)}{\sigma_0(\text{HeII})} \left(\frac{\lambda_0(\text{HeII})}{\lambda_0(k)} \right)^3 \gtrsim \\ &\gtrsim \frac{\alpha_k}{\alpha_{\text{He}}} \frac{\sigma_0(k)}{\sigma_0(\text{HeII})} \left(\frac{228 \text{ \AA}}{\lambda_0(k)} \right)^3, \end{aligned} \quad (2.10)$$

where σ_0 is the cross section at the corresponding edge. Using solar abundances from Asplund et al. (2009), $\lambda_0(\text{C}) \approx 35 \text{ \AA}$ and $\lambda_0(\text{O}) \approx 20 \text{ \AA}$, $\sigma_0 \approx 1.6, 0.9$, and $0.5 \cdot 10^{-18} \text{ cm}^2$ for the threshold cross sections of He ii, carbon (K-shell), and oxygen (K-shell), respectively, we find $\kappa_{\text{C}}/\kappa_{\text{HeII}}(35 \text{ \AA}) \gtrsim 0.42$ and $\kappa_{\text{O}}/\kappa_{\text{HeII}}(20 \text{ \AA}) \gtrsim 2.3$. Thus, for cool and/or He-recombined winds, the He ii opacity dominates at the carbon K-shell edge, whilst at the oxygen edge the K-shell opacities are substantially larger than the background. Thus, we would predict that somewhat below $\approx 20 \text{ \AA}$ (beyond 620 eV) restriction (ii) becomes valid, and that κ_{ν} should become depth independent. Vice versa, the mass absorption coefficient should vary with radius longward from the oxygen or carbon K-shell edge whenever the background mass absorption coefficient varies, which is mostly due to changes in the He ii ionization throughout the wind.

In the following, we discuss these issues by means of our grid models; all of these models have shock emission described by our typical parameters ($T_s^{\infty} = 3 \cdot 10^6 \text{ K}$ and $f_X = 0.03$). In particular, we provide estimates for suitable means of κ_{ν} , as a function of T_{eff} .

¹⁹Additionally, the outer-shell ionization of O iv with edge at $\approx 160 \text{ \AA}$ and the bound-free opacities from other, strongly abundant ions can play a minor role, particularly if He ii is weak or absent.

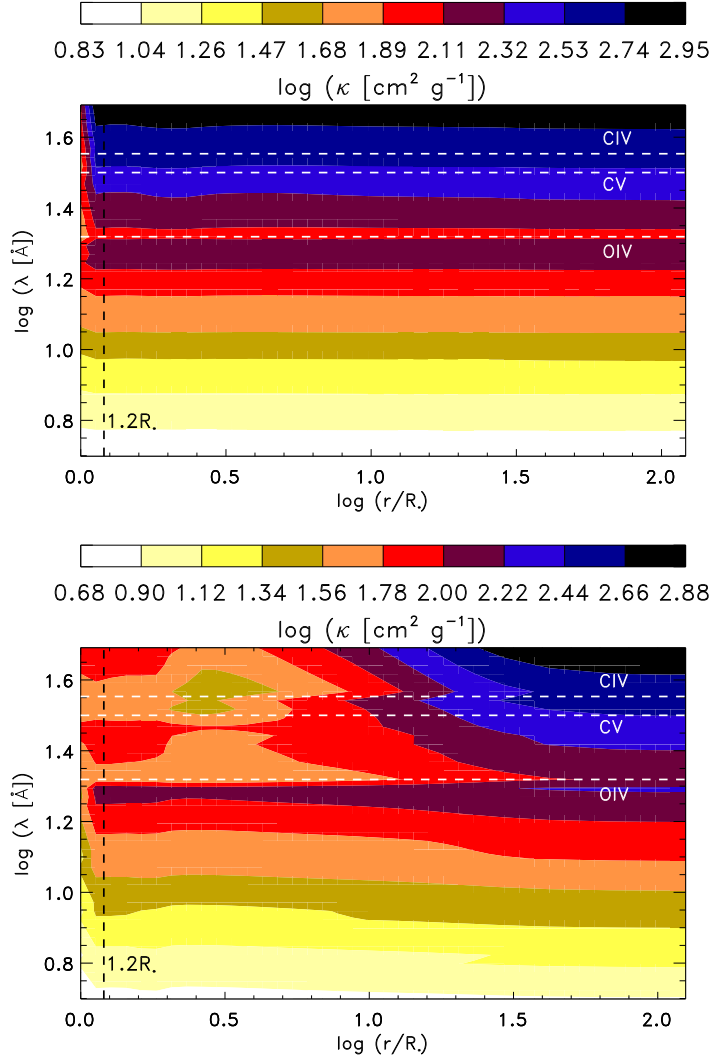


Figure 2.18: Contour plots illustrating the radial dependence of the mass absorption coefficient, $\kappa_\nu(r)$, as a function of wavelength. The top panel refers to model D30, and the bottom panel indicates model S40, which both have typical X-ray emission parameters ($T_\infty^\infty = 3 \cdot 10^6$ K and $f_X = 0.03$). The positions of the C v edge (outer-shell ionization) and the C iv and O iv K-shell edges are indicated.

Figure 2.18 shows contour plots of the radial dependence of the mass absorption coefficient in the D30 model (upper panel) and in the S40 model (lower panel) as a function of wavelength. In accordance with our expectation from above, in both panels we note that κ_ν becomes constant when $r \geq 1.2 R_*$ and the wavelength is lower than 20 \AA ($\log \lambda \lesssim 1.3$), to be on the safe side. In most cases, the radial limit, arising from fluctuations in the opacity background, is even lower.

Longward of the O iv K-shell edge ($\lambda > 21 \text{ \AA}$), the radial variation of κ_ν depends on effective temperature and wind density. For the D30 model, κ_ν increases significantly with wavelength, but

nevertheless does not vary with radius because in this case the dominating ionization fraction of He II remains constant throughout the wind. In contrast, somewhat hotter models (e.g., D35), but particularly models with denser winds such as S40 display a different behavior. Here, the lower wind is dominated by He III, so that the background is weak, and one can already discriminate the C IV and C V edges around $10 R_*$ (indicated as dashed lines). Compared to the dwarf models, the total κ_ν in the inner wind is much lower, shows much more structure, and is influenced by the carbon and nitrogen opacities. Once helium begins to recombine in the outer wind, the background begins to dominate again and the K-shell features vanish.

Fig. 2.19 (upper part) illustrates the radial variation of the mass absorption coefficient for different wavelengths, and for our dwarf models with T_{eff} from 30 to 50 kK. Independent of T_{eff} , the radial variation of κ_ν is marginal at (and below) 10 \AA . Around 20 \AA , the variations in the inner/intermediate wind (until $10 R_*$) are somewhat larger, due to changes in the oxygen ionization, where the specific positions of the corresponding edges play a role (see also Fig. 2.20, upper panel). At 30 \AA , we see a separation between D30 (black) with high values of κ_ν (He II dominating), hot models with low values of κ_ν (C V + low background, since helium completely ionized), and D35 (green) with a significantly varying κ_ν , due to the recombination of He III in the external wind. At 40 \AA , finally, the behavior is similar, and only the κ_ν values for the cooler models are larger, because of the increasing He II background.

The analogous situation for supergiants is shown in Fig. 2.19, lower part. Whilst for dwarfs the variation of κ_ν (when present) vanishes at around $10 R_*$, here it is visible throughout the wind up to large radii for all but the coolest (black) and hottest (red) models. The limiting values (at the outermost radius) are similar to those of the corresponding dwarf models at $T_{\text{eff}} = 30$ and 35 kK (recombined) and at $T_{\text{eff}} = 50$ kK (He III). In contrast, for models with $T_{\text{eff}} = 40$ and 45 kK the opacity continues to increase outward, since the recombination is still incomplete.

Hervé et al. (2013) provided a similar figure to investigate the radial variation of κ_ν , in this case for a model of ζ Pup calculated by CMFGEN. While the stellar parameters roughly agree with our S40 model, these authors considered a clumpy wind (with volume filling factor $f_V = 0.05$), and nuclear processed CNO abundances. Because this model shows an earlier recombination of helium with a larger nitrogen and weaker oxygen K-shell edge, the actual values of κ_ν are somewhat different from our results (except at shortest wavelengths), but the basic trends are quite similar. In particular, our results support the idea of Hervé et al. (2013) of parameterizing the run of κ_ν : In any of the $\kappa_\nu(r)$ -curves shown in Fig. 2.19, these curves either increase or slightly decrease, but eventually reach a plateau from a certain radius on (which differs for each model). This radius then separates two different regimes of κ_ν that might be parameterized in an appropriate way (see Hervé et al. 2013 for details).

Instead of a parameterization, it is also possible to calculate meaningful averages of κ_ν and the corresponding scatter. The size of this scatter then allows us to conclude when (w.r.t. wavelength and T_{eff}) a spatially constant mass absorption coefficient might be used to analyze X-ray line profiles. Instead of a straight average, we use a density-weighted average (and a corresponding variance) to account for the fact that the optical depth, τ_ν , is the quantity that needs to be calculated with high

precision

$$\tau_\nu = \int_{R_{\min}}^{R_{\max}} \kappa_\nu(r) \rho(r) dr =: \bar{\kappa}_\nu \int_{R_{\min}}^{R_{\max}} \rho(r) dr \quad \Rightarrow$$

$$\bar{\kappa}_\nu = \int_{R_{\min}}^{R_{\max}} \kappa_\nu(r) f(r) dr, \quad (2.11)$$

$$\text{Var}(\kappa_\nu) = \int_{R_{\min}}^{R_{\max}} (\kappa_\nu(r) - \bar{\kappa}_\nu)^2 f(r) dr \quad (2.12)$$

$$\text{with p.d.f. } f(r) dr = \rho(r) dr / \left[\int_{R_{\min}}^{R_{\max}} \rho(r) dr \right].$$

In this approach, the density weights correspond to a probability distribution function (p.d.f.). The quantity R_{\min} indicates the lower boundary for the averaging process and must not be confused with the onset radius of the X-ray emission.

Fig. 2.20 (upper panel) shows such mean mass absorption coefficients, $\bar{\kappa}_\nu$, as a function of wavelength, averaged over the interval between 1.2 and 110.0 R_* , for our dwarf models; the impact of this chosen interval is discussed below. The lower panel denotes the relative standard deviation, $\sqrt{\text{Var}(\kappa_\nu)}/\bar{\kappa}_\nu$. Also here, cold and hot models are clearly separated with D35 in between (cf. with Fig. 2.19, upper part): For $\lambda \gtrsim 21 \text{ \AA}$, the cold models are affected by a strong He II-background, whilst this background is weak for the hotter models. In this long wavelength region, the radial variation of κ_ν is large for model D35, as a result of recombining helium. There is also a considerable scatter between 18 and 21 \AA because of radial changes in the oxygen ionization. Overall, however, the assumption of a constant mass absorption coefficient (suitably averaged) is not too bad for the complete wavelength range (scatter below 20%), if we exclude model D35. Below 18 \AA , the scatter becomes negligible, except at the Ne, Mg, and Si edges.

Even if $\kappa_\nu(r)$ can be approximated by a single number, $\bar{\kappa}_\nu$, the question is then about its value. For comparison, the dashed line in Fig. 2.20 shows the (analytic) estimate, κ_ν^{appr} as provided by Eq. 2.9, using only solar abundances and K-shell opacities with cross sections from C IV, N IV, O IV, Ne IV, Mg IV, and Si IV. At least for hotter dwarf models, this estimate is quite appropriate when comparing to the actual case, except for a somewhat erroneous description of the carbon edge(s): Since C v dominates in the hotter models and there is a $\sim 4 \text{ \AA}$ difference between the C IV K-shell and the C v edge, this region is badly described by our approximation. For cooler dwarf models, on the other hand, the difference between the dashed and solid curves is (mostly) due to the helium background, which varies as a function of T_{eff} , $\log g$, and wind density, thus affecting the actual value of $\bar{\kappa}_\nu$. Even below 18 \AA , this background is still non-negligible for model D30 with a maximum deviation of roughly 30% close to the oxygen edge. Nevertheless, we conclude that for all dwarf models with $T_{\text{eff}} \geq 35 \text{ kK}$, the assumption of a constant mass absorption coefficient approximated by κ_ν^{appr} is justified when $\lambda \leq 18 \text{ \AA}$ (at least within our present assumptions, i.e., solar abundances and unclumped winds with optical depths that are not too large, such that the averaging down to 1.2 R_* is reasonable). In all other cases, results from NLTE-atmosphere modeling should be preferred.

The situation for our supergiant models is displayed in Fig. 2.20, lower panel. Below 20 \AA , the situation is similar to the dwarf case, although here the background is lower, even for the coolest model, and the approximation of $\bar{\kappa}_\nu$ by κ_ν^{appr} might now be applied at all temperatures. For $\lambda > 30 \text{ \AA}$,

however, almost all models (except for S50) can no longer be described by a radially constant κ , since all models with $T_{\text{eff}} \leq 45$ kK show recombining helium of different extent, leading to strong variations throughout the wind.

Thus far, we considered models with solar abundances and unclumped winds. To illustrate the variation of the total and K-shell opacities with abundance (already investigated for particular models by, e.g., Cohen et al. 2010, 2014b), the dotted lines in Fig. 2.20 denote the approximate K-shell opacities, $\kappa_{\nu}^{\text{appr}}$, for the case of highly processed CNO material based on the abundances derived for ζ Pup by Bouret et al. (2012). Here, the carbon and oxygen abundances are depleted by 0.8 and 0.6 dex, respectively, whilst the nitrogen abundance is extremely enhanced (by ~ 1.3 dex) compared to the solar values. Such a composition leads to weak C and O K-shell edges, but to an enormous nitrogen edge (dotted vs. dashed line).

Now, if the individual abundances are known during an analysis, there is no problem, and κ_{ν} might be approximated by either $\kappa_{\nu}^{\text{appr}}$ below 18 \AA or calculated by means of NLTE-model atmospheres, simply accounting for these abundances. However, considerable uncertainties even in the low wavelength regime might result when the abundances are not known. From comparing the dashed and dotted line, we estimate this uncertainty as roughly 50% for $\bar{\kappa}_{\nu}$, and thus for τ_{ν} and \dot{M} (when the mass-loss rate shall be derived). A similar value has already been estimated by Cohen et al. (2014b). In the range between the oxygen and carbon edge (20 to 35 \AA), the situation is even worse and we conclude that the corresponding absorption coefficients are prone to extreme uncertainties when the abundances have to be adopted without further verification. In particular, getting κ_{ν} right around 25 \AA is important for measuring the N emission lines at and close to that wavelength (e.g., N VI 24.9, N VII 24.78), and thus measuring the N abundance directly. At longer wavelengths, however, where κ_{ν} varies even more strongly with radius, and even though nitrogen emission lines are not directly affected, the (direct) ionization of elements such as CNO is affected, and so optical and UV line strengths are affected too, as discussed in the previous sections.

The impact of clumping is less severe. Comparing Fig. 2.34 (Appendix) with Fig. 2.20, we see that models accounting for optically thin clumping (“micro-clumping”) with typical clumping factors ($f_{\text{cl}} = 20$ corresponding to a volume filling factor, $f_{\nu} = 0.05$) and adequately reduced mass-loss rates give rather similar results compared with unclumped models. Again, the scatter of κ_{ν} is negligible below 18 \AA . ‘The region longward of 20 \AA is the only region that is more strongly contaminated by the He II background, since the clumped models recombine earlier than the unclumped models. The K-shell mass absorption coefficients themselves are not affected by optically thin clumping, since the opacities scale linearly with density.

Finally, Fig. 2.35 (Appendix) investigates the consequences of averaging κ_{ν} in the outer wind alone (in the interval between 10 and $110 R_{*}$), which would be adequate if the wind would become optically thick at such radii (which for short wavelengths and O-star winds is quite unlikely because of the low value of κ_{ν}). Anyway, below 18 \AA the differences to the original values are small. The hot dwarf models now behaves almost exactly as estimated by $\kappa_{\nu}^{\text{appr}}$ because He II vanishes in the outer regions of these objects. Further conclusions on this topic are provided in the next section.

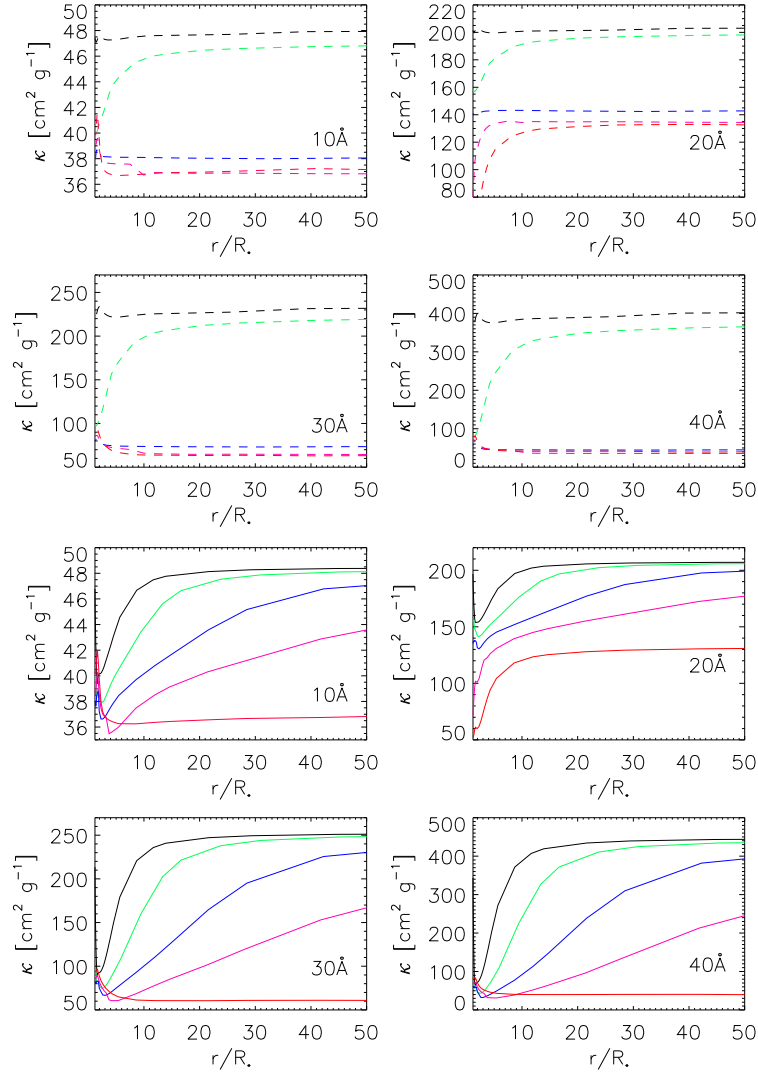


Figure 2.19: **Upper four panels:** radial variation of the mass absorption coefficient in dwarf models for specific values of wavelength. Black: $T_{\text{eff}} = 30\text{kK}$; green: 35 kK; blue: 40 kK; magenta: 45 kK; and red: 50 kK. All models have been calculated with $T_s^\infty = 3 \cdot 10^6$ K and $f_X = 0.03$. We note the different scales for κ_ν . **Lower four panels:** as above, but for supergiant models.

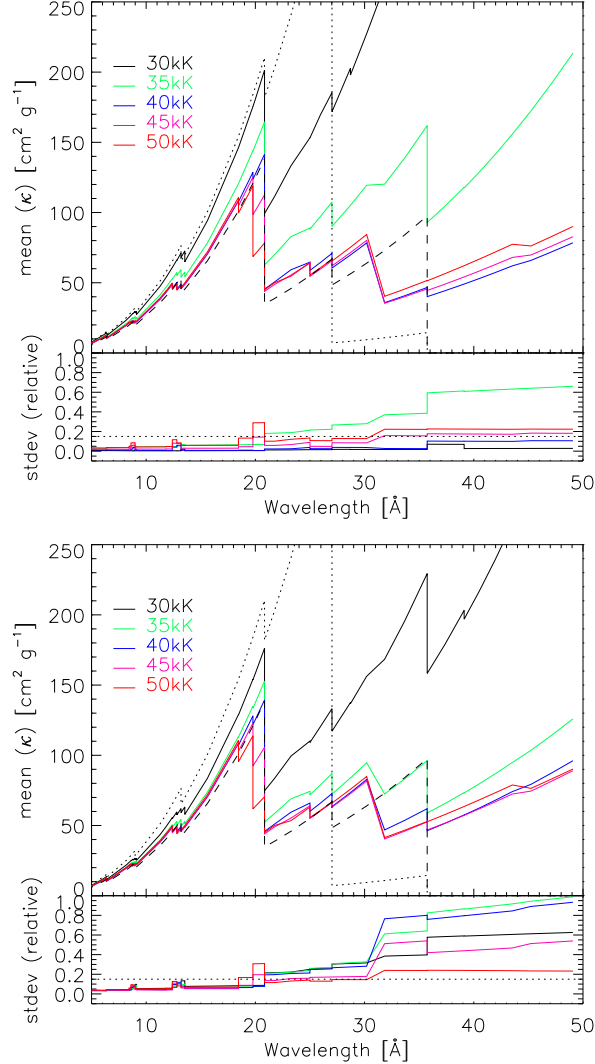


Figure 2.20: **Upper panel, top:** density-weighted mean (Eq. 2.11) of the mass absorption coefficient, $\bar{\kappa}_\nu$, for the interval between 1.2 and $110 R_*$, as a function of wavelengths and for dwarf models with $T_s^\infty = 3 \cdot 10^6$ K and $f_X = 0.03$. Solar abundances following Asplund et al. (2009) were adopted. Dashed: approximate, radius-independent κ_ν^{appr} (Eq. 2.9), using only solar abundances and K-shell opacities with cross sections from C IV (with threshold at 35.7 \AA), N IV (27.0 \AA), O IV (20.8 \AA), Ne IV (13.2 \AA), Mg IV (9.0 \AA), and Si IV (6.4 \AA). The C V edge (at 31.6 \AA) appears to be unresolved in our frequency grid. Dotted: same as dashed, but with nuclear processed CNO abundances as derived for ζ Pup by Bouret et al. (2012). The nitrogen abundance is more than a factor of 10 larger than the solar abundance. Dashed and dotted lines also serve as a guideline for comparison with similar figures. **Bottom:** relative standard deviation, $\sqrt{\text{Var}(\kappa_\nu)}/\bar{\kappa}_\nu$ (see Eq. 2.12), for the same models. The dotted line denotes a relative scatter of 15%.

Lower panel: as above, but for supergiant models.

2.6 Summary and conclusions

In this paper, we described the implementation of X-ray emission from wind-embedded shocks into the unified, NLTE atmosphere/spectrum synthesis code FASTWIND, discussed various tests, and presented some initial results.

Our implementation follows closely corresponding work by Pauldrach et al. (2001) for WM-BASIC, which in turn is based on the shock cooling zone model developed by Feldmeier et al. (1997a) with the additional possibility of considering isothermal shocks. The (present) description of the shock distribution and strength is provided by four input, “X-ray emission parameters”, controlling the filling factor, the run of the shock temperature, and the radial onset of the emitting plasma. We account for K-shell absorption and Auger ionization, allowing for more than one final ionization stage due to cascade ionization processes.

Most of our test calculations are based on a grid of 11 models (supergiants and dwarfs within $T_{\text{eff}} = 30$ to 55 kK), each of them with nine different X-ray emission parameter sets, but we calculated many more models for various comparisons, including models with optically thin clumping.

A first test investigated the reaction when varying important X-ray emission parameters. For radially increasing shock strengths, the emergent flux remains almost unaffected if the onset radius is lowered compared to its default value (roughly $1.5 R_*$), whilst increasing the onset has a considerable effect in the range between $\sim 350 \text{ \AA}$ and at least the He II edge. Filling factor and maximum shock temperature affect the ionization fractions, particularly of the highly ionized species. We confirm some earlier predictions for scaling relations for X-ray luminosities (as a function of \dot{M}/v_∞) in the case of optically thin and thick continua, (though a discrepancy with recent work by Owocki et al. 2013 was identified, which needs to be investigated further), but we noted that for our hottest models these luminosities can become contaminated by normal stellar radiation for energies below $\sim 150 \text{ eV}$. Thus, we suggested choosing a lower integration limit of 0.15 keV (or even 0.3 keV, to be on the safe side) when comparing the X-ray luminosities of different stars or theoretical models. Finally, we found an excellent agreement between FASTWIND and WM-BASIC fluxes, demonstrating a similar ionization balance, and a satisfactory agreement between corresponding X-ray luminosities. Overall, the impact of typical shock emission affects the radiation field in the wind for all wavelengths $\lambda < 350 \text{ \AA}$, thus modifying all photo rates for ions with ionization edges in this regime.

Investigating the ionization fractions within our model grid allowed us to study the impact of shock radiation for the proper description of important ions, i.e., those with meaningful wind lines (e.g., C IV, N IV, N V, O V, O VI, Si IV, and P V). If we denote models with $T_{\text{eff}} = 30$ to 35 kK as “cool”, models with $T_{\text{eff}} = 35$ to 45 kK as “intermediate”, and models with $T_{\text{eff}} = 45$ to 55 kK as “hot” (note the overlap), we can summarize our findings as follows. Those ions *not* (or only marginally) affected by shock emission (with typical parameters and our parameterization of the shock strengths) are

- in dwarfs: C III, C IV, N III (cool), N IV (cool), O IV (intermediate), Si IV, P V (cool+intermediate)
- in supergiants: C III (hot), C IV (hot), N IV (cool), O IV (intermediate), Si IV (hot).

In almost all of the other cases, the lower stages (C III, C IV, N III, N IV, O IV (hot), Si IV, and P V) are depleted, i.e., corresponding wind lines become weaker, and the higher stages (N V, O IV (cool), O V,

O VI) become enhanced, i.e., corresponding wind lines become stronger when accounting for shock emission.

We studied in some detail how the ionization fractions change when the two most important parameters, filling factor and maximum shock temperature, are varied. For most ions, the filling factor has a larger influence than T_s^∞ , but particularly O VI and P V (the latter only for higher filling factors and shock temperatures) show a strong reaction to both parameters.

As a result of the importance of P V with respect to mass loss and wind-structure diagnostics, we reinvestigated the behavior of P V and confirm previous results that for typical X-ray emission parameters this ion is only weakly or moderately affected (by factors of two for intermediate and hot supergiants at $v(r)/v_\infty = 0.5$ and by factors of 10 at $v(r)/v_\infty = 0.8$). For a strong X-ray radiation field, however, the depletion can reach much higher factors. A comparison of P V ionization fractions with results from CMFGEN (Bouret et al. 2012) provided a reasonable agreement.

Not only metals, but also He can be affected by shock emission because of the location of the He II edge and He II 303 in the EUV. Significant effects, however, have only been found in the winds of cool supergiants, where particularly He II 1640 (emission and high-velocity absorption) and He II 4686 (emission) become stronger because of increased recombination cascades and increased pumping of the $n = 2$ level in the case of He II 1640.

When comparing our ionization fractions with those calculated by WM-BASIC, we found a good, though not perfect, agreement, which we found to be true for various UV line profiles as well. When comparing with Krtićka & Kubát (2009), on the other hand, a similar agreement over the complete covered temperature range was found only for few ions; for the majority, such agreement is present only at specific temperatures.

It is well known that Auger ionization can play an important role for the ionization balance of specific ions. To further investigate this issue, we compared the ionization fractions of all ions considered in this study when including (default) or excluding this process in our NLTE treatment. Overall, we found that only N VI and O VI (as previously known) are significantly affected by Auger ionization, but, at least in our models (with radially increasing shock temperatures), these ions are only affected in the outer wind. For the inner and intermediate wind, direct EUV/XUV ionization due to shock emission dominates, which is generally true for all other considered ions. (Additionally, the presence of a low-density interclump medium is essential for the formation of O VI in clumped winds; see Zsargó et al. 2008.)

As an interesting by-product of our investigation, we found that dielectronic recombination of O V can have a considerable influence on the ionization balance of oxygen (O IV vs. O V), particularly for dwarfs around 45 kK.

In the last part of this paper, we provided an extensive discussion of the high-energy mass absorption coefficient, κ_ν , regarding its spatial variation and dependence on T_{eff} . This topic is particularly relevant for various approaches to analyzing X-ray emission lines. To summarize and conclude, we found that (i) the approximation of a radially constant κ_ν can be justified for $r \gtrsim 1.2R_*$ and $\lambda \lesssim 18 \text{ \AA}$, and also for many models at longer wavelengths. (ii) In order to estimate the actual value of this quantity, however, the He II background and, to a lesser extent, the bound-free background from highly abundant metals needs to be considered from detailed modeling, at least for wavelengths longer than 18 to 20 \AA . Moreover, highly processed CNO material can change the actual value of κ_ν considerably,

particularly for $\lambda \gtrsim 20 \text{ \AA}$, and estimates for the optical depth, τ_ν , become highly uncertain in this regime if the individual abundances are unknown.

In this context, it is reassuring to note that, for example, the mass-loss determinations by Cohen et al. (2014b) using X-ray line spectroscopy (via determining the optical depths of the cool wind material, under the assumption of spatially constant κ_ν) rely on 16 lines observed by CHANDRA, where 14 out of these 16 lines are shortward of 19 \AA . The issues summarized above will be a much bigger problem for O VII and nitrogen X-ray emission line measurements (O VII at $21.6\text{-}22.1 \text{ \AA}$, N VII at 24.78 \AA , and N VI at 24.9 \AA), which are planned to independently constrain, with high precision, the nitrogen/oxygen content in (a few) massive O stars (Leutenegger et al. 2013a). To this end, a detailed modeling of κ_ν (particularly regarding the helium ionization) will certainly be advisable for such an analysis.

Now that we have finalized and carefully tested our implementation of emission from wind-embedded shocks, we are in a position to continue our work on the quantitative spectroscopy of massive stars. As outlined in the introduction, we will concentrate on determining the carbon and oxygen abundances in O and early B stars observed during the two VLT-FLAMES surveys conducted within our collaboration, by means of optical and, when available, UV spectroscopy. During such an analysis, the X-ray emission parameters need to be derived in parallel with the other, main diagnostics, at least in principle. We then have to check how far the derived abundances depend on corresponding uncertainties.

We further note that any such UV analysis also needs to consider the effects of optically thick clumping (e.g., Oskinova et al. 2007, Sundqvist et al. 2011, Šurlan et al. 2013, Sundqvist et al. 2014). In parallel with the implementation of wind-embedded shocks presented here, we have updated FASTWIND to account properly for such optically thick clumping (porosity in physical and velocity space), following Sundqvist et al. (2014); these models will be presented in an upcoming (fourth) paper of this series.

Regarding quantitative spectroscopic studies accounting for X-ray ionization effects, the parameterization represented by Eq. 2.7 is certainly not the final truth, and is actually not the best encapsulation of the results from current numerical simulations. Though this probably does not matter too much for most applications, it might be worth considering a better representation and how our results would change if the stronger and weaker shocks were allowed to be more spatially mixed.

LDI simulations (e.g., Feldmeier et al. 1997b, Dessart & Owocki 2003, Sundqvist & Owocki 2013) indicate that the velocity dispersion peaks quite close to R_{\min} ($\sim 1.5\text{-}2.0 R_*$) and then falls off. And the same simulations also show some strong shocks near R_{\min} . From the observational side, f/i ratios of ions that form at higher temperatures (e.g., Si XIII) indicate a substantial amount of high-temperature plasma ($\sim 10^7 \text{ K}$) near R_{\min} (e.g., Waldron & Cassinelli 2001, Waldron & Cassinelli 2007), and Leutenegger et al. (2006) found an onset radius of $1.1^{+0.4/-0.1} R_*$ for the S xv line. On the other hand, Cohen et al. (2014a) showed that the shock temperature distribution is very strongly skewed toward weak shocks and our parameterization Eq. 2.7 already allows us to include that feature now.

2.A Appendix A: Ionization fractions of selected ions: Dependence on X-ray filling factor and shock temperature

Figures 2.21 to 2.30 show the reaction of C iv, N v, O v, O vi, and P v on varying the X-ray filling factors and shock temperatures within our supergiant and dwarf models as a function of T_{eff} . For further explanation and discussion, see Sect. 2.5.1.

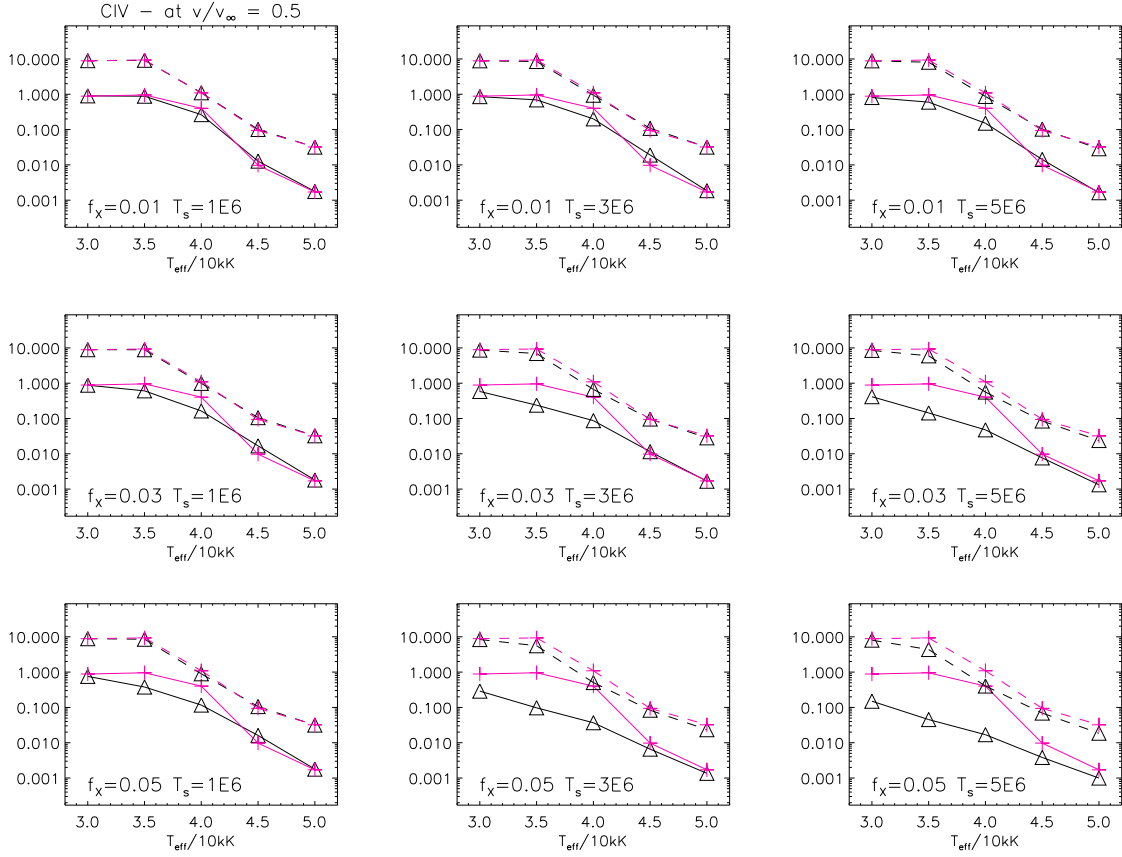


Figure 2.21: Ionization fractions of C IV (at $\nu(r) = 0.5v_\infty$), as a function of T_{eff} , and for different X-ray emission parameters. Solid: supergiant models; dashed: dwarf models; black: models with shock emission; magenta: models without shock emission. For clarity, the ionization fractions of dwarf models have been shifted by one dex.

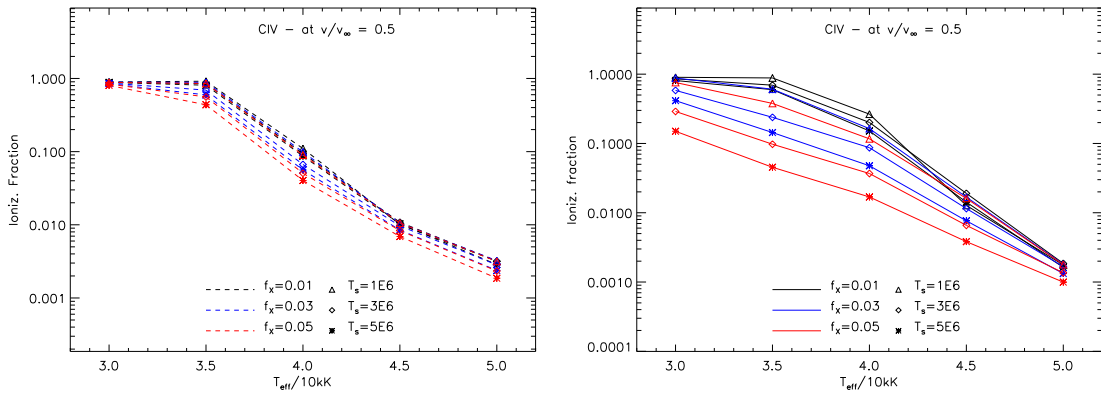


Figure 2.22: *Left panel:* As above (C IV at $\nu(r) = 0.5v_\infty$), but now for dwarf models alone and for all X-ray emission parameters included in our grid. The fractions have not been shifted here. *Right panel:* as left, but for supergiant models.

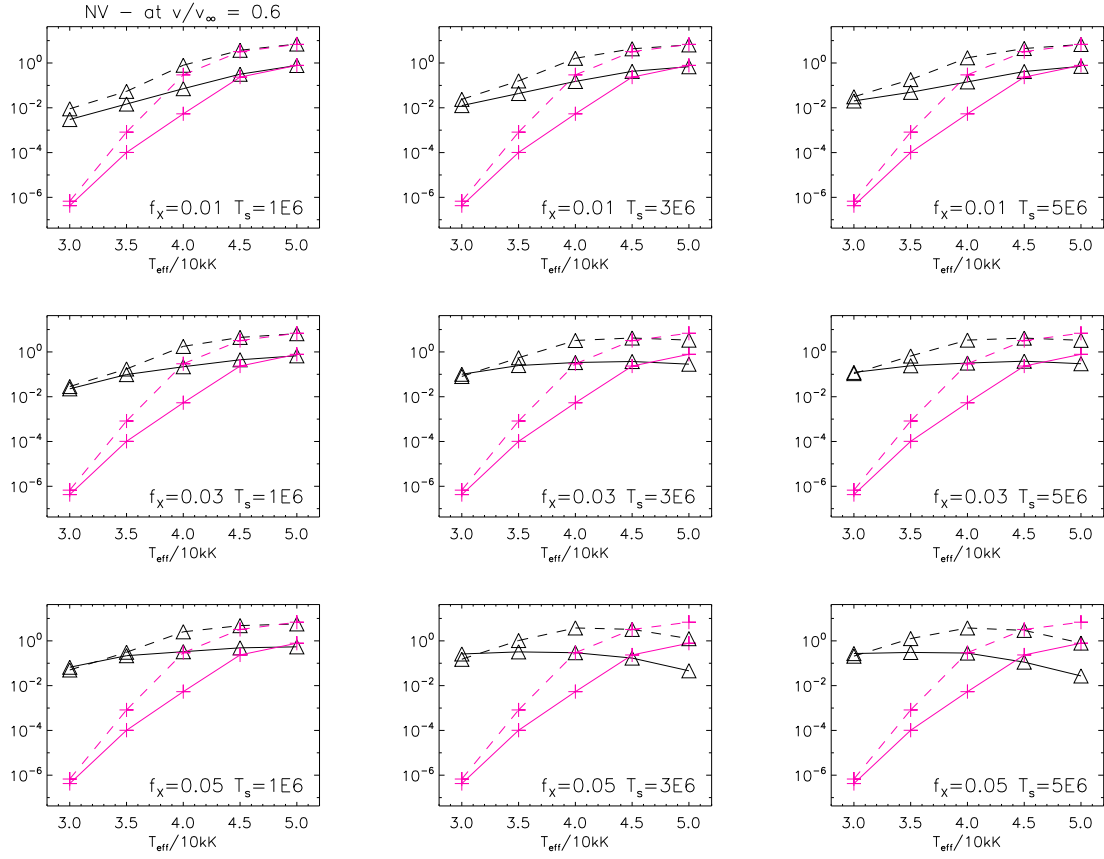


Figure 2.23: As Fig. 2.21, but for N v at $v(r) = 0.6v_\infty$

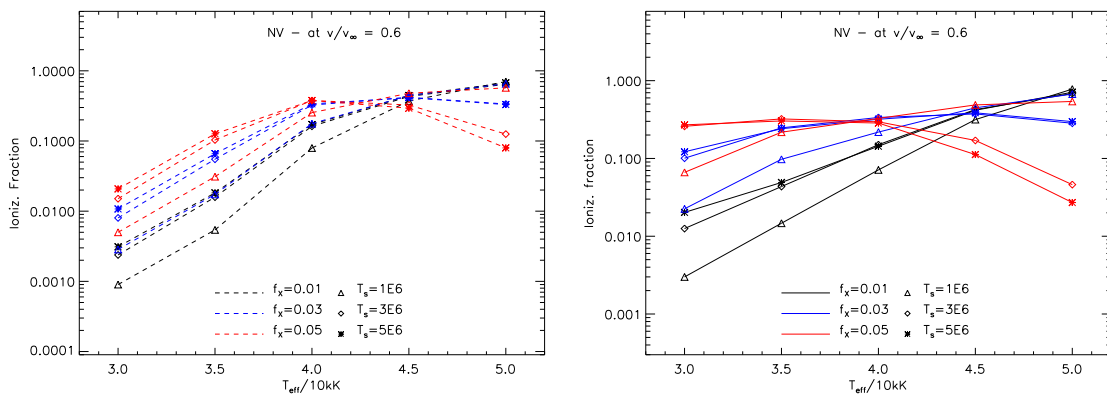


Figure 2.24: As Fig. 2.22, but for N v ($v(r) = 0.6v_\infty$)

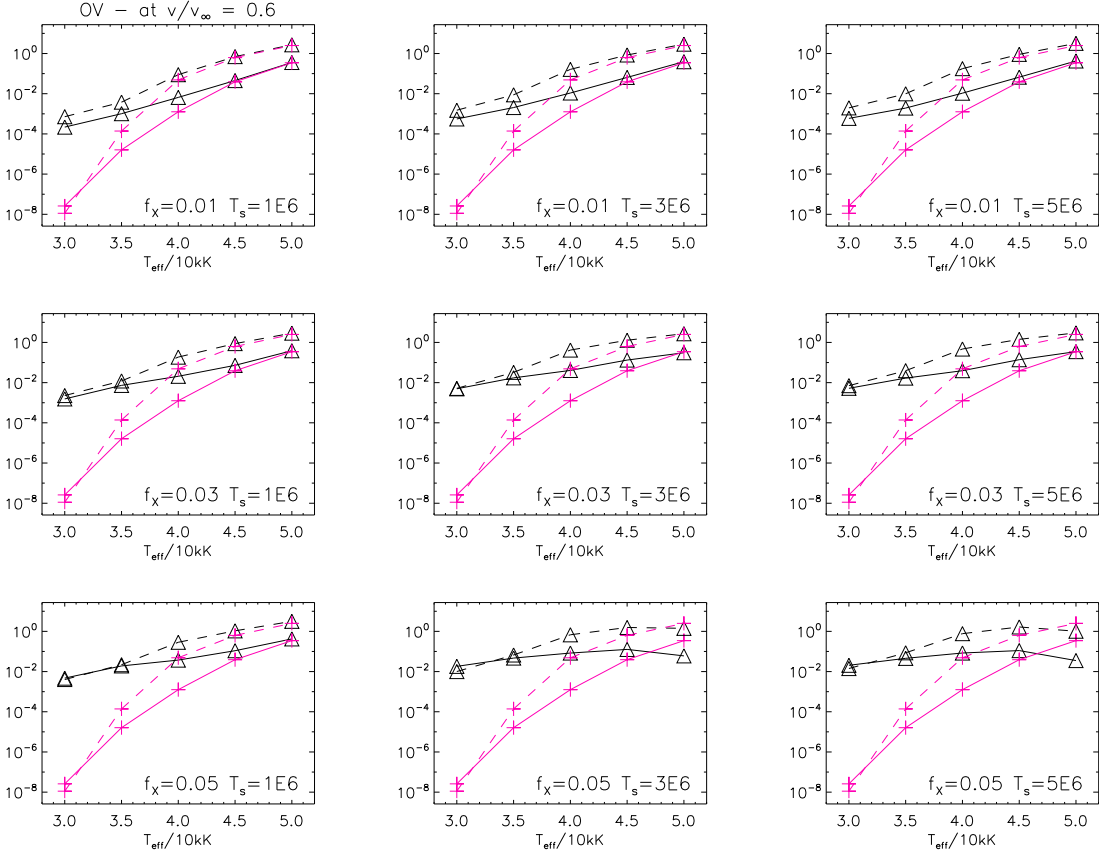


Figure 2.25: As Fig. 2.21, but for O v at $v(r) = 0.6v_\infty$.

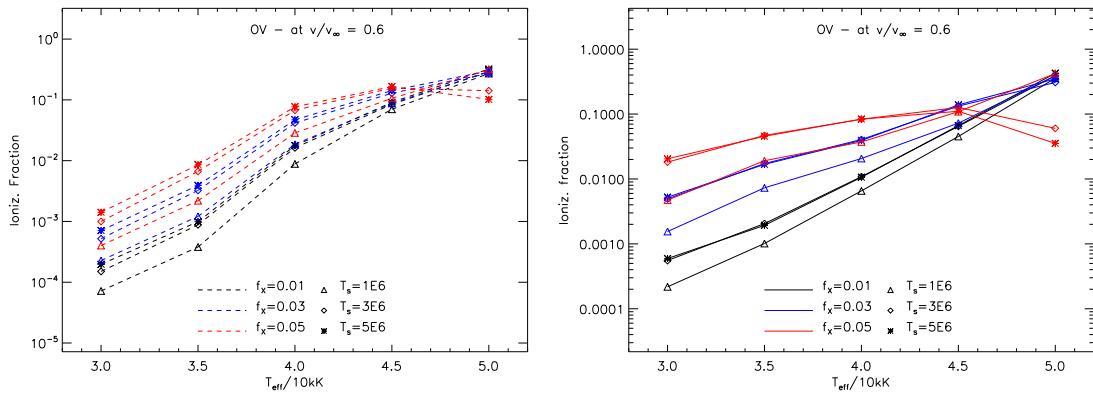


Figure 2.26: As Fig. 2.22, but for O v ($v(r) = 0.6v_\infty$).

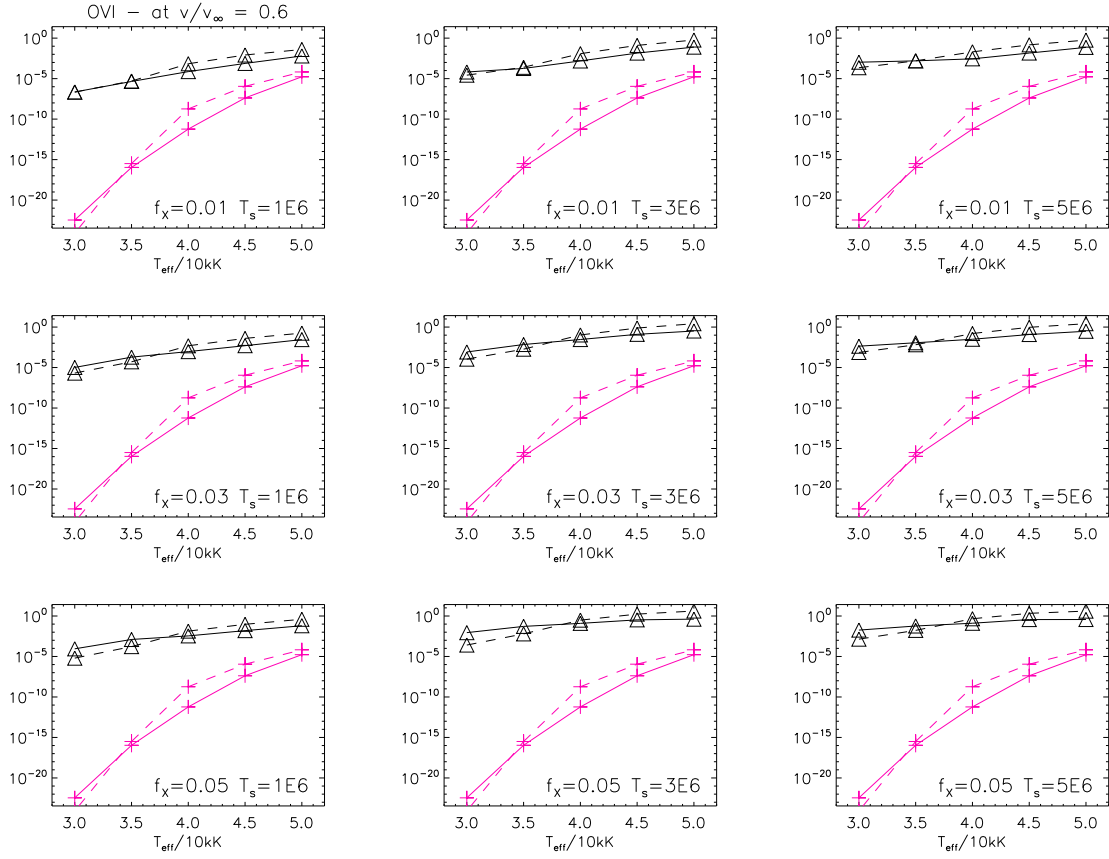


Figure 2.27: As Fig. 2.21, but for O VI at $v(r) = 0.6v_\infty$.

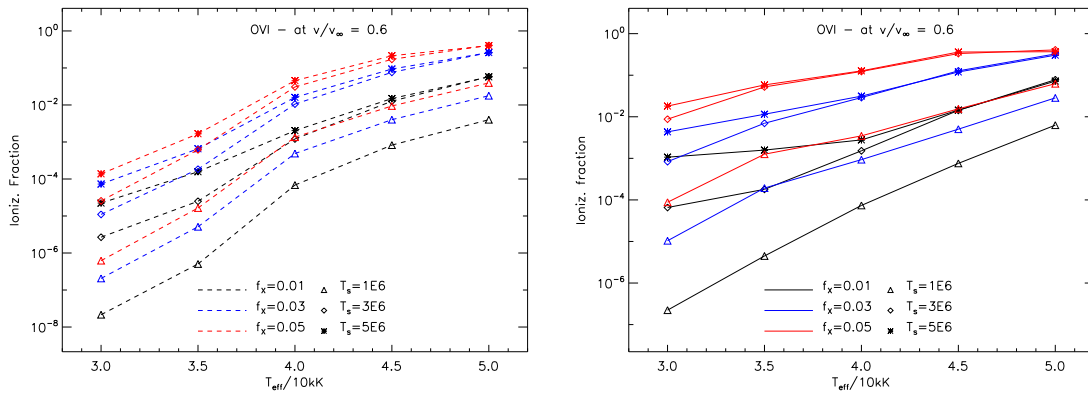


Figure 2.28: As Fig. 2.22, but for O VI ($v(r) = 0.6v_\infty$).

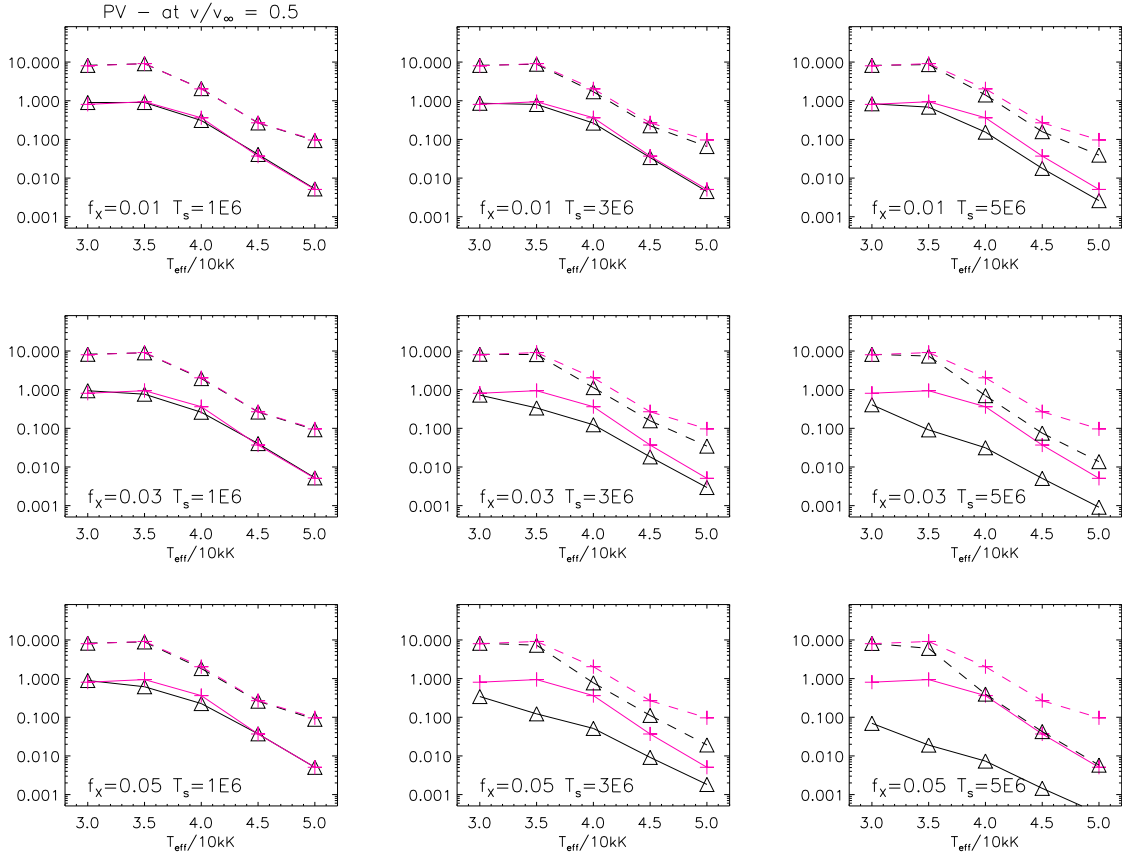


Figure 2.29: As Fig. 2.21, but for P v at $v(r) = 0.5v_{\infty}$.

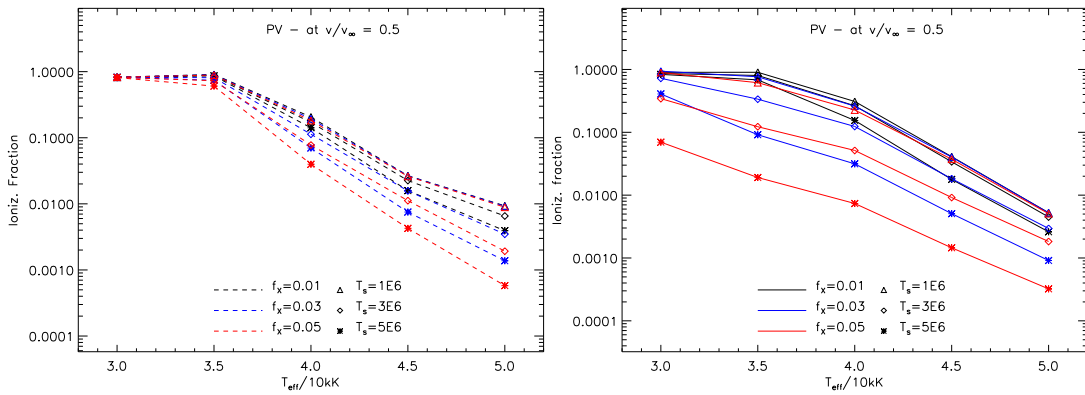


Figure 2.30: As Fig. 2.22, but for P v ($v(r) = 0.5v_{\infty}$).

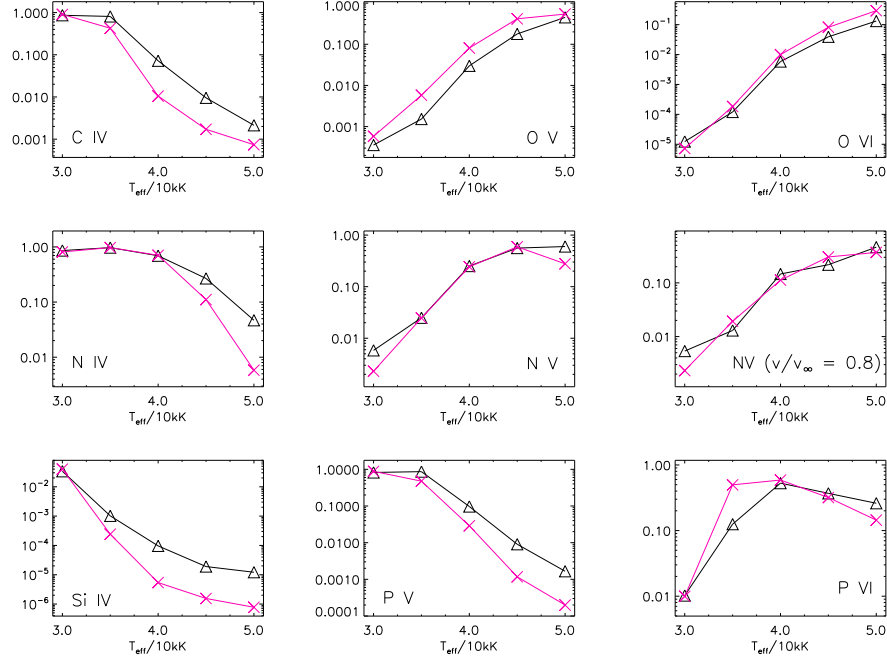


Figure 2.31: Ionization fractions of specific ions, as calculated by FASTWIND (black) and WM-BASIC (magenta) for our dwarf models and as a function of T_{eff} . If not stated explicitly inside the individual panels, the fractions were evaluated at $v(r) = 0.5v_{\infty}$. See Sect. 2.5.1.

2.B Appendix B: Comparison with WM-BASIC: Ionization fractions and UV line profiles

In Figs. 2.31 and 2.32, we compare the ionization fractions of specific ions, as calculated by FASTWIND and WM-BASIC, for dwarf and supergiant models, respectively. Fig. 2.33 compares corresponding strategic UV-line profiles for N IV 1720, N V 1238,1242, O V 1371, O VI 1031,1037, and P V 1117,1128. Further explanation and discussion is provided in Sect. 2.5.1.

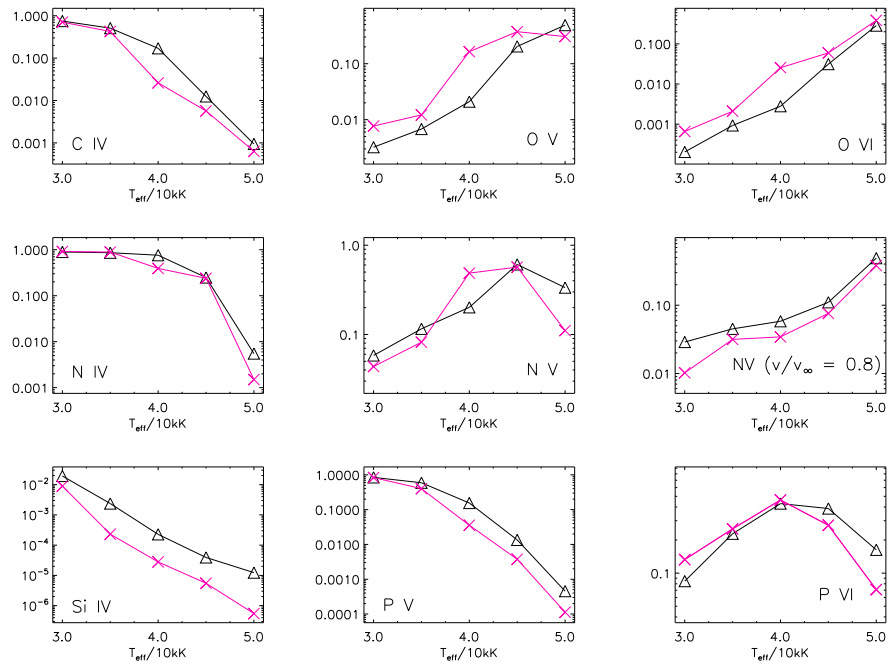


Figure 2.32: As Fig. 2.31, but for supergiant models.

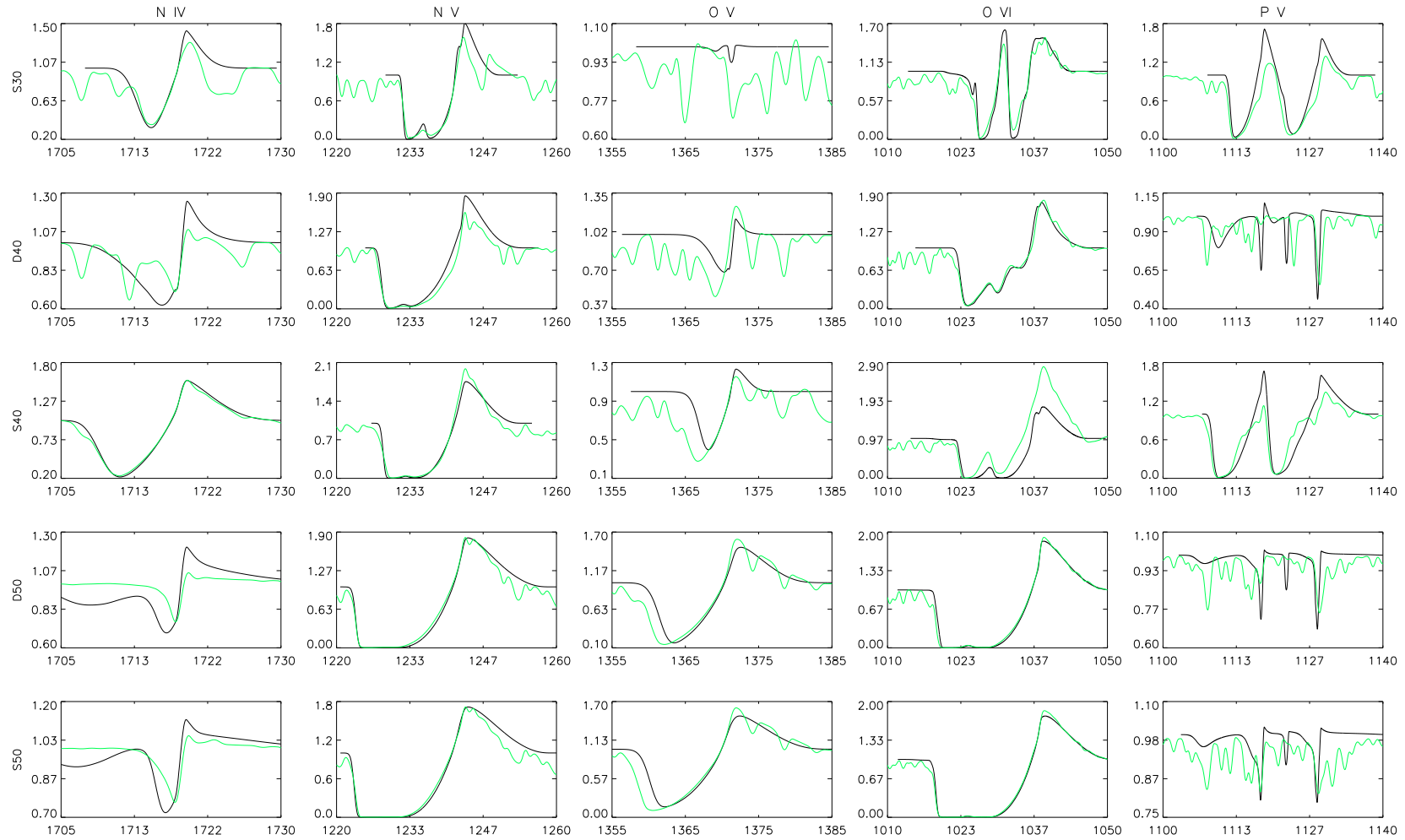


Figure 2.33: Emergent line profiles for strategic UV lines (N IV 1720, N V 1238,1242, O V 1371, O VI 1031,1037, and P V 1117,1128), as calculated by WM-BASIC (green) and FASTWIND (black), for models S30 (top), D40, S40, D50, and S50 (bottom). All profiles were calculated with a radially increasing microturbulence, with maximum value $v_{\text{turb}}(\text{max}) = 0.1v_{\infty}$, and have been convolved with a typical rotation velocity, $v \sin i = 100 \text{ km s}^{-1}$. The absorption feature between the two P v components is due to Si IV 1122. See Sect. 2.5.1.

2.C Appendix C: Averaged mass absorption coefficients: Clumped winds and dependence on averaging interval

Fig. 2.34 shows the density-weighted mean (Eq. 2.11) of the mass absorption coefficient as a function of wavelength for dwarf (left) and supergiant (right) models. The figure has a similar layout as Fig. 2.20, but has been calculated for clumped models ($f_{cl} = 20$) and mass-loss rates reduced by a factor of $\sqrt{20}$. Fig. 2.35 is also analogous to Fig. 2.20, but now the absorption coefficient has been averaged over the interval between 10 and $110 R_*$. For details and discussion, see Sect. 2.5.4.

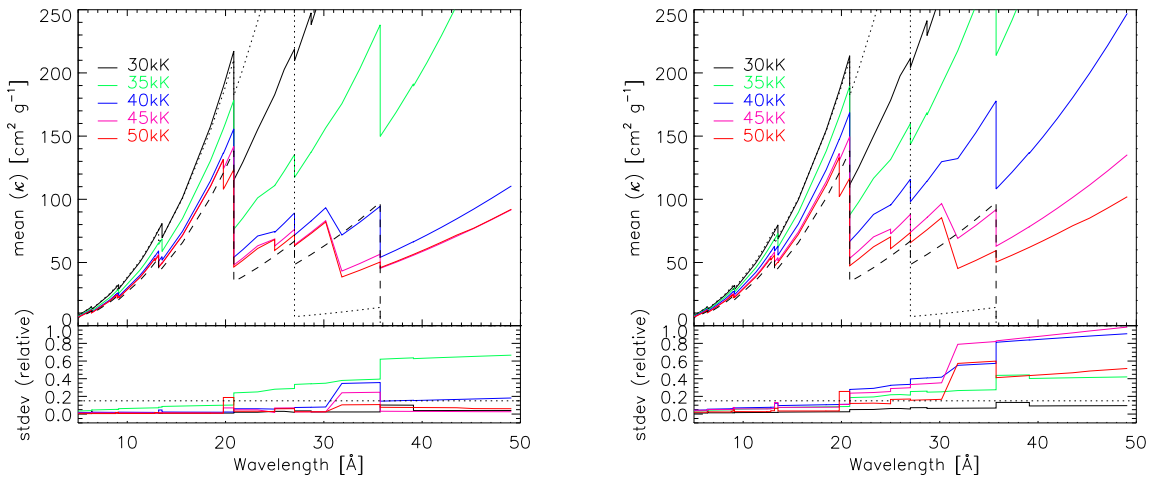


Figure 2.34: As Fig. 2.20, but for clumped models with $f_{cl} = 20$ (corresponding to $f_V = 0.05$) and mass-loss rates reduced by a factor of $\sqrt{20}$. Left: dwarf models; right: supergiant models.

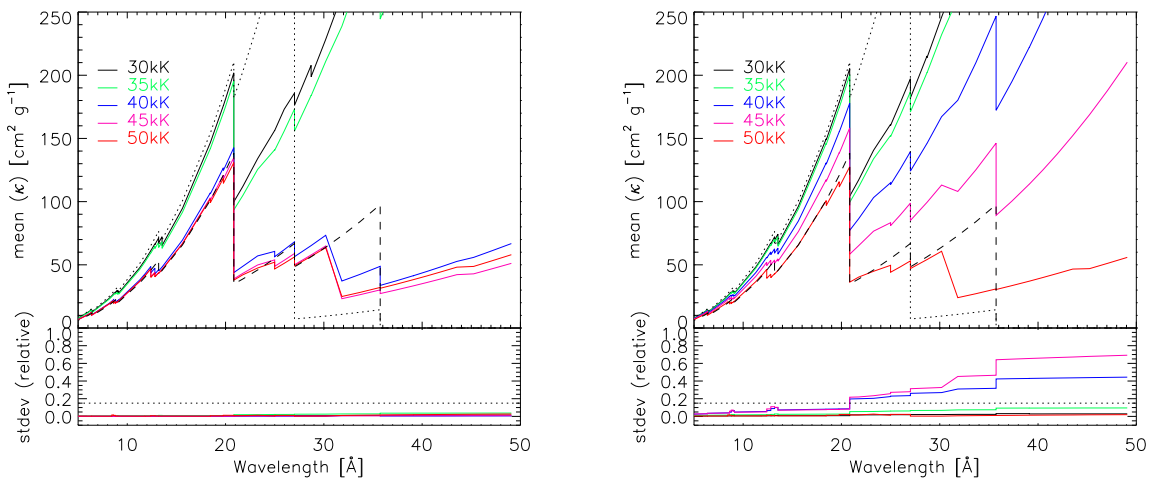


Figure 2.35: As Fig. 2.20, but averaged over the interval between 10 and $110 R_*$. Left: dwarf models; right: supergiant models.

Chapter 3

Carbon line formation and spectroscopy in O-type stars

This chapter is a copy of Carneiro, Puls, & Hoffmann (2018), *Astronomy & Astrophysics*, 615, A4, 2018.

Abstract The determination of chemical abundances constitutes a fundamental requirement for obtaining a complete picture of a star. Particularly in massive stars, CNO abundances are of prime interest, due to the nuclear CNO-cycle, and various mixing processes which bring these elements to the surface. The precise determination of carbon abundances, together with N and O, is thus a key ingredient for understanding the different phases of stellar evolution.

We aim to enable a reliable carbon spectroscopy for our unified NLTE atmosphere code FASTWIND.

We have developed a new carbon model atom including C II/III/IV/V, and we discuss specific problems related to carbon spectroscopy in O-type stars. We describe different tests we have performed to examine the reliability of our implementation, and investigate which mechanisms influence the carbon ionization balance. By comparing with high-resolution spectra from six O-type stars, we verified to what extent observational constraints can be reproduced by our new carbon line synthesis.

Carbon lines are even more sensitive to a variation of T_{eff} , $\log g$, and \dot{M} , than hydrogen and helium lines. We are able to reproduce most of the observed lines from our stellar sample, and to estimate those specific carbon abundances which bring the lines from different ions into agreement (three stages in parallel for cool objects, two for intermediate O-types). For hot dwarfs and supergiants earlier than O7, X-rays from wind-embedded shocks can have an impact on the synthesized line strengths, particularly for C IV, potentially affecting the abundance determination. Dielectronic recombination has a significant impact on the ionization balance in the wind.

We demonstrate our capability to derive realistic carbon abundances by means of FASTWIND, using our recently developed model atom. We find that complex effects can have a strong influence on the carbon ionization balance in hot stars. For a further understanding, the UV range needs to be explored as well. By means of detailed and available nitrogen and oxygen model atoms, we will be able to perform a complete CNO abundance analysis for larger samples of massive stars, and to

provide constraints on corresponding evolutionary models and aspects.

3.1 Introduction

Quantitative spectroscopy provides decisive constraints on our understanding of stellar evolution, chemical composition, and nucleosynthesis. The analysis of stellar spectra using atmospheric models tests the accuracy of present theoretical knowledge in this regard. Therefore, any further theoretical development relies, to a significant part, on the accuracy of data which describe the atomic processes present in a thermodynamic system. Any inconsistency or imprecision of the data directly affects a realistic representation of nature.

However, the calculation of atmospheric models is complex. In our working field – hot stars – the strong radiation field leads to non-LTE effects and causes a radiation-driven wind. This situation can be handled by different codes, as for example CMFGEN (Hillier & Miller 1998), PHOENIX (Hauschildt 1992), PoWR (Gräfener et al. 2002), WM-BASIC (Pauldrach et al. 2001), and FASTWIND (Puls et al. 2005, Rivero González et al. 2012a). A brief comparison of these different codes is given by Puls (2009).

Precise spectroscopic analysis (by means of accurate atmospheric models) can lead to important conclusions about the chemical composition of galaxies (Chiappini 2001, 2002) and corresponding metallicity gradients (Daflon & Cunha 2004), especially when performed using observations of early-type stars. Furthermore, it can also give insights into mixing processes. At least in single stars, the surface chemical composition is controlled by the efficiency of mixing processes, which to a large part are associated with stellar rotation. A high rotational velocity favors the transport of metals from the stellar core to the surface, and consequentially the chemical enrichment of the photosphere (Maeder & Meynet 2000a, Meynet & Maeder 2000).

In massive stars, nitrogen is a decisive indicator of such enrichment. Rivero González et al. (2011) investigated the formation of N III 4634-4640-4642, and derived nitrogen abundances of O stars in the Magellanic Clouds with a set of N II-III-IV lines. However, even more precise constraints on stellar evolution can be obtained using the N to C ratio, since it is less sensitive to the initial metal content, compared to N/H (Martins et al. 2012). In particular the combination of N/C vs. N/O (see Przybilla et al. 2010, Maeder et al. 2014) gives strong constraints on the enrichment and mixing history of CNO material (Martins et al. 2015a), and allows individual spectroscopic abundances to be tested. For these (and other) objectives, we have developed a new carbon model atom to be used in spectroscopic analysis by means of FASTWIND, suitable for the early B- and the complete O-star regime.

Carbon plays a special role within the light elements. It is the basis of all organic chemistry, but it is also essential for the nucleosynthesis of H into He through the CNO cycle in massive hot stars. Unfortunately, however, the analysis of carbon in such stars is difficult, mainly because the number of carbon lines detectable in O-type spectra is even smaller to the number of nitrogen lines.

Unsöld (1942) pioneered the analysis of carbon spectra from early-type stars. Since then, numerous studies aimed at the same objective, and we highlight here the contribution by Nieva & Przybilla (2008), which is the last in a series of three publications dedicated to developing and applying a car-

bon model atom within the spectrum analysis code `DETAIL/SURFACE` (Giddings 1981, Butler & Giddings 1985). By means of this new model atom, Nieva & Przybilla were able to establish a consistent carbon ionization balance for a sample of early B-type stars¹. Later on, Martins & Hillier (2012) explored the formation of C III 4647-50-51 and C III 5696 in detail, and found a tight coupling of these lines to UV-transitions that regulate the population of the associated levels.

Though data and observations improved with time, some “classical” problems are still discussed and partly an issue even to-date, particularly regarding the establishment of a consistent ionization equilibrium for C II/III/IV: Often, C II provides solar, but also subsolar abundances in early-type main sequence stars (Daflon et al. 1999 or Daflon et al. 2001a); C III might display solar abundances in OB dwarf stars and O supergiants (Daflon et al. 2001b and Pauldrach et al. 2001); and C IV can lead to all sorts of results, mostly because of the very restricted number of lines (four in the optical, but only in the rarely observed range between 5,000 and 6,000 Å; furthermore, two of these four lines are weak, and seldom, if at all, discussed and analyzed). Differences in abundance from C II vs. C III can reach a factor of 5 to 10 (Hunter et al. 2007), and even when considering C II lines alone, there can be significant line-by-line variations.

In B4-O6 stars, C II 4267 might indicate a very low abundance when compared with weaker lines such as the doublet at 6578-6582 Å (Kane et al. 1980). The latter problem had already been tackled by Nieva & Przybilla (2006), and solved for a sample of early B-type stars.

Recent studies (e.g., Najarro et al. 2006, Nieva & Simón-Díaz 2011, Rivero González et al. 2012a) have called the attention to the importance of implementing precise atomic data when some of these and other problems are addressed: Inadequate data might produce systematic discrepancies in the final results, independent of the specific atmospheric model used, since these data describe interactions governed by the laws of quantum mechanics, independent of their environment.

On the other hand, this dependence can be used to test specific atomic models regarding their capability to reproduce the observed spectral features. Prior to this final proof of reliability, though, a series of tests should be performed, including a comparison with alternative models, in order to investigate the impact of the various components of the model atom on the final result. For our purpose, the atmospheres of late to early O-type stars represent suitable testbeds, because within this temperature range the main ionization stage of carbon changes drastically. Therefore, a grid of representative O-type stars permits us to examine the quality of the results produced by our newly developed carbon model atom.

Obviously, a spectroscopic analysis does not only depend on the atomic data and the atmospheric model, but also on the quality of the observational data. This even more for the tests outlined above: High S/N spectra are needed, preferably from slowly rotating single stars. The projected rotational velocity, $v \sin i$, is one of the major broadening agents capable of making the majority of carbon lines almost invisible in the entire optical spectrum, recognizing that these are mostly weak lines (Wolff et al. 1982). $v \sin i$ also affects the blending of a set of diagnostic lines by lines from other atoms, (e.g., the strong C III 4647-50-51 complex blended by many O II lines).

As already pointed out, the optical diagnostics of carbon in O-type stars is also influenced by a

¹ The study presented here might be considered as an extension of their work, applying a new model atom within a different atmosphere code (`FASTWIND`) to the analysis of O-type stars.

variety of UV transitions. Thus, a proper treatment of the UV radiation is necessary, both for the optical analysis and for an independent or combined investigation of UV carbon lines. If at least part of these lines are formed in the wind, the inclusion of X-rays and extreme ultraviolet (EUV) emission from wind-embedded shocks becomes essential. As a first step of this complex analysis, we can identify those optical lines that have levels pumped by UV transitions, and investigate how strong the radiation from wind-embedded shocks must be to influence the line shapes significantly.

Besides the X-ray emission, the UV region is also influenced by micro- and macro-clumping, and porosity in velocity space, which makes the analysis even more complex. This issue, however, will be addressed in a forthcoming study, after we have convinced ourselves of the reliability of our carbon model.

This paper is organized as follows. Sect. 3.2 summarizes important characteristics of our atmosphere code, FASTWIND, and details our newly developed carbon model atom, the set of diagnostic lines used, and the model grid adopted as testbed. In Sect. 3.3 we provide various tests performed to check our model atom. Sect. 3.4 presents all relevant results from comparing synthetic carbon spectra with observed ones, for the case of six slowly-rotating O-type stars of various spectral type and luminosity class. Moreover, we discuss the potential impact of X-ray and EUV radiation from wind-embedded shocks on the optical carbon lines. In Sect. 3.5 we conclude with an overview of the present work as the basis for a more detailed future analysis.

3.2 Prerequisites for a carbon diagnostics

All the calculations described in this work have been performed with the latest update (v10.4.5) of the NLTE model atmosphere and spectrum synthesis code FASTWIND (Puls et al. 2005, Rivero González et al. 2012a). It includes the recent implementation of emission from wind-embedded shocks and related physics, which will be used here to investigate potential effects of X-rays/EUV radiation on the selected optical carbon lines. A detailed description of the X-ray implementation in FASTWIND is given by Carneiro et al. (2016).

3.2.1 The code

For the diagnostics of early-B and O-type stars, FASTWIND thus far used models atoms for H, He, N (developed by Puls et al. 2005 and Rivero González et al. 2012b), Si (see Trundle et al. 2004), while data for C, O, and P have been taken from the WM-BASIC database (Pauldrach et al. 2001). We call these elements "explicit" (or foreground) elements. Briefly², such foreground elements are used as diagnostic tools and treated with high precision by detailed atomic models and by means of comoving frame radiation transport for all line transitions. Most of the other elements up to Zn are treated as so-called background elements. Since these are necessary 'only' for the line-blocking and blanketing calculations, they are treated in a more approximate way, using parameterized ionization cross-sections in the spirit of Seaton (1958). Only for the most important lines from background elements, a comoving frame transfer is performed, while the multitude of weaker lines is calculated by means of

² For a more detailed description of FASTWIND, and the philosophy of explicit and background elements, see Puls et al. (2005) and Rivero González et al. (2011).

the Sobolev approximation. The latter approximation is applicable for the wind regime, but it may fail for regions with a curved velocity field (transition between photosphere and wind), and in the deeper photosphere. The Sobolev approximation, when applied to regions with a pronounced velocity field curvature, yields too highly populated upper levels in line transitions (see, e.g., Santolaya-Rey et al. 1997). This could directly affect our carbon analysis, and is one more reason to use carbon as an explicit element and to develop a corresponding, more detailed carbon model.

3.2.2 The carbon model atom

The first step regarding the development of a new model atom concerns the decision of how many and which states shall be included into each ion. We established a sequence of criteria to define our choice of levels. At first, as suggested by Hubeny (1998), the gap of energy between the highest ion level and the ground state of the next ionization stage should be less than kT . Since our conventional O-star grids include a minimum T_{eff} of ~ 28 kK, this temperature was chosen to establish a first guess for the uppermost levels of C III and C IV. In the case of C II, we used a temperature of 22 kK to obtain a better representation of this ion in B stars.

With a first list of levels, the second criterium was to account for all levels within a given subshell, up to and including the subshell considered by criterium one, which extends our previous list by a few more levels. Subsequently, a third and final criterium was to re-check the Grotrian diagram and to include higher lying levels with multiple transitions downward.

At this point, the uppermost considered level has an energy far beyond the limit established by the first criterium. Even though, the second criterium was revisited for completeness, and few more levels (partly with very weak cross-sections) included as a final step.

Basically, the list, configuration and energies of levels were taken from NIST³ (for individual data, see following references), but we cross-checked with other databases relying on independent calculations. In particular, the list of levels used in this work agrees to a large part with the WM-BASIC database⁴ and also with the OPACITY Project online database⁵ (TOPbase hereafter, see Cunto & Mendoza 1992 for details). The order of levels may appear, in few cases, interchanged in different databases, due to slightly different energies.

Oscillator strengths were mainly taken from NIST, though this database only provides data for allowed transitions. For a given radiative bound-bound transition, the gf -values are very similar in the different databases inspected by us: NIST, WM-BASIC, and data from an application of the Breit-Pauli method (Nahar 2002). Data for forbidden transitions were essentially taken from the WM-BASIC database. Radiative intercombinations have been neglected, because of negligible oscillator strengths.

TOPbase displays photoionization cross-section data from calculations by Seaton (1987) for almost all the levels included in our model atom. Already Nieva & Przybilla (2008) presented a comparison between the radiative bound-free data from TOPbase and Nahar & Pradhan (1997), concluding

³ <http://www.nist.gov/physlab/data/asd.cfm>, described in Kelleher et al. (1999)

⁴ See Pauldrach et al. (1994). Briefly, the atomic structure code SUPERSTRUCTURE (Eissner & Nussbaumer 1969, Eissner 1991) has been used to calculate all bound state energies in LS and intermediate coupling as well as related atomic data, particularly oscillator strengths including those for stabilizing transitions.

⁵ <http://cdsweb.u-strasbg.fr/topbase/topbase.html>

that the use of TOPbase reproduces more accurately the C II 4267, 6151 and 6462 transitions, which are also of our interest. On the other hand, within the OPACITY Project no data were calculated for highly excited terms (e.g., C2_37: 2G or C2_38: $^2H^0$, see Table 3.4), because the quantum defect is zero, which means that such levels can be approximated as hydrogen-like. For these cases, we used the resonance-free cross-sections provided in terms of the Seaton (1958) approximation

$$\alpha(\nu) = \alpha_0[\beta(\nu_0/\nu)^s + (1 - \beta)(\nu_0/\nu)^{s+1}], \quad (3.1)$$

with α_0 being the threshold cross-section at ν_0 , and β and s fit parameters, all taken from the WM-BASIC database.

The radiative bound-free data from TOPbase, which is our primary source, include the numerous complex resonance transitions relevant for the description of dielectronic recombination and reverse ionization processes. For the few levels where no data are present (see above), we used the explicit method accounting for individual stabilizing transitions (see, e.g., Rivero González et al. 2011), with data from WM-BASIC (a further discussion on this approach will be provided in Sect. 3.3).

Collisional ionization rates are calculated following the approximation by Seaton (1962). The corresponding threshold cross-sections are taken from WM-BASIC and Nahar (2002), which present similar values for the majority of levels, and these also in agreement with TOPbase.

For collisional excitations, we used a variety of suitable data-sets, discussed in the following together with particularities for each carbon ion:

C II is described by 41 LS-coupled levels (Moore 1993), roughly up to principal quantum number $n = 7$ and angular momentum $l = 5$, with all fine-structure levels being packed⁶. These levels are displayed in Table 3.4. For the 16 lowermost levels of this boron-like ion, effective collision strengths were taken from R-matrix computations by Wilson et al. (2005, 2007). For the remaining transitions without detailed data, collisional excitation is calculated using the van Regemorter (1962) approximation for optically allowed transitions, and by means of the Allen (1973) expression for the optically forbidden ones. For the latter, corresponding collision strengths Ω vary from 0.01 ($\Delta n \geq 4$) to 100 ($\Delta n = 0$). Over 300 radiative (Nussbaumer & Storey 1981, Yan et al. 1987, Tachiev & Fischer 2000) and 1000 collisional transitions have been included.

C III consists of 70 LS-coupled levels (Moore 1993), until $n = 9$ and $l = 2$, with fine-structure levels being packed. The levels are detailed in Table 3.5. For electron impact excitation of the lowest 24 levels, we used the Maxwellian-averaged collision strengths calculated by Mitnik et al. (2003) through R-matrix computations. The collisional bound-bound data for the other levels were treated in analogy to corresponding C II transitions. This Be-like ion comprises approximately 700 radiative (Glass 1983, Allard et al. 1990, Tully et al. 1990) and 2000 collisional transitions.

C IV includes 50 LS-coupled terms (Moore 1993), until $n = 14$ and $l = 2$, with fine-structure levels again being packed, and described in Table 3.6. Aggarwal & Keenan (2004) provide electron impact excitation data for the lowest 24 fine-structure levels, which have been added up in such a way as to be applicable for our first 14 terms. All remaining collisional bound-bound transitions were treated

⁶ To calculate the final synthetic profiles by means of the formal integral, these levels are unpacked. To this end, we have assumed that n_i/g_i (occupation number divided by statistical weight) is similar within each of the sublevels belonging to a packed level, due to collisional coupling.

Table 3.1: Diagnostic carbon lines in the optical spectra of early B- and O-type stars, together with potential blends. Lines with wavelengths written in bold-face are visible in a wide temperature range, and quite sensible to carbon abundance variations. Therefore, they are most important for an optical carbon analysis (see also Sect. 3.4.3). The labels displayed in Column 3 (“transition”) are detailed in Tables 3.4, 3.5, and 3.6. The last column provides a short comment on the specific lines. “Weak” and “strong” refers here to the observed line strength in a high resolution O-star spectrum, with intermediate $v \sin i$ ($\sim 50 \text{ km s}^{-1}$), and parameters such that the considered ion is clearly present. “X-ray sensitive” indicates lines which might be affected by emission from wind-embedded shocks (see Sect. 3.4.4).

Ion	Wavelength(Å)	Transition	f	$\log(gf)$	Blends	Comment
C II	3918.98	C2_7 - C2_11	0.1470	-0.533	N II $\lambda 3919.00$, O II $\lambda 3919.2$	weak doublet
	3920.69	C2_7 - C2_11	0.1460	-0.232	S III $\lambda 3920.29$	”
	4267.00	C2_9 - C2_16	0.9140	0.563	S II $\lambda 4267.76$	strong doublet
	4267.26	C2_9 - C2_16	0.8670	0.716	Fe II $\lambda 4267.82$	”
	4637.63	C2_12 - C2_27	0.0295	-1.229	Fe I $\lambda 4637.50$	region dominated by O II $\lambda 4638.9$
	4638.91	C2_12 - C2_27	0.0266	-0.973	Si III $\lambda 4638.28$	”
	4639.07	C2_12 - C2_27	0.00295	-1.928	Ti I $\lambda 4639.94$	”
	5132.94	C2_13 - C2_33	0.3070	-0.211	-	weak doublet
	5133.28	C2_13 - C2_33	0.1660	-0.178	-	”
	5139.17	C2_13 - C2_33	0.0491	-0.707	-	visible in slow rotators
	5143.49	C2_13 - C2_33	0.1530	-0.212	-	”
	5145.16	C2_13 - C2_33	0.2580	0.189	-	”
	5151.09	C2_13 - C2_33	0.1100	-0.179	-	”
	5648.07	C2_13 - C2_31	0.0943	-0.249	Fe II $\lambda 5648.89$	not visible
	5662.47	C2_13 - C2_31	0.0939	-0.249	Ti I $\lambda 5662.14$, Fe I $\lambda 5662.51$	”
	6151.53	C2_14 - C2_28	0.0049	-1.310	-	”
	6461.94	C2_16 - C2_29	0.1150	0.161	Mn II $\lambda 6462.21$	”
	6578.05	C2_6 - C2_7	0.7140	0.154	-	strong doublet
	6582.88	C2_6 - C2_7	0.2380	-0.323	N II $\lambda 6582.60$	”
	C III	4056.06	C3_24 - C3_44	0.3700	0.267	Ti I $\lambda 4055.01$, Mn I $\lambda 4055.54$
4068.90		C3_20 - C3_39	0.9830	0.838	Sc III $\lambda 4068.66$, O II $\lambda 4069.62$	strong doublet
4070.26		C3_20 - C3_39	0.9960	0.953	O II $\lambda 4069.88$	”
4152.51		C3_23 - C3_43	0.2580	-0.112	N III $\lambda 4152.13$, Ne III $\lambda 4152.58$	strong line
4156.50		C3_23 - C3_43	0.2290	0.059	Li II $\lambda 4156.45$, Fe I $\lambda 4156.67$	strong doublet
4162.86		C3_23 - C3_43	0.2360	0.218	S VI $\lambda 4162.28$, S II $\lambda 4162.66$	”
4186.90		C3_22 - C3_40	1.1800	0.918	Fe I $\lambda 4187.03$, Fe I $\lambda 4187.59$	X-ray sensitive
4647.42		C3_7 - C3_10	0.3920	0.070	S II $\lambda 4648.17$	”
4650.25		C3_7 - C3_10	0.2350	-0.151	Ti I $\lambda 4650.01$, O II $\lambda 4650.84$	”
4651.47		C3_7 - C3_10	0.0783	-0.629	”	”
4663.64		C3_13 - C3_26	0.0984	-0.530	Al II $\lambda 4663.05$	strong doublet
4665.86		C3_13 - C3_26	0.2210	0.044	Si III $\lambda 4665.87$	”
5253.57		C3_13 - C3_25	0.0654	-0.707	Fe II $\lambda 5253.46$	weak line
5272.52		C3_13 - C3_25	0.0653	-0.486	N V $\lambda 5272.18$, Fe II $\lambda 5372.22$	X-ray sensitive
5695.92		C3_9 - C3_12	0.3460	0.017	Al III $\lambda 5696.60$	”
5826.42		C3_24 - C3_34	0.5220	0.417	Fe II $\lambda 5826.52$	weak line
6731.04		C3_13 - C3_23	0.1700	-0.293	O III $\lambda 6731.13$	”
6744.38		C3_13 - C3_23	0.1900	-0.022	-	not visible
8500.32		C3_8 - C3_9	0.3280	-0.484	Fe II $\lambda 8499.61$	X-ray sensitive
C IV		5801.33	C4_3 - C4_4	0.3200	-0.194	-
	5811.98	C4_3 - C4_4	0.1600	-0.495	O II $\lambda 5011.79$	”
	5016.62	C4_11 - C4_15	0.1750	-0.456	Ar II $\lambda 5016.47$	weak line
	5018.40	C4_11 - C4_15	0.1750	-0.155	Fe II $\lambda 5018.43$	”

in analogy to C II. Overall, this Li-like ion is described by roughly 200 radiative (Lindgård & Nielsen 1977, Bièmont 1977, Peach et al. 1988) and 1000 collisional transitions.

Thus far, C V consists of only one level, the ground state (C5_1: $1s^2 \ ^1S$), required for ionization and recombination processes from and to C IV. Anyhow, this is a suitable description, since (i) a further ionization is almost impossible under O-star conditions, due to a very high ionization energy, and (ii) the excitation energies of already the next higher levels are also quite large, so that C V should remain in its ground state.

To summarize, our carbon model atom comprises 162 LS-coupled levels, basically ordered following NIST. In few cases, we interchanged the order and adapted the corresponding energies, to obtain a compromise with the level-lists from WM-BASIC and TOPbase, which have been used for a large part of bound-bound and the majority of bound-free data, respectively. We note that such a task has to be done with specific care, since any wrong labeling would lead to spurious results. The definition of C II/III/IV/V accounts all together for more than 1000 radiative and 4000 collisional transitions.

3.2.3 Diagnostic optical carbon lines

We selected a set of 43 carbon lines visible (at least in principle) in the optical spectra of OB-stars, which allow us to approach some of the classical problems already mentioned in Sect. 3.1, as for example: (i) inconsistent carbon abundances implied by C II 4267 and C II 6578-82 (Grigsby et al. 1992, Hunter et al. 2007), (ii) abundances derived from C II and C III may differ by a factor of 5-10 (Daflon et al. 2001b, Hunter et al. 2007), (iii) the difficulty to establish a consistent ionization equilibrium for C II/III/IV (Nieva & Przybilla 2006, 2007, 2008).

The NIST database identifies all relevant lines in the spectrum, together with corresponding oscillator strengths. This was our first source for building a prime sample of lines. We inspected various observed spectra (partly described below) to identify which of these lines are blended, and to find additional lines not included so far. In the end, we defined a set of lines similar to the ones used by Nieva & Przybilla (2008), with some relevant additions. For the final synthetic spectra, we adopt Voigt profiles, with central wavelengths from NIST, radiative damping parameters from the Kurucz database⁷, and collisional damping parameters computed according to Cowley (1971).

Table 3.1 presents three different blocks, divided into C II, C III, and C IV. The second column displays the wavelengths of the lines, followed by the lower and upper level of the considered transition. Columns 4, 5, and 6 display the oscillator strengths, the $\log(gf)$ -values, and potential blends. The last column provides a short comment about each line.

3.2.4 Model grid

In this study, we have used the “theoretical” O-star model grid originally designed by Pauldrach et al. (2001, their Table 5)⁸, revisited by Puls et al. (2005) to compare results from an earlier version of FASTWIND with the outcome of WM-BASIC calculations, and again revisited by Carneiro et al. (2016)

⁷ e.g., www.pmp.uni-hannover.de/cgi-bin/ssi/test/kurucz/sekur.html

⁸ This grid, in turn, is based on observational results from Puls et al. (1996), which at that time did not include the effects of wind inhomogeneities, so that the adopted mass-loss rates might be too large, by factors from $\sim 3 \dots 6$.

Table 3.2: Stellar and wind parameters of our grid models with homogeneous winds, following Pauldrach et al. (2001). For all models, the velocity field exponent has been set to $\beta=0.9$, and a micro-turbulent velocity, $v_{\text{turb}} = 15 \text{ km s}^{-1}$, has been used.

Model	T_{eff}	$\log g$	R_*	v_∞	\dot{M}
	(kK)	(cm s^{-2})	(R_\odot)	(km s^{-1})	($10^{-6} M_\odot \text{yr}^{-1}$)
Dwarfs					
D30	30	3.85	12	1800	0.008
D35	35	3.80	11	2100	0.05
D40	40	3.75	10	2400	0.24
D45	45	3.90	12	3000	1.3
D50	50	4.00	12	3200	5.6
D55	55	4.10	15	3300	20
Supergiants					
S30	30	3.00	27	1500	5.0
S35	35	3.30	21	1900	8.0
S40	40	3.60	19	2200	10
S45	45	3.80	20	2500	15
S50	50	3.90	20	3200	24

to test our recently developed X-ray implementation. Table 3.2 displays the stellar and wind parameters of the grid models. The adopted models allow us to study, for a certain range of spectral types, how changes in stellar parameters (e.g., T_{eff} , $\log g$, carbon abundance) will affect the shape and strength of significant carbon lines. At the same time, these models define a reasonable testbed for a series of tests described in Sect. 3.3. We have adopted solar abundances from Asplund et al. (2009), together with a helium abundance, by number, $N_{\text{He}}/N_{\text{H}} = 0.1$. Carbon abundances different from the solar value are explicitly mentioned when necessary.

The main focus of this work is set on the analysis of photospheric carbon lines, which should not be affected by wind clumping. In the scope of this work, we thus only consider homogeneous wind models. Nevertheless, our unclumped models with mass-loss rate \dot{M}_{uc} roughly correspond to (micro-)clumped models with a lower mass-loss rate, \dot{M}_c ,

$$\dot{M}_c = \dot{M}_{uc} / \sqrt{f_{cl}}, \quad (3.2)$$

where $f_{cl} \geq 1$ is the considered clumping factor.

3.2.5 Observational data

In Sect. 3.4, we use optical spectra (kindly provided by Holgado et al. 2018) from prototypical O-type stars, to from prototypical O-type stars, to compare with the carbon line profiles as calculated using our new model atom. These stars are included in the grid of O-type standards, as defined in Maíz Apellániz et al. (2015)⁹. From the observed sample, we selected six presumably single stars in different ranges of temperature and with low $v \sin i$. The spectra have been collected by means of three different instruments: HERMES (with a typical resolving power of $R = 85,000$, see Raskin et al. 2004) at the MERCATOR 1.2 m telescope, FEROS ($R = 46,000$, see Kaufer et al. 1997) at the ESO 2.2 m telescope, and FIES ($R = 46,000$, see Telting et al. 2014) at the NOT 2.6 m telescope. Table 3.3 lists the instrument and S/N of each spectrum analyzed in this work. More details are provided in Sect. 3.4.2.

For the temperature range considered in this work, we expect that carbon line profiles from ionizations stages C II/III/IV are visible around ~ 30 kK. On the other hand, for the hottest objects (~ 50 kK), we will have to rely on estimates using C IV lines alone.

3.3 Testing the atomic model

This section describes some of the tests we performed after having constructed a new carbon model atom using high quality data, to investigate the outcomes from using this model atom in an atmospheric code, for various stellar conditions. Specific tests are briefly summarized below:

(i) As outlined in Sect. 3.2.1, previous FASTWIND calculations used the carbon model atom from the WM-BASIC database, independent of whether carbon was treated as a foreground or background element. Thus we were able to compare the results from our former practice and our new (and more detailed) description (see also Fig. 3.1). As expected, in terms of ionization fraction, both methods display the same results in the stellar photosphere. Irrespective of wind-strength, significant differences appear only in the outer wind (e.g., for model S30, around $\tau_{\text{Ross}} \leq 10^{-4}$, corresponding to $r \geq 6 R_*$ or $v(r) \geq 0.8 v_\infty$) for all considered ions except for C II, for which differences begin to appear deeper in the wind (again for model S30, around $\tau_{\text{Ross}} \leq 10^{-2}$, corresponding to $r \geq 3 R_*$ or $v(r) \geq 0.2 v_\infty$). Our new carbon description displays consistently less C II for a wide range of temperatures (for both dwarf- and supergiant-models), where the maximum difference (0.7 dex) is reached in our coolest model at 30 kK. This behavior is due to less C III and C IV (see below), though the differences for these ions are lower (less than 0.5 dex), and appear only in the outer wind.

As an example of the issues just discussed, Fig. 3.1 compares the ionization fractions of our former (using explicit dielectronic recombination data, see below) and new description of each carbon ion, as a function of τ_{Ross} . This is done for model D45, since this model will be closer inspected in the following subsection. For C IV, the ratio between former and new ionization fraction is close to unity within the whole atmosphere, and the same is true for C II and C III in the photosphere. For both ions, however, the situation is different in the outer wind, where, as outlined above, our new treatment results in lower populations. To assess the effects described here and in the following on

⁹ covering 131 Galactic stars in the spectral range from O2 to O9.7 (all luminosity classes) in the northern and southern hemisphere.

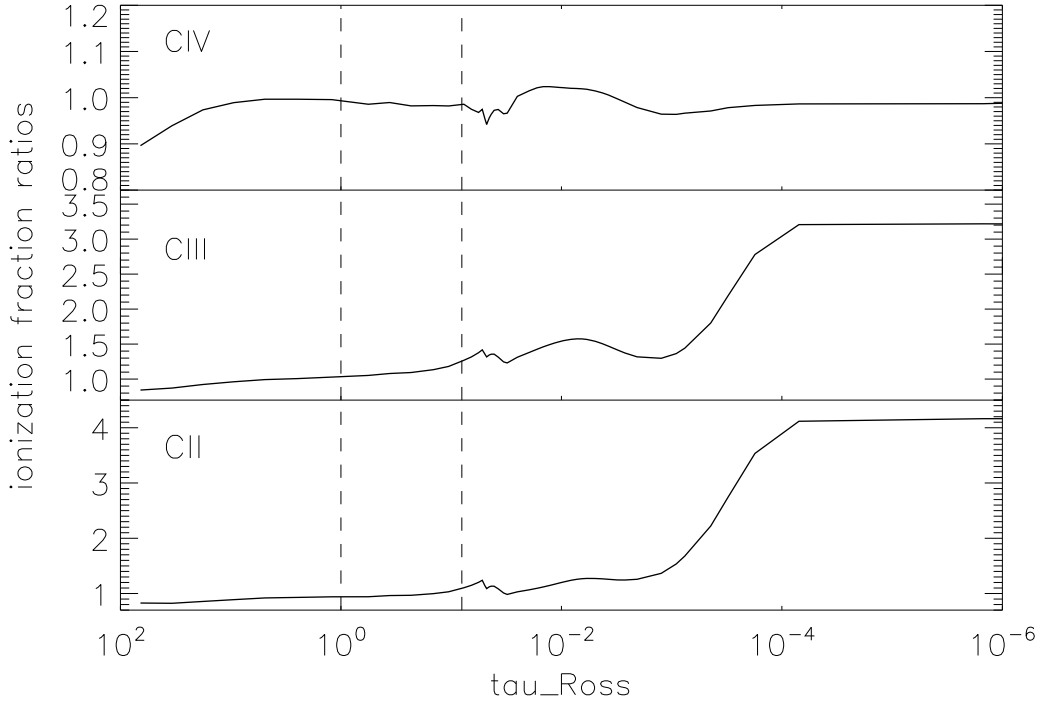


Figure 3.1: Ratios of ionization fractions resulting from our former and our new model atom, as a function of τ_{Ross} , for model D45. The major changes appear for C II and C III ions in the outer wind. The dashed lines enclose the typical line-forming region of optical photospheric lines.

the optical carbon lines, we have also indicated the line-forming region of the lines described in Table 3.1. The cores of weak lines are formed at $\tau_{\text{Ross}} \gtrsim 1$, and that of strong lines at $\tau_{\text{Ross}} \lesssim 0.07$. For the displayed dwarf model, this means that essentially all lines are formed in the photosphere, whilst for a corresponding supergiant model (e.g., Fig. 3.5), the strong line cores are already formed in the wind. Obviously, in the case considered here, only the strongest photospheric carbon lines should be affected by our new model atom.

(ii) In our model atom, we use the expression from Allen (1973), with individual Ω values from 0.01 to 100, to describe those collisional bound-bound transitions where the radiative ones are forbidden and where we lack more detailed data (usually, between quite highly excited levels). We tested the impact of uncertainties in Ω on the final results, by setting $\Omega = 1.0$ for all these transitions, and found that this has a negligible impact on our results regarding the optical lines. Indeed, the “exact” value of the collisional strength is only important for a specific part of the atmosphere in between the LTE regime and the much lesser dense wind. Since we use Allen’s expression only for those transitions where the radiative ones are forbidden, meaning those which have a very low oscillator strength ($\leq 10^{-5}$), the weak impact of Ω is understandable when considering the dominating effect of the other radiative transitions included in the model atom. We expect, however, that specific IR-transitions might be influenced though.

In this context, we also refer the reader to Nieva & Przybilla (2008, their Sect. 3.2) where they discuss the impact of ab initio collisional data (contrasted to approximations), and showed that the

use of approximate data might yield completely inconsistent abundances when derived from either NLTE-sensitive lines (usually the stronger ones) or from (weaker) lines that are insensitive to NLTE effects. The reason for this discrepancy is that the former react on the specific values of the collision strengths (which might be erroneous when approximations are used, particularly when applying $\Omega = 1$ in general – what we are not doing), whilst the latter are (almost) insensitive to any detail of the model atom.

(iii) We also tested a possible interplay between nitrogen and carbon, which might arise when combining different foreground elements in FASTWIND. To this end, we considered three different model series: one with H/He + carbon + nitrogen as foreground elements, one with H/He + only carbon, and one with H/He + only nitrogen. In the latter two cases, either nitrogen or carbon are used as background elements, respectively, with atomic data from WM-BASIC. These tests resulted in irrelevant differences regarding the carbon ionization stratification (~ 0.1 dex in the outer wind), when comparing the HHeCN and the HHeC models. The same, now regarding nitrogen, holds when comparing HHeCN vs. HHeN: we found no visible difference in the nitrogen description, whether carbon is included or not. We emphasize though that this test does not consider potential C/N line overlap effects, particularly regarding the EUV resonance lines from C and N at $\sim 321 \text{ \AA}$ ¹⁰. This issue deserves a separate investigation.

These first tests confirm our expectations, illuminating specific aspects that have low interference on the final results. We have also tested our model atom much more extensively than presented in this paper. In the following, some of these tests are discussed in more detail.

3.3.1 Dielectronic recombination

One advantage of testing our carbon description is the availability of two independent codes in our scientific group (FASTWIND and WM-BASIC), which can be used to calculate the same atmospheric models but employing different atomic models. A comparison of the carbon ionization stratification then, for a set of models calculated with FASTWIND and WM-BASIC, gives a quick overview about differences between our results and former work (see Pauldrach et al. 1994, 2001).

In this spirit, we calculated all grid models described in Table 3.2 also with WM-BASIC. After comparing these models with corresponding FASTWIND ones, we find a rather similar run of C IV and C V, both in the stellar photosphere and also in the wind. In contrast, C II and C III displayed a recurrent difference for all the models: in the wind part, our results lay consistently one or two dex below the outcome from WM-BASIC.

Though this finding does not allow for premature conclusions (at least at this stage, we do not know what is the better description), it nevertheless caught our attention, especially since the same discrepancy had been found for a wide range of temperatures. We thus recalculated the FASTWIND models, but this time using the complete WM-BASIC dataset for carbon. Comparing with our initial models, we found the same difference in C II and C III as described in the previous paragraph. Thus the differences need to be attributed to the different datasets and not to the different atmospheric models, and we set out to compare both datasets in detail.

¹⁰similar to the case of overlap between N and O resonance lines at $\sim 374 \text{ \AA}$, which is decisive for the formation of N III 4634-40-42 (see Rivero González et al. 2011).

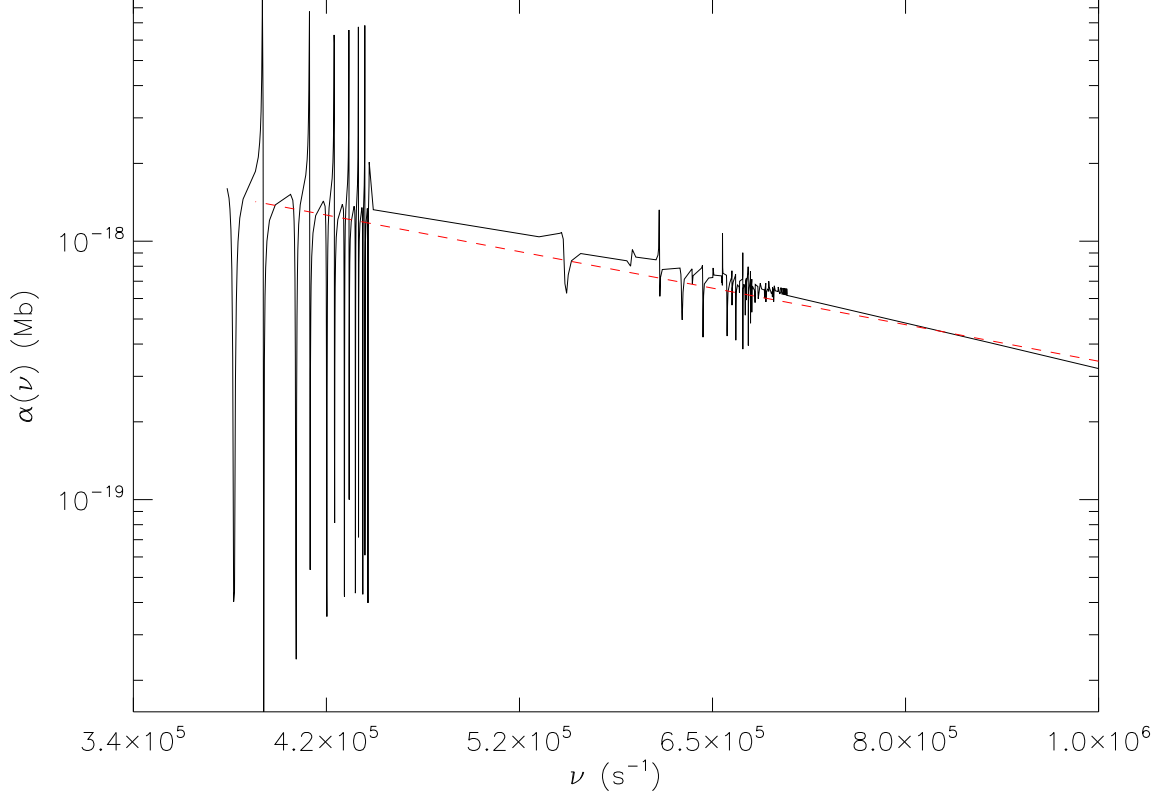


Figure 3.2: Bound-free cross-section of the C III ground state including resonances (from OPACITY Project, used in our new model atom, black line), and the resonance-free data (from WM-BASIC, red line).

In the end, we identified the origin of the discrepancy within the radiative bound-free transitions, where each of both datasets describes these transitions differently. While within our new model atom we have used an **implicit method** to define the dielectronic recombination (henceforth DR¹¹) data within the photoionization cross-sections, the WM-BASIC database adopts an **explicit method**. Both methods are implemented into FASTWIND: Within the implicit method, the resonances appear “naturally” in the photoionization cross-sections (from OPACITY Project data, Cunto & Mendoza 1992), whereas the explicit method considers explicitly the stabilizing transitions from autoionizing levels together with the resonance-free cross-sections. As an example, Fig. 3.2 displays the data available from the OPACITY Project (black line) with the numerous complex resonances for the ground state of C III, together with the Seaton (1958) approximation using data from WM-BASIC (red line), to which the stabilizing transitions (data input: frequencies and oscillator strengths) would need to be added.

For further details, and advantages and disadvantages of both methods, we refer to Hillier & Miller

¹¹Dielectronic recombination can be summarized as “the capture of an electron by the target leading to an intermediate doubly excited state that stabilizes by emitting a photon rather than an electron” (Rivero González et al. 2011).

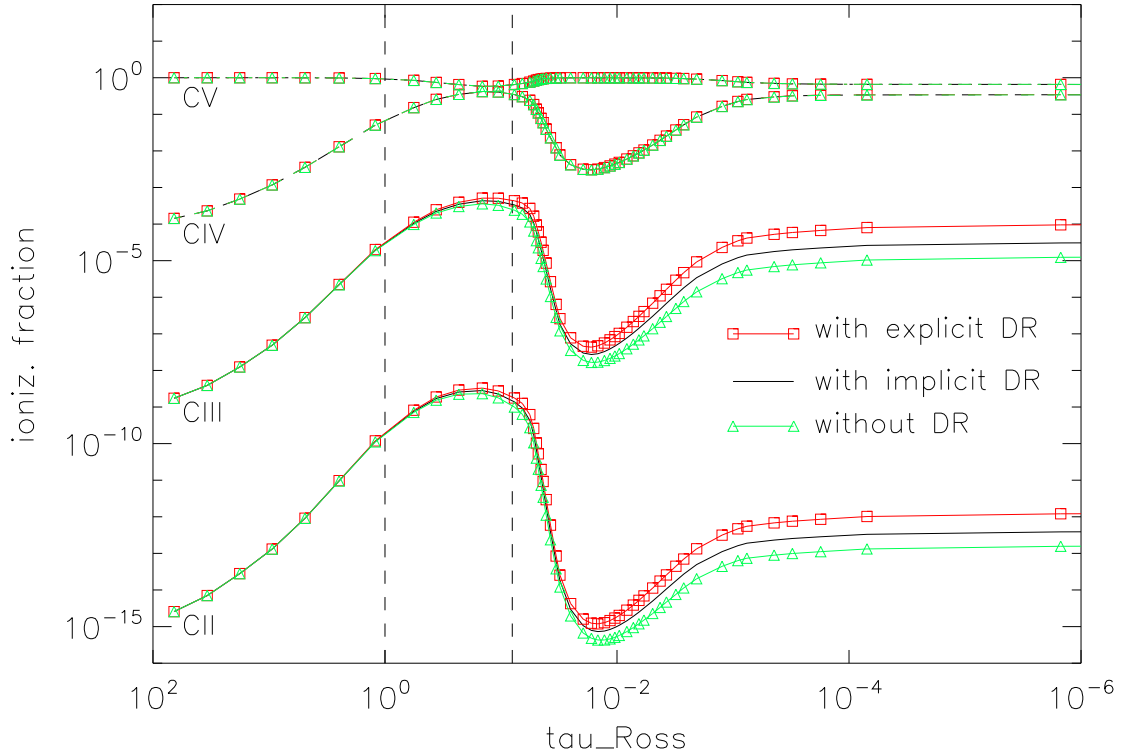


Figure 3.3: Ionization fractions of carbon ions, as a function of τ_{Ross} , for model D45. Note the impact of DR onto C II and C III in the wind region. The dashed lines enclose the typical line-forming region of optical photospheric lines. For details, see text.

(1998) and Rivero González et al. (2011). The important point with respect to this work is the following: Since in the explicit method one defines each stabilizing transition by corresponding data, we have the possibility to remove any of those transitions by setting the corresponding oscillator strengths to a very low value.

Figure 3.3 shows the ionization fraction of different carbon ions in the atmosphere, for model D45 (see Table 3.2). We calculated three different models, where only the bound-free dataset for carbon was changed, leaving all other data at their original value, defined by our new carbon model atom. In the first model, we used the implicit method with bound-free cross-sections from OPACITY Project data, in the second we used corresponding WM-BASIC data (explicit method), and in the third model we discarded the DR-processes in the WM-BASIC data, that is, we used only the resonance-free cross-sections by excluding all stabilizing transitions.

As displayed in Fig. 3.3, the effect of DR is irrelevant **or marginal** in the stellar photosphere, where due to the high temperatures and densities the “normal” ionization/recombination processes dominate. In the wind part, the impact of DR remains irrelevant for C IV, but becomes crucial for a precise description of C III. In the case of C II, the difference is mostly a consequence of changes in

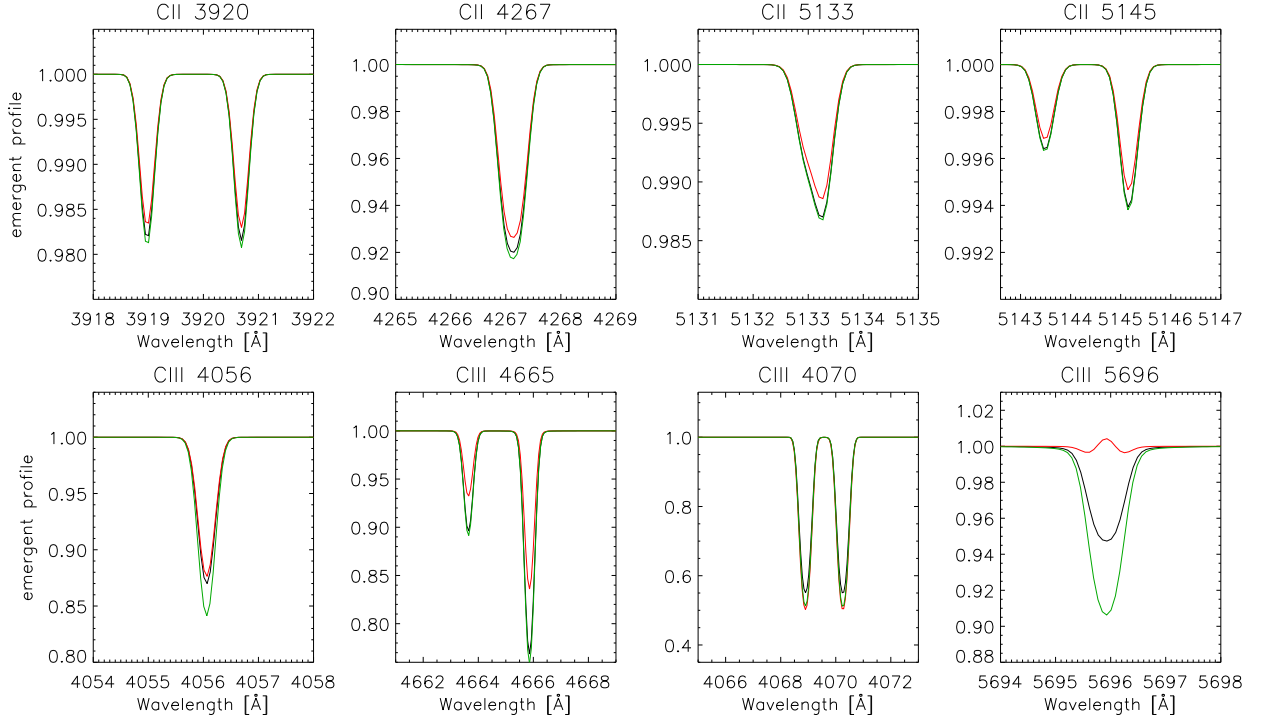


Figure 3.4: Impact of dielectronic recombination on C II/III lines, for our D35 model (same color-coding as in Fig. 3.3). The displayed lines are those which are the most influenced ones within our complete set, all others show basically no reaction. Each color represents a different treatment of DR. See text.

C III: Without DR, less ions are recombining from C IV to C III, and thus also from C III to C II, due to the lower population. Thus, the differences seen in C III are reproduced in C II, whether DR is present or not. Since C IV is the main ionization stage, the slight increase in its ionization fraction (without DR) is almost invisible.

All models described in Table 3.2 produce the same effect for C III and C II when DR data are removed. Here we have concentrated on model D45, since for this model we already investigated the effect of DR on the ionization of oxygen in a previous study (Carneiro et al. 2016).

We also investigated which transitions (regarding their lower levels – C III) are responsible for such a change in the wind ionization. It turned out that almost all of the first 40 states are involved, but that levels C3_19, C3_29, and C3_30 (for configuration and term designation, see Table 3.5) are responsible for already half of the total effect, where these levels ionize to the second state of C IV.

As shown in Figs. 3.3 and 3.5 (see next section), a different treatment of DR can affect the ionization balance of C II and C III in the line-forming region of corresponding optical lines, particularly if this region extends into the wind. Even if such impact is expected to be weak, it should be visible in the synthetic profiles. To see a clear-cut effect, we will concentrate on our (cooler) model D35, where the C II/III lines are certainly visible. Figure 3.4 compares such lines arising from models calculated with our three different approaches for DR as discussed above (same color-coding as in Fig. 3.3).

In general, the omission of DR leads to more, while the explicit method leads to less absorption, and our current description lies in between (slightly closer to the non-DR profiles). For most lines, the differences are weak (roughly at the 5 to 10% level at the core), except for C III 4665 (roughly 20%) and C III 5696. The impact of DR on the latter has been already explored by Martins et al. (2012) for a similar model, however with a much lower $\log g$, which turns the line into emission (see also Fig. 3.6 for a similar behavior in our models). Qualitatively, the effect displayed by both studies is very similar: a larger strength of the stabilizing transitions or resonances leads to more line emission, while reducing these quantities (until a final omission) leads to more absorption.

In conclusion, DR will have no big impact on our and forthcoming spectroscopic analyses, except for C III 5696, which is also affected by other processes such as X-ray emission. For UV-lines that may form throughout the complete atmosphere, however, a realistic description of DR is essential, not only to obtain a fair representation of the observations, but also to achieve consistency with the optical regime.

Finally, we note that also the models calculated with WM-BASIC show the same reaction when DR is excluded (with respect to all or individual stabilizing transitions). We conclude that the two codes independently show a lower degree of C II and C III, once DR is neglected. On the other hand, when actually accounting for DR, the detected differences can be attributed to different strengths of the stabilizing transitions or resonances, where according to our tests all recombining states are relevant, though specific transitions (see above) have a particularly strong impact. As a final test on this issue, we explicitly compared the strengths for the latter transitions (see also Rivero González et al. 2011, Sect. A3), finding a discrepancy of roughly a factor of two (with WM-BASIC data providing larger values).

3.3.2 Further comparison with WM-BASIC

Once the importance of DR in transitions from C IV to C III and its indirect impact on C II has been understood, we can continue in our comparison between FASTWIND and WM-BASIC results.

We remind the reader that both codes are completely independent (except that FASTWIND uses WM-BASIC data for the background elements, i.e., for all elements different from H, He, and C in the case considered here), and use different methods and assumptions. In addition to the different treatment of metal-line blocking, WM-BASIC calculates the velocity field from a consistent hydrodynamic approach, leading to certain differences particularly in the transonic region. Furthermore, while WM-BASIC uses the Sobolev approximation for all line transitions and depths, FASTWIND uses a comoving-frame transport for the transitions from explicit elements and for the strongest lines from the background ones. As we have already mentioned, this can lead to significant discrepancies for those lines that are formed in the region between the quasi-static photosphere and the onset of the wind.

Figure 3.5 displays the comparison of ionization fractions for carbon ions in the photosphere and wind (as a function of τ_{Ross}) for our S45 model (see Table 3.2). Red lines represent the carbon ionization stratification as derived by WM-BASIC, black lines show the FASTWIND solution using our new model atom, and blue lines display FASTWIND models, where the carbon bound-free transitions including DR are calculated using the explicit method with WM-BASIC data.

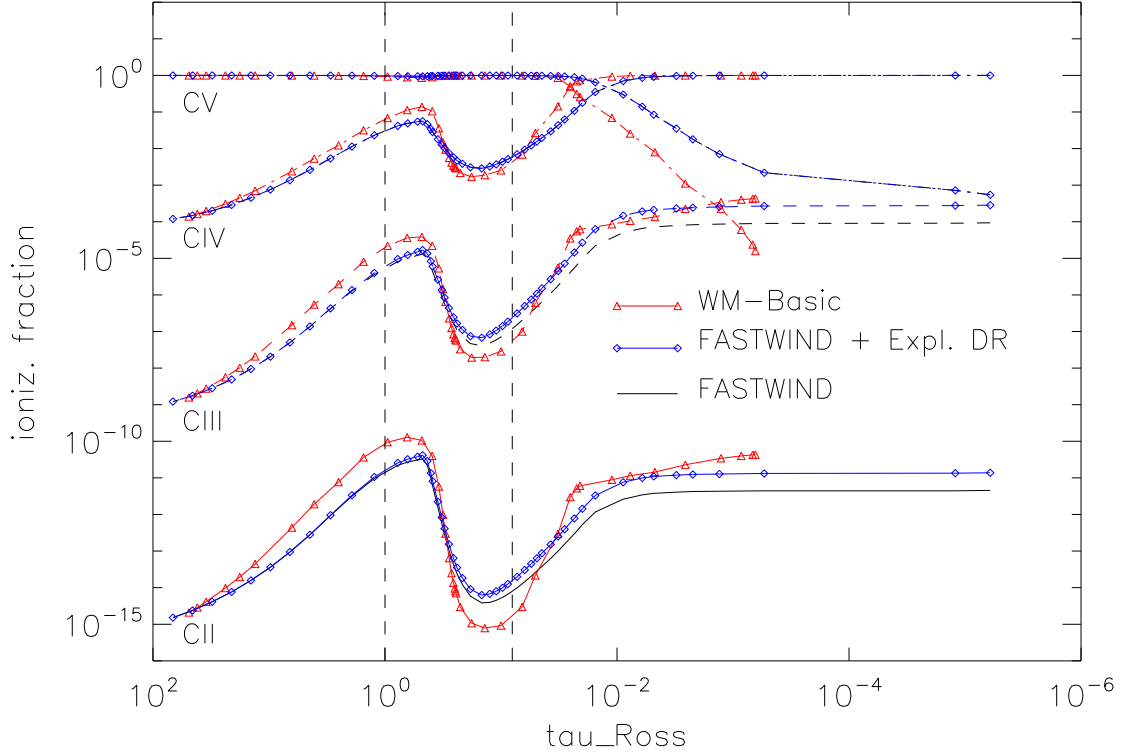


Figure 3.5: Ionization fraction of carbon ions, as a function of τ_{Ross} , for the S45 model, as calculated by WM-BASIC and FASTWIND using different approaches for DR. The dashed lines enclose the typical line-forming region of optical photospheric lines. For details, see text.

For this grid model, C III and C IV (the main ionization stage in the wind) are of major relevance regarding a carbon line diagnostics, though we also display C II (irrelevant at this T_{eff}) and C V, approximated by only one ground-state level in our atomic model. Within the photosphere, differences become visible at certain depths, mostly because of deviations in the density, and due to differences in the line transfer method (see above). In the wind, the standard FASTWIND and the WM-BASIC solution disagree, not only for S45, but also the other grid-models. These differences have been already described in Sect. 3.3.1, and are due to the different description of DR. When we then manipulated our new model atom to use the bound-free data from WM-BASIC with their larger strengths for the stabilizing transitions, we indeed see much more similar fractions in the outer wind, except for C V, which remains unaffected by DR, since it is insignificant for the C IV/C V balance.

In conclusion, we find a reasonable agreement between results from FASTWIND and WM-BASIC in the photosphere (at least for C III/IV/V). The differences apparent in the wind are due to the fact that the stabilizing transitions in WM-BASIC are larger (or considerably larger for specific transitions) than implied by the resonances provided by the OPACITY Project data. Since we are no experts in this field, we cannot judge which data set is the more realistic one, but until further evidence becomes

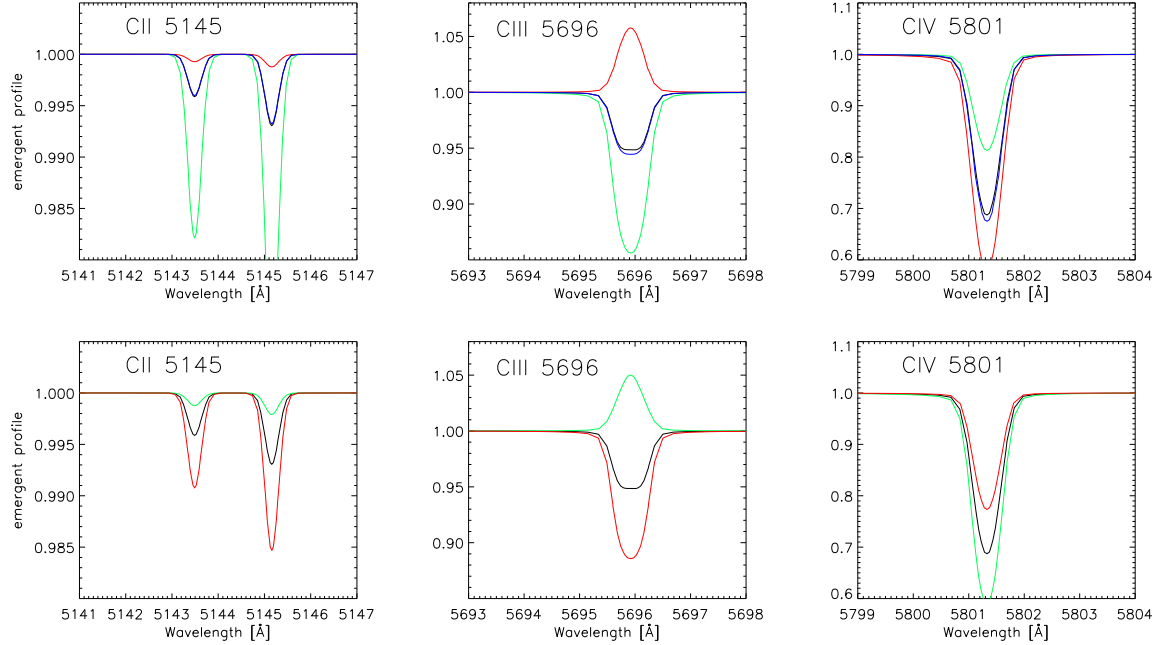


Figure 3.6: C II 5145, C III 5696, and C IV 5801 line profiles for model D35 (black lines) and similar models with relatively small changes in effective temperature (T_{eff}) and gravity ($\log g$). In the upper panels, the red lines correspond to a D35 model with T_{eff} increased by 1500 K, the green lines to a model with T_{eff} decreased by the same value, while the blue lines display the reaction to a decrease of \dot{M} by a factor of three. In the lower panels, the red lines correspond to a D35 model with $\log g$ increased by 0.2 dex, and the green lines with $\log g$ decreased by 0.2 dex.

available we prefer to use the OPACITY Project data, since they are well documented, tested, and applied within a variety of codes and studies.

3.3.3 Optical carbon lines – dependence on stellar parameters

The typical precision of a spectral analysis of massive stars using H/He lines is on the order of ± 1.5 kK in effective temperature and ± 0.1 dex in $\log g$ (e.g., Repolust et al. 2004). Since we aim for a non-LTE carbon abundance determination by line profile fitting, we need to test the sensitivity of our set of strategic lines to a variation of these parameters.

Due to the distinct complexity in each line formation process, almost each of the carbon lines will react differently. Figure 3.6 (and analogous figures) displays one spectral line per each carbon ion in each of the three columns. The first column shows C II 5145, the middle column C III 5696, and the third one C IV 5801. These lines have been chosen because they are strong (highlighted in Table 3.1), often discussed in the literature (e.g., Nieva & Przybilla 2008 or Daflon et al. 2004), and visible in different temperature ranges (see Figs. 3.9 to 3.14).

In each panel of Fig. 3.6, the black profiles refer to model D35. In the upper panels, red profiles

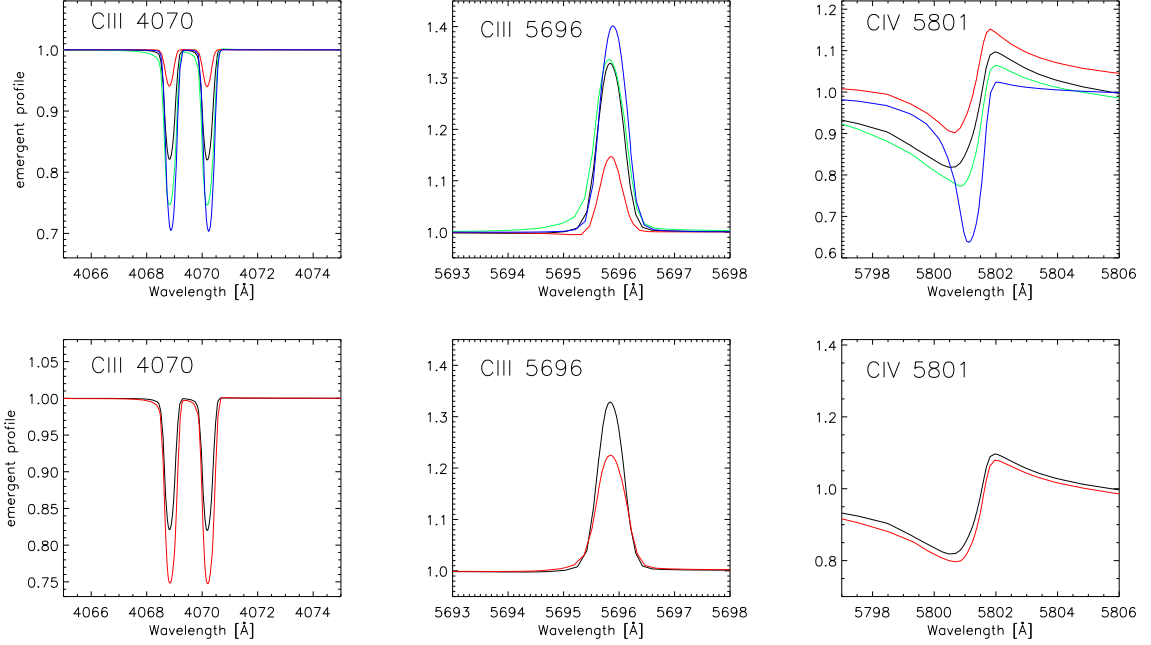


Figure 3.7: As Fig. 3.6, but for model S35. Since the C II lines are absent in such a model, we display another strategic line for this temperature range, C III 4068-70. We note that $\log g$ has only been varied by +0.2 dex (red profiles) in the lower panel. See text for details.

correspond to the same model, however with T_{eff} increased by 1.5 kK, while the green profiles, in turn, correspond to a T_{eff} reduced by 1.5 kK. Thus, we are able to study the variation of important carbon lines within the typical uncertainty of T_{eff} . Moreover, the upper panels also display profiles corresponding to model D35, but now with a mass-loss rate (\dot{M}) reduced by a factor of three, to estimate the impact of variations in this parameter. The effect of this reduction becomes most obvious for supergiant models (as for example displayed in Fig. 3.7). In the lower panels, finally, we study the reaction to variations in $\log g$ (± 0.2 dex).

As shown in the upper left panel, the decrease of temperature leads to a deeper C II absorption, while rising T_{eff} results in a shallower C II profile. This effect is easily understood: lower temperatures increase the fraction of low ionized stages, while higher temperatures favor the presence of higher ions, in this case C IV. From the lower left panel, we see that for the C II profile a decrease of $\log g$ leads to a shallower line (less recombination), while the opposite is seen once $\log g$ increases (red line).

The panels on the right present the reversed effects for C IV, as expected. For C III 5696 (middle panel), on the other hand, the behavior is quite complex, and has been explored comprehensively by Martins & Hillier (2012). Briefly, the strength of C III 5696 depends critically on the UV C III lines at 386, 574, and 884 Å, because these lines control the population of the lower and upper levels of specific optical C III lines including C III 5696. Indeed, we find a very sensitive reaction of this line on small variations in T_{eff} (upper middle panel), and a similar effect when varying $\log g$ (lower middle

panel). Without going into further details, during our tests we were able to reproduce all basic effects described by Martins & Hillier (2012), both regarding C III 5696, and also for the triplet C III 4647-50-51.

The consequences of a reduction in \dot{M} are clearly seen in the corresponding ionization fractions, where our D35 model with lower \dot{M} displays less C II and C III (less recombination) in the wind (~ 1 dex). Though these differences do not affect the line profiles in a notable way, the weak effect seen in the middle and right panel indicates that these lines are not completely photospheric.

Figure 3.7 displays a similar study on the reaction of specific carbon lines, now for the supergiant model S35. Since for supergiants the C II lines are already very weak or absent in this temperature range, we display another important C III line instead of the C II profile. Indeed, C III 4068-70 behave similarly to what has been discussed for the C II line in the previous figure. C III 5696 (the one with complex formation) is now in emission, for all cases shown, and C IV 5801 starts to display a P-Cygni shape. For this specific model, a reduction of $\log g$ by 0.2 dex brings the model very close to the Eddington limit ($\Gamma_e \approx 0.77$ already for a pure Thomson scattering opacity). The corresponding stratification becomes very uncertain, and we refrain from displaying corresponding profiles.

Since a supergiant (model) exhibits a denser wind than a dwarf, the effects of a mass-loss reduction on the line profiles are more obvious than for model D35. Also here, the model with reduced \dot{M} displays a lower fraction of C II and C III in the outer wind. Particularly in the line forming region, however, the ionization fractions of all ions become larger. The leftmost panel shows that a reduction of \dot{M} leads to a stronger C III 4068-70 absorption, where the effect is even more pronounced than the effect of the temperature reduction or the gravity increase. In the middle panel, the effect is similar, now acting on an emission profile. Again, we see a larger response than on the temperature decrease, which is also true for the right panel. Additionally, the P-Cygni shape almost vanishes, due to the inward shift of the line-forming region.

Finally, and for completeness, Appendix 3.B provides the same analysis, now for the cooler and hotter dwarf and supergiant models at 30 kK and 40 kK, and for partly lower changes in T_{eff} and $\log g$. In addition to mostly similar reactions as described above, we note the different reaction of C III 5696 on the variation of $\log g$ in the supergiant models: While for largest $\log g$ both S30 and S35 yield the lowest emission, this behavior switches for S40, where the highest $\log g$ results in the largest emission. Again, this nonmonotonic behavior is due to the complex formation process of this line. Additionally, Fig. 3.20 displays the reaction of our complete set of lines on a change of stellar parameters.

Overall, the tests performed in the section indicate that most of our strategic carbon lines are quite sensitive to comparatively small variations of the stellar parameters, variations that are within the precision of typical atmospheric analysis of massive stars performed by means of H and He. Moreover, some of them depend on UV transitions (as, e.g., C III 5696). Since X-ray emission affects UV lines, we need to check which of our optical lines indirectly depend on the strength of the X-ray emission (see Sect. 3.4.4).

By the end of this test, we are able to conclude that even in those cases where the stellar parameters are “known” from a H/He analysis, a small model grid needs to be calculated for each stellar spectrum which should be analyzed with respect to carbon. This grid needs to be centered at the (previously) derived T_{eff} and $\log g$ values found from H/He alone, and should extend these values in the ranges

considered above¹². One of these models should then allow for a plausible fit for the majority of our C II/III/IV lines (and not destroy the H/He fit quality), for a unique abundance and micro-turbulent velocity, v_{turb} .

Finally, we emphasize that all the tests discussed thus far only give a first impression on the capabilities of our new model atom. The quality and reliability of these results can be estimated only via a detailed comparison with observations, for a large range of stellar parameters. A first step into this direction is the main topic of the next section.

3.4 First comparison with observed carbon spectra

3.4.1 Basic considerations

For our comparison with observations and a first analysis, we used six spectra of presumably single Galactic O-type stars in different temperature ranges. Because of the weakness of most lines and the blending problem, rotational broadening is of major concern for a meaningful comparison of synthetic and observed spectra. Usually, hot massive stars are fast rotators (e.g., Simón-Díaz & Herrero 2014), and any large value of $v \sin i$ (particularly in combination with a significant extra-broadening due to “macroturbulence”, v_{mac}) makes the majority of carbon lines very shallow or even too shallow to be identified. Thus, we restricted ourselves to comparatively slow rotators.

Our subsample comprises three dwarf and three supergiant O stars, observed with different instruments. However, all spectra cover the wavelength range relevant for this work. As in our previous tests, we cover the same interval of temperature, from ~ 30 kK to ~ 50 kK. Thus, we expect to analyze C II / C III for the coldest stars, while the hotter stars provide an opportunity to check our precision in reproducing C III and C IV lines.

The reduced and normalized¹³ spectra were kindly provided and extracted from the work by Holgado et al. (2018). In this work, the parameters of a large sample of Galactic O-stars were obtained by quantitative H/He spectroscopy using FASTWIND, where we have already summarized some observational details in Sect. 3.2.5.

For our subsample, we double-checked their results by an independent FASTWIND analysis (fitting by-eye, contrasted to the semi-automatic fitting method applied by Holgado et al. (2018) using precalculated grids of synthetic spectra and the GBAT-tool, Simón-Díaz et al. 2011b), and found an agreement of photospheric and wind parameters (in particular, T_{eff} , $\log g$, $\log Q$ – see below –, $v \sin i$, and v_{mac}) on a $1-\sigma$ level. We also checked the radial velocities using the H/He lines, and confirmed the values provided by Holgado et al. (2018) for almost all subsample stars (differences less than 10 km s^{-1}), except for CygOB2-7, where we found a difference of 20 km s^{-1} .

Holgado et al. (2018) estimated the wind-strength parameter, $Q = \dot{M}/(R_* v_{\infty})^{1.5}$ (e.g., Puls et al. 2005) for each star in their sample, though they did not provide individual values for \dot{M} , R_* , and v_{∞} as required for the FASTWIND input. We estimated these quantities using their Q -values, an estimate

¹²We note that a variation of the wind-strength might be required as well.

¹³For some of the spectra, certain problems in normalization (e.g., for C II 6578 in HD 35612), and overall shape, partly due to the difficulty of connecting different orders (reduction by the available pipelines), are obvious. In this work, however, we refrain from a corresponding renormalization, but will comment on such problems when necessary.

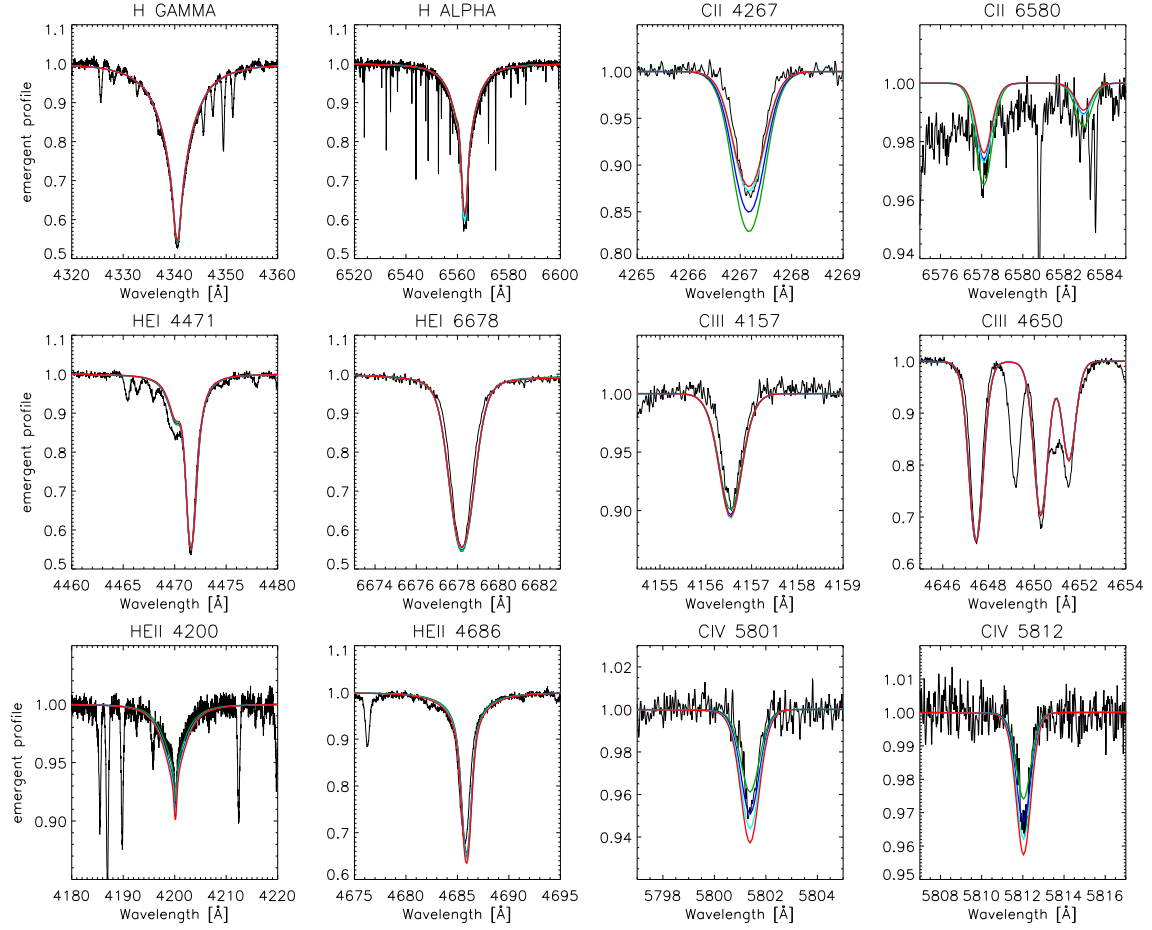


Figure 3.8: Fine-tuning of stellar parameters (here, T_{eff}), for the case of HD 36512 (O9.7V). The stellar parameters initially estimated from the H/He lines (green) still need some additional fine tuning, since some of the carbon lines are much more sensitive to small changes than H/He. The color coding for T_{eff} is as follows. Green: 33 kK (see Holgado et al. 2018), blue: 33.6 kK, turquoise: 33.8 kK, and red: 34 kK (the latter displaying too much C IV).

of v_{∞} (via v_{esc} , using $\log g$, R_* , and T_{eff} , see Kudritzki & Puls 2000), and an adopted stellar radius, R_* , following the Martins et al. (2005) calibration between spectral type and radius.

As shown in Sect. 3.3.3, the uncertainties (error bars) on the stellar and wind parameters derived from H/He alone are quite large when accounting for the sensitivity of the carbon lines. Therefore, after having defined a first guess of these parameters, there is still a sufficiently large interval in T_{eff} and $\log g$ to vary those parameters and to find the best matching carbon ionization balance (in those cases where more than one ion is present), while preserving the overall fit-quality of the H/He lines. To this end, we varied T_{eff} and $\log g$ inside intervals of $\pm 1,000$ K and ± 0.1 dex, respectively, centered at the initial values derived by Holgado et al. (2018).

Figure 3.8 displays the T_{eff} -sensitivity of important diagnostic carbon lines (right two columns) in comparison to H/He lines (left two columns). For this example, we have chosen our coldest dwarf

object (HD 36512, O9.7V), where further details will be discussed in the next section. On the figure we plot the initial model calculated with the values obtained by Holgado et al. (2018). Obviously, this model has much stronger C II and weaker C IV than the observations. Evidently, the effective temperature needs to be adjusted, even though it reproduces well the H/He profiles. In this case, C III does not display a remarkable sensitivity, since it is the main ion throughout the atmosphere.

All colored lines represent models with the same $\log g$, $\nu \sin i$, ν_{mac} , Q , and $[C/H] = \log C/H + 12$ (by number) values (see Table 3.3), but with different T_{eff} . We note that $[C/H]$ had already been reduced by 0.2 dex with respect to solar abundance (see below), to obtain reasonable fits. The color coding is described in the figure legend. All models reproduce equally well the H/He lines, though the variation in carbon is significant. We conclude that in this case, the $T_{\text{eff}} = 33.8$ kK profiles are closest to observations, and that it is possible to represent all three ionization stages in parallel with the adopted abundance. We note that here we did not have to change $\log g$.

As we have double-checked all stellar and wind-parameters (but varied T_{eff} and $\log g$ to improve on the carbon ionization balance), and these parameters turned out to be sufficient to reproduce the H/He and C profiles, we have not performed an independent error analysis, and refer to the values suggested by Holgado et al. (2018).

Regarding the carbon abundances, we used, at least in principle, all the lines from our set as indicators, through a by-eye fit, but lines which eventually displayed an unexpected behavior (e.g., too much emission), were discarded. In this context, we remind on the complexity of spectroscopic analyses for hot stars, compared to cooler ones. Due to the presence of, for example, strong NLTE effects, winds, and possibly clumping, which might “contaminate” individual lines, our goal is to obtain a best compromise solution from lines of the available carbon ions, and to constrain the carbon abundance within a reasonable range. In our opinion, it is better to obtain such a compromise solution for as many lines and ions as possible, instead of aiming at perfect fits for few lines only. We note here that deviations between synthetic and observed profiles are not as strongly related to inadequate atomic data as it is the case in cooler stars, but also depend on all the other uncertainties mentioned above.

The above compromise solution was achieved as follows. At first, we calculated a model with solar carbon abundance¹⁴, and two more models with this abundance varied by ± 0.2 dex. This first step allowed us to identify if, in general, the visible carbon lines agree better with a solar, supersolar, or subsolar abundance. In a second step, we fine-tuned T_{eff} and $\log g$ as outlined above. To specify the final carbon abundances and their uncertainties (i.e., the above range), we used the first estimate of $[C/H]$, and calculated, if necessary, one further model, with $[C/H]$ enhanced or decreased by 0.2 dex (in dependence of the result from step one). In case – this was not necessary for our sample –, this process needs to be repeated, and the final range should comprise reasonable fits for all lines of our set. As quoted abundance then, we adopt the center of this range. The chosen interval of ± 0.2 dex allows us also to obtain a rough estimate on the associated uncertainty. If a step of ± 0.2 dex was too large, the process was repeated with abundances increased or decreased by only 0.1 dex, as indicated by the line fits, Figs. 3.9 to 3.14.

¹⁴For reference, the solar carbon abundance is 8.43 ± 0.15 dex in terms of number density according to Asplund et al. (2009), while Przybilla et al. (2008) estimated, from quantitative spectroscopy of B-dwarfs, a carbon abundance of 8.32 ± 0.03 dex as a cosmic abundance standard for the solar neighborhood.

Table 3.3: Stellar and wind parameters adopted for and derived from fitting the H/He plus carbon lines displayed in Figs. 3.9 to 3.14. The two values for T_{eff} and $\log g$ refer to the values provided by Holgado et al. (2018) and our final values, respectively. The carbon abundances derived for our two hottest objects (HD 93128 and CygOB2-7) rely mostly on only two lines from C IV, and should be considered with caution. See text.

Name	SpType-LC	Instrument	S/N at 4500 Å	$v \sin i$ (kms^{-1})	v_{mac} (kms^{-1})	T_{eff} (kK)	$\log g$ [dex]	Y_{He}	$\log Q$ [dex]	[C/H] [dex]
HD 36512	O9.7V	HERMES	210	13	33	33.0 — 33.8	4.02 — 4.06	0.105	-13.4	8.25 ± 0.22
HD 303311	O6V	FEROS	148	47	61	40.1 — 41.2	3.91 — 4.01	0.107	-13.0	8.33 ± 0.25
HD 93128	O3.5V	FEROS	186	58	56	49.3 — 48.8	4.09 — 4.09	0.103	-12.7	8.23 ± 0.30
HD 188209	O9.5Iab/I	HERMES	207	54	93	30.1 — 30.3	3.03 — 3.03	0.145	-12.4	8.23 ± 0.25
HD 169582	O6Ia	FEROS	71	66	97	38.9 — 39.0	3.70 — 3.70	0.225	-12.3	8.53 ± 0.20
CygOB2-7	O3I	FIES	31	75	10	50.3 — 51.0	4.09 — 4.09	0.139	-12.1	$8.03^{+0.3}_{-0.4}$

Table 3.3 summarizes the final values derived from our fits to the optical H/He¹⁵ and C-lines, for all objects considered. The table includes two values for T_{eff} and $\log g$, corresponding to the initial (from Holgado et al. 2018, partly priv. comm.) and updated values.

3.4.2 Details on individual spectra

In the following, each of the spectra and corresponding fits will be discussed in fair detail. Figures 3.9 to 3.14 present the observed spectra and our best compromise solution, corresponding to the parameters as given in Table 3.3. The colors in the figure refer to a carbon abundance increased and decreased by 0.2 dex (see figure caption). These profiles not only provide us with an estimate on the error of our finally derived abundance (see above), but also allow us to identify which of the lines are more or less sensitive to abundance variations.

The source *HD 36512* (ν Ori) is an O9.7V slow rotator, observed with the HERMES spectrograph (see Fig. 3.9). We fitted the H/He and C lines with a temperature of 33.8 kK and $\log g = 4.02$. The obtained stellar parameters agree well with the values derived by Holgado et al. (2018). This is one of the stars where all the carbon ions have well-defined observable lines.

Our synthetic spectra reproduce quite well the C II and C IV lines. C II 4637 is absent (O II 4638.9 dominates the range), as well as C II 5133. The region around C II 6578 is badly normalized, but even with a renormalization the line would still be reproduced inside the adopted range. For C III, most lines are reproduced, except for C III 5272 and the C III 4068-70 doublet, which always seems to indicate a lower carbon abundance than inferred from the other lines. At least for this object, the discrepancy seems to be stronger for the C III 4068 component than for its $\lambda 4070$ Å companion, but we note that the blue component is strongly influenced by O II 4069.8. Finally, C III 6744 is too weak in comparison to our models.

As a compromise, we derive a carbon abundance of $[C/H] = 8.25$ dex, which brings most carbon lines into agreement. Few of our lines point to slightly higher abundances (e.g., C III 4056-5696-

¹⁵including H_{α} and He II 4686

8500), and therefore we estimate a range of ± 0.22 dex for the involved uncertainties. This spectrum is an example for an ideal scenario, mainly due to the low rotation rate ($v \sin i = 13 \text{ km s}^{-1}$) and low macroturbulence ($v_{\text{mac}} = 33 \text{ km s}^{-1}$), where our carbon model produces very satisfactory results. Martins et al. (2015a) have analyzed this star as well, and they derived, in addition to rather similar stellar parameters, also a carbon abundance ($[C/H] = 8.38 \pm 0.15$) that is consistent with our result.

The star *HD 303311* is an O6V star with a projected rotational velocity of 47 km s^{-1} , and a macroturbulence of 61 km s^{-1} (Fig. 3.10). The spectrum has been collected with the FEROS spectrograph. We obtained a final value of 41.2 kK for the temperature and of 4.01 for $\log g$, both slightly adjusted after the reproduction of the H/He lines to the best agreement with the different carbon lines. At this temperature (and rotational velocity), the lines of C II already vanish, and the C III profiles are weak, while the C IV lines are still easily detectable. In this case, however, C IV is the main ionization stage, and therefore not as sensitive to variations in the stellar parameters as the other carbon ions¹⁶. Our synthetic lines show a good reproduction of the C III lines. Once more, C III 4068-70 indicate a lower abundance when compared to the other C III profiles, however the difference is not larger than 0.2 dex. C III 6731 surprisingly displays an emission profile. There seems to be a disagreement between the carbon abundance indicated by the C III and C IV lines. Both C IV profiles point to a higher [C/H]-value, but again the difference is not larger than 0.22 dex. The best compromise was found for a carbon abundance of 8.33 ± 0.25 dex.

The star *HD 93128* is an O3.5V star rotating with 58 km s^{-1} , a macroturbulence of 56 km s^{-1} , and was observed with the FEROS spectrograph (Fig. 3.11). The temperature has been decreased by 300 K from the value obtained by the pure H/He analysis, but is still in agreement with the value from Holgado et al. (2018) when considering their $1-\sigma$ interval. We used 48.8 kK for the temperature, and 4.09 for $\log g$. In this temperature regime, some weak signs of C III might be seen only by chance. Furthermore, also the C IV-analysis becomes difficult, because the lines start to switch from absorption to emission, and a distinction from the continuum is harder in this case. Additionally, He II 5800 broadens C IV 5801.

Nevertheless, at least a rough estimate for the carbon abundance might be provided, mostly from C IV. In Fig. 3.11, we fit the weak sign of C III 4650, and also C IV 5812, and we infer $[C/H] \approx 8.23$ dex. Due to the very low number of available lines, we adopt a larger uncertainty in our estimate, ± 0.3 dex.

The star *HD 188209* is an O9.5Iab star with $v \sin i$ of 54 km s^{-1} , a macroturbulence of 93 km s^{-1} , and has been observed with the HERMES spectrograph (Fig. 3.12). The temperature and gravity obtained from fitting the H/He lines agree well with the stellar parameters derived from Holgado et al. (2018) ($\Delta T_{\text{eff}} = 200 \text{ K}$), and were used in our final model including the carbon line diagnostics ($T_{\text{eff}} = 30.3 \text{ kK}$, $\log g = 3.03$). C III and C IV lines are easily identified, while C II lines are not present in this case, except a subtle sign of C II 4267, which is well reproduced by our synthetic profile. The C III and C IV lines, even being weak, are well described by the synthetic profiles, and the discrepancy of C III 4068-70 is somewhat lower than found in the cases above. Here, C III 4650 shows the largest deviations. We note also the poor normalization around C III 4070 and C III 5800. Our final solution for [C/H] is 8.23 dex, and due to nonfitting lines we increase our error budget to ± 0.25 dex. Also this star has been analyzed by Martins et al. (2015a). Again, the stellar parameters are in very good

¹⁶an analogous behavior of C III in a cooler model was shown in Fig. 3.8.

agreement, but here the derived carbon abundance ($[C/H] = 7.85 \pm 0.3$ dex) only marginally overlaps with our value within the quoted error intervals.

The star *HD 169582* (O6Ia) rotates with $v \sin i = 66 \text{ km s}^{-1}$, has a macroturbulence of 97 km s^{-1} , and was observed with the FEROS spectrograph (Fig. 3.13). A temperature of 39 kK and $\log g$ of 3.7 were used to synthesize the carbon lines. Both values agree with the ones suggested by Holgado et al. (2018). C III is very weak and almost invisible, and only the C IV profiles are easily visible. Firm conclusions about C III are not possible, though we note that the synthetic lines indicate a weak signal. A carbon abundance of 8.53 dex gives a fair compromise for the C III/C IV lines, though C IV seems to indicate a slightly higher abundance than C III. We note however that none of the lines requires an abundance outside the ± 0.2 dex interval.

The star *Cyg OB2-7* is one of the few O3I stars in the Milky Way. Its spectrum (Fig. 3.14) has been recorded by the FIES-spectrograph, and extends “only” to a maximum of 7000 Å, so that C III 8500 is not available. We note that this spectrum has the lowest S/N within our subsample. A T_{eff} of 51 kK and a $\log g$ of 4.09 (together with $v \sin i = 75 \text{ km s}^{-1}$ and an astonishingly low $v_{\text{mac}} = 10 \text{ km s}^{-1}$) enable a satisfactory fit to the H/He lines. In this temperature regime, only C IV is visible, switching from absorption to emission (at least at the given \dot{M}). This behavior complicates the reproduction of the C IV profiles, and forbids any stringent conclusions. Especially in this case, one would also need to analyze the UV spectrum. If we believe in the ionization equilibrium and the mass-loss rate, we derive an abundance around $[C/H] \approx 8.0$, which would be the lowest value in our sample. From the fit quality and since we have to firmly rely on our theoretical models (no constraint on the ionization equilibrium), we adopt an asymmetric error interval, -0.4 and $+0.3$ dex.

As mentioned in Sect. 3.2.3, one of the “classical” problems in carbon spectroscopy is an inconsistent abundance implied by C II 4267 and C II 6578-82. Once more, we remind on the work by Nieva & Przybilla (2006) who thoroughly investigated and solved this problem for a set of stars cooler (with stronger C II lines) than the ones considered in this work. These C II lines are clearly visible and well reproduced with the same value of $[C/H]$ in our coldest dwarf, HD 36512. This provides strong evidence that our present data are sufficient to overcome this issue. Also for our coldest supergiant, HD 188209, C II 4267 is present and well reproduced. On the other hand, C II 6578-82 is absent, and thus no further conclusions can be asserted.

We finish this section by noting that part of the problems in fitting certain lines might be related to our assumption of a smooth wind (and neglecting X-ray effects, but see Sect. 3.4.4). Effects due to clumping etc. will be investigated in a forthcoming paper. In this regard, the abundance estimates presented in Table 3.3 should be taken with caution: Contrasted to cooler-type stars where the synthetic profiles depend primarily on the precision of atomic data, for early type stars with winds much more uncertainties have to be accounted for (and approximated in a reasonable way).

3.4.3 Which lines to use?

After our first analysis, we acquired enough experience to judge in which lines to “trust” when deriving carbon abundances. In Table 3.1, we provided a comprehensive list, comprising many more lines than previously studied, which are strong enough to be easily identified in different temperature ranges. Instead of describing which of these lines are the most useful, we summarize which may be discarded,

since this results in a shorter list.

For C II, the range around C II 4637 is dominated by O II 4638, and therefore the carbon lines are barely visible. C II 5648-62 are isolated lines which can be important, but are not visible in the range of spectral types studied in this work (O9-O3). The same is true for C II 6461. The lines at 5139 and 6151 Å are formed by transitions with low oscillator strength, and might be too weak for a meaningful spectral diagnostics. Excluding these lines, we were able to identify all the other C II lines as listed in Table 3.1 in the observed spectra (for the cooler spectral types), and to use them within our analysis.

The largest number of lines is provided by C III, when considering the complete O-star range. Particularly, all the listed lines are visible in the coldest dwarf of our sample (Fig. 3.9). C III 4068-70 always (i.e., for the complete temperature range) point to lower abundances (compared to the majority of other lines), and it might be that particularly the λ 4068 Å component is either mistreated by our approach, or that there is a problem with its oscillator strength. The lines at 4650 and 5696 Å always deserve special attention, because of their complex formation process, even though we were able to reproduce these lines well in the majority of cases studied here. The lines at 5826, 6731, and 6744 Å are also good diagnostics, but vanish quickly for spectral types earlier than O9.

For C IV, basically four lines are available in the optical range, but the ones at 5016-18 Å are outshone by He I 5015. Therefore, and to our knowledge, all optical C IV analysis performed until to-date have concentrated on C IV 5801-12, and this most likely will not change in future.

Discarding the lines quoted above, we end up with a list of 27 lines from C II/III/IV that are useful for determining reliable carbon abundances, indicated in boldface in Table 3.1.

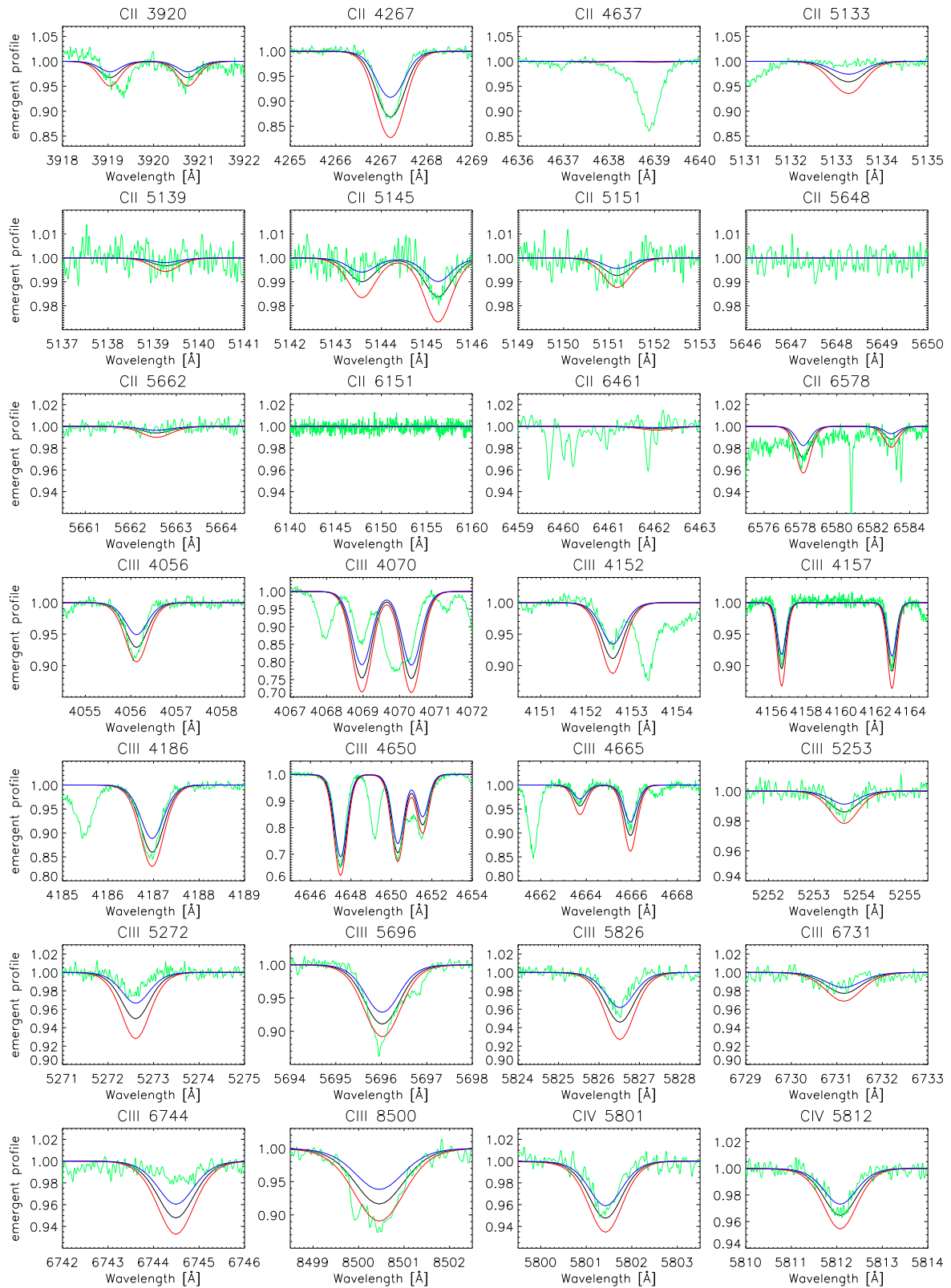


Figure 3.9: Observed carbon spectrum of HD 36512 (O9.7V, green), and synthetic lines (black), calculated with $[C/H] = 8.25$ dex. The red and blue profiles have been calculated with an abundance increased and decreased by 0.2 dex, respectively.

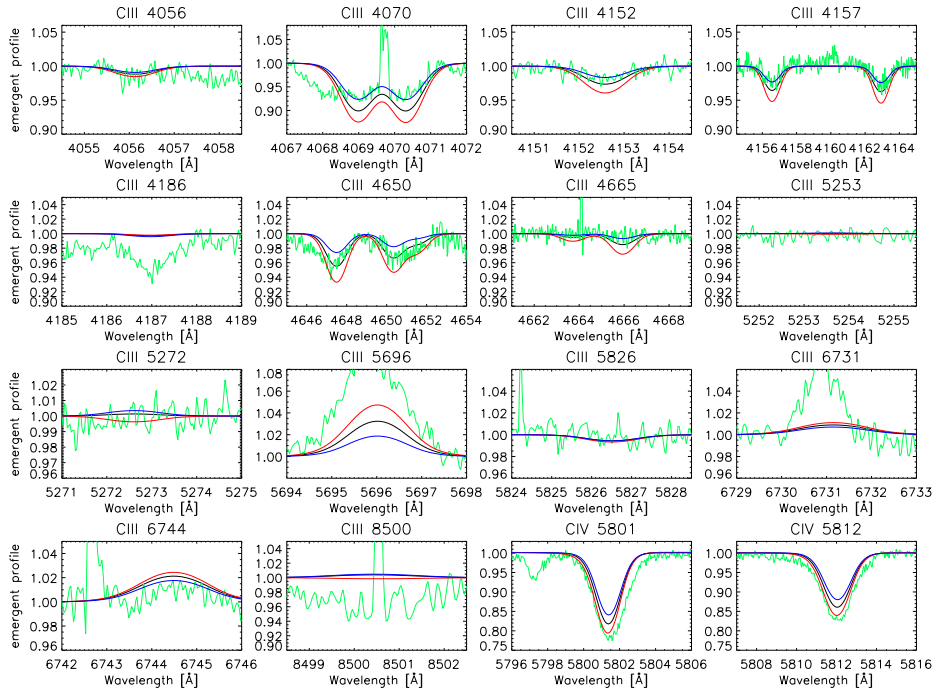


Figure 3.10: As Fig. 3.9, but for HD 30331 (O6V), and a carbon abundance of 8.33 dex. The optical C II lines are not visible, and thus not displayed.

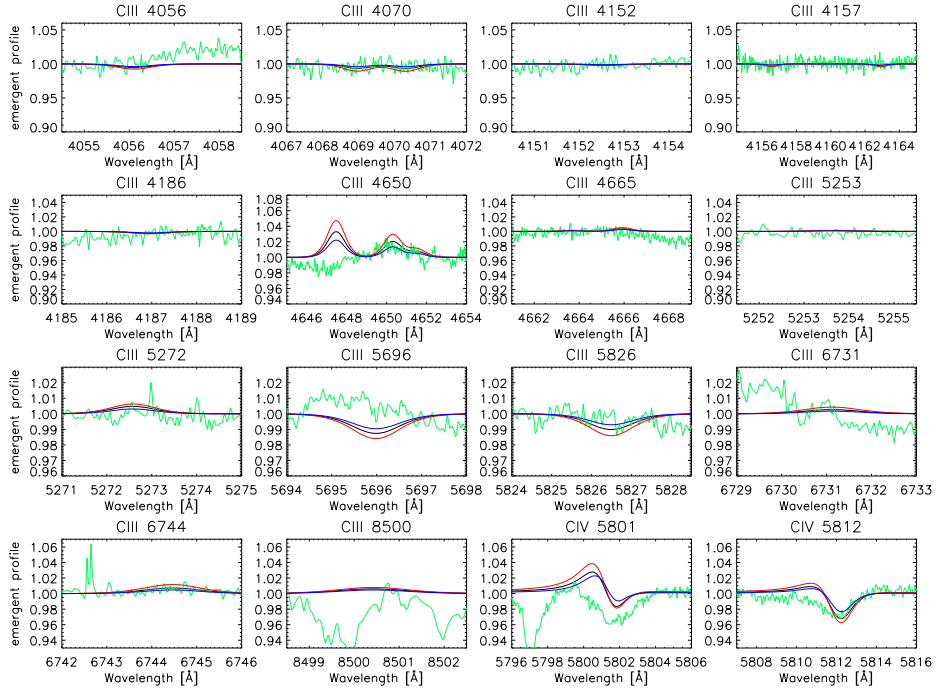


Figure 3.11: As Fig. 3.10, but for HD 93128 (O3.5V), and a carbon abundance of $[C/H] = 8.23$ dex.

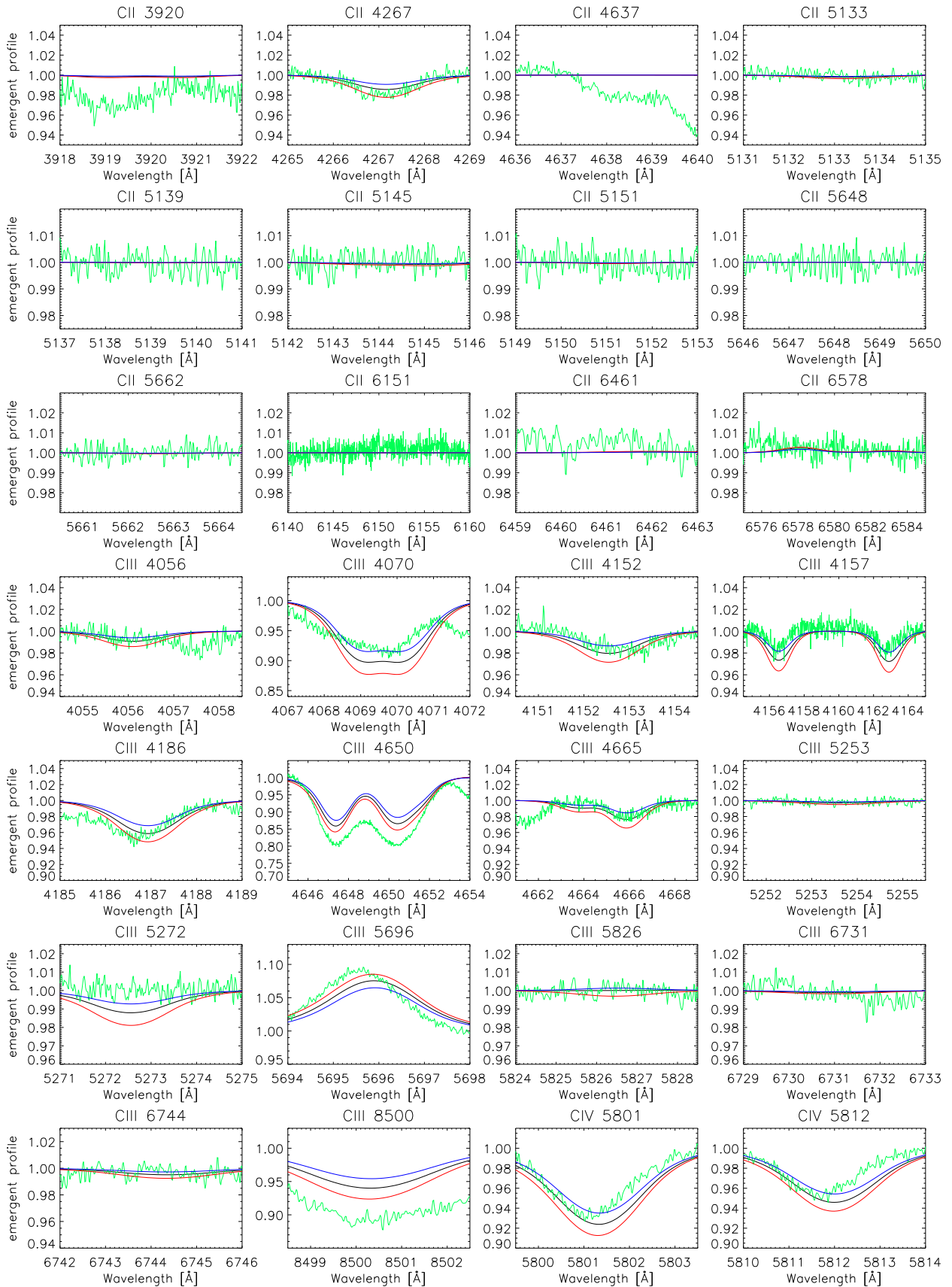


Figure 3.12: As Fig. 3.9, but for HD 188209 (O9.5Iab), and a carbon abundance of 8.23 dex.

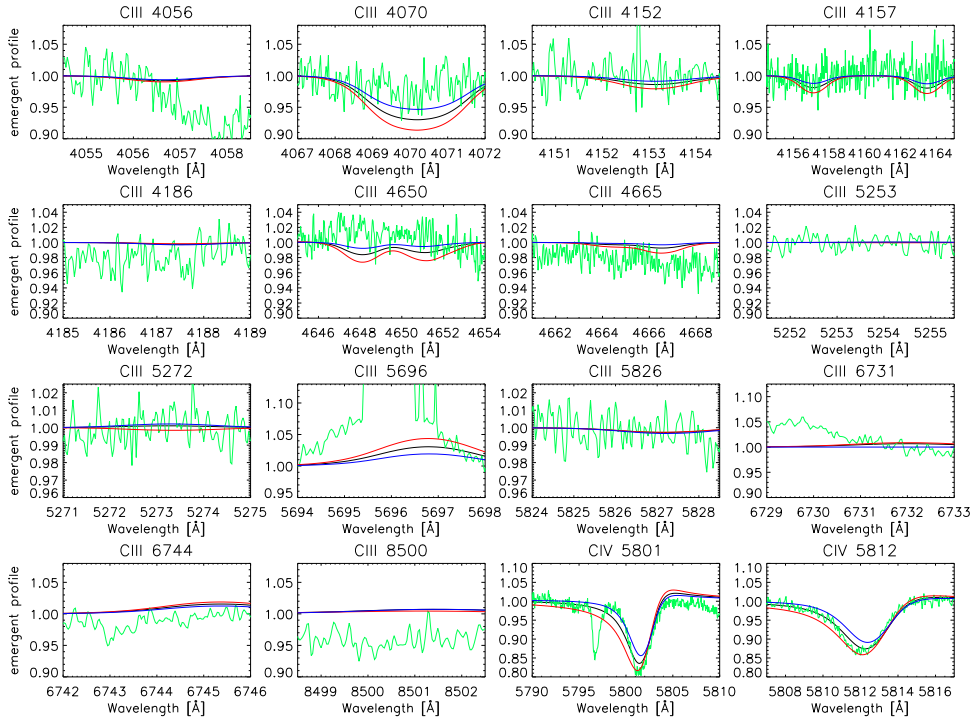


Figure 3.13: As Fig. 3.10, but for HD 169582 (O6Ia), and carbon abundance of 8.53 dex.

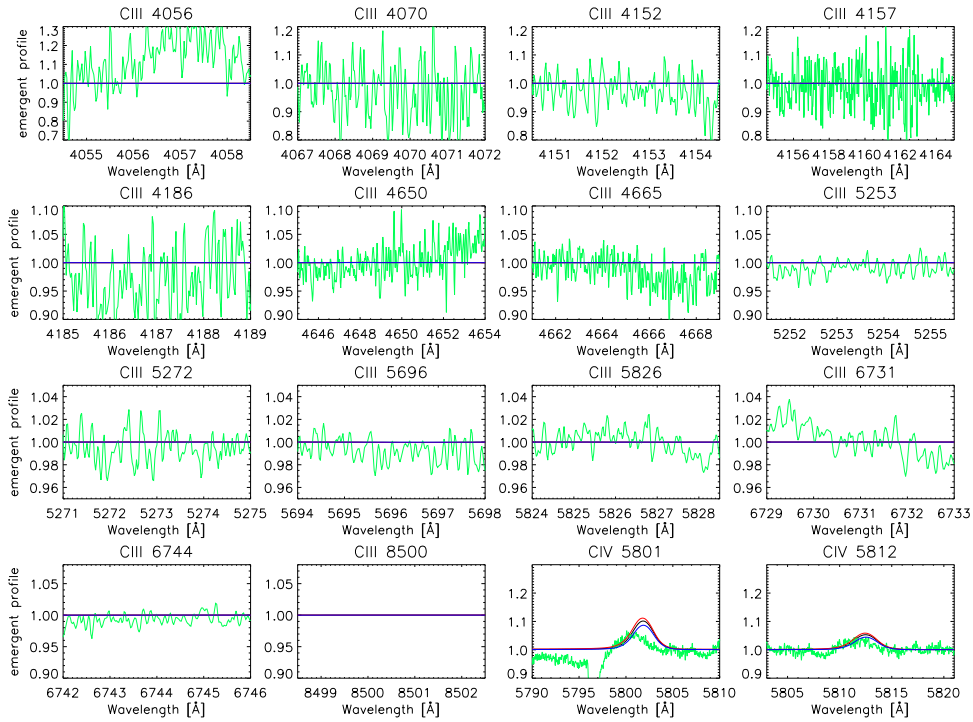


Figure 3.14: As Fig. 3.10, but for CygOB2-7 (O3I), and a carbon abundance of 8.03 dex.

3.4.4 Impact of X-rays

In a previous paper (Carneiro et al. 2016), we already discussed the impact of X-ray radiation on the ionization stratification of different ions, including carbon. Here we investigate which of the optical lines are affected by emission from wind-embedded shocks, and how intense the X-ray radiation must be to have a relevant impact on the lines. As pointed out before, purely photospheric lines without any connection to UV-transitions should not be affected by X-rays, at least in principle. However, lines that are purely photospheric for thin winds are partly formed in the wind when the mass-loss rate becomes larger, and also the lower boundary of the X-ray emitting volume is important in controlling how much X-ray/EUV radiation can reach the photosphere. Even more, since the X-ray luminosity scales with the mass-loss rate (or, equivalently, with the stellar luminosity, e.g., Owocki et al. 2013), carbon lines in high-luminosity objects might become affected by X-ray emission even when they are not connected with UV-transitions.

The main idea of our study is to adopt the strongest possible (and plausible) shock radiation, and to check which lines will change. For the present analysis, few parameters will describe the shock radiation in each model, leaving the others at their default (see Carneiro et al. 2016 for details). These are the X-ray filling factor, f_x , which is related to (but not the same as) the (volume) fraction of X-ray emitting material, and the maximum shock temperature, T_s^∞ . Both are set here to the maximum values used in our previous analysis: $f_x = 0.05$, and $T_s^\infty = 5 \cdot 10^6$ K. Besides this “maximum-model”, we checked also the impact for intermediate values of the X-rays parameters ($f_x = 0.03$, and $T_s^\infty = 3 \cdot 10^6$ K). Another important parameter is the onset of X-ray emission, R_{\min} . Guided by theoretical models on the line-instability and/or by constraints from X-ray line diagnostics, R_{\min} is conventionally adopted as $\sim 1.5 R_*$ (e.g., Hillier et al. 1993, Feldmeier et al. 1997a, Cohen et al. 2014b). Since we want to maximize any possible effect from the X-ray radiation, we set $R_{\min} = 1.2 R_*$.

Before turning to the general results of our simulation, we remind on the sensitivity of C III 5696 and C III 4647-50-51, showing significant changes in strength and shape for small variations of local conditions in the 30-40 kK regime (see Fig. 3.6 and Martins et al. 2012 for a thorough analysis). As expected (both transitions are connected to UV resonance lines), these lines are indeed sensitive to the presence of X-rays.

After checking all lines tabulated in Table 3.1 regarding a potential influence of X-ray emission, no changes were found for the 30 kK and 35 kK dwarf and supergiant models. Even for C II in these coolest models, no impact was seen, which indicates that either the X-ray radiation is still too weak (because of low mass-loss rates), or that it cannot reach the photosphere.

From 40 kK on, however, the situation changes. In almost all cases, only the C IV lines become weaker, and by a considerable amount for supergiants (see below) and our D50 model. Most C III lines become only marginally stronger or weaker, if at all, and the only more significant reaction is found for the strongly UV-influenced C III 4647-50-51 and C III 5696 lines. When including shock radiation, their strength increases at hottest temperature(s), comparable to an increase in carbon abundance of 0.1 dex,

Beyond 40 kK, the ionization fraction of C IV decreases (both in the line-forming region and the wind) when the X-ray emission is included. For dwarfs, the corresponding line-strengths of C IV 5801-5811 (in emission) decrease in parallel, by an amount still weaker than 0.1 dex in [C/H].

For the supergiants, this effect becomes stronger in the 40 to 45 kK regime, while for S50, finally, the impact of X-rays on the C iv lines becomes weak again, presumably because in this temperature range the stellar radiation field dominates in controlling the ionization equilibrium. We note that for the D50 dwarf model the changes remain considerable though.

In Fig. 3.15, we detail this behavior, for our S40 model, where the effect is strongest. On the figure we plot a model without X-rays, a model with intermediate shock radiation, and the model with our strongest X-ray emission. The dotted profiles give an impression of a corresponding decrease in carbon abundance which would be necessary to mimic the X-ray effect, which is 0.3 and 0.6 dex, respectively. The other way round, for stars that have been analyzed without X-rays but exhibit a strong X-ray radiation field, the originally derived carbon abundance might need to be increased by such an amount to compensate for the missing X-ray field. Our investigation clearly indicates that X-rays may be important for the C iv analysis of supergiant stars with temperatures around 40 to 45 kK (e.g., the prototypical ζ Pup) and for (very) hot dwarfs, in particular if no lines from other carbon ions are present.

In summary, the changes are marginal for not too hot dwarfs, and affect only a few C iii lines (the triplet at 4647-50-51, the doublet at 4663-65, and C iii 4186, 5272, 5696, 5826, 6744, 8500 Å) which might be used with a lower weight in abundance analysis.

In contrast, and at least for supergiants in the range between 40 to 45 kK, various lines become substantially modified when accounting for strong emission from wind-embedded shocks, in particular the two C iii lines that are strongly coupled to the UV, and the C iv lines. The potential differences in abundances derived from these lines (~ 0.1 dex from C iii 4647-50-51 and C iii 5696, and ~ 0.3 to 0.6 dex from C iv 5801-5811) may complicate the analysis considerably, and we conclude that the carbon analysis of supergiants earlier than O7 should include X-ray radiation using typical default values, as already standard for CMFGEN modeling. We note (i) that this problem might have also affected our analysis of HD 169582, and (ii) that X-rays might need to be considered in the analysis of (very) hot dwarfs as well, due to their impact on C iv.

3.5 Summary and conclusions

In this work, we aimed to enable a reliable carbon spectroscopy by means of our unified NLTE atmosphere code FASTWIND. To this end, we developed a new carbon model atom using high-accuracy data from different databases. The data adopted to describe the radiative and collisional transitions have been cross-checked (with similar data from alternative databases) to ensure their reliability. We implemented an adequate number of levels following certain rules, though additional levels might be required for the analysis of IR-transitions in future studies. In total, we considered 162 LS-coupled levels, more than 1000 radiative, and more than 4000 collisional transitions.

One major issue for this study was a rigorous test of our new model atom. For this purpose, we calculated a sufficiently spaced grid of atmospheric models, to investigate the carbon ionization structure, and to compare with previous results using more simplified model atoms.

Interestingly, dielectronic recombination (DR) turned out to be of major importance for the de-

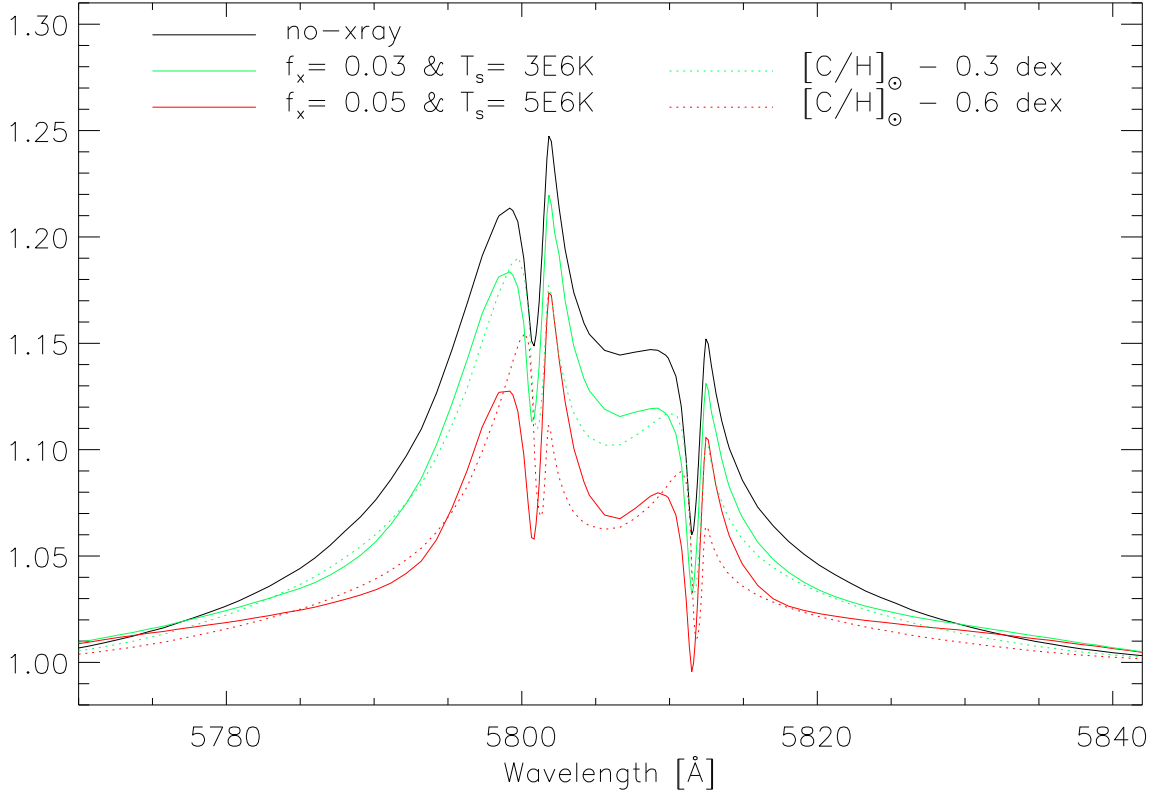


Figure 3.15: Impact of X-ray radiation on the C IV 5801-12 lines, for a supergiant model with $T_{\text{eff}} = 40$ kK (S40). Black: Line profiles for the “standard” model without shocks; green: model with an intermediate X-ray strength; red: model with strong X-ray radiation. The dotted profiles refer to alternative, no-shock models with reduced carbon abundance, mimicking the effect of shock radiation. We note that the displayed sensitivity is strongest for the considered lines and parameter range, see text.

scription of C II and C III in the wind, for almost all temperatures¹⁷. When DR is neglected, we find less recombination from C IV to C III, and consequently also less C II. Typical differences amount to 1 dex. Similar results were reproduced with WM-BASIC, though we found an important difference between the underlying data: The strengths of the stabilizing transitions used in WM-BASIC are typically larger (up to a factor of approximately two) than those corresponding to the strengths of the resonances included in the OPACITY Project data we have used, leading to stronger recombination in WM-BASIC models. Even though this potential uncertainty will not affect the majority of optical lines formed in the photosphere, it can be influential in upcoming analysis of UV wind lines. In the end, we preferred to use the OPACITY Project data, for reasons outlined in Sect. 3.3.1.

Unfortunately, optical carbon lines are rare, and often blended by other lines, which hampers

¹⁷except for $T_{\text{eff}} \gtrsim 50$ kK

the spectral diagnostics, particularly for large $v \sin i$ and/or v_{mac} . Thus, we compiled and selected a maximum set of potential diagnostic lines, including blended ones and also those with a complex formation mechanism controlled by UV transitions (as described by Martins et al. 2012).

Since the majority of metal lines are weak, they are very sensitive to comparatively small variations of stellar parameters, and this is particularly true for carbon lines. A change of ± 1000 to 1500 K in effective temperature, or ± 0.2 dex in $\log g$, results in considerable changes of line strength. Additionally, some of the lines are also sensitive to \dot{M} variations. Mainly in supergiants (and hot dwarfs), due to their dense winds, a decrease in \dot{M} by a factor of three produces an effect stronger than a decrease of 1500 K in T_{eff} or an increase of 0.2 dex in $\log g$. Thus one needs to precisely determine \dot{M} by reproducing, for example H_{α} and $\text{He II } 4686$, before aiming at a carbon analysis.

As a first application of our “new” capability to analyze carbon lines by means of FASTWIND, using our newly developed model atom, we investigated the spectra of a sample of six O-type dwarfs and supergiants, kindly provided to us by Holgado et al. (2018). We first convinced ourselves that the stellar and wind parameters derived by Holgado et al. (2018) are reproduced by our own H and He analysis. Thereafter, we varied T_{eff} and $\log g$ inside a range where the fit quality of the H/He lines could be preserved (roughly, ± 1000 K and ± 0.1 dex, respectively), while fitting the carbon lines from different ions in an optimum way, with an (almost) unique abundance in most cases. The finally quoted abundance was taken, if necessary, from the best-compromise solution, and from the reaction of the carbon lines when varying the abundances, we obtained a rough estimate on the corresponding error, typically in the range ± 0.2 to ± 0.3 dex.

Only for the coolest (O9.7) dwarf, lines from all three ionization stages are present in parallel, and our analysis resulted in a satisfactory reproduction of the ionization balance. In most other stars, only C III and C IV are visible in parallel. For one object with $T_{\text{eff}} \approx 40$ kK (HD 169582), these C III/IV lines disagree by ~ 0.2 dex in $[\text{C}/\text{H}]$, which might be related to the influence from X-ray radiation (see below). The hottest (O3) supergiant, CygOB2-7, displays only C IV, which renders the analysis quite uncertain (and there are only two suitable C IV lines in the optical).

We were, nevertheless, able to derive carbon abundances for all the considered objects, and found in most cases a moderate depletion compared to the solar value by Asplund et al. (2009), except for CygOB2-7, where a larger depletion by 0.4 dex was derived (though more uncertain than the other values). Two of our cool objects had already been analyzed by Martins et al. (2015a). For both of them we confirmed rather similar stellar parameters, but only for one of them (a dwarf) also the carbon abundances are quite similar, while for the other (a supergiant), there is an only marginal overlap within the errors.

To obtain further constraints on the reliability of our new set of synthetic carbon lines, we have to repeat the same exercise in particular for cooler stars, since C II already disappears for $T_{\text{eff}} \gtrsim 30$ to 35 kK, in dependence of luminosity class.

From our accumulated experience of analyzing basically all optical carbon lines, we finally provided a list of more than 25 lines of different strength and from different ions, which we consider as reliable carbon abundance indicators.

As a first step toward future work, we studied the direct and indirect (via UV-lines) impact of X-ray emission from wind-embedded shocks onto our sample of optical carbon lines, by simulating an X-ray radiation field that is at the upper limit of realistic values.

For the dwarf models, we found an almost negligible impact, except for very hot objects (≥ 50 kK). In contrast, carbon lines from supergiants with $T_{\text{eff}} \approx 35$ kK already show changes due to shock radiation, and at 40 to 45 kK the impact of X-rays is strong enough to complicate a reliable abundance measurement. Mostly, the C III lines become stronger (corresponding to an increase of up to 0.1 dex in [C/H]; the largest changes occur in the UV-influenced C III 5696 and C III 4647-50-51), and the C IV lines become weaker (corresponding to a decrease of 0.3 to 0.6 dex in [C/H]). Consequently, it might become more difficult (or even impossible) to find a value of [C/H] which brings different carbon lines into agreement, when strong X-ray emission would be present. Thus we concluded that in the spectral regime earlier than O7 I, it might be necessary to include the impact of X-rays by default (though a deeper understanding of typical X-ray parameters might be required as well). For supergiants with $T_{\text{eff}} \geq 50$ kK, the X-rays lose their impact, since direct ionization due to the stellar radiation field dominates over Auger-ionization and ionization from the EUV-component of the shock radiation (see Carneiro et al. 2016).

This study has been performed as a first step toward a complete CNO analysis. Particularly the investigation of the ratio N/C vs. N/O (as already begun by Martins et al. 2015a,b) will allow us to derive better constraints on the mixing history and chemical enrichment in massive stars than from a pure nitrogen analysis alone. We intend to continue such work, also by including the information provided by UV carbon lines, and by investigating the impact of wind inhomogeneities, which might play an important role also in the UV range, due to porosity effects and because of affecting the ionization balance in the wind.

Table 3.4: C II levels: label, electronic configuration, and term designation.

C2.#	Configuration	Term	C2.#	Configuration	Term
1	$1s^2 2s^2 2p$	2P	22	$1s^2 2s^2 5g$	2G
2	$1s^2 2s 2p^2$	4P	23	$1s^2 2s^2 6s$	2S
3	$1s^2 2s 2p^2$	2D	24	$1s^2 2s 2p(^3P^0) 3p$	4D
4	$1s^2 2s 2p^2$	2S	25	$1s^2 2s 2p(^3P^0) 3p$	2P
5	$1s^2 2s 2p^2$	2P	26	$1s^2 2s^2 6p$	$^2P^0$
6	$1s^2 2s^2 3s$	2S	27	$1s^2 2s^2 6d$	2D
7	$1s^2 2s^2 3p$	$^2P^0$	28	$1s^2 2s^2 6f$	$^2F^0$
8	$1s^2 2p^3$	$^4S^0$	29	$1s^2 2s^2 6g$	2G
9	$1s^2 2s^2 3d$	2D	30	$1s^2 2s^2 6h$	$^2H^0$
10	$1s^2 2p^3$	$^2D^0$	31	$1s^2 2s 2p(^3P^0) 3p$	4S
11	$1s^2 2s^2 4s$	2S	32	$1s^2 2s^2 7s$	2S
12	$1s^2 2s^2 4p$	$^2P^0$	33	$1s^2 2s(^3P^0) 3p$	4P
13	$1s^2 2s 2p(^3P^0) 3s$	$^4P^0$	34	$1s^2 2s^2 7p$	$^2P^0$
14	$1s^2 2s^2 4d$	2D	35	$1s^2 2s^2 7d$	2D
15	$1s^2 2p^3$	$^2P^0$	36	$1s^2 2s^2 7f$	$^2F^0$
16	$1s^2 2s^2 4f$	$^2F^0$	37	$1s^2 2s^2 7g$	2G
17	$1s^2 2s^2 5s$	2S	38	$1s^2 2s^2 7h$	$^2H^0$
18	$1s^2 2s^2 5p$	$^2P^0$	39	$1s^2 2s 2p(^3P^0) 3p$	2D
19	$1s^2 2s 2p(^3P^0) 3s$	$^2P^0$	40	$1s^2 2s^2 8g$	2G
20	$1s^2 2s^2 5d$	2D	41	$1s^2 2s 2p(^3P^0) 3d$	$^4F^0$
21	$1s^2 2s^2 5f$	$^2F^0$			

3.A Appendix A: Electronic states of each carbon ion

This section provides a short description of each ion considered in our new carbon model atom, except for C v which is described by the ground level only (see Sect. 3.2.2). All the next three tables have the same format: the first column displays the label of the level, the second column the electronic configuration of that level, and the third column presents the term designation. Table 3.4 refers to C II, Table 3.5 to C III, and Table 3.6 to C IV.

Table 3.5: As Table 3.4, but for C III.

C3.#	Configuration	Term	C3.#	Configuration	Term
1	$1s^22s^2$	1S	36	$1s^22s5p$	$^3P^0$
2	$1s^22s2p$	$^3P^0$	37	$1s^22p(^2P^0)3p$	1S
3	$1s^22s2p$	$^1P^0$	38	$1s^22s5d$	3D
4	$1s^22p^2$	3P	39	$1s^22s5g$	3G
5	$1s^22p^2$	1D	40	$1s^22s5g$	1G
6	$1s^22p^2$	1S	41	$1s^22s5d$	1D
7	$1s^22s3s$	3S	42	$1s^22p(^2P^0)3d$	$^1P^0$
8	$1s^22s3s$	1S	43	$1s^22s5f$	$^3F^0$
9	$1s^22s3p$	$^1P^0$	44	$1s^22s5f$	$^1F^0$
10	$1s^22s3p$	$^3P^0$	45	$1s^22s6s$	3S
11	$1s^22s3d$	3D	46	$1s^22s6s$	1S
12	$1s^22s3d$	1D	47	$1s^22s6p$	$^3P^0$
13	$1s^22p(^2P^0)3s$	$^3P^0$	48	$1s^22s6p$	$^1P^0$
14	$1s^22s4s$	3S	49	$1s^22s6d$	3D
15	$1s^22p(^2P^0)3s$	$^1P^0$	50	$1s^22s6g$	1G
16	$1s^22s4s$	1S	51	$1s^22s6g$	3G
17	$1s^22s4p$	$^3P^0$	52	$1s^22s6d$	1D
18	$1s^22p(^2P^0)3p$	1P	53	$1s^22s6h$	$^3H^0$
19	$1s^22s4d$	3D	54	$1s^22s6h$	$^1H^0$
20	$1s^22s4f$	$^3F^0$	55	$1s^22s6f$	$^3F^0$
21	$1s^22s4f$	$^1F^0$	56	$1s^22s6f$	$^1F^0$
22	$1s^22s4p$	$^1P^0$	57	$1s^22s7s$	3S
23	$1s^22p(^2P^0)3p$	3D	58	$1s^22s7p$	$^1P^0$
24	$1s^22s4d$	1D	59	$1s^22s7d$	3D
25	$1s^22p(^2P^0)3p$	3S	60	$1s^22s7g$	3G
26	$1s^22p(^2P^0)3p$	3P	61	$1s^22s7d$	1D
27	$1s^22p(^2P^0)3d$	$^1D^0$	62	$1s^22s7f$	$^3F^0$
28	$1s^22p(^2P^0)3p$	1D	63	$1s^22s8p$	$^1P^0$
29	$1s^22p(^2P^0)3d$	$^3F^0$	64	$1s^22s8d$	3D
30	$1s^22p(^2P^0)3d$	$^3D^0$	65	$1s^22p9d$	3D
31	$1s^22s5s$	1S	66	$1s^22p(^2P^0)4s$	$^3P^0$
32	$1s^22s5s$	3S	67	$1s^22p(^2P^0)4p$	1P
33	$1s^22p(^2P^0)3d$	$^3P^0$	68	$1s^22p(^2P^0)4p$	3D
34	$1s^22p(^2P^0)3d$	$^1F^0$	69	$1s^22p(^2P^0)4p$	3P
35	$1s^22s5p$	$^1P^0$	70	$1s^22p(^2P^0)4p$	1D

Table 3.6: As Table 3.4, but for C IV.

C4.#	Configuration	Term	C4.#	Configuration	Term
1	1s ² 2s	² S	26	1s ² 7i	² I
2	1s ² 2p	² P ⁰	27	1s ² 7h	² H ⁰
3	1s ² 3s	² S	28	1s ² 8s	² S
4	1s ² 3p	² P ⁰	29	1s ² 8p	² P ⁰
5	1s ² 3d	² D	30	1s ² 8d	² D
6	1s ² 4s	² S	31	1s ² 8f	² F ⁰
7	1s ² 4p	² P ⁰	32	1s ² 8g	² G
8	1s ² 4d	² D	33	1s ² 8h	² H ⁰
9	1s ² 4f	² F ⁰	34	1s ² 8i	² I
10	1s ² 5s	² S	35	1s ² 9s	² S
11	1s ² 5p	² P ⁰	36	1s ² 9p	² P ⁰
12	1s ² 5d	² D	37	1s ² 9d	² D
13	1s ² 5f	² F ⁰	38	1s ² 9f	² F ⁰
14	1s ² 5g	² G	39	1s ² 9g	² G
15	1s ² 6s	² S	40	1s ² 9h	² H ⁰
16	1s ² 6p	² P ⁰	41	1s ² 9i	² I
17	1s ² 6d	² D	42	1s ² 10p	² P ⁰
18	1s ² 6f	² F ⁰	43	1s ² 10d	² D
19	1s ² 6g	² G	44	1s ² 11p	² P ⁰
20	1s ² 6h	² H ⁰	45	1s ² 11d	² D
21	1s ² 7s	² S	46	1s ² 12p	² P ⁰
22	1s ² 7p	² P ⁰	47	1s ² 12d	² D
23	1s ² 7d	² D	48	1s ² 13p	² P ⁰
24	1s ² 7f	² F ⁰	49	1s ² 13d	² D
25	1s ² 7g	² G	50	1s ² 14d	² D

3.B Appendix B: Dependence on stellar parameters

This appendix displays the sensitivity of synthetic carbon spectra from dwarf and supergiant models at 30 and 40 kK, with respect to variations in T_{eff} , $\log g$, and \dot{M} . Figs. 3.16 to 3.19 have the same layout as Fig. 3.6, and refer to Sect. 3.3.3, where also the corresponding discussion has been provided. For completeness, Fig. 3.20 displays the sensitivity with respect to variations in T_{eff} and $\log g$ for our complete set of lines, with the same color coding as in Fig. 3.6.

The general behavior is similar to the lines already discussed in this Appendix and Sect. 3.3.3, but not identical, due to different formation regions and processes. (We note that C II 5648 is absent for this model.) The major exception is C II 6461, where the emission displayed by the central model is reduced when any kind of variation in T_{eff} or $\log g$ is applied. However, the predicted line is so weak that an actual understanding of the actual origin of this behavior is difficult to obtain.

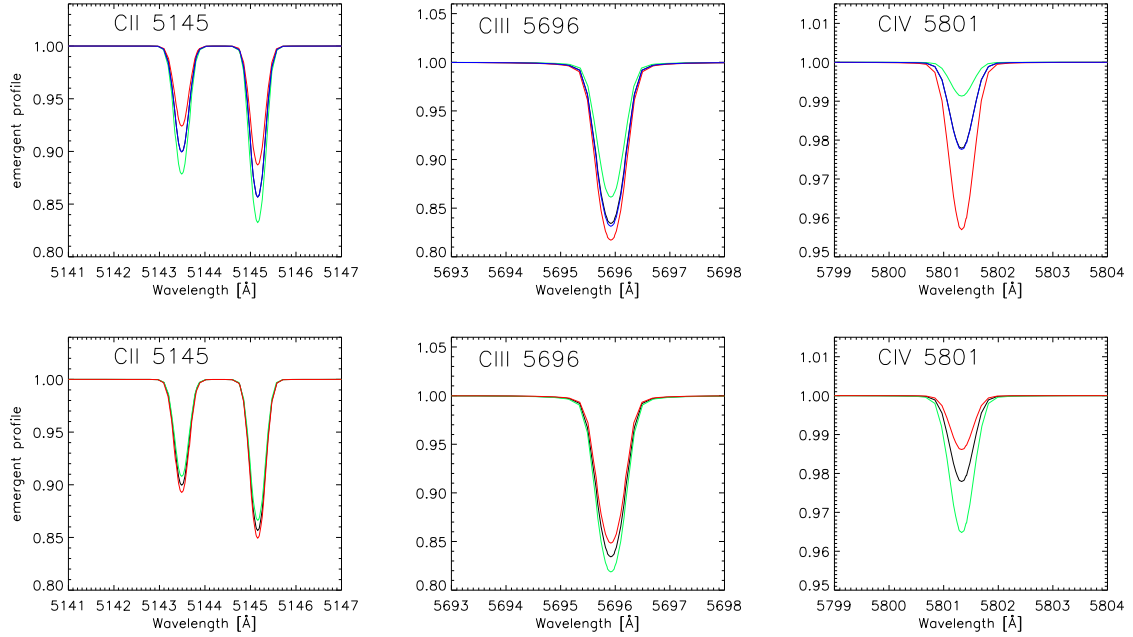


Figure 3.16: C II 5145, C III 5696, and C IV 5801 line profiles for model D30 (black lines, see Table 3.2) and similar models with relatively small changes in effective temperature (T_{eff}) and gravity ($\log g$). In the upper panels, the red lines correspond to a D30 model with T_{eff} increased by 1000 K, the green lines to a model with T_{eff} decreased by the same value, while the blue lines display the reaction to a decrease of \dot{M} by a factor of three. In the lower panels, the red and green lines correspond to a D30 model with $\log g$ increased and decreased by 0.15 dex, respectively

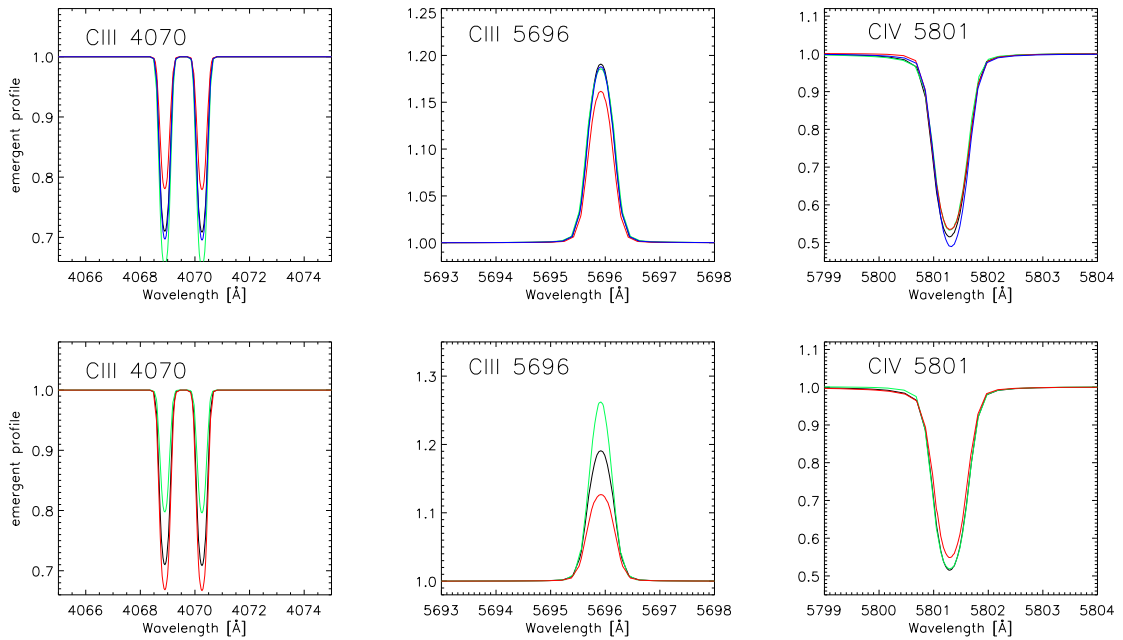


Figure 3.17: As Fig. 3.6, but for model D40, and C III 4068-70, instead of C II 5145.

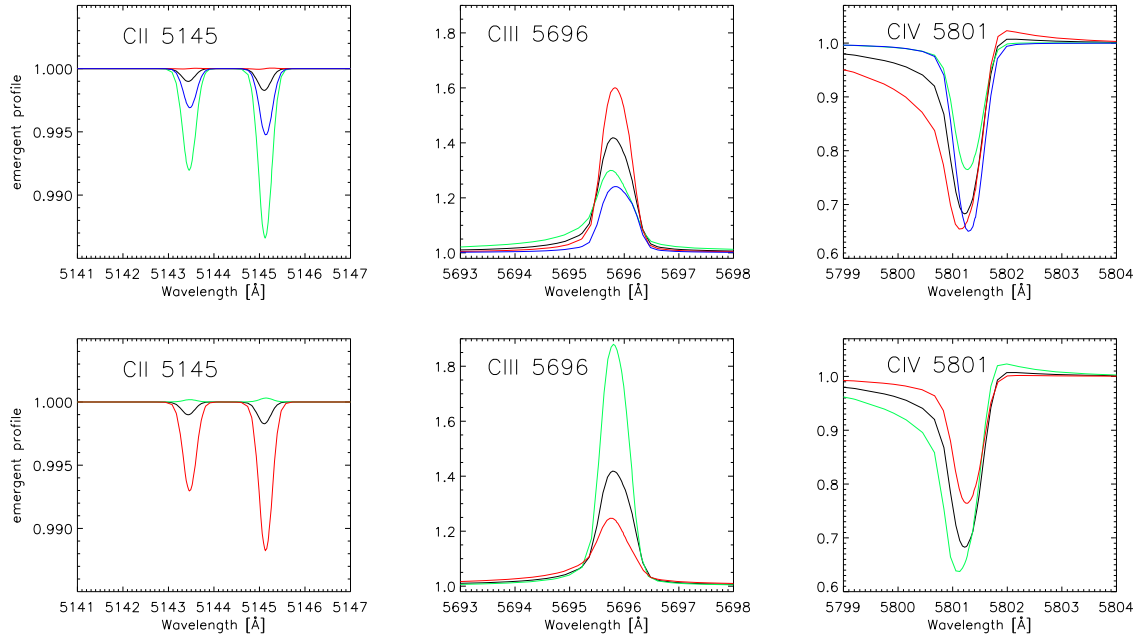


Figure 3.18: As Fig. 3.16, but for model S30, and $\Delta \log g = 0.1$.

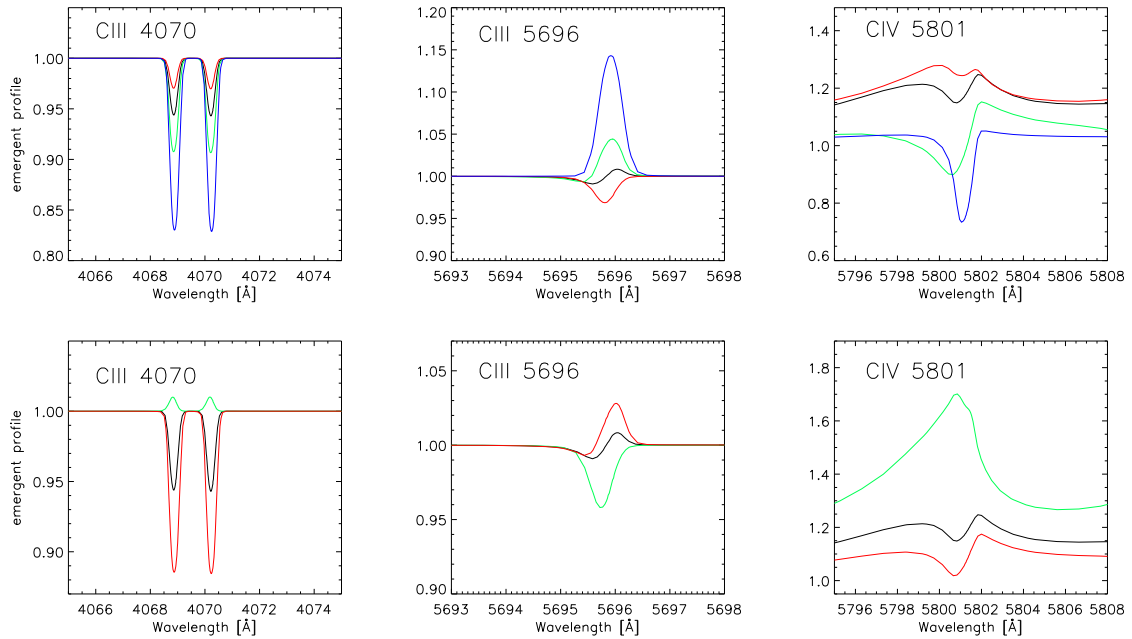


Figure 3.19: As Fig. 3.17, but for model S40.

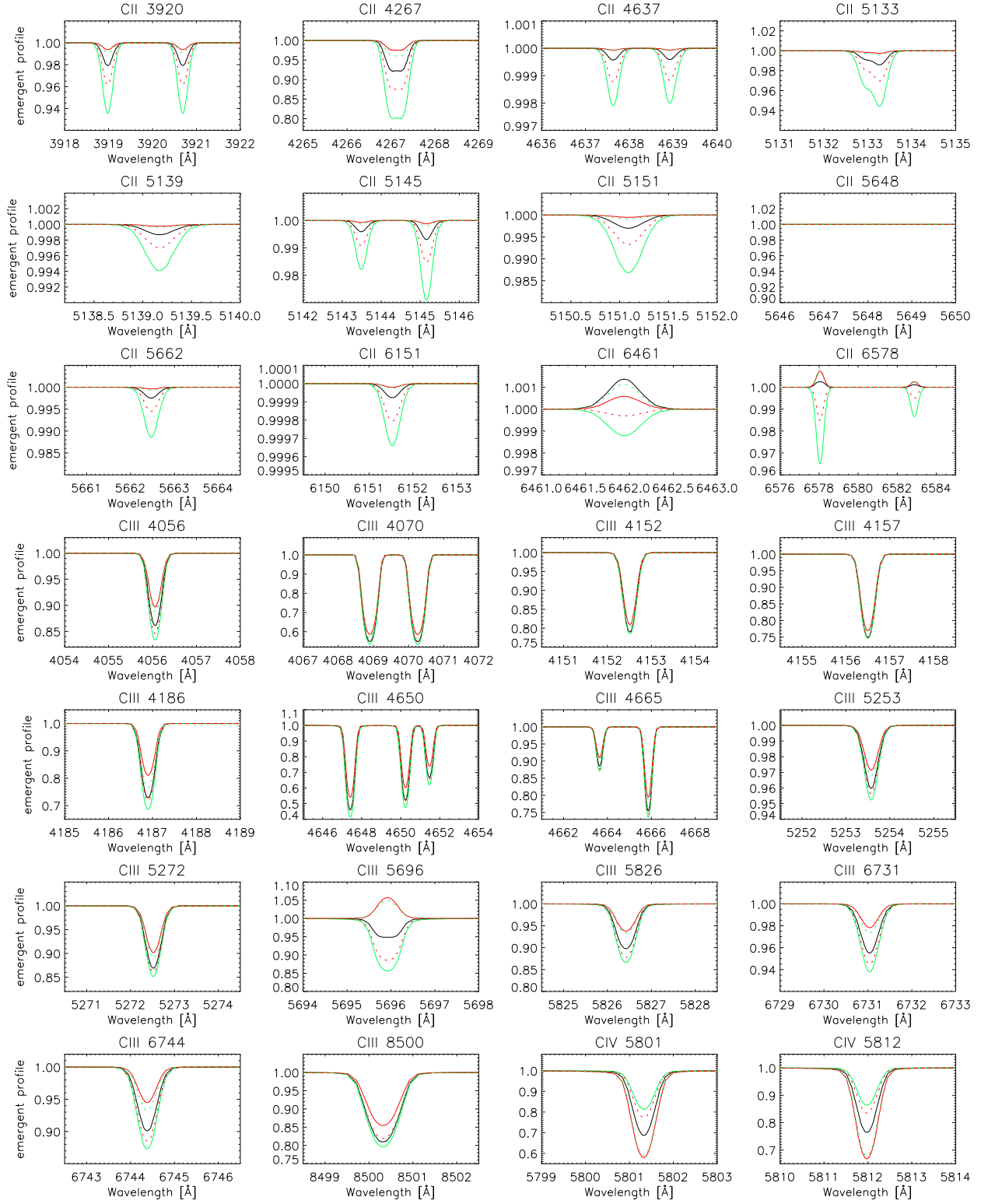


Figure 3.20: Carbon line profiles for model D35 (black), and dependence on stellar parameters, for our complete set of lines. The red and green solid line profiles correspond to an increase and decrease by 1500 K in T_{eff} , respectively, whereas the red and green dashed profiles correspond to a variation of +0.2 dex and -0.2 dex in $\log g$.

Chapter 4

Surface abundances of CNO in Galactic O-stars: A pilot study with FASTWIND

This chapter is a copy of Carneiro et al. (2018b), recommended for publication in *Astronomy & Astrophysics* by the referee.

Abstract Rotational mixing is known to significantly affect the evolution of massive stars; however, we still lack a consensus regarding the various possible modelling approaches and mixing recipes describing this process. The empirical investigation of surface abundances of carbon, nitrogen, and oxygen (CNO) in large samples of O- and B-type stars will be essential for providing meaningful observational constraints on the different available stellar evolution models.

Setting up and testing adequate tools to perform CNO surface abundance determinations for large samples of O-type stars, by means of the fast performance, NLTE, unified model atmosphere code FASTWIND.

We have developed a set of semi-automatic tools for measuring and analyzing the observed equivalent widths of strategic optical C, N, and O lines from different ions. Our analysis strategy is based on a χ^2 minimization of weighted differences between observed and synthetic equivalent widths, the latter computed from tailored model grids. We pay special attention to the (significant) errors introduced by typical uncertainties in stellar parameters. In this pilot study, we describe these tools, and test their performance and reliability using a set of high quality spectra of a sample of 18 presumably single Galactic O-type stars with low projected rotational velocities ($v \sin i \lesssim 100 \text{ km s}^{-1}$), and previously determined stellar parameters. In particular, we compare the outcome of our analysis with results from existing studies and theoretical stellar evolution models.

Most of our results for carbon and nitrogen agree, within the errors, with both theoretical expectations and literature values. While many cooler dwarfs display C and N abundances close to solar, some of the early- and mid-O dwarfs – and most supergiants – show significant enrichment in N and depletion in C. Our results for oxygen in late-O dwarfs are, however, unexpectedly low, possibly indicating deficiencies in the adopted oxygen model atom. For all other objects, no systematic problems

in their oxygen content have been identified. Specific stars in our sample show peculiarities in their abundances, and we suggest hypotheses regarding their origin.

Our method is (almost) ready to be applied to large samples of late and mid O-type stars – although the oxygen model atom needs to be improved and carefully tested first. For early O-type stars (O4 and hotter), a simultaneous UV analysis seems to be inevitable, due to the scarcity and weakness of optical C and O lines. This will necessarily imply a more complex modeling, additionally accounting for the effects of X-rays from wind-embedded shocks and wind inhomogeneities.

4.1 Introduction

Nucleosynthesis is the primary agent that controls stellar evolution. Although the nuclear processes are well understood (also quantitatively), the transport and mixing (if there is any) of nuclear processed material into the envelope and stellar surface is still disputed. If present, such mixing is significant not only because it alters the surface abundances, but also, e.g., since it might change the mean molecular weight and opacity, giving rise to larger convective cores and higher luminosities (see Maeder 2009).

In massive stars, this transport can be particularly strong, mostly due to rotational mixing (e.g., Langer et al. 1997, Meynet & Maeder 2000, Heger et al. 2000, Paxton et al. 2013): rotation may trigger internal instabilities, leading to flows that transport material from the core to the stellar surface and vice versa. Indeed, many massive stars are rapidly rotating (e.g., Howarth et al. 1997, Dufton et al. 2013, Ramírez-Agudelo et al. 2013, Simón-Díaz & Herrero 2014 and references therein), resulting in longer main-sequence lifetimes (e.g., Brott et al. 2011, Ekström et al. 2012, Köhler et al. 2015) and different evolutionary tracks in the Hertzsprung-Russell diagram. In parallel, rotation may also affect mass loss and consequently angular momentum loss (see Maeder 2009 and Langer 2012).

State-of-the-art evolutionary codes do account for such rotational mixing, but the various mixing “recipes” are different from code to code, as is the treatment of angular momentum transport which governs the internal angular velocity profile. This induces significant differences in the predicted evolution, not only with respect to surface abundances, but also with respect to the evolution of luminosities, mass-loss, rotational speed, and, most importantly, the dependence of the end products (supernova types, GRBs, neutron stars, black holes) on the initial masses.

Massive star nucleosynthesis shows that during the main sequence the nitrogen content increases at the expense of carbon and – later on – oxygen, through the CNO cycle, and rotation-induced mixing may display the altered composition at the surface. Helium may also serve as a tracer of rotationally induced mixing. However, as the second-most abundant element, its surface enrichment is more difficult to identify than the N-enrichment and C/O-depletion.

Adding to the complexity, binary interactions can also modify the surface abundances (e.g., Langer et al. 2008). For example, in short-period binaries, the more massive component fills its Roche lobe first, dumping processed material onto the surface of the secondary component (de Mink et al. 2013). The peculiar surface abundances of specific objects (e.g., the so-called ON-stars) might be explained by such binary interactions (see Bolton & Rogers 1978, Boyajian et al. 2005, Martins et al. 2015b).

Observational studies of surface abundances can provide us with important clues on the valid-

ity of the various hypotheses and modeling approaches. The tool for such studies is quantitative spectroscopy, i.e., the comparison of observed and synthetic spectra. This is a complex task for early-type stars, due to their strong radiation fields which lead to severe non-LTE effects and cause radiation-driven winds. The numerical computation of their spectra becomes even more difficult and ambiguous when considering wind inhomogeneities and emission from wind-embedded shocks, due to the numerous parameters and assumptions which enter the corresponding modeling. Both processes have a particularly strong effect in the UV (e.g., Pauldrach et al. 1994, Crowther et al. 2002, Hamann & Oskinova 2012) due to optically thick clumping¹ (Oskinova et al. 2007, Sundqvist et al. 2010, Šurlan et al. 2013), in parallel with porosity in velocity space (Owocki 2008, Sundqvist et al. 2014) and the circumstance that X-ray emission typically starts around $1.4 R_*$ (e.g., Hillier et al. 1993, Cohen et al. 2014b), thus mostly affecting the conditions in the outer wind where the UV P Cygni lines still form.

The optical CNO lines, on the other hand, are comparatively weak, and thus mostly form in photospheric regions, remaining uncontaminated by such ambiguities. While many analyses of CNO abundances of B-type stars (negligible winds, only weak departures from LTE) can be found in the literature, the situation for O-type stars is different, particularly regarding their optical spectra.

For these stars, the complete set of CNO abundances has been mostly derived by means of the model atmosphere/spectrum synthesis code CMFGEN (Hillier & Miller 1998), e.g., by Bouret et al. (2012, 2013) for Galactic and SMC O-stars (optical and UV, small samples), and by Martins et al. (2015a,b, 2016, 2017), for Galactic O-stars (optical, small and intermediate size samples, up to ~ 70 objects).

While these authors argue that, on the whole, the observed surface abundances are consistent with the theoretical predictions (particularly those from Ekström et al. 2012), the size of the analyzed samples is still too small to allow for final conclusions (see, e.g., Markova et al. 2018 for problems regarding nitrogen alone), given the large variety of O-type stars and the multitude of parameters (initial rotational speed, mass-loss rate, environment) which affect the actual and predicted values.

To get more insight into these problems (highlighted by Hunter et al. 2008, who found, already in early B-type stars, a significant fraction of slowly-rotating, but strongly nitrogen-enriched objects; but see also Maeder et al. 2014), the CNO analysis of larger O-star samples is urgently required. From an observational point of view, high quality data from such larger samples already exist, for example the VLT-FLAMES survey of massive stars (Milky Way, LMC, SMC, summarized by Evans et al. 2008), the VLT-FLAMES Tarantula survey (LMC, Evans et al. 2011), the IACOB survey (Milky Way, Simón-Díaz et al. 2011b, 2014, 2015), and the OWN survey (Milky Way, Barbá et al. 2010, 2017).

However, the analysis of such large samples also requires comparatively fast codes and (at least semi-) automatic analysis tools. For this end, spectrum synthesis using the FASTWIND code (Puls et al. 2005, Rivero González et al. 2012a) has proven advantageous, either in combination with a genetic algorithm (Mokiem et al. 2005), or for calculating huge model grids which are subsequently compared with observations using minimization methods (e.g., Lefever 2007, Simón-Díaz et al. 2011b).

Thus far, FASTWIND has only been used to infer stellar and wind-parameters, and for pure nitro-

¹ Sometimes referred to as “macro-clumping”.

gen analyses. Examples for the latter are Rivero González et al. (2012a,b), Grin et al. (2017), and Markova et al. (2018). Carbon and oxygen have not been studied with FASTWIND in the O-star regime, since corresponding model atoms were not available. Meanwhile, Carneiro et al. (2018) have developed and tested a suitable carbon model atom, and we are now in a better position to tackle the analysis of CNO elements.

The present work is intended to serve as a pilot study for future investigations concentrating on such analyses for large, statistically significant samples, and tries to show what can be done with FASTWIND in this respect. Although a carefully tested oxygen model atom suitable for hot star conditions is still missing (to be developed soon), in order to prepare for these future investigations we have here opted for a compromise, namely to use the oxygen model atom and data set from the WM-basic database (Pauldrach et al. 2001), which has been shown to deliver sensible results at least in the UV (e.g., Pauldrach et al. 1994, 2001).

To enable a clear-cut test, we have concentrated in this work on favorable conditions, i.e., we have analyzed high-quality, optical CNO-spectra from a small sample of presumably single Galactic O-stars with different spectral types, and low $v \sin i$. In this way, we avoid, as far as possible, the contamination by blends, and enable a comparison with *single-star* evolutionary predictions. Our sample, even being small, allows us then to test the reliability of our method and to automatize some of the steps for an eventual future work on much bigger datasets, which will very likely suffer from those problems avoided by our selection criteria in the present work.

This paper is organized as follows. Sect. 4.2 introduces our observational dataset and the target selection. The basic strategy of our abundance analysis is outlined in Sect. 4.3, including a list of the diagnostic lines used throughout this work. In Sect. 4.4, we provide a detailed description of our analysis method, which bases on a χ^2 minimization between observed and synthetic equivalent widths. Sect. 4.5 discusses our results, particularly in view of some basic theoretical expectations, and compares with results from previous studies on overlapping targets. In Sect. 4.6, we perform a more detailed comparison with specific evolutionary calculations, also regarding the expected evolution of the individual abundances. In Sect. 4.7, we conclude by providing an overview of the present work as the basis for future analysis of statistically significant samples.

4.2 Observations and target selection

Our spectroscopic sub-sample has been drawn from the much larger sample of Galactic O-stars analyzed by Holgado et al. (2018), which is based on optical, high resolution spectra collected within the IACOB (Simón-Díaz et al. 2011b, 2014, 2015) and OWN (Barbá et al. 2010, 2017) surveys. The objects of the original sample are included in the grid of O-type standards, as defined in Maíz Apellániz et al. (2015), covering 128 Galactic stars in the spectral range from O2 to O9.7 (all luminosity classes, and located both in the Northern and in the Southern hemisphere).

All the spectroscopic observations considered by Holgado et al. (2018) were obtained with any of the following high-performance spectrographs: HERMES (with a typical resolving power of $R = 85,000$ and wavelength coverage of 3770–9000 Å, see Raskin et al. 2004) at the MERCATOR 1.2 m telescope, FEROS ($R = 48,000$ and range 3530–9210 Å, see Kaufer et al. 1997) at the ESO 2.2 m

telescope, and FIES ($R = 46,000$ and range $3750\text{--}7250 \text{ \AA}$, see Telting et al. 2014) at the NOT 2.56 m telescope. As stated by Holgado et al. (2018), most of the O-type stars in the IACOB and OWN spectroscopic databases include more than two spectra, obtained at different epochs. All available spectra were used by Holgado et al. to check for spectroscopic variability, though they considered only the spectrum with the highest signal-to-noise ratio to perform the quantitative spectroscopic analysis presented there. We note that the same “best” spectra have been also used in the current work.

In the spirit outlined in Sect. 4.1, we selected ten dwarfs and ten more evolved objects (6 supergiants and 4 bright giants, summarized as “supergiants” in the following) that match the following criteria: (i) the complete O-star temperature range should be covered; (ii) the maximum projected rotational velocity ($v \sin i$) was restricted to 120 km s^{-1} , to allow for a clear signal and to avoid (as far as possible) blending; (iii) the stars are neither classified as line-profile variable, nor as a spectroscopic binary; (iv) all H/He lines could be fitted in parallel by Holgado et al., without major problems (their quality flags Q1 or at least Q2).

After having defined our core sample in this way, during the equivalent width (W_{eq}) measurements it turned out that two of the originally chosen supergiants had to be discarded: HD 191781 (ON9.7Iab), due to its low-quality spectrum (SNR of 28 at 4500 \AA) which hindered the identification of most metal lines, and HD 190429 (O4 If), because of its high temperature together with a rather large line-broadening ($v \sin i \approx 90 \text{ km s}^{-1}$, $v_{\text{mac}} \approx 113 \text{ km s}^{-1}$), giving rise to absent or extremely weak lines from low and intermediate ions.

For the rest of our sample, we expected and indeed found that (in almost all cases) at least two different ionization stages from each element (carbon, nitrogen and oxygen) are visible. Table 4.1 provides the name, spectral type, and stellar, wind, and line-broadening parameters for each object, where part of the latter have been (re-)evaluated by us in the course of our analysis.

Obviously, our final sample is certainly statistically incomplete, and, most important, heavily biased due to our selection criteria regarding $v \sin i$.

4.3 Abundance analysis: strategy

4.3.1 Basic considerations

A spectroscopic determination of abundances can be performed by analyzing either line profiles or the corresponding equivalent widths (W_{eq}). In this work, we used the latter method, since W_{eq} ’s are insensitive (or only weakly sensitive) to broadening by rotation, $v \sin i$, and macroturbulence, v_{mac} (when adopting standard assumptions, such as that broadening preserves the equivalent width). On the other hand, both processes have a major impact on the line shape, particularly in the core. Thus, a meaningful comparison of line-profiles to infer abundances can be only performed if $v \sin i$ and v_{mac} (together with the radial velocity, v_{rad}) have been precisely determined (even if they are not large). Though in high S/N spectra $v \sin i$ can be measured with high precision, by using a Fourier-transform method (e.g., Simón-Díaz & Herrero 2007, 2014), the determination of v_{mac} is more difficult, and is usually done in parallel with the minimization of the differences between observed and theoretical profiles. For the analysis of abundances, this might lead to certain ambiguities, and we have thus opted for the

Table 4.1: Stellar, wind, and line-broadening parameters for the 18 sample stars. Stellar and wind parameters (the latter condensed in the wind-strength parameter, $\log Q$) together with $v \sin i$ as derived by Holgado et al. (2018). The helium abundance is given as the number fraction $Y_{\text{He}} = N_{\text{He}}/N_{\text{H}}$. Macroturbulence (v_{mac}) values as obtained by Holgado et al. (first entry), and during the present work (second entry). We note that stars #11 and #20 from our original sample were discarded during the course of our analysis, due to reasons described in the text.

#	Name	Sp. class.	T_{eff} (kK)	$\log g$ (dex)	Y_{He}	$\log Q$ (dex)	$v \sin i$ (km s^{-1})	v_{mac} (km s^{-1})
Dwarfs								
1	HD36512	O9.7 V	33.0	4.02	0.10	-13.4	13	33 — 25
2	HD34078	O9.5 V	34.5	4.07	0.12	-13.0	13	32 — 20
3	HD46202	O9.2 V	34.9	4.13	0.10	-13.1	11	38 — 20
4	HD214680	O9 V	35.2	3.89	0.10	-13.5	14	43 — 30
5	HD97848	O8 V	35.6	3.67	0.10	-13.3	41	77 — 65
6	HD46966	O8.5 IV	35.9	3.84	0.10	-13.0	40	66 — 66
7	HD93222	O7 V((f))	36.8	3.63	0.11	-12.9	50	90 — 90
8	HD12993	O6.5 V((f)) Nstr	39.2	3.89	0.16	-13.2	70	79 — 60
9	HD303311	O6 V((f))z	40.1	3.91	0.11	-13.0	47	61 — 50
10	HD96715	O4 V((f))z	45.2	3.91	0.13	-12.8	59	86 — 86
Supergiants and Bright Giants								
12	HD195592	O9.7 Ia	28.0	2.91	0.12	-12.1	38	100 — 100
13	HD152249	OC9 Iab	31.1	3.20	0.10	-12.5	71	70 — 70
14	HD71304	O8.7 II	32.0	3.30	0.11	-12.7	52	100 — 100
15	HD207198	O8.5 II(f)	33.1	3.31	0.15	-12.7	52	97 — 97
16	HD225160	O8 Iabf	33.2	3.34	0.13	-12.2	77	103 — 90
17	HD171589	O7.5 II(f)	36.5	3.65	0.15	-12.6	100	86 — 86
18	HD151515	O7 II(f)	36.0	3.55	0.13	-12.6	67	98 — 98
19	HD169582	O6 Iaf	38.9	3.70	0.23	-12.3	66	97 — 97

W_{eq} method, since equivalent widths depend almost exclusively on abundance and microturbulence. We note that also Grin et al. (2017) used an W_{eq} method to analyze the nitrogen content of O-type giants and supergiants observed in the VLT-FLAMES Tarantula survey.

The synthetic spectra and equivalent widths used in this work have been calculated with the latest update (v10.4.5) of the NLTE model atmosphere/spectrum synthesis code FASTWIND (Puls et al. 2005, Rivero González et al. 2012a), which includes (though it is not used here, see below) the most recent implementation of X-ray emission from wind-embedded shocks and related physics (Carneiro et al. 2016).

Since in this work we focus on the analysis of photospheric CNO lines, wind clumping should play a minor role, if at all. Thus, we have only considered homogeneous wind models. Though clumping is not considered here, the unclumped models with mass-loss rate \dot{M}_{uc} would *roughly* correspond to (micro-)clumped models with a lower mass-loss rate of

$$\dot{M}_{\text{c}} = \dot{M}_{\text{uc}} / \sqrt{f_{\text{cl}}}, \quad (4.1)$$

where $f_{\text{cl}} \geq 1$ is the considered clumping factor.

Although we used the most recent version of FASTWIND in this work, its X-ray module (Carneiro et al. 2016) required to account for the X-ray emission from wind-embedded shocks was not used in our calculations. In the latter publication, the authors examined in detail the effects of X-ray emission; with respect to CNO, the ionization fractions of C v, N v, O v, and O vi are the most affected when including X-rays (Carneiro et al. 2016, their Fig. 8). However, within our present sample, only for one star (the hottest dwarf, HD 96715 [O4 V((f)z)], the results derived in the following depend on one of these ions (N v). Furthermore, the corresponding lines are quite weak and still form in the photosphere, so that they should remain uncontaminated (the typical onset of X-rays is around $1.4 R_{\odot}$, e.g., Hillier et al. 1993, Cohen et al. 2014b). One may argue about the impact on N iv, but as also seen in our previous work, this impact becomes visible only for objects hotter than ~ 45 kK, which again does not affect our current sample. Meanwhile, our group has tested different descriptions of the shock structure responsible for the high energy emission (in particular, Feldmeier et al. 1997b vs. Owocki et al. 2013), and in our planned work on larger samples including many hotter objects we will certainly check and account for corresponding effects regarding a CNO surface abundance analysis. To this end, however, we will also need to analyze the UV spectrum (if available) in parallel, to constrain the multitude of X-ray parameters required as input (X-ray luminosity, filling factors, onset and radial run of shock temperatures).

4.3.2 Stellar parameters and model grids

At first, we convinced ourselves that the stellar and wind parameters already derived by Holgado et al. (2018) from fits to the hydrogen and helium line profiles² could be reproduced by the “Munich-version” of the FASTWIND code.

Reliable photospheric parameters are of major importance, since, as discussed in our previous work on optical carbon diagnostics (Carneiro et al. 2018), most diagnostic metal lines are weak and

² By means of pre-calculated grids of synthetic spectra and the GBAT-tool (Simón-Díaz et al. 2011b).

sensitive to relatively small variations of stellar parameters: a change of ± 1000 to 1500 K in effective temperature, or ± 0.2 dex in $\log g$ can result in considerable changes of line strength.

Moreover, some of the lines are also sensitive to mass-loss rate. For carbon lines from supergiants and hot dwarfs (dense winds), for example, a decrease in \dot{M} by a factor of three produces an effect stronger than a decrease of 1500 K in T_{eff} or an increase of 0.2 dex in $\log g$. Thus, a quite precise determination of \dot{M} (e.g., by reproducing H α and He II 4686) is required before an abundance analysis of other elements can be tackled.

In their study, Holgado et al. quote only the wind-strength parameter, $Q = \dot{M}/(R_*v_\infty)^{3/2}$ (e.g., Puls et al. 2005) resulting from their analysis, but do not provide individual values for the mass-loss rate \dot{M} , stellar radius R_* , and terminal velocity v_∞ required for FASTWIND input. We obtained these quantities using their Q -values, an estimate of v_∞ (via escape velocity v_{esc} , using $\log g$, R_* , and T_{eff} , see Kudritzki & Puls 2000), and an adopted stellar radius following the Martins et al. (2005) calibration between spectral type and radius.

For all sample stars, we found no problems in reproducing the final synthetic spectra displayed by Holgado et al. when using their stellar and wind parameters, and thus we used these parameters as the center points in our own model grid constructed to infer the CNO abundances.

We note that during these first comparisons of H/He spectra, we adopted the values for $v \sin i$, v_{mac} (first entries in the corresponding column of Table 4.1, but see below), and v_{rad} as provided by Holgado et al. Moreover, at this point, all profiles were calculated using a single value for the microturbulence, $v_{\text{mic}} = 10 \text{ km s}^{-1}$.

With the stellar and wind-parameters defined, we were able to set up an intermediate-size model grid accounting for a variety of CNO compositions, where the individual abundances were centered at the solar values from Asplund et al. (2009) (Table 4.4). Since the interference of the CNO ions in the model atmospheres is rather weak (as long as their abundances remain well below the He abundance, and except for specific effects between N III and O III resonance lines as discussed by Rivero González et al. (2011), which are anyhow neglected in the current FASTWIND version), we could set up a grid where more than one abundance is changed per grid point. Basically, instead of using three models with identical parameters where only the abundance of either C, N, or O has been changed, we can use one model where C, N, and O abundances have been changed simultaneously. We convinced ourselves that this approach is valid, by comparing with models where the abundances had been changed individually.

Initially, we considered an interval of ± 0.5 dex around the central value (solar) for the three elements, with grid-points separated by 0.1 dex. Later on, we had to increase this interval, when required by the analysis.

Almost equally important, one has to consider that the value adopted for v_{mic} has a decisive impact on the derived abundance. Since this value can be only vaguely derived from H and He line profiles (see, e.g., Holgado et al. 2018), and anyhow might be different for different atomic species (variation as a function of formation depth), one has to determine this parameter in parallel with the abundance. This can be done either by semi-automatic methods, requiring the search to find the same abundance from different lines of different ions for the same v_{mic} (e.g., Urbaneja 2004, Markova & Puls 2008), or, as done in this work, by including v_{mic} as a fit-parameter in the analysis. In particular, each synthetic line was calculated for a variety of v_{mic} -values, in our case 5, 7.5, 10, 15, and 20 km s^{-1} . Fortunately,

Table 4.2: Diagnostic carbon, nitrogen, and oxygen lines in the optical spectrum, used to derive corresponding abundances of O-type stars. Rest wavelengths (in air) taken from NIST.

Ion	Wavelength (Å)				
C II	3918.98	3920.69	4267.00	6578.05	6582.88
C III	4186.90	4647.42	4650.25	4651.47	5695.92
C IV	5801.33	5811.98			
N II	3995.85	4447.03	4601.47	4607.16	4621.39
N III	4097.35	4379.11	4510.88	4514.85	4518.18
	4634.13	4640.64	4641.85		
N IV	4057.76	6380.77			
N V	4603.74	4619.97			
O II	3954.36	4075.86	4414.90	4416.97	4661.63
O III	3961.59	4081.02	5268.30	5508.24	5592.37

the occupation numbers for optical lines do not depend significantly on the value of ν_{mic} used in the model atmosphere (in contrast to the corresponding quantities for specific IR transitions such as Br_α , e.g., Najarro et al. 2011), and thus we are able to simulate the variation of the line-profiles / equivalent widths as a function of ν_{mic} by calculating the final formal integrals for the different ν_{mic} values alone.

To obtain sensible errors on the derived abundances, one has also to account for the inaccuracy of stellar parameters. Typical uncertainties on the order of 1000 K in T_{eff} and 0.1 dex in $\log g$ (for O-type stars) affect the photospheric H and He profiles only marginally, at least when T_{eff} and $\log g$ are changed in the same direction, since lower temperatures are then compensated by a lower density – lower $\log g$ –, and vice versa. On the other hand, such changes might affect the derived abundances significantly, as pointed out above. To include these effects into our error-analysis, we calculated two additional grids with similar abundances and the same ν_{mic} values as in our initial grid, but with either T_{eff} and $\log g$ decreased by 1000 K and 0.1 dex, respectively, or with T_{eff} and $\log g$ values increased by the same amount. The resulting equivalent widths were then compared with the observed ones in the same way as done for the original models with parameters from Holgado et al., and the differences in the derived abundances accounted for in the total error budget (see below).

4.3.3 Diagnostic lines in the optical

When performing an abundance analysis, the selection of the most sensitive lines is of prime importance, as well as the consideration of at least two ionization stages for each element (if possible). The reproduction of lines from different ions of the same element verifies a proper ionization balance, which depends on the validity of the atmospheric parameters (and the quality of the code and the atomic data). For hotter objects, the scarcity of metal lines sometimes precludes the presence of lines

from different ions, and larger rotational rates give rise to very shallow lines, which often vanish in the noise. If more than one element is analyzed though, the chances are higher that at least one of them displays lines from two ions, allowing to check the corresponding ionization balance and thus the validity of the stellar parameters (or the code/data).

Carbon. In a recent study, Carneiro et al. (2018) enabled the carbon spectroscopy of hot stars by means of FASTWIND, in parallel with testing the effects of various physical processes on the outcome. To this end, they also developed a new carbon model atom, and implemented it into the FASTWIND code. Based on this knowledge and the experience acquired from analyzing the carbon abundance of a relatively small sample of O-stars (six objects)³, we selected a sub-sample of meaningful lines from C II to C IV that are visible at different temperatures and sensitive to abundance variations. These lines are listed in Table 4.2, and have been used throughout this work. We note that this list includes the triplet C III 4647/4650/4651 and C III 5696, which both have a quite complex formation mechanism (due to a strong coupling with EUV lines), as detailed by Martins & Hillier (2012) (and revisited by Carneiro et al. 2018).

Nitrogen. Nitrogen is visible in a wide range of ionization stages (N II to N V) in the optical spectra of O/B-stars, and important lines (in particular, N III 4634/4640/4641 and N IV 4057) have a rather complicated formation mechanism that has been explored by Rivero González et al. (2012a,b), extending the work by Mihalas & Hummer (1973). Rivero González et al. presented a detailed nitrogen model atom, which has been also used in our calculations. The set of lines used in our analysis (Table 4.2) includes all the typical transitions that have been also analyzed in previous studies. In particular, Grin et al. (2017) tested the sensitivity of the corresponding equivalent widths to justify their specific choice of lines, and the lines used in the present work coincide with their primary diagnostic indicators.

Oxygen. In comparison to carbon and nitrogen, oxygen presents more difficulties, since only O II and O III have optical lines that are visible in O/B-stars (some hotter O-stars might have few O IV lines that are marginally visible; whether these can be used diagnostically needs to be checked, though). As O II quickly vanishes with increasing temperatures, and as many O III lines are not visible already at intermediate values of $v \sin i$ ($> 90 \text{ km s}^{-1}$), there are cases where the oxygen abundance needs to be obtained from only one or two lines. Besides these complications, oxygen is the only element for which we did not develop and test our “own” model atom. Instead (see also Sect. 4.1), we used the model atom from the WM-basic database (Pauldrach et al. 2001), and note that those model atoms describe radiative bound-free transitions “only” by means of the Seaton-parameterization (Seaton 1958), while resonances leading to dielectronic recombination are treated as line transitions to the continuum (e.g., Nussbaumer & Storey 1983). Moreover, these models also lack a detailed description of specific collisional bound-bound transitions. At least for the formal integrals, we used wavelengths and oscillator strengths taken from NIST⁴, and broadening parameters, if available, from VALD⁵.

³ In contrast to the present approach, Carneiro et al. (2018) used a by-eye fitting method.

⁴ <http://www.nist.gov/physlab/data/asd.cfm>, described by Kelleher et al. (1999).

⁵ <http://vald.astro.uu.se/~vald/php/vald.php>, described by Piskunov et al. (1995), Ryabchikova et al. (1997, 2015), and Kupka et al. (1999, 2000).

4.4 Analysis of CNO abundances

As already stated above, the general idea of our analysis is to derive abundances from a comparison of observed and synthetic equivalent widths. In the more recent literature on O-star abundances, Grin et al. (2017) explored such an equivalent-width method for the analysis of nitrogen, and we follow their approach in certain aspects. Since in our case we additionally analyze the carbon and oxygen abundances, and have to deal with substantially more lines, the method needed to be adapted, though. In particular, we aimed to reproduce the W_{eq} of observed lines for the highest number of lines possible.

4.4.1 Equivalent width measurements

In a first step, the equivalent widths of all target lines were measured. We developed an interactive algorithm (in IDL) that determines the equivalent widths from both a Gaussian fit to the observed profiles (both absorption and emission), and from direct integration. In this procedure, the continuum neighboring the considered line is renormalized, then the start and end points of the line wings are defined (by clicking-events), and finally the W_{eq} measured, either from the parameters of the fitted Gaussian, or from the direct integral. We refer to Appendix 4.A for a typical example of such a fit. Generally, the W_{eq} values obtained from the Gaussian fit and from direct integration turned out to be very similar, and for the most part deviate by less than 5%. This convinced us that a Gaussian shape is indeed applicable for the considered lines. Whenever there was a larger discrepancy, we considered the problem in detail, and re-measured the corresponding line.

Mainly due to blending with neighboring lines, it was not always possible to obtain the W_{eq} from direct integration. In these cases, we fitted only the uncontaminated part of the profile (usually the central region) by a corresponding Gaussian, and checked that the wings (not visible in the observations) of the synthetic profile are reasonable (again, see Appendix 4.A for an example). From the parameters of the fitted Gaussian, we then obtained an W_{eq} as if the analyzed line was isolated. For consistency, all finally used values were taken from the Gaussian fits.

The described method works nicely for almost all considered lines (including emission lines), except for N III 4097. This is an important indicator of nitrogen abundance, however difficult to analyze with respect to W_{eq} , due to its location in the wing of H $_{\delta}$, which at 4097 Å is already well below the continuum. In this case, we proceeded as follows. Though somewhat unphysical, here also we derived the observed “equivalent width”, now from renormalizing the H $_{\delta}$ line wing to unity. Unphysical, because the measured quantity does not depend on the nitrogen line alone, but also on the strength and opacity-stratification of H $_{\delta}$. Nevertheless, we then determined the corresponding theoretical W_{eq} analogously by renormalizing the theoretical spectrum (with overlapping H $_{\delta}$ and N III 4097) in the same way, and measuring the “equivalent width” of the renormalized theoretical line by numerical integration. Thus, the measured observed and theoretical quantities are not real equivalent widths, but they contain the same information (unless theory would not reproduce the observed H $_{\delta}$ profile, which was never the case), and can be compared to infer the abundance information.

To determine the error of our W_{eq} measurements, we assumed that the major error source is given by the uncertainty of the continuum and the photon noise, and performed two additional W_{eq} deter-

minations; one were we placed the continuum at the top of the continuum noise, and one were it was placed at the corresponding lower limit.

At the end of our measurements, we had an (automatically created) table for every star, containing the W_{eq} of each renormalized line and the uncertainty of the measurement due to uncertainties in the continuum placement. After analyzing the errors, we found that in more than 70% of all cases they were larger than 10% (typically, on the order of 20 to 30%, depending on the signal-to-noise ratio), and this 10% threshold was used as a lower limit in our follow-up analysis, to avoid unrealistically low errors.

4.4.2 Which lines to use?

Before continuing with the quantitative analysis, we needed to check which lines were reliable (from an observational point of view) for our objective. As unreliable we considered those lines which displayed either an anomalous shape (blends!), or were too weak (rotation, temperature, gravity) to be considered in our χ^2 -minimization (see below).

For each star, such lines were sorted out manually. We also checked the impact of including *all* measurable lines, and usually the differences were small, except for specific targets. We note already here that we never sorted out those lines which might not be fitted by our approach (in particular, the N III triplet lines for cooler objects, see Sect. 4.5.1).

The number of lines finally used for the analysis (see Table 4.3) decreases with T_{eff} of the considered object, and supergiants provide usually less useful lines than dwarfs: as the ionization shifts to higher ionization stages (due to higher T_{eff} and/or lower $\log g$), fewer lines become visible in the optical regime, at least for carbon and oxygen⁶. This becomes particularly critical in our hottest supergiant, HD 169582 (star #19, see Table 4.1), for which only C IV is clearly present among the carbon ions – though some very weak or absent C III lines give additional constraints –, and where only one oxygen line (O III 5592) is easily distinguishable from the continuum. Rotation also plays an important role in determining the number of lines that can be clearly identified and analyzed. As an example, HD 171589 (star #17) has a $v \sin i$ of 100 km s⁻¹, and just a few carbon and oxygen lines are clearly visible. These problems point already here to some limits for a reliable C and O abundance determination: since our hottest supergiant still has a spectral type of O6, it is clear that for earlier spectral types, particularly if they have a significant $v \sin i$, an optical analysis alone might prove to be very difficult or even impossible, and one might have to include the information from the UV, with its own innate set of problems (see Sect. 4.1). We remind the reader that the hottest supergiant in our original sample, HD 190429, was discarded from a final analysis precisely because of too weak lines, due to ionization and rotation.

4.4.3 χ^2 -minimization and error estimates

Having (i) defined the equivalent widths plus errors for all lines and objects, (ii) calculated the three model-grids (at, above, and below the central stellar parameters provided by Holgado et al.), for a

⁶ For nitrogen, there is still a variety of N III, N IV, and N V lines present at early spectral types.

variety of CNO abundances and v_{mic} values, and (iii) sorted out unreliable/weak lines, we are now in a position to derive the abundances for the individual objects.

To this end, we have used a χ^2 -minimization, in the spirit of the IACOB-GBAT tool described by Simón-Díaz et al. (2011b) and in Appendix A of Holgado et al., which we have here applied to the deviation between observed and theoretical⁷ equivalent widths (and not to the deviation between observed and theoretical line profiles as done in those studies).

All the following calculations/visualizations have been performed with a custom IDL script written by the authors. Without going into too much details, for each of our objects K we calculate, for each of the considered elements C, N, and O, the (reduced) χ^2 for all models $M \in M_K$ of our central grid (described by T_{eff} , $\log g$ and $\log Q$ from Holgado et al., and a variety of specific abundances and v_{mic} values),

$$\chi_{\text{red}}^2(K, M) = \frac{1}{N_{\text{lines}}(K)} \sum_{i=1}^{N_{\text{lines}}(K)} \frac{(EW_i^{\text{obs}}(K) - EW_i^{\text{theo}}(K, M))^2}{\sigma_i^2(K)}. \quad (4.2)$$

$N_{\text{lines}}(K)$ is the number of useful lines for the considered object K , and σ_i the uncertainty of the equivalent width for line i . Taken at face value, this expression would be simply the standard definition of a χ_{red}^2 , if σ_i were a (normally distributed) Gaussian measurement error. However, to account for potential and actual problems in the theoretical spectra to reproduce certain lines (particularly N III 4634/4640/4641, C III 4647/4650/4651, and C III 5696, see Sect. 4.3.3), we used a method in analogy to the one described by Holgado et al. (2018, Appendix A). This method accounts for an (implicit) weighting factor for “problematic” lines that cannot be reproduced by the spectrum synthesis within the observed errors (see Eqs. A.2, A.3, and the corresponding text of Holgado et al.). In our case,

$$\sigma_i(K) = \max[\sigma_i^{\text{obs}}(K), \sigma_i^{\text{fit}}(\text{best-fitting model} \in M_K)], \quad (4.3)$$

where $\sigma_i^{\text{obs}}(K)$ is the uncertainty of the measured EW_i^{obs} as derived from our equivalent width measurements (Sect. 4.4.1), and

$$\sigma_i^{\text{fit}}(\text{best-fitting model}) = |EW_i^{\text{obs}} - EW_i^{\text{theo}}(\text{best-fitting model})| \quad (4.4)$$

among all models $M \in M_K$. The “best-fitting model” (i.e., the one with the lowest χ_{red}^2) needs to be determined from an iterative procedure, as described by Holgado et al. In this way, we renormalize the individual contribution of line i (to a value of unity for the best-fitting model, and to a larger or smaller value for the others) if the corresponding equivalent width cannot be reproduced by the best-fitting model within the observational errors. The other way round, this line becomes implicitly weighted by a factor

$$w_i = \min \left[1, \frac{(\sigma_i^{\text{obs}})^2}{(EW_i^{\text{obs}} - EW_i^{\text{theo}}(\text{best-fitting model}))^2} \right], \quad (4.5)$$

⁷ For a detailed investigation of the sensitivity of theoretical W_{eq} values as a function of abundance for nitrogen lines, we refer to Grin et al. (2017), who also discuss certain limitations and the impact of varying v_{mic} .

if χ_{red}^2 is expressed as

$$\chi_{\text{red}}^2 = \frac{1}{N_{\text{lines}}(K)} \sum_{i=1}^{N_{\text{lines}}(K)} w_i \frac{(EW_i^{\text{obs}} - EW_i^{\text{theo}})^2}{(\sigma_i^{\text{obs}})^2}. \quad (4.6)$$

For most lines and stars, our simulations give theoretical W_{eq} 's that are well within the observational errors (with an adopted minimum of 10%), i.e., $w_i = 1$, but in “bad” cases, w_i can reach values of 0.25 or even less⁸.

The above procedure gives a fair “compromise solution”, by limiting, after convergence and for the best-fitting model, the impact of non-reproducible lines to a value of unity in the sum defining χ^2 (Eq. 4.2). If we would not apply such a weighting, the finally derived χ^2 would be dominated by non-reproduced lines, due to their large deviation compared to the observational uncertainty.

Having calculated the reduced χ_{red}^2 for all theoretical models M_K (i.e., for all abundances and v_{mic} -values present in the grid), and independently for C, N, and O, the resulting abundance corresponds to the model with the lowest χ_{red}^2 ,

$$\chi_{\text{red,min}}^2(K) = \min_{M \in M_K} [\chi_{\text{red}}^2(K, M)], \quad (4.7)$$

and the errors on the abundances and microturbulences can be derived from analyzing the projected (roughly corresponding to the marginalized) χ_{red}^2 distribution, with n - σ errors corresponding to the location where

$$\chi_{\text{red}}^2(K, M \in M_K) := \chi_{\text{red,min}}^2(K) + \frac{n^2}{N_{\text{lines}}(K)}. \quad (4.8)$$

We note that the resulting error estimates would be strictly valid only for a large number of terms in the χ^2 sum (for a more rigorous study of the properties of a weighted sum of chi squares, see Feiveson & Delaney 1968). For our purpose, however, the limiting expression is sufficient, given the fact that, as we will discuss below, the impact of uncertain stellar parameters is usually of similar size or even larger.

Our IDL script not only provides the final values plus (asymmetric) errors for abundances and v_{mic} , but also displays the corresponding χ^2 iso-contours in the abundance– v_{mic} plane⁹, together with the projected distributions. Moreover, it tabulates also those lines where the weighting factor is lower than 0.5, to check for problematic lines. Examples for the described analysis are given in Appendix 4.B.

From the above description, it should be clear that we determined the best-fitting v_{mic} -values individually, i.e., per element. Reassuringly, for almost all objects these values are identical or quite similar for C, N, and O, so that in Table 4.3 we quote only one value per object. One might argue that different v_{mic} -values would be “allowed” if v_{mic} varies with height (which is most likely true), but then all those lines from different elements/ions that have the same formation depth should display the same v_{mic} . Since in our approach we investigate different lines from different ions of one atomic

⁸ $w_i = 0.25$ means that the deviation between observation and theory is twice as large as the observational error.

⁹ This allows identifying whether the suggested minimum is located at one of the grid-boundaries; if the abundance was affected, additional grid models have been calculated, and the procedure repeated.

species, such a variation should be present already within one such species. Thus, the derived v_{mic} -values are certainly only representative averages, and their similarity within C, N, and O tells that the overall formation depths are not too different (or that v_{mic} varies only mildly, if at all, with depth).

Subsequent to the χ^2 minimization, we compared the synthetic profiles from the best-fitting model with observations, to check the overall representation of the line profiles, and to check for the problematic lines already identified within the script. This step also allows to constrain the macroturbulence v_{mac} (see corresponding entry in Table 4.1), by varying – if necessary – this quantity until the line-shape is matched. This is possible here, since we have reliable values for $v \sin i$ and v_{rad} (from Holgado et al.) already at our disposal: if the observed and theoretical W_{eq} 's are identical/similar (as true for the majority of analyzed lines in the best-fitting model), the solution is unique, as long as a variation of v_{mac} preserves the equivalent width. Examples for the agreement between observed and theoretical line profiles are provided in Appendix 4.C.

In the last step of our analysis, we investigated the errors due to uncertain stellar parameters (we remind the reader that we have here concentrated on T_{eff} and $\log g$, leaving $\log Q$ at the value suggested by Holgado et al.). In this step, we repeat the above procedure, now using the two additional model grids with either T_{eff} and $\log g$ increased or decreased. For most objects, this indeed results in different abundances (v_{mic} mostly remains at the original value), where typically the derived abundances for the hotter and higher-gravity models turned out to be larger by 0.1 dex, and lower by 0.1 dex for the cooler and lower-gravity models. The corresponding (intrinsic) uncertainties were found to be quite similar to the values derived for the original grid. Thus, we estimate the total error from both sources of error – (1) from the χ^2 distribution, and (2) from uncertain stellar parameters – as the direct sum of both quantities, where for error (1) we used the corresponding $1-\sigma$ error. In rare cases (e.g., star #1), the contribution of error (2) is negligible, and for a few other cases both the hotter and the cooler models produce changes in the same direction, so that the total error becomes strongly asymmetric (e.g., for carbon in star #13). For a comparison of the total errors and error (1) alone, see Fig. 4.1.

4.5 Results

4.5.1 Basic considerations

Our final sample comprises 18 presumably single O-type stars with spectral types in the range O9.7 – O4, including ten dwarfs and eight supergiants/bright giants. Our sample is biased by our selection of objects with comparatively low $v \sin i$, and by most of the stars being in a different stage of evolution (see Sect. 4.6.1): if at all, our sample comprises only one object per spectral type, which might be atypical.

Regarding our equivalent width analysis, microturbulence plays a major role due to its impact on W_{eq} , and consequently on the derived chemical abundance. Each profile/equivalent width was calculated for multiple v_{mic} , and by our χ^2 minimization we searched for the best compromise for all the lines of the different elements. Table 4.3 displays the final estimated v_{mic} value for each star, collecting the information from C, N, and O.

Lines for which it was not possible to measure the observed W_{eq} due to their weakness or absence, and lines with atypical shape due to blends were discarded from our statistical analysis, though in all

Table 4.3: Carbon, nitrogen and oxygen abundances obtained from our analysis, and the best fitting v_{mic} for the CNO lines. For each abundance, the (asymmetric) errors refer to the $1-\sigma$ errors derived from the χ^2_{red} distribution (first number), and to the total error estimated from additionally accounting for typical uncertainties in the stellar parameters (second number, separated by |). The table also provides the number of lines used for the χ^2 analysis of a specific object/atomic species. For comparison, the maximum number of lines (for all ions) considered in our spectrum synthesis is 12 for carbon, 17 for nitrogen, and 10 for oxygen. The oxygen abundances for (at least) the cooler dwarfs (#1 to #5) should be considered with caution, since they might be affected by an imperfect model atom (see text).

#	Name	Sp. class.	v_{mic}	ϵ_{C}	# C	ϵ_{N}	# N	ϵ_{O}	# O
Dwarfs									
1	HD36512	O9.7 V	≤ 5	$8.13^{+0.07 +0.17}_{-0.07 -0.17}$	7	$7.83^{+0.07 +0.07}_{-0.07 -0.07}$	10	$8.39^{+0.06 +0.06}_{-0.08 -0.08}$	10
2	HD34078	O9.5 V	7.5	$8.23^{+0.06 +0.16}_{-0.09 -0.29}$	6	$7.93^{+0.10 +0.10}_{-0.10 -0.30}$	8	$8.39^{+0.20 +0.30}_{-0.20 -0.30}$	7
3	HD46202	O9.2 V	7.5	$8.13^{+0.20 +0.30}_{-0.20 -0.20}$	7	$7.83^{+0.13 +0.13}_{-0.13 -0.23}$	8	$8.29^{+0.20 +0.40}_{-0.20 -0.40}$	8
4	HD214680	O9 V	7.5	$8.33^{+0.10 +0.10}_{-0.10 -0.30}$	8	$8.03^{+0.11 +0.11}_{-0.11 -0.11}$	9	$8.39^{+0.07 +0.17}_{-0.07 -0.27}$	9
5	HD97848	O8 V	7.5	$8.53^{+0.16 +0.26}_{-0.16 -0.26}$	5	$8.13^{+0.10 +0.10}_{-0.20 -0.20}$	7	$8.39^{+0.12 +0.22}_{-0.05 -0.05}$	8
6	HD46966	O8.5 IV	7.5	$8.23^{+0.20 +0.30}_{-0.20 -0.30}$	9	$7.93^{+0.13 +0.23}_{-0.13 -0.13}$	7	$8.59^{+0.07 +0.17}_{-0.10 -0.20}$	9
7	HD93222	O7 V((f))	10	$8.43^{+0.20 +0.30}_{-0.20 -0.30}$	7	$7.73^{+0.12 +0.22}_{-0.12 -0.12}$	8	$8.69^{+0.20 +0.80}_{-0.20 -0.20}$	4
8	HD12993	O6.5 V((f)) Nstr	≥ 20	$7.93^{+0.12 +0.22}_{-0.12 -0.12}$	6	$8.33^{+0.16 +0.26}_{-0.10 -0.10}$	7	$8.19^{+0.20 +0.30}_{-0.06 -0.06}$	3
9	HD303311	O6 V((f))z	≥ 20	$8.23^{+0.05 +0.15}_{-0.11 -0.21}$	6	$7.73^{+0.08 +0.18}_{-0.13 -0.33}$	5	$8.29^{+0.19 +0.39}_{-0.19 -0.19}$	3
10	HD96715	O4 V((f))z	20	$7.73^{+0.10 +0.30}_{-0.10 -0.10}$	3	$8.43^{+0.10 +0.30}_{-0.10 -0.10}$	8	$8.49^{+0.27 +0.37}_{-0.25 -0.45}$	2
Supergiants and Bright Giants									
12	HD195592	O9.7 Ia	15	$8.13^{+0.10 +0.10}_{-0.10 -0.10}$	6	$8.63^{+0.20 +0.40}_{-0.46 -0.66}$	7	$8.39^{+0.30 +0.30}_{-0.18 -0.18}$	5
13	HD152249	OC9 Iab	15	$8.53^{+0.23 +0.43}_{-0.04 -0.04}$	8	$7.63^{+0.15 +0.35}_{-0.09 -0.09}$	8	$8.59^{+0.06 +0.16}_{-0.06 -0.06}$	10
14	HD71304	O8.7 II	15	$8.13^{+0.10 +0.20}_{-0.10 -0.10}$	7	$8.33^{+0.18 +0.38}_{-0.12 -0.12}$	7	$8.39^{+0.10 +0.20}_{-0.12 -0.12}$	6
15	HD207198	O8.5 II(f)	15	$8.43^{+0.22 +0.32}_{-0.11 -0.11}$	5	$8.23^{+0.09 +0.09}_{-0.11 -0.11}$	7	$8.49^{+0.10 +0.20}_{-0.10 -0.20}$	7
16	HD225160	O8 Iabf	10	$8.23^{+0.09 +0.09}_{-0.14 -0.24}$	5	$8.53^{+0.18 +0.28}_{-0.32 -0.42}$	6	$8.59^{+0.19 +0.29}_{-0.29 -0.29}$	3
17	HD171589	O7.5 II(f)	15	$8.43^{+0.08 +0.18}_{-0.19 -0.19}$	7	$8.63^{+0.16 +0.26}_{-0.09 -0.19}$	7	$8.39^{+0.15 +0.15}_{-0.15 -0.25}$	3
18	HD151515	O7 II(f)	≥ 20	$8.43^{+0.28 +0.38}_{-0.23 -0.23}$	4	$8.33^{+0.23 +0.33}_{-0.18 -0.28}$	8	$8.49^{+0.20 +0.20}_{-0.20 -0.20}$	2
19	HD169582	O6 Iaf	≥ 20	$8.33^{+0.06 +0.26}_{-0.25 -0.45}$	5	$8.83^{+0.08 +0.28}_{-0.11 -0.31}$	8	$8.39^{+0.30 +0.50}_{-0.40 -0.60}$	1

cases we tried to keep the highest number of lines possible. Table 4.3 displays the number of lines used to obtain the abundance of each atom in our targets. Considering all measurable lines (partly with different weights determined by our minimization algorithm, see Sect. 4.4.3), we obtained our final estimates for the individual abundances, also displayed in Table 4.3. Hereafter, we use the notation $\epsilon_X = \log_{10}(N_X/N_H) + 12$, where N_X is the particle number density of element X (here: C, N, O), and N_H is the number density of hydrogen.

The corresponding (logarithmic) uncertainties (first error entry) range between 0.1 and 0.2 dex, and result from the properties of the χ^2 distribution when assuming that the stellar parameters are perfectly known. Accounting also for corresponding errors, the second entry (usually larger than the first one) gives the resulting total error.

These quite large uncertainties in the abundances are typical for massive, early-type stars, since for these objects it is more difficult to obtain precise constraints on the stellar parameters, due to the presence of (inhomogeneous) winds and the NLTE conditions, contrasted to the conditions in late-type stars, which moreover display significantly more optical lines and rotate slower. Finally, when evaluating the abundance errors, many investigations do not account for the propagation of errors associated with the uncertainty in the stellar parameters.

Table 4.3 is divided into dwarfs (upper part) and supergiants/bright giants (lower part), with a subdivision into hotter and cooler objects denoted by different colors in the figures in the following sections.

4.5.2 General comments

Though most of our diagnostic lines could be consistently reproduced, both with respect to W_{eq} and line profile, there are also some lines which would indicate different abundances than the majority of the others. The triplet N III 4634/4640/4641 (in emission for hotter objects) is an example well documented by Rivero González et al. (2012a) and Grin et al. (2017). From our results, we confirm their findings, at least for the cooler stars of our sample (Fig. 4.12), while for most hotter objects we have not found particular difficulties, and were able to fit the corresponding emission line complex either well or at least qualitatively (Figs. 4.13 and 4.14). Presumably, the former problem relates to an inaccurate description (in FASTWIND) of the population of the upper levels of these transitions, which depend, in the “cooler” domain of our sample, on the interaction between two overlapping nitrogen and oxygen resonance lines in the EUV (see Rivero González et al. 2011). In terms of our fitting procedure, the N III triplet lines receive a low weight when they cannot be reproduced.

We also suspect (again mostly for the cooler objects) that O III 5592 tends to imply higher oxygen abundances compared to its peers. This would be even more dangerous than in the former case, since this line, due to its strength, is often used as main abundance indicator (e.g., Martins et al. 2015a, 2017). We will come back to this problem in Sect. 4.5.6.

Finally, also C III 4647/4650/4651 and C III 5696 (see previous sections) often cannot be satisfactorily reproduced (here, both in the cooler and hotter domain), and often receive a low weight as well.

At the end of this section, we note that Table 4.1 compares the values of v_{mac} as derived by Holgado et al. and by us. Basically, both works used different methods: regarding v_{mac} , Holgado et al.

mostly concentrated on O III 5592, whereas in our work we adapted, if necessary¹⁰, v_{mac} to fit the shape of all visible CNO lines as well as possible (see Sect. 4.4.3). Overall, both results are quite consistent, and the mean deviation is $v_{\text{mac}}(\text{ours}) - v_{\text{mac}}(\text{Holgado et al.}) = -5.9 \text{ km s}^{-1}$, with a dispersion of $\pm 7.0 \text{ km s}^{-1}$. The fact that our values are systematically lower than those from Holgado et al. (at least for the dwarfs; for the supergiants, the values are basically equal) might be partly explained as follows (see also Fig. 5 in Simón-Díaz & Herrero 2014): whereas Holgado et al. assumed a delta-function for the intrinsic profile, our theoretical profiles already include a thermal + micro-turbulent broadening, giving rise to lower v_{mac} compared to observations.

4.5.3 Microturbulence

Before concentrating on the results for the individual abundances, we briefly discuss our findings for the v_{mic} values (see Table 4.3¹¹). Interestingly, the majority of the values are consistent with those estimated by Holgado et al. from a pure H/He analysis, though our results show a clearer trend: except for one case, all supergiants display (in CNO) a $v_{\text{mic}} = 15$ to 20 km s^{-1} , where the larger value only appears for the two hottest objects. For the dwarfs, a clear increase with temperature, from 5 to 20 km s^{-1} , seems to be present, where, again, only the (three) hottest objects reach the maximum value. We note here that since both 5 km s^{-1} and 20 km s^{-1} are located at the borders of our grids, these values must be considered as upper or lower limits only, with the exception of star #10. In this case, the quoted $v_{\text{mic}} = 20 \text{ km s}^{-1}$ value is not a lower limit but a typical value, derived from a compromise between our results for C, N, and O.

The analysis of much larger samples than the present one might allow for tighter constraints on this quantity (as a by-product of the CNO analysis), and might provide useful insights into the question whether there is a physical interpretation for this quantity (in the photosphere!), and whether indeed it might be related to sub-surface convection as suggested by Cantiello et al. (2009).

4.5.4 Stellar evolutionary models

In the next sections, we will compare the outcome of our study with theoretical predictions. In particular, we will compare with two well-known evolutionary grids for single massive stars, namely the tracks from Ekström et al. (2012), henceforth referred to as Geneva tracks, and from Brott et al. (2011), referred to as the Bonn models. Details on the differences between these two investigations can be found, e.g., in Keszthelyi et al. (2017) and Markova et al. (2018). Both grids include rotation (adopting different descriptions for angular momentum transport and mixing), with a variety of initial velocities (Bonn grid), or one specific initial rotation rate, corresponding to 40% of critical rotation (Geneva). The Bonn tracks additionally adopt magnetic fields, which have been accounted for in the angular momentum transport, but not for mixing. For our concern, important distinctions between both tracks are initial metallicities and the core overshooting parameter.

Table 4.4 compares the different initial CNO compositions used in each of the tracks, together with the solar abundances from Asplund et al. (2009), which serve as central values for our atmospheric

¹⁰ i.e., if the value provided by Holgado et al. resulted in problematic line shapes.

¹¹ In this table, we do not provide the individual errors, but note here that the typical uncertainties in v_{mic} are on the order of 2.5 to 5.0 km s^{-1} .

Table 4.4: Initial values of CNO abundances adopted in the evolutionary grids referred to in this work, and corresponding solar values from Asplund et al. (2009). The abundances from Brott et al. (2011) have been tailored to represent the CNO abundances from the young open cluster NGC 6611 (see text).

	solar	Brott et al. (2011)	Ekström et al. (2012)
ϵ_C	8.43	8.13	8.39
ϵ_N	7.83	7.64	7.78
ϵ_O	8.69	8.55	8.66

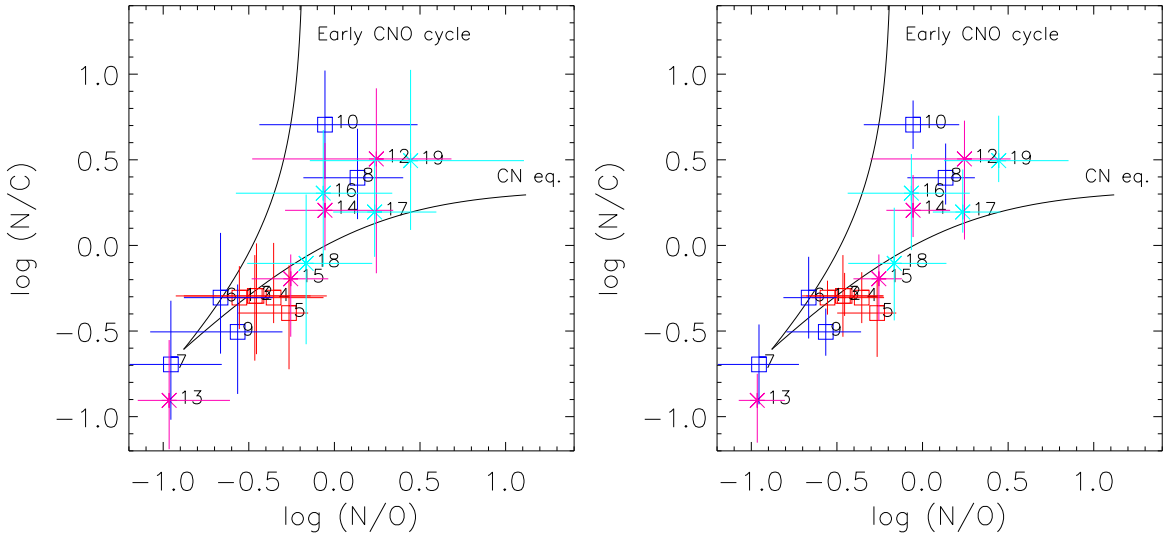


Figure 4.1: The relation between nitrogen-to-carbon and nitrogen-to-oxygen ratios. The left panel displays our results with errors when including the uncertainties in T_{eff} and $\log g$, while on the right panel we display only those uncertainties that arise from our method when relying on the T_{eff} and $\log g$ values provided by Holgado et al. (see Sect. 4.5.1). “Hot” and “cold” dwarfs are denoted by blue and red squares, and “hot” and “cold” supergiants/bright giants by cyan and magenta asterisks. For our division between hot and cold objects, and the correspondence between number and object, see Table 4.3. The solid lines represent the theoretical limits for the early phases of the CNO cycle (less massive stars), and for the conversion of O to N after a fast establishment of CN equilibrium (most massive stars). Both curves adopt the initial abundances from the Geneva models.

model grids. While the chosen initial conditions from the Geneva grid are quite similar to the solar ones (for details, see Ekström et al. 2012), the values adopted in the Bonn tracks have been tailored to represent the conditions in the young open cluster NGC 6611¹², basically using data from early B-type stars and H II regions located in this cluster (for details, see Brott et al. 2011).

The initial metallicity has a moderate effect on the individual abundances and abundance ratios when evolving with time. Since the mixing efficiency parameter is larger in the Bonn tracks (at least for the mass range of our sample), also the time-scales of the chemical evolution at the surface differ in both models. On the other hand, overshooting plays a major role for the duration of the main sequence, and a larger overshooting (Bonn models) results in a more extended main sequence phase (reaching into the B-supergiant regime), compared to the Geneva tracks.

4.5.5 A consistency check – mixing-sensitive ratios

Due to their sensitivity to mixing, the nitrogen-to-carbon (N/C) and nitrogen-to-oxygen (N/O) ratios allow us to obtain constraints on the evolutionary stage of a star, particularly since the CN cycle and the ON loop might not happen simultaneously. In the most massive stars, for example, the conversion of C to N occurs on very fast time-scales, and these objects spend most of their subsequent life in converting O to N (e.g., Maeder 2009, Maeder et al. 2014). Thus, it is also important to study the individual C, N, and O abundances in the light of the evolutionary tracks, and to identify any atypical over- or underabundances.

Before concentrating on these issues in Sect. 4.6, at first we will investigate the (N/C) ratios as a function of (N/O). This behavior is tightly constrained, independent of specific evolutionary tracks, and thus allows us to check the reliability of our data.

Basically, two limiting scenarios can be formulated analytically (see Przybilla et al. 2010 and Maeder et al. 2014). In the case of the most massive stars ($\gtrsim 40 M_{\odot}$), the CN equilibrium is quickly established through the CN cycle ($^{12}\text{C} \rightarrow ^{14}\text{N}$), and thereafter the number of carbon atoms can be adopted as constant. Then,

$$\frac{d(\text{N/C})}{d(\text{N/O})} = \frac{\text{N/C}}{\text{N/O}} \frac{1}{1 + \text{N/O}}, \quad (4.9)$$

and integration (with C = constant) yields¹³

$$\frac{\text{N}}{\text{C}} = \left(\frac{\text{N}}{\text{C}} \right)_{\text{init}} \frac{1 + (\text{N/O})_{\text{init}}}{(\text{N/O})_{\text{init}}} \frac{\text{N/O}}{1 + \text{N/O}}. \quad (4.10)$$

The second scenario applies to lower mass stars (though still massive), for which one may assume that during the first phase of the CNO cycle (the CN sub-cycle) ^{16}O remains constant while ^{12}C is converted to ^{14}N . Following again Przybilla et al. (2010) and Maeder et al. (2014),

$$\frac{d(\text{N/C})}{d(\text{N/O})} = \frac{\text{N/C}}{\text{N/O}} \left(1 + \frac{\text{N}}{\text{C}} \right), \quad (4.11)$$

¹²to enable a comparison with objects from this cluster within the VLT-FLAMES survey on massive stars, the latter summarized by Evans et al. (2008).

¹³Assuming the so-called dilution factor – i.e., the fraction of the mass with initial composition divided by the total mass which is mixed – as close to unity, the initial values of the ratios can be used instead of the abundances after CN equilibrium (for further details, see Maeder et al. 2014).

which has a solution symmetric to Eq. 4.10,

$$\frac{N}{O} = \left(\frac{N}{O}\right)_{\text{init}} \frac{1 + (N/C)_{\text{init}}}{(N/C)_{\text{init}}} \frac{N/C}{1 + N/C}. \quad (4.12)$$

To express (N/C) as a function of (N/O) , this can be rewritten as

$$\frac{N}{C} = \frac{N/O}{\left(\frac{N}{O}\right)_{\text{init}} + \frac{(N/O)_{\text{init}}}{(N/C)_{\text{init}}} - N/O}. \quad (4.13)$$

Both limits, Eqs. 4.10 and 4.12, are represented by solid black lines in Fig. 4.1, and actual objects should be located in the area between these two lines. We stress that the actual location of this area depends on the initial composition, where in Fig. 4.1 we have used the values adopted by the Geneva models, which are close to the solar ones. We note that a similar comparison has been provided by Martins et al. (2015a, their Fig. 5), also for a sample of Galactic O-type stars (see next section).

The right panel of this figure displays our results with error bars from considering only the uncertainties within our statistical analysis, keeping T_{eff} and $\log g$ at the values provided by Holgado et al. The left panel accounts for a more complete error propagation, considering also the typical uncertainties of the former parameters. This panel shows clearly that the actual uncertainties in abundances can be much larger than conventionally quoted.

Inspecting now the “observed” ratios, we see that most of the dwarfs are indeed located at or close to the beginning of the limiting curves, as should be expected (initial phase of their chemical evolution), though the values also indicate that the cooler dwarfs might suffer from too low values of oxygen. We will return to this problem in the next section. HD 96715 (#10), our hottest dwarf, is separated from its peers and close (at least with respect to its central value) to the early CNO cycle limit which means that most probably this star is still within the CN sub-cycle, though already in a later phase with depleted C together with a high N abundance. Cases in analogy to HD 96715 were discussed by Rivero González et al. (2012a), who also found a few, highly nitrogen-enriched early O-type dwarfs, within a sample of LMC O-stars. Taken at face value, the location of this object seems to be reasonable. In Sect. 4.6.1, however, we will see that this object has quite a large mass (from its position in the HRD), and should thus be located closer to the lower limiting curve. We stress, however, that part of this peculiarity might vanish when accounting for the considerable error bars.

The supergiants are mainly located close to the lower limit (at or close to CN equilibrium), with different stages of nitrogen enrichment. Since all of them turn out to be quite massive (Sect. 4.6.1 and Table 4.5), this behavior is as expected. At first glance, the position of HD 152249 (#13) is quite intriguing, and in the next section we provide further details on this object. Anyhow, the large error bars also suggest that the actual position of this star is compatible with a (close to) solar initial composition.

In summary, except for the cooler dwarfs and few specific objects, the derived abundance ratios of our targets are consistent with the theoretical expectations related to their classification. Further constraints on the reliability of our data will be provided in the next section.

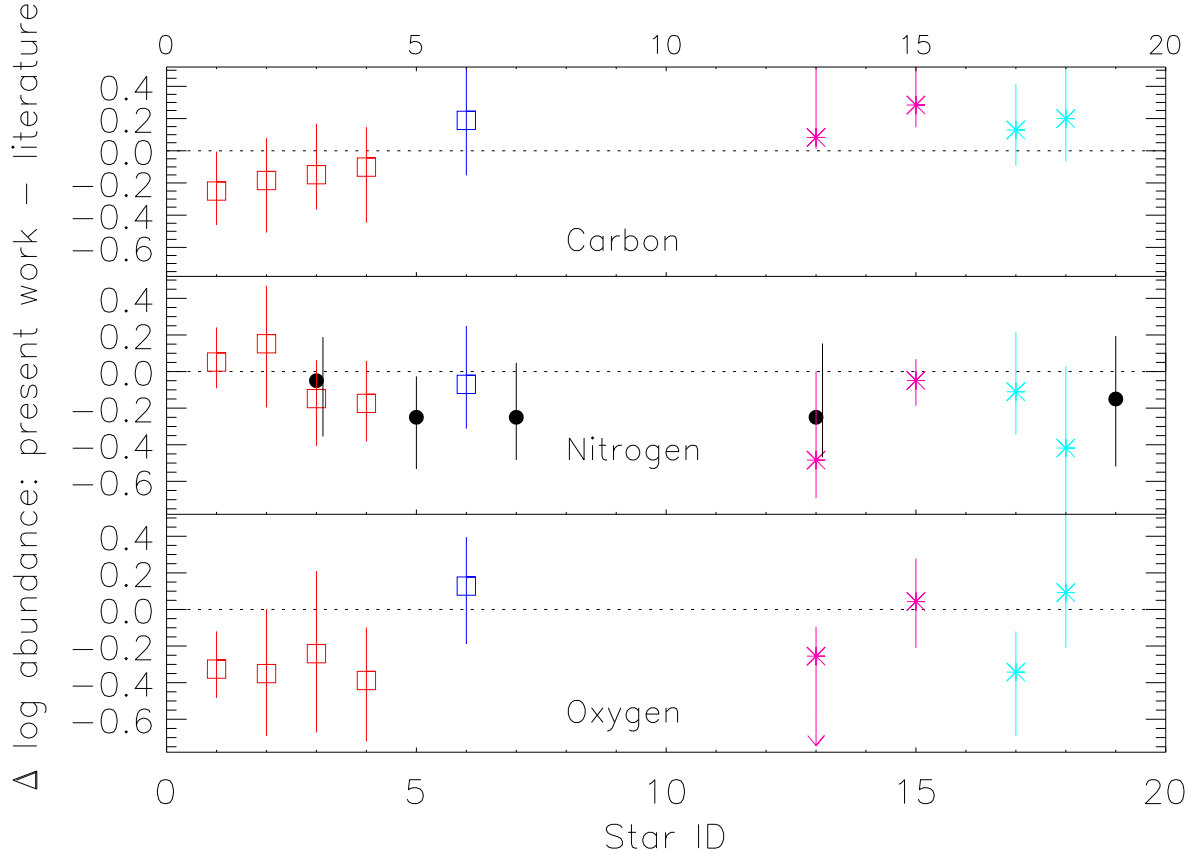


Figure 4.2: Differences between the logarithmic chemical abundances obtained in the present work and those from Martins et al. (2015a, 2017) (colored symbols as in Fig. 4.1) and Markova et al. (2018) (nitrogen only, black circles). Errors of own data include typical uncertainties in stellar parameters.

4.5.6 Comparison with previous studies

Three objects of our present sample were already studied (with respect to ϵ_C) in our previous work (Carneiro et al. 2018), to test the reliability of our carbon model atom. Back then we used a simple by-eye fitting method, and reassuringly our new results (based on a more objective method) are fairly similar (and overlap within the error bars) for all three objects. In particular, for HD 36512 (#1) and HD 303311 (#9), our previously derived carbon abundances were 0.1 dex higher, while for HD 169582 (#19) we found identical values (significantly constrained by the absence or weakness of specific C III lines, cf. Carneiro et al. 2018, their Fig. 10).

Half of our sample overlaps with objects investigated by Martins et al. (2015a) and Martins et al. (2017), both by means of a complete CNO analysis. Moreover, for five of our objects, we can also compare with the nitrogen abundances derived by Markova et al. (2018). We refrain from a detailed comparison of stellar parameters, and only note that there is a reasonable agreement¹⁴. In the follow-

¹⁴Remember that specific deviations – even if considered as minor – can have a significant effect on the resulting abun-

ing, we focus on a comparison of the derived abundances.

Fig. 4.2 displays the differences between the logarithmic C, N, and O abundances obtained in the present work and those from Martins et al., for the stars common to both samples (IDs on the x -axis), #1, #2, #3, #4, #6, #13, #15, #17, and #18 (see Table 4.1). Since the target IDs follow the spectroscopic designation (with dwarfs below #10, and supergiants/bright giants above), this figure enables the identification of potential trends in the differences: though in most cases the results coincide within the error bars, our values for the C and O abundances of the cooler dwarfs are generally lower, on average by 0.17 and 0.32 dex, respectively. Moreover, our C abundances for the supergiants are generally larger, by a mean of 0.18 dex. For other elements/objects, no clear pattern can be identified.

Large differences in nitrogen (middle panel) are found for HD 152249 (#13) and HD 151515 (#18). Though it is difficult to find the actual reason for this disagreement, we note that star #13 is an OC-star, characterized (among other features) by having little nitrogen enrichment. Indeed, our abundance is much closer to solar than the value obtained by Martins et al. (2015a) (see also Martins et al. 2016 for a study of the four presently known Galactic OC-stars).

On the other hand, our nitrogen abundance for star #18 basically relies on N III (and one weak line of N IV), and has quite a large uncertainty.

In this panel, we also compare (via black dots) our nitrogen abundances with the values estimated by Markova et al. (2018). These authors obtained ϵ_N through a by-eye fit of the nitrogen line profiles (synthesized also by FASTWIND, using the same model atom), giving a larger weight to those lines that are stronger and not affected by stellar winds. The comparison was possible for stars #3, #5, #7, #13, and #19. Markova et al. (2018) did not quote individual uncertainties, but provide a typical error of ± 0.2 dex, which has been considered in the black error bars. The values derived by Markova et al. (2018) are consistently higher than ours (on average by 0.19 dex), both for the three dwarfs and the two supergiants, but still agree within the $1\text{-}\sigma$ range, where HD 97848 (#5) just marginally touches this range, due to a quite low positive error from our side. Their nitrogen abundance for HD 152249 (#13), the OC-star, is also closer to the solar value than that of Martins et al. (2015a), but still 0.25 dex larger than ours. This example instructively quantifies typical deviations in derived abundances from hot stars even when using identical synthesis tools, but different methods¹⁵ to infer the parameters and abundances.

As already pointed out, our oxygen abundances for the cooler dwarfs are considerably lower than those derived by Martins et al., while for the other objects there is no clear trend. Here also, however, two objects show considerably less oxygen. There might be (at least) two reasons for this discordance: (i) as mentioned in Sect. 4.3.3, our present oxygen model atom lacks a detailed description for specific transitions, and thus might lead to an inaccurate description of certain level populations. (ii) Martins et al. (in both papers) provide an extensive list of lines used for their oxygen analysis, but most of these refer to O II, and only O III 5592 is used for O III. Thus, at least for higher T_{eff} and/or higher $v \sin i$, O III 5592 is the only diagnostic oxygen line in their analyses. From our own experience accumulated in the present study, this line almost always indicates larger oxygen abundances than the other O III lines used by us in addition to O III 5592 when possible (see Table 4.2). Since our

dances.

¹⁵and, when comparing results obtained via by-eye fits, different persons

diagnostic method always searches for a “compromise solution”, this leads to lower derived oxygen abundances. We have checked that using O III 5592 exclusively would result in ϵ_{O} values rather close to those derived by Martins et al., but presently we have no reason to exclude the other lines.

From the comparisons performed in the previous and this section, we conclude that our carbon and nitrogen abundances should be, overall and within the error bars, reliable, and significant differences to the studies by Martins et al. are present only in the N abundance of two stars.

For the cooler dwarfs, the comparison with the theoretical limits of CNO burning points towards too low oxygen abundances, and the discrepancies with Martins et al. are systematic. Moreover, it would be difficult to explain why our cooler dwarf sample should display (on average) considerably less oxygen than B-stars in the solar neighborhood ($\epsilon_{\text{O}} \sim 8.76$, Przybilla et al. 2008) or at least B-stars in the young open cluster NGC 6611 ($\epsilon_{\text{O}} \sim 8.55$). We note here that problems with FASTWIND itself are unlikely, since Simón-Díaz (2010) analyzed 16 B-type stars in the Ori OB1 association with this code, and found highly homogeneous oxygen abundances, in good agreement with the quoted work by Przybilla et al. (2008). Unfortunately, their oxygen model atom was tailored for early B-type dwarfs, and could not be used for the analyses of the hotter sample investigated here.

Since the identified, systematic discrepancies in the oxygen abundance are specific for our cooler dwarfs (dense atmospheres), it is quite possible that this problem – if there is one – is indeed rooted in our current model atom, since (i) problematic ionization cross-sections can lead to an erroneous ionization balance, which might explain our almost perfect fits for O II (Fig. 4.12), and (ii) imperfect collisional strengths have a major effect particularly at high densities and comparatively cool temperatures. Although the situation for the other objects is more promising, both in terms of the location of these objects in Fig. 4.1, and in comparison to Martins et al., the validity of our oxygen analysis as a whole needs to be clarified in forthcoming work. We stress, however, that our results do reproduce the observed oxygen lines – admittedly, O III 5592 to a lesser extent – but we advise considering our oxygen results with caution until further evidence.

4.6 Comparison with evolutionary calculations

Already with our inspection of the abundance ratios (Fig. 4.1), we obtained some insights into the evolutionary phases of our targets. However, the correlation between evolutionary stage and nucleosynthesis evolution is complex, due to the many processes to be considered. Stars of different masses experience different phases of the CNO cycle at different times, where, e.g., carbon reaches equilibrium considerably faster in more massive stars. Before proceeding with our investigation of the abundance evolution, we therefore briefly constrain the evolutionary stages of our sample stars by comparing with suitable diagrams, which then allows us to cross-check with our first and following conclusions obtained from the abundance analysis. Since we have used the stellar parameters from Holgado et al., and since part of our sample overlaps with the samples from Martins et al. (2015a, 2017) and Markova et al. (2018), corresponding conclusions on masses etc. can be already found in these studies.

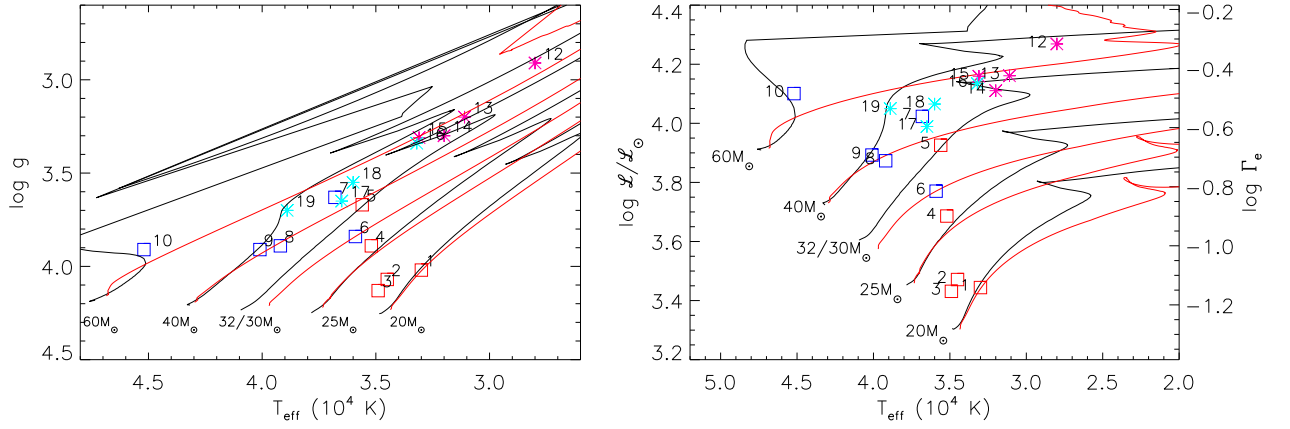


Figure 4.3: *Left*: Kiel diagram ($\log g$ vs. T_{eff}) for our sample stars. Overplotted are the rotating Geneva (Ekström et al. 2012) (black) and Bonn (Brott et al. 2011) (red) tracks for the mass range 20 to 60 M_{\odot} , with initial rotation velocities of 40% of their critical speed. *Right*: Corresponding spectroscopy HR diagram (sHRD, see text), with both ordinate-axes proportional to L/M . The Eddington Γ_e has been calculated with solar Helium content, assumed to be completely ionized. Symbols in both panels as in Fig. 4.1.

4.6.1 Evolutionary stages

To avoid any uncertainty induced by uncertain distances (in the same spirit as Holgado et al.), we consider only those diagrams/variables that are independent of stellar radius, and only depend on quantities derived by means of quantitative spectroscopy.

To this end, we examined the location of our sample stars in the $\log g$ – T_{eff} (Kiel) diagram, and, because of the clearer separation of the theoretical tracks, in the spectroscopic HR diagram (sHRD, Langer & Kudritzki 2014). The latter uses as ordinate the variable $\log(\mathcal{L}/\mathcal{L}_{\odot})$, where

$$\log \mathcal{L} = 4 \log T_{\text{eff}} - \log g_{\text{true}} \propto \log(L/M). \quad (4.14)$$

and g_{true} is the (spectroscopic) gravity, corrected for centrifugal acceleration¹⁶. Since $\log \mathcal{L} \propto \log(L/M)$, it is also proportional to the Eddington Γ_e for electron scattering, which we have additionally indicated on the right ordinate of the corresponding figures.

As already outlined in Sect. 4.5.4, we have based our investigations on the rotating Geneva and Bonn evolutionary tracks, which are represented in the next figures by black and red lines, respectively, with an initial rotation velocity of 40% (or close to this value) of the critical speed. For the mass range considered (20 to 60 M_{\odot}), this corresponds to ~ 270 to 350 km s^{-1} . We note that the Geneva tracks do not include a track for 30 M_{\odot} , but for 32 M_{\odot} .

As evident from the left (Kiel diagram) and the right panel (sHRD) of Fig. 4.3, our stars populate the considered mass range, with the majority of dwarfs being in the early main sequence phase.

¹⁶ $g_{\text{true}} = g_{\text{spec}} + g_{\text{cent}}$, with $g_{\text{cent}} \approx (v \sin i)^2/R_*$ (Repolust et al. 2004). In our sample, the maximum difference between $\log g_{\text{true}}$ and $\log g_{\text{spec}}$ is $\lesssim 0.02$ dex when the stellar radius has been estimated from typical calibrations (e.g., Martins et al. 2005).

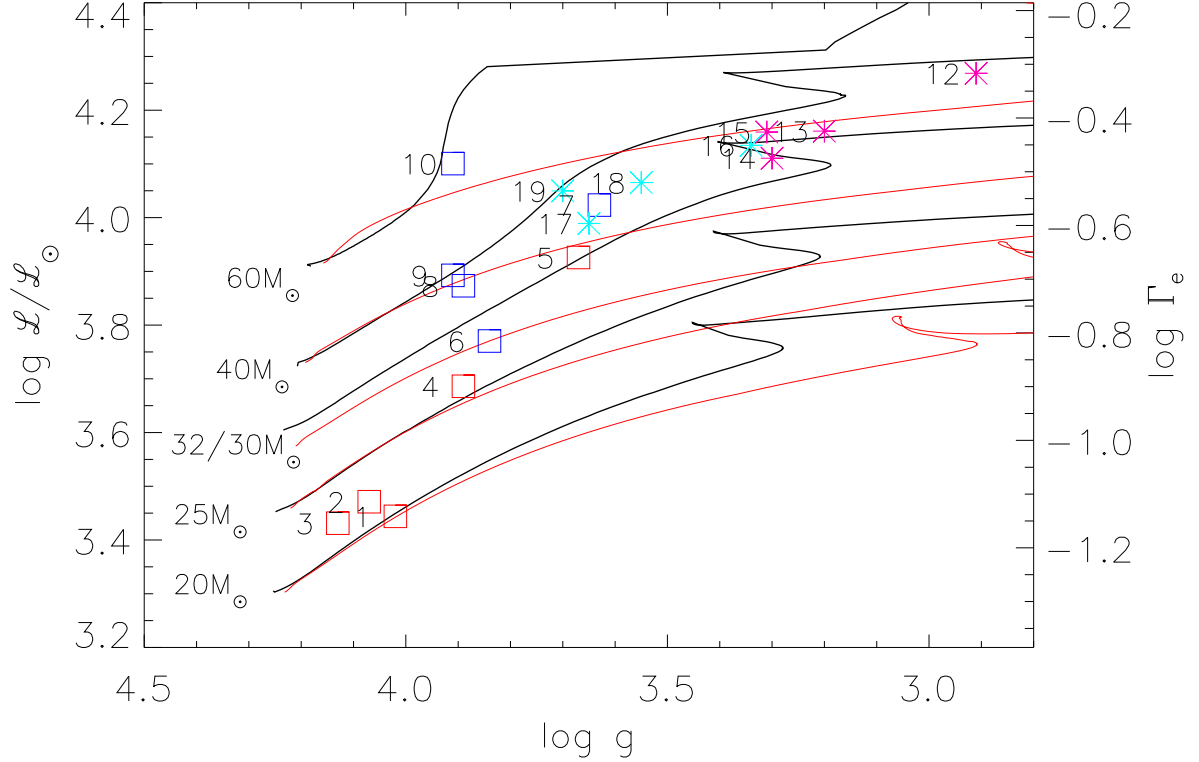


Figure 4.4: Modified sHRD, with abscissa $\log g$ (instead of T_{eff}), providing a clearer separation between the tracks. Two distinct gravity regimes populated by our sample stars become obvious (see text).

The early supergiants are mostly located in the intermediate phase, around $40 M_{\odot}$, while the cooler supergiants (together with the hot supergiant HD 225160 (#16)) are either in the late MS phase (Bonn tracks, with larger overshooting), or already at or close to the TAMS (Geneva tracks). Star #12 is the most evolved star, which according to the Geneva tracks might be already in the hydrogen shell-burning phase.

From Figs. 4.3 and 4.4 (discussed below), a clear lack of massive stars close to the ZAMS is obvious. Though this might be pure coincidence due to our small sample, such findings have been reported already previously, for different samples (e.g., Herrero et al. 1992, Repolust et al. 2004, Martins et al. 2005, Simón-Díaz et al. 2014). More recently, and for much larger samples, Sabín-Sanjulián et al. (2017) (with respect to the VFTS, Evans et al. 2011) and Holgado et al. (with respect to the Galactic O-type standards) identified the same problem¹⁷.

In addition to our present lack of knowledge of how pre-main-sequence stars initiate their evolution on the main-sequence (e.g, Bernasconi & Maeder 1996, Behrend & Maeder 2001, Haemmerlé et al. 2016), very young massive stars could still be enshrouded by the dust from their birth cocoon, which would hide these targets from optical observations (e.g, Garmany et al. 1982,

¹⁷Recall that our sample is a subsample from the objects studied by Holgado et al., thus our finding is not surprising.

Herrero et al. 2007, Castro et al. 2014), and might explain the observed deficit of massive stars close to the ZAMS. A more detailed discussion on this topic will be presented in a forthcoming paper of the IACOB series (Holgado et al., in prep.).

Regarding the implied stellar masses, both tracks basically agree for all dwarfs, with the exception of HD 97848 (#5: $32 M_{\odot}$ from the Geneva, and $40 M_{\odot}$ from the Bonn tracks). For the supergiants, however, there are clear differences. From the Geneva tracks, our most evolved stars range from 32 to $40 M_{\odot}$, while from the Bonn tracks they range from 40 to $\sim 65 M_{\odot}$. In particular, for HD 195592 (#12) the Geneva tracks imply a mass of $\sim 40 M_{\odot}$, contrasted with $\sim 65 M_{\odot}$ from the Bonn models. These disagreements presumably relate to the different treatment of angular momentum transport and mixing (in particular, the effects from mean molecular weight barriers), which results, in the Geneva models, in higher luminosities and consequently higher mass loss. Accounting for the higher luminosities and the increased mass loss, both the actual and the initial masses of more evolved objects are lower than in the Bonn models. For more details on these discrepancies, we refer to Markova et al. (2018).

Concentrating now on the sHR diagram (right panel of Fig. 4.3), which provides a distance-independent luminosity-to-mass ratio¹⁸, we note that \mathcal{L} increases in parallel with the ID numbers of our dwarfs, and two of them (HD 93222 (#7), and HD 96715 (#10)) belong to the stars with the highest luminosity-to-mass ratio, headed by HD 195592 (#12).

For the sake of clarity, we display \mathcal{L} also as a function of $\log g$ in Fig. 4.4, which shows an even better distinction between the tracks for the individual masses, and provides an impression of the different location of the TAMS in the alternative evolutionary models. From this figure, we can divide our sample in two regimes, divided around $\log g \sim 3.65$. On the left side, we find the stars with higher gravities and mostly lower luminosities (dwarfs). In this regime, the atmospheres are denser, and the ionization balance is shifted towards lower ionization stages. Since these have more lines in the optical (which improves the abundance analysis), the stars in this regime are also the stars with the most precise results, i.e., with the smallest uncertainty ranges (see Table 4.3).

4.6.2 CNO evolution

The different evolutionary stages occupied by our sample provide us with a well-suited laboratory for the analysis of general trends (and outliers). The division into two regimes, particularly seen in Fig. 4.4, should be also present when comparing ϵ_{C} vs. ϵ_{N} as done in Fig. 4.5. Lower-mass dwarfs should be still passing through the CN cycle (and in most cases, through its early phases), with carbon and nitrogen abundances not too different from their initial values (which might vary as a function of environment, see Table 4.4), while the supergiants and the more massive dwarfs should become significantly nitrogen-enriched and carbon-depleted.

Even though we already discussed the behavior of mixing-sensitive abundance ratios in Sect. 4.5.5, there are indeed good reasons to study at first the ϵ_{C} vs. ϵ_{N} relation, without relying on the oxygen abundance: (i) at least for the cooler dwarfs, the ϵ_{O} values derived in the present work need to be rechecked (potential deficiencies within our oxygen model atom, see Sect. 4.5.6). (ii) At least from intermediate O-types on, the oxygen abundance is the most difficult to determine among the three

¹⁸For a comparison between results from the conventional and the spectroscopic HR diagram, see again Markova et al. (2018).

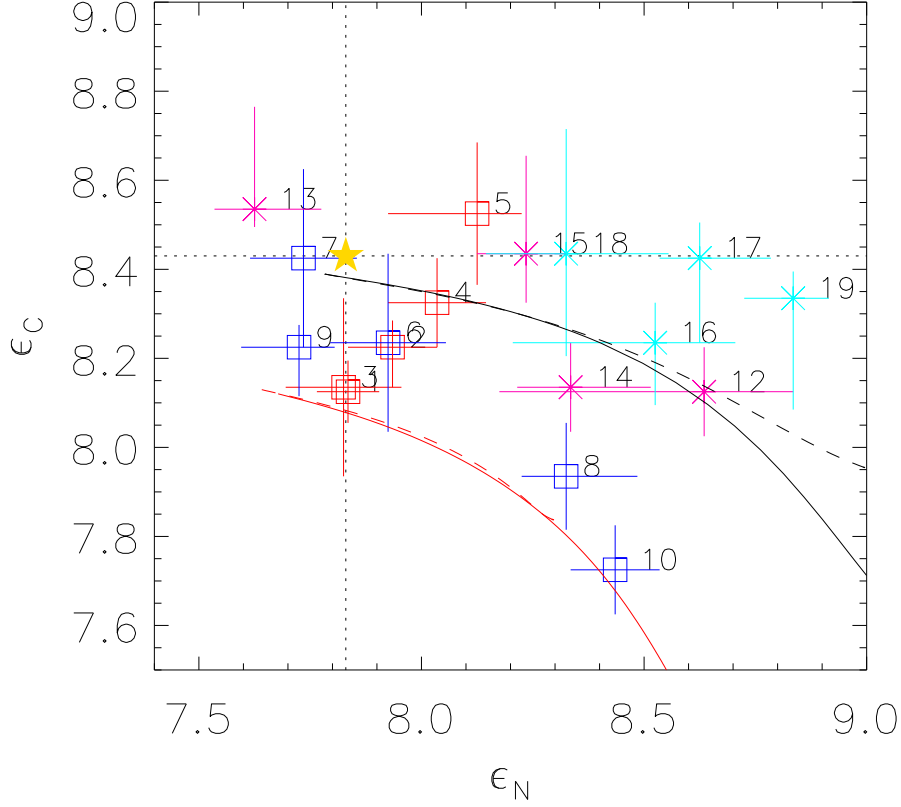


Figure 4.5: The relation ϵ_C vs. ϵ_N in the light of evolutionary tracks. The black and red lines display the corresponding Geneva and Bonn tracks with $v_{\text{rot}}^{\text{init}} \approx 0.4 v_{\text{crit}}$, respectively, where the solid lines refer to the $60 M_{\odot}$, and the dashed lines to the $40 M_{\odot}$ tracks. The dotted lines represent the solar C and N abundances, and their intersection the position of the sun in this diagram. Symbols as in Fig. 4.1. Error bars include typical uncertainties in the stellar parameters.

elements C/N/O, due to the restricted number of ions (only O III) and corresponding lines in the optical, and the potentially peculiar behavior of O III 5592 (Sect. 4.5.2).

Together with the relation of ϵ_C vs. ϵ_N for our sample stars, Figure 4.5 displays the evolution of these (surface) abundances as predicted by the Geneva (black) and Bonn (red lines) tracks (again with $v_{\text{rot}}^{\text{init}} \approx 0.4 v_{\text{crit}}$). Except for the different initial conditions, the predicted evolutionary paths are similar, with only slightly diverging curves for the $60 M_{\odot}$ tracks, though the evolution of the individual abundances as a function of other parameters (evolutionary time or T_{eff}) is quite different, as we will see in Fig. 4.6. This clearly shows that the evolution of the surface abundance ratios is mainly triggered by nucleosynthesis when mixing is efficient.

In Fig. 4.5, we only display the tracks for $60 M_{\odot}$ and $40 M_{\odot}$, which provides a fair representation also for less massive stars, except that in the case of lower masses, the range of abundance variation becomes somewhat smaller. For example, for the $20 M_{\odot}$ Geneva track, ϵ_C decreases from 8.39 to ~ 8.12 , and ϵ_N increases from 7.78 to ~ 8.43 (see below).

In general, our sample follows, within the error bars, the trend suggested by the tracks, with the majority of the stars in between the two curves, which might be indicative for the potential variation of (initial) CN abundances in the solar surroundings.

Concentrating at first on nitrogen, the majority of the dwarfs have ϵ_N values much closer to solar¹⁹ than the supergiants, as expected. Two dwarfs (#8 and #10) and one supergiant (#13) are an exception to this behavior. Regarding the dwarfs, HD 12993 (#8) has been classified with the suffix “Nstr”²⁰, implying an increased nitrogen and decreased C abundance (as derived here). HD 96715 (#10), our hottest and most massive dwarf, and already referred to in Sect. 4.5.5, displays even more ϵ_N and less ϵ_C , indicating the products of a rapid CN cycle, which, following Fig. 4.1, has not yet reached equilibrium though. The OC-supergiant HD 152249 (#13) has already been mentioned in Sect. 4.5.6.

Turning now to carbon, here also most of the dwarfs have ϵ_C close to initial values. For the hotter supergiants and bright giants (except for #16), however, the predicted depletion is not (or at least not clearly) visible, contrasted to the cooler supergiants (except for the OC-star) which follow the predicted trend.

Accounting for the uncertainties, one might argue that also our hotter supergiants are still compatible with the Geneva tracks, except maybe for #17 (HD 171589), which shows the largest difference to the predictions (all hotter supergiants need to be compared with the $40 M_\odot$ track, see Table 4.5). We remind the reader that regarding the abundance ratios (Fig. 4.1), #17 “fits” perfectly, which emphasizes the importance of considering the individual abundances as well.

At this point, we stress the prime role of rotation in defining the position of each target in Fig. 4.5, and the position of the theoretical tracks. Initial rotational rates lower than $0.4 v_{\text{crit}}$ will decrease the range of predicted enhancements and depletions (and a very low initial rotation results in a negligible evolution of CNO surface abundances), which might explain the position of our OC-supergiant #13 with $v \sin i \approx 70 \text{ km s}^{-1}$ (see also Martins et al. 2016, who suggested the same scenario). Indeed, according to our selection criteria, most of our objects should be in a present state of slow rotation (if, as reasonable, only few of them were observed close to pole-on). Nevertheless, almost all hotter supergiants plus the dwarfs #8 and #10 show a significant abundance evolution, and this would imply that there is a significant loss of angular momentum already before the potential bi-stability braking (Vink et al. 2010) around 25 to 20 kK. Moreover, at least for those few stars that show a very strong enrichment, there is the chance that they rotate much faster than suggested by their $v \sin i$, and for those stars a higher initial rotation than assumed here might be possible, with consequences for the predicted CNO evolution.

Thus far, our investigations have concentrated on surface-abundance ratios, where, assuming that the mixing-processes are similar for the considered elements, Figs. 4.1 and 4.5 mostly reflect the conversion of elements due to the CNO cycle, in dependence of initial composition. Thus, these diagrams are (almost) independent of the actual evolution as a function of time, which is strongly affected by the description of the mixing processes themselves, which in turn depend on the stratification of physical quantities such as internal velocity fields (rotation, turbulence, meridional circulation).

To obtain some insight into this temporal evolution, and to allow a comparison with the alternative

¹⁹Within the two alternative tracks, the differences in initial ϵ_N are much lower than in initial ϵ_C .

²⁰Defined by Sota et al. (2011, their Table 3) as a moderate case of enhanced N absorption, with C and O deficient.

Table 4.5: Ranges in initial evolutionary mass and initial masses for the objects analyzed in this study, roughly estimated from the sHRDs for $v_{\text{rot}}^{\text{init}} \approx 0.4 v_{\text{crit}}$ (Figs. 4.3 and 4.4). For identification and parameters, see Table 4.1.

star #	symbol in figures	$M_{\text{init}} (M_{\odot})$ (Geneva)	$M_{\text{init}} (M_{\odot})$ (Bonn)
1–5	red squares	20–30	20–30
6–10	blue squares	30–60	30–65
12–15	magenta asterisks	32–40	40–65
16–19	cyan asterisks	32–40	40–60
8		~40	~40
10		~60	~65
13		~32	~60
19		~40	~55

approaches from the Geneva and Bonn models, Fig. 4.6 displays the theoretical predictions (with T_{eff} as a proxy for time) for the individual elements (from top to bottom: C, N, O) and different mass regimes, together with our results. The dotted lines represent the solar abundance for each element, and the dashed and the dashed-dotted lines show the initial abundances of the Geneva (left side panels) and Bonn (right side panels) tracks, respectively.

Comparing both evolutionary tracks in all panels, the consequences of the distinct mixing descriptions used in each of the two sets becomes evident. In the Bonn tracks, all surface abundances reach their equilibrium value considerably faster, due to the larger mixing efficiency used. A consequence of this rapid mixing in the Bonn tracks is that the “hooks” (when the stars begin to contract at the end of the main sequence) are not visible, even if we would extend our T_{eff} range to lower temperatures, while in the Geneva tracks they are clearly visible, independent of mass regime. Moreover, although the predicted maximum depletion of C is similar in the Geneva and Bonn tracks (though the numbers are different because of different initial conditions), the Geneva models predict both a larger maximum N-enrichment and a larger maximum O-depletion²¹. For more details on the differences in the ϵ_{N} evolution, see Markova et al. (2018).

Before further comments are given, we provide in Table 4.5 some typical mass ranges to be accounted for when comparing our data with the predictions. These ranges in initial mass have been estimated from the sHRDs (Figs. 4.3 and 4.4) referring to the Geneva and Bonn tracks with initial rotation $\approx 0.4 v_{\text{crit}}$. In addition, this table also displays the initial masses for specific objects discussed in the following. As already mentioned in Sect. 4.6.1, the initial (and also the actual) masses for more evolved stars as derived from the Bonn tracks are larger than those from the Geneva ones.

²¹These similar ϵ_{C} and different ϵ_{N} values that are finally reached lead to the slightly diverging curves found in Fig. 4.5.

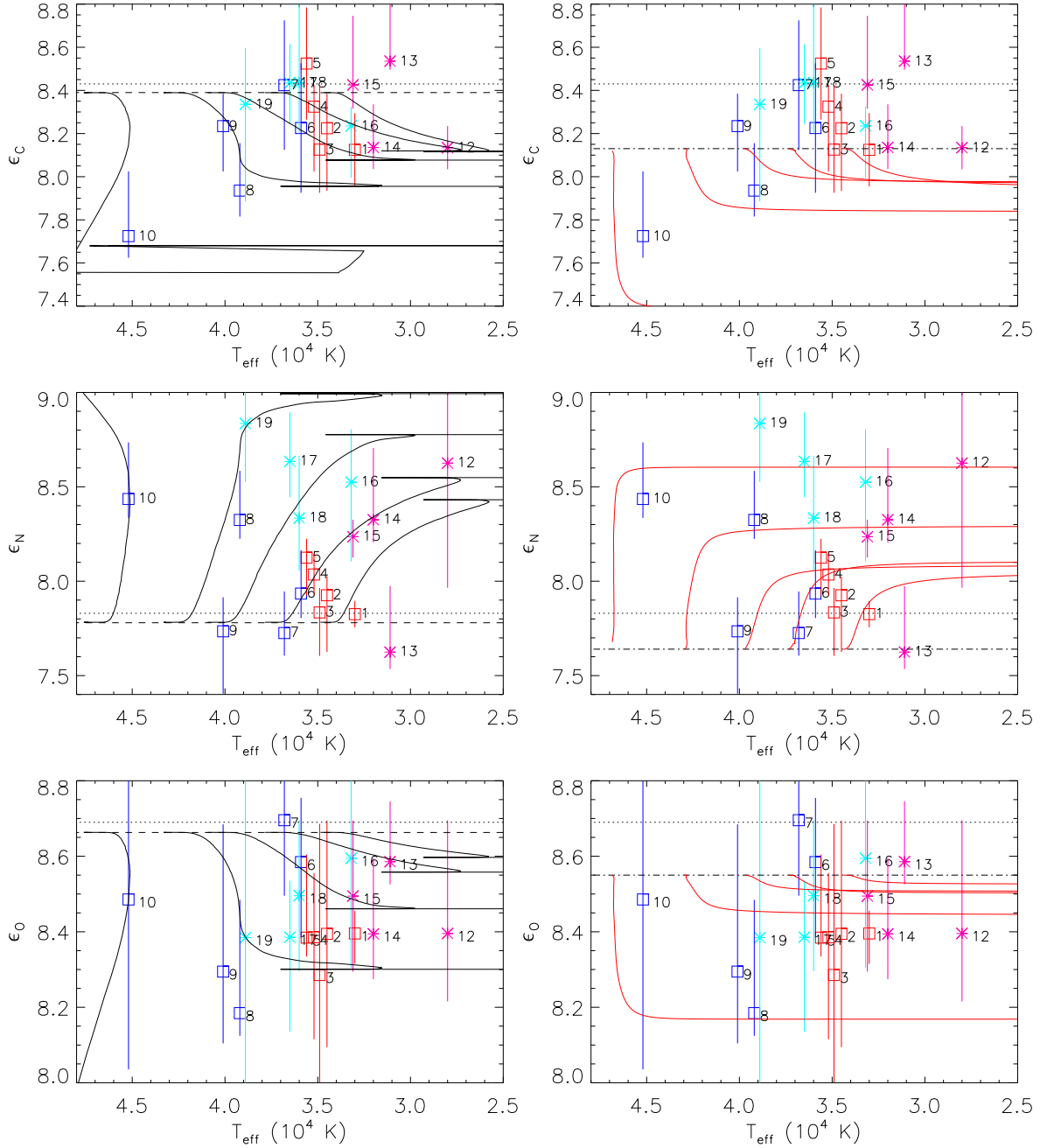


Figure 4.6: Evolution of C/N/O abundances for different masses (from left to right: 60 , 40 , ~ 30 , 25 , and $20 M_{\odot}$) as a function of T_{eff} , as predicted by the rotating Geneva (black lines, left panels) and Bonn tracks (red lines, right panels). The dotted line represents the solar abundance. The dashed and the dash-dotted lines display the initial abundances used in the Geneva and in the Bonn calculations, respectively. Our results (symbols as in Fig. 4.1) are shown with errors accounting for typical uncertainties in stellar parameters. For initial evolutionary masses of sample stars, see Table 4.5.

Overall, Fig. 4.6 is compatible with typical expectations. Most dwarfs present abundances close to the initial values, except for HD 12993 (#8) which is our “Nstr” object, and HD 96715 (#10), our hottest and most massive dwarf, both discussed already previously. The supergiants and bright giants show different degrees of chemical evolution, except for HD 152249 (#13, see above), which shows a close-to-solar abundance also for oxygen, consistent with our hypothesis (and the one by Martins et al. 2016) that this star should have formed with a low rotational speed. A closer look into the specific elements and objects reveals the following:

Carbon. While the carbon abundances of the cooler dwarfs and the cooler supergiants (the most-evolved objects in this study) are consistent with the predictions, for both the hotter dwarfs (except for #8 and #10) and the hotter supergiants (i.e., higher mass stars at early or intermediate MS-phases), the derived carbon abundance is larger than predicted, i.e., the “observed” depletion is lower. The least evolved stars have ϵ_C similar to the solar abundance, and are thus located closer to the Geneva than to the Bonn tracks.

Nitrogen. The cooler dwarfs agree with both tracks, while the hotter ones (again except for #8 and #10) mostly display less nitrogen than predicted. This could be a selection effect, since at least in the LMC there are many early O-dwarfs that show the opposite, see Rivero González et al. (2012b). Comparing with the nine Galactic O-dwarfs earlier than O8 analyzed by Markova et al. (2018), they found a significant nitrogen enrichment in five out of these nine stars, while the other four objects displayed values close to solar. Thus, a final conclusion on *typical* nitrogen abundances in early O-dwarfs is still not possible, and this discussion needs to be revisited after the analysis of a larger dataset. Anyhow, in combination with the discrepancies found for carbon in this work, our results might indicate that either the carbon depletion sets in later than expected, or, more likely, that these sample stars had a lower initial v_{rot} than considered in the tracks.

Regarding the cooler and hotter supergiants, the agreement is better, particularly compared with the Bonn tracks.

Oxygen. Here, most of the hotter objects are in fair agreement with the predicted depletion, and also the cooler supergiants follow the predicted trend, though they are more consistent with the Bonn tracks (which start from a lower initial O-abundance). The cooler dwarfs, however, display too little oxygen, compared with both tracks ($M_{\text{init}} \approx 20 \dots 30 M_{\odot}$), again indicating problems with the abundances as derived for these objects (Sect. 4.5.6). Taken together, it is quite likely that the deficits in our oxygen analysis mostly concern the cooler O-dwarf domain, while for the rest the analysis appears to deliver reasonable results.

We end this discussion by pointing out that our two hottest stars within the dwarfs and supergiants, #10 and #19, are in very good agreement with the Geneva tracks, particularly regarding nitrogen and oxygen, though at least the latter two elements are also matched by the Bonn tracks within the errors.

Our final diagram, Fig. 4.7, displays the mixing-sensitive ratio nitrogen-to-carbon vs. $v \sin i$, and is a variant of the meanwhile well-known “Hunter diagram” (ϵ_N vs. $v \sin i$, Hunter et al. 2008), where in this variant the surface enrichment of N becomes amplified by the parallel depletion of C. This kind of analysis was recently applied to a set of Galactic giants by Martins et al. (2017), who found no clear trend for their sample.

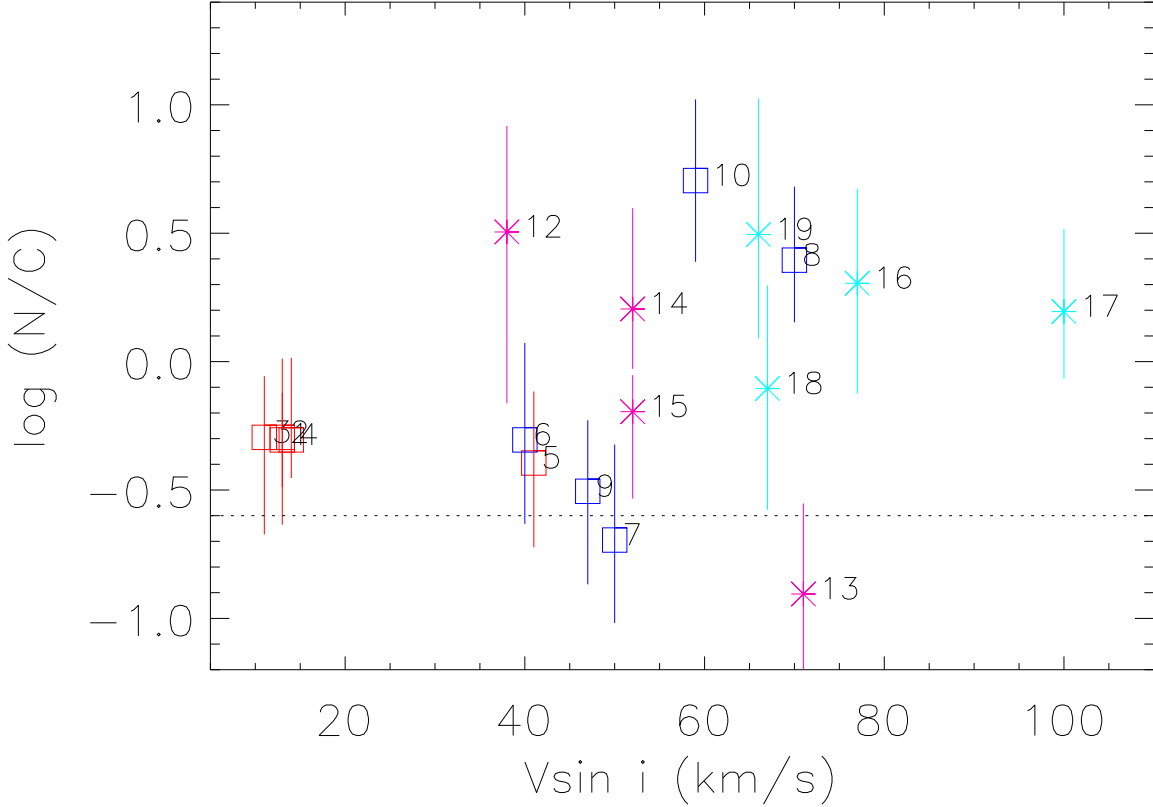


Figure 4.7: Nitrogen-to-carbon ratio vs. $v \sin i$ for our sample stars. The dotted line represents the solar value.

For the further discussion, two remarks might be necessary: (i) since the inclination $\sin i$ is unknown, the provided abscissa values are lower limits on the actual rotational speed v_{rot} . (ii) the untypically low (for O-type stars) values of $v \sin i$ are a consequence of one of our selection criteria.

Though Fig. 4.7 implies no obvious trend (such a trend would certainly not have been expected for our sample), it underpins some of our previous conclusions and hypotheses. All cool dwarfs have close to initial surface abundances (whether solar or somewhat different), and this is consistent with any kind of track, be it rotating or not. Three of the five hotter dwarfs also have close to initial abundances, while they should have, if beginning their lives with $v_{\text{rot}}^{\text{init}} \approx 0.4 v_{\text{crit}}$, already a well developed N/C ratio. Thus, for these stars it is quite likely that they have started their evolution as slow rotators, in line with the arguments from above. Except for object #18, all hotter supergiants plus the dwarfs #10 and #8 have a well-developed N/C pattern (consistent with or lower than the predictions from the rotating tracks), which indicates that a considerable braking mechanism (presumably due to the significant mass loss of these objects) must be present already at relatively early phases. We refrain here from discussing the theoretical predictions regarding the evolution of v_{rot} , and only refer to Keszthelyi et al. (2017) and Markova et al. (2018) for a closer study on this topic. Similar conclusions (i.e., previous braking) might be also drawn for the cooler supergiants (except for #13 and #15, which most likely

started their life with low v_{rot} as well). In both tracks, these objects are still far away from the bi-stability jump with potential bi-stability braking. At least in the Geneva models, however, they are very close to the “hook” (end of the MS phase), where mass-loss and angular momentum might change strongly, due to the significant changes in stellar structure.

4.7 Summary, conclusions, and future work

In this work, we presented a pilot study on the optical analysis of CNO surface abundances in O-type stars by means of FASTWIND, to be applied to large, statistically significant samples in future investigations (where an analysis by this code is advantageous due to the low computational costs). We have concentrated on targets and observations which should favor a straightforward abundance analysis: high-quality spectra from presumably single Galactic O-stars (which allows us to compare with single-star evolutionary tracks), and low $v \sin i$ (to avoid blending).

In particular, we selected a subsample of 18 O-type stars with low $v \sin i$ ($\leq 100 \text{ km s}^{-1}$) from the original sample by Holgado et al. (2018), covering ten dwarfs (O4 to O9.7) and eight supergiants/bright giants (O6 to O9.7), with well-determined stellar and wind-strength parameters.

The required model grids for the synthetic spectra have been calculated with the most recent version of FASTWIND, using our well-tested model atoms for nitrogen (Rivero González et al. 2011, 2012a) and carbon (Carneiro et al. 2018). For oxygen, we applied the model atom from the WM-basic database (Pauldrach et al. 2001), since thus far we have no “own” oxygen model atom suitable for O-star conditions at our disposal, and since the quoted one has been successfully used in various UV analyses (but not in the optical). When calculating the model grid(s), it turned out that a variation of all three C/N/O-abundances in parallel (per model) is possible, which saves a factor of three computation time and storage.

To derive the CNO abundances, we developed a semi-automatic method accounting for observational and systematic uncertainties, the latter arising due to problems in reproducing specific lines in specific spectral regimes. This method is based on a χ^2 -minimization of the (weighted) deviation between observed and theoretical equivalent widths. We have chosen such an equivalent width method to avoid problems related to line-broadening (rotation and macroturbulence) which might occur if alternatively fitting the profile shape. The minimization accounts for abundance and microturbulence in parallel, where the latter quantity is important for the final outcome. In our method, we also account for typical uncertainties in the stellar parameters, which introduces a significant contribution to the total error budget.

After analyzing the observed equivalent widths by means of our minimization method, we found that the derived v_{mic} -values are fairly similar for each of the considered elements, and were thus able to provide, per star, a unique value for this quantity. For all supergiants, we obtained values between 15 and $\geq 20 \text{ km s}^{-1}$, whereas the dwarfs displayed a clear trend, with v_{mic} increasing from $\leq 5 \text{ km s}^{-1}$ to $\geq 20 \text{ km s}^{-1}$ with spectral type.

After the best-fitting model for each star had been identified, we compared the corresponding line profiles with the observed ones, to check their consistency. This step allowed us to obtain final constraints on v_{mac} , which were found to be similar to the values provided by Holgado et al.

To check the reliability of our analysis, at first we investigated the abundance ratios (N/C) as a function of (N/O), where this relation is tightly constrained from theoretical considerations, independent of actual evolutionary calculations (Przybilla et al. 2010, Maeder et al. 2014). Most of our targets display abundance ratios consistent with the theoretical limits, though already here the OC9 Iab star HD 152249 caught our attention, due to an abundance pattern indicating a very early stage of evolution, though spectroscopically classified as supergiant. More severe deviations (though still within the total errors) were “only” found for the cooler (lower-mass) dwarfs within our sample, with too low oxygen abundances compared to the limits.

Part of our sample overlaps with the samples studied by Martins et al. (2015a, 2017) using the CMFGEN code. Except for specific differences that have been discussed in detail, the only major systematic discrepancy refers again to the oxygen abundance of the cooler O-dwarfs, where Martins et al. found much larger values than we did. Though part of this discrepancy might be attributed to the behavior of O III 5592 (which in our simulations implied larger abundances than the other O III lines, but was exclusively used by Martins et al. for this ion), we suspect that certain deficiencies of the oxygen model atom adopted in our work (see above) might be responsible for this deviation, and caution against using our oxygen results (at least in this spectral domain) until further tests are performed. To this end, we certainly need to develop our own, detailed, and well-tested oxygen model atom that is suitable for O-star conditions also in the optical.

Interestingly, five stars of our sample also overlap with the sample investigated by Markova et al. (2018), including a nitrogen analysis, by means of the same code and the same nitrogen model atom. Though the results of both works are compatible within their $1\text{-}\sigma$ ranges, the central values differ by roughly 0.2 dex, which tells about the accuracy of abundance determinations in hot stars that can be achieved using different methods.

The outcome of our study was compared with two well-known evolutionary grids for massive single stars, namely the rotating ($v_{\text{rot}}^{\text{init}} \approx 0.4 v_{\text{crit}}$) tracks from Ekström et al. (2012) (“Geneva models”), and from Brott et al. (2011) (“Bonn models”). Most important for our concerns are the different overshooting parameters, initial metallicities, and chemical mixing recipes/efficiencies used, due to their impact in prescribing stellar and chemical evolution.

Using the corresponding Kiel and spectroscopic HR diagrams, we obtained an overview on the evolutionary stage of our sample, and on the initial masses, ranging in between 20 to $60 M_{\odot}$, where the Bonn tracks imply higher masses for the more evolved objects, compared to the Geneva tracks.

According to the tracks, part of our sample is at the beginning or in an intermediate phase of the MS, while another is at later MS-phases (Bonn) or already close or even beyond the TAMS (Geneva). This division is also found in an ϵ_{C} vs. ϵ_{N} diagram: lower-mass dwarfs are passing through the early CN cycle, while massive supergiants have become significantly nitrogen-enriched. Few objects with particular compositions (e.g., the OC-star) have been discussed, but our major finding on more systematic discrepancies regards the hotter supergiants: though well-enriched in nitrogen, the corresponding depletion in C remains below the predictions. At this stage, it is difficult to interpret this case, also because we do not know the initial v_{rot} of these objects.

In addition to the ϵ_{C} vs. ϵ_{N} diagram, we studied the individual C/N/O abundances as a function of T_{eff} (as a proxy of time) in the light of the evolutionary tracks. Many sample stars follow the theoretical expectations, though certain objects are better represented by the Geneva tracks (e.g., our hottest dwarf

and supergiant), and others by the Bonn tracks (oxygen in most supergiants). Chances are high that our “oxygen problem” mostly affects the cooler dwarfs, since we found no real discrepancies for the other objects.

Due to the small sample size and our selection criterion regarding $v \sin i$, however, definite conclusions are not yet possible, and many questions remain, such as: Is there a fast (Bonn) or slower (Geneva) enrichment? What is the “typical” nitrogen content (if there is any) of early O-dwarfs? To answer these and related questions, many more objects per spectral type need to be analyzed. Nevertheless, and in combination with Fig. 4.7 (N/C as a function of $v \sin i$), some hypotheses could be formulated: Three of the five hotter dwarfs are located close to the initial abundances, while they should already have a well-developed N/C ratio if their initial v_{rot} was significant. Thus, it is likely that these stars started their evolution as slow rotators. From the derived abundance pattern, the same should be true for the OC-supergiant, in line with an identical hypothesis by Martins et al. (2016). Except for HD 151515, all hotter supergiants plus two hotter dwarfs (HD 12993 and HD 96715) have a well-developed N/C pattern, which indicates that an efficient braking mechanism must be present already at relatively early phases (at least if most of these stars were not observed pole-on). Similar conclusions (i.e., previous angular momentum loss, well before the potential bi-stability braking) might also be drawn for two (of four) cooler supergiants (HD 195592 and HD 71304). These notions might provide indirect clues on the “true”²² mass-loss rates of O-stars, assuming that this braking is due to mass loss.

Since in this work we focused on photospheric CNO lines, clumping and X-rays should play a minor role, particularly since the ions that are most influenced by the emission from wind-embedded shocks (C v, N v, O v, and O vi, Carneiro et al. 2016) are basically not included in our present analysis. On the other hand, an optical CNO analysis of the hottest O-stars is significantly hampered by the absence or weakness of corresponding C and O lines (which is the reason that the hottest supergiant in our sample has spectral type O6). For these objects, which are particularly interesting because of their higher masses, a UV analysis is inevitable, and at least then X-ray and clumping effects will need to be accounted for. This is possible already now, thanks to the work by Carneiro et al. (2016) and Sundqvist & Puls (2018), respectively, where the latter included a suitable treatment of porosity effects (also in velocity space) into the FASTWIND code, which might be essential for analyzing abundances from UV lines.

We end our study by concluding that we have developed and tested a method that is big-data-ready, and that FASTWIND is now (almost) well-equipped to be useful in the CNO analysis of statistically significant O-star samples, such as the already available VLT-FLAMES, IACOB, and OWN surveys. On the technical side, we still have to work on the oxygen model atom and to perform careful tests, particularly in the cooler O-dwarf domain. On the scientific side, we note that though the analysis of large samples is of prime importance, also the analysis of individual, peculiar objects such as, e.g., HD 12993 (the “Nstr” star) and HD 152249 (the OC-star) can lead to considerable progress in our understanding of massive stars, since often one might learn more from the deviations than from the consistencies with current theories.

²²i.e., uncontaminated by inhomogeneity-effects

4.A Appendix A: Equivalent width measurements – three typical examples

As discussed in Sect. 4.4.1, we have developed an interactive algorithm (in IDL) to measure the W_{eq} 's of all target lines. Figure 4.8 displays three typical examples, namely for an emission (C III 5696), an absorption (N III 4514), and a blended line (O III 3961), all in the spectrum of HD 46966 (#6). The blue line shows the Gaussian fit (line center of the Gaussian indicated in blue as well), while the red color indicates the wavelength interval used for the fitting procedure and for a direct integration, which was applied to obtain a second, independent measurement. The W_{eq} 's resulting from these two methods are usually very similar (less than 5% difference). In the cases displayed in the upper two panels, we measured, for example, for C III 5696, $W_{\text{eq}}(\text{Gaussian}) = -62 \text{ m\AA}$ vs. $W_{\text{eq}}(\text{direct}) = -57 \text{ m\AA}$, and for N III 4514, $W_{\text{eq}}(\text{Gaussian}) = 112 \text{ m\AA}$ vs. $W_{\text{eq}}(\text{direct}) = 117 \text{ m\AA}$. In cases of blended lines (as in the lowermost panel), we fitted the uncontaminated part of the profile by a corresponding Gaussian, and extended the line wings to simulate the blended part. In this case, a direct integration makes no sense. For the displayed example, O III 3961, we found $W_{\text{eq}}(\text{Gaussian}) = 141 \text{ m\AA}$. For consistency between the first two and the latter cases, we finally used only the values obtained by the Gaussian fit for all lines. Our procedure to derive an estimate on the corresponding errors is described in Sect. 4.4.1.

4.B Appendix B: χ^2 minimization – exemplary cases

To determine the optimum set of abundances and microturbulence(s) for each of our objects, we calculated and analyzed the (reduced) χ^2 for C, N, and O, via a self-written IDL script (see Sect. 4.4.3). In Figs. 4.9, 4.10, and 4.11, we exemplify our analysis by means of the plots produced by this script. These examples refer to the analysis of different elements in different objects, chosen to obtain a fair impression on the general results and problems. The first figure shows our “best” case with many lines available, the second an intermediate one, and the last a case where only few lines are visible.

All three figures have the same organization: The upper panel displays the reduced χ^2 iso-contours in the abundance– v_{mic} plane, where the 1-, 2-, and 3- σ iso-contours (Eq. 4.8) are indicated by the thick lines. The middle panel provides a comparison between the measured and the theoretical W_{eq} 's, including error bars. In particular, the black bars display the measurement uncertainties, while the colored ones correspond to those finally used in our minimization, following Eq. 4.3. Thus, if both bars are equal, the line has been considered with full weight (Eq. 4.5). In this middle panel, the colored squares correspond to the measured W_{eq} , with red for ion II, green for ion III, and blue for ion IV. The theoretical W_{eq} 's are plotted as black asterisks, and are always (by definition) located inside the *used* error bars. The lower panel is divided into two sub-plots, resulting from projecting the reduced χ^2 distribution. On the left, we show χ^2 as a function of abundance, and on the right, as a function of v_{mic} . Each black square represents a model within our grid. The red dash-dotted line refers to the minimum χ^2 value, and the red dashed lines the corresponding 1-, 2-, and 3- σ limits.

Figure 4.9 shows the analysis of oxygen in HD 36512 (O9.7 V) (#1). The upper and lower panels illustrate that the lowest χ^2 is found for $\epsilon_{\text{O}} \sim 8.4$, with an upper limit of 5 km s^{-1} for v_{mic} . The middle panel verifies the generally good agreement between theoretical and observed equivalent widths,

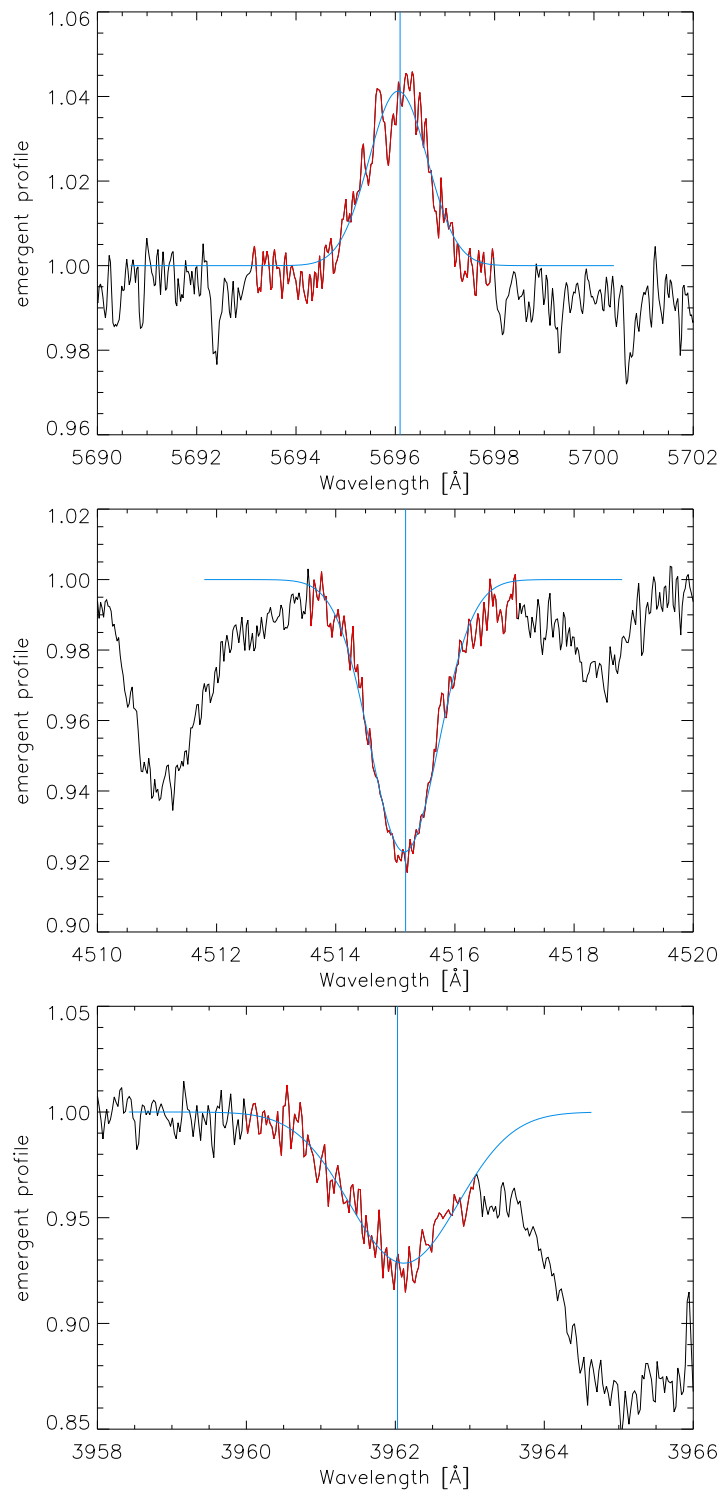


Figure 4.8: Examples for equivalent width measurements via Gaussian fits (blue) and direct integration (with respect to the interval indicated in red): C III 5696, N III 4514, and O III 3961, in the spectrum of HD 46966 (#6).

except for O III 5592, which indicates a larger ϵ_{O} value (see discussion in Sect. 4.5.6).

An example for our nitrogen analysis is displayed in Fig. 4.10, for HD 12993 (O6.5 V((f)) Nstr) (#8). The innermost contour occurring in the upper panel, at $\epsilon_{\text{N}} \sim 8.35$ and $v_{\text{mic}} \sim 16$, represents the model with the lowest χ^2 . The middle panel stresses the good reproduction of the observed lines used in the χ^2 -minimization. The lower panel confirms the estimate of the upper plot: the lowest χ^2 is found for the model calculated with $\epsilon_{\text{N}} = 8.33$, and from a broad distribution centered at $v_{\text{mic}} = 15 \text{ km s}^{-1}$. Since, for this target, the carbon and oxygen analysis suggests $v_{\text{mic}} = 20 \text{ km s}^{-1}$ as the best fitting value, we decided to quote this higher v_{mic} as a general value (see discussion in Sect. 4.4.3).

Finally, Fig. 4.11 provides an example for our carbon analysis, in this case for HD 151515 (O7 II(f)) (#18). The upper panel displays a somewhat degenerate solution, with lowest χ^2 between $8.3 < \epsilon_{\text{C}} < 8.6$, and a large range of possible v_{mic} values. In the middle panel, the restricted number of carbon lines is clearly visible, which are well reproduced. The lower panel allows us to find tighter constraints than the uppermost one. The best-fitting model is given by $\epsilon_{\text{C}} \sim 8.43$, and the optimum v_{mic} can be limited by $\geq 15 \text{ km s}^{-1}$, though the other two elements require an even higher limit, $\geq 20 \text{ km s}^{-1}$.

4.C Appendix C: Line profiles

After identifying the best-fitting model (regarding equivalent widths) via our χ^2 -minimization, we compared the corresponding synthetic profiles with the observed ones. Since now the equivalent widths should agree (on average, and except for non-reproducible lines), also the profiles should agree, if rotational and macroturbulent broadening are accounted for. Since we relied on the $v \sin i$ values inferred by Holgado et al., we only checked for v_{mac} , and adapted this value when necessary (see Sect. 4.5.2), by means of a simple by-eye inspection.

Figures 4.12, 4.13, and 4.14 provide instructive examples for the agreement or disagreement between synthetic and observed line profiles, for the same stars used in the previous appendix 4.B, but now for all analyzed elements. For the sake of clarity, the theoretical profiles have different colors, black for carbon, blue for nitrogen, and red for oxygen.

Figure 4.12 shows the comparison for basically all of our target lines from HD 36512 (#1). For this star, just a few lines have not been used in our χ^2 minimization, namely: C II 3918, 6582; C III 4650, 4651, 5696; N II 4601, 4621; N III 4379, 4641. Moreover, N IV 6380, and the N V lines are not visible in the observed spectrum, and are therefore not included in our analysis.

The carbon and nitrogen lines are generally well reproduced, except for the triplet N III 4634/4640/4641, which, particularly in this temperature range, shows a transition from being refilled into weak emission, and cannot be reproduced by the current FASTWIND version. For details and the origin of this problem, we refer to Rivero González et al. (2011). Also for all of our oxygen target lines there is a satisfactory agreement, aside from O III 5592 which indicates a higher oxygen abundance, as already obvious from the comparison of equivalent widths (Fig. 4.9, middle panel).

For hotter objects as HD 12993 (#8), the analysis becomes more challenging. From Fig. 4.13, it is obvious that C II, N II, and O II lines can no longer be used. Rotation adds to these difficulties. In this case, we used the following lines for the χ^2 minimization: C III 4186, 4647, 4650, 5696; C IV 5801,

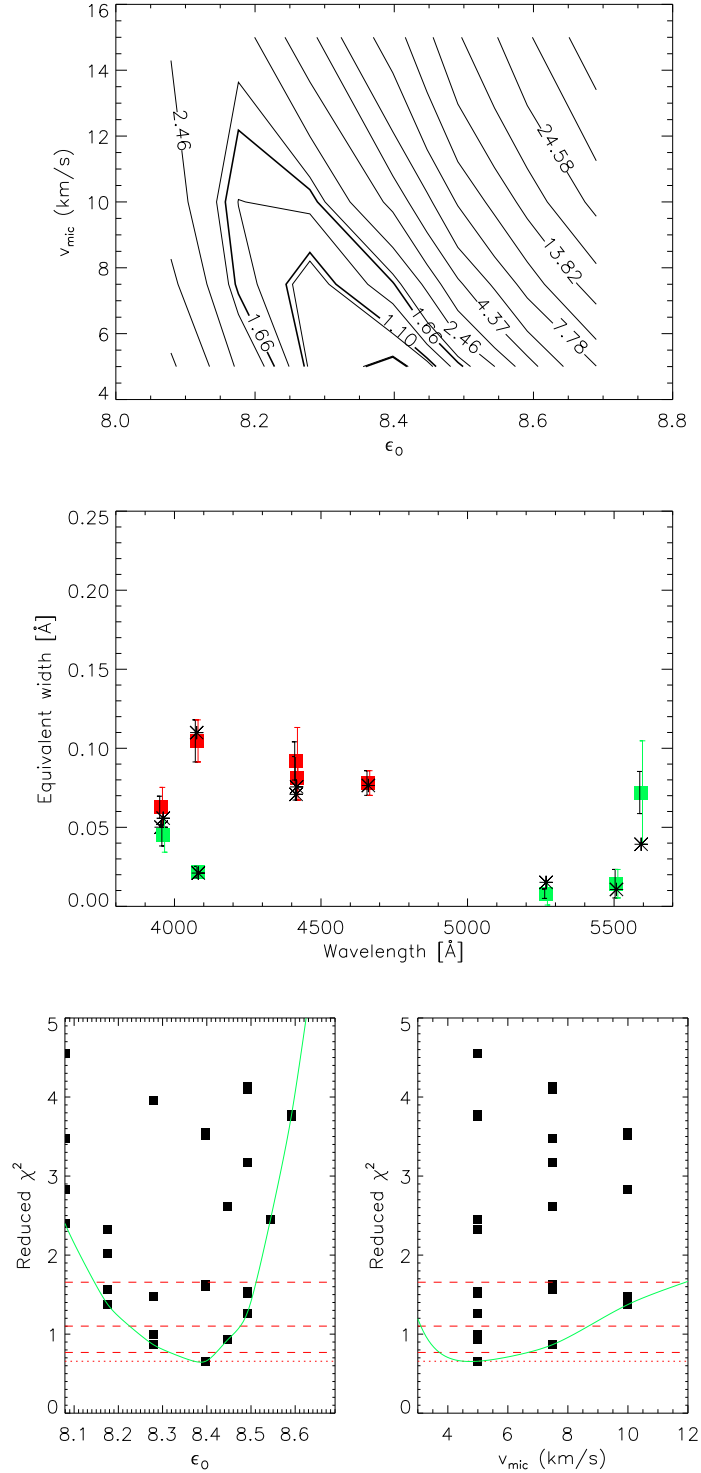


Figure 4.9: Oxygen analysis for HD 36512 (O9.7 V) (#1). The upper panel displays the χ^2_{red} isocontours in the ϵ_0 - v_{mic} plane. The middle panel compares the observed and theoretical equivalent widths including error bars (see text), and visualizes the quality of the best-fitting model. In this case, major discrepancies are only found for O III 5592, which indicates a larger value of ϵ_0 . The lower panels display the χ^2 distribution projected onto the ϵ_0 (left) and the v_{mic} (right) axis.

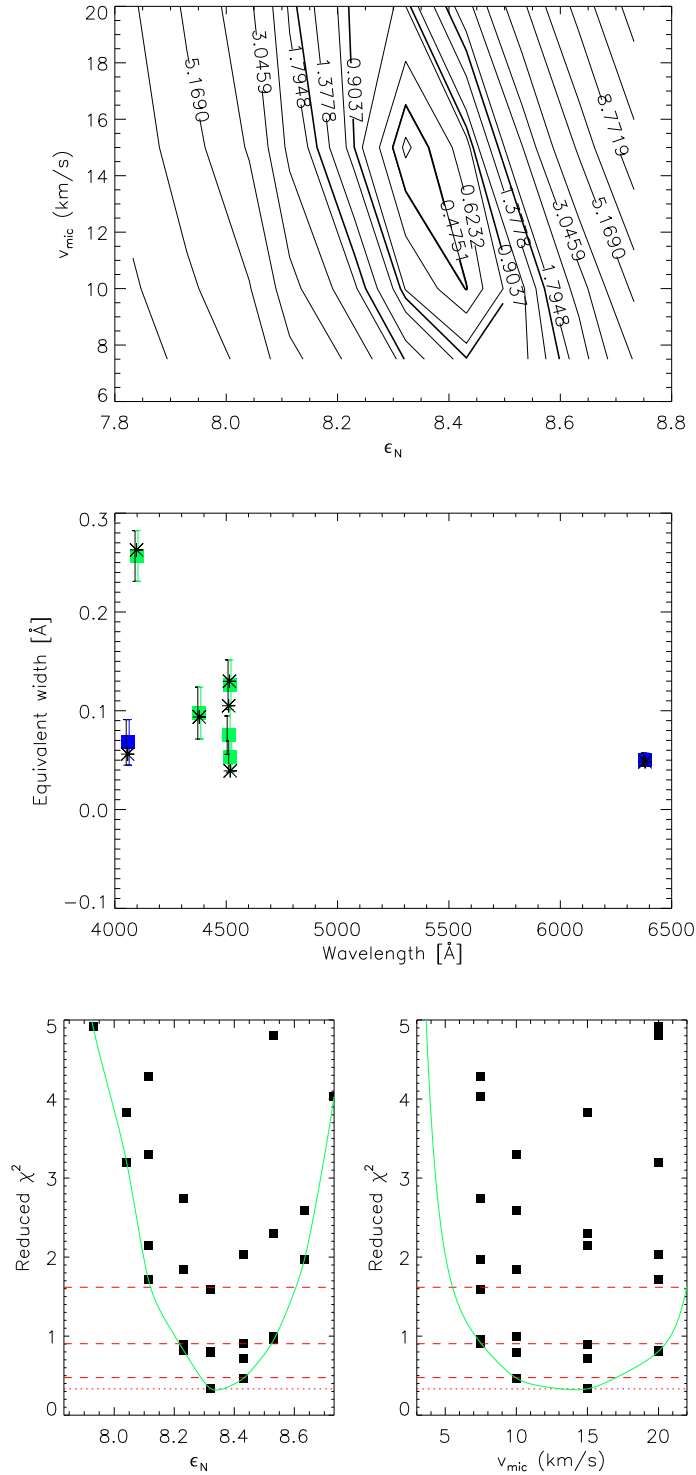


Figure 4.10: As Fig. 4.9, but for nitrogen in HD12993 (O6.5 V((f) Nstr) (#8). In this case, all nitrogen lines are well reproduced.

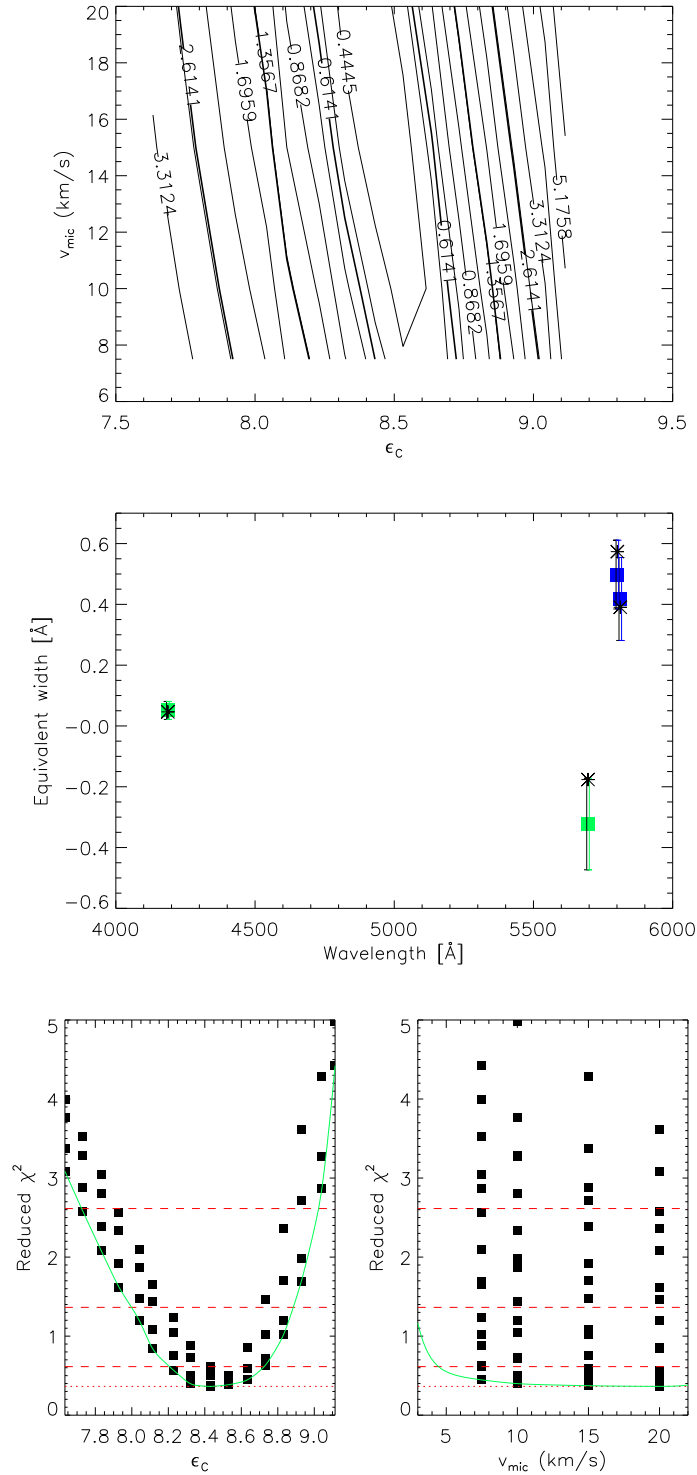


Figure 4.11: As Fig. 4.9, but for carbon in HD151515 (O7 II(f)) (#18). The middle panel clearly shows the restricted number of carbon lines available in hotter supergiants. Only a lower limit can be estimated for v_{mic} (see text).

5811; N III 4097, 4379, 4511, 4515, 4518; N IV 4058, 6380; O III 3961, 4081, 5592. Though the C II lines are basically indistinguishable from the continuum, most of the C III and C IV lines are reproduced (except for C III 5696, which is in a transition phase from absorption to emission, and would require a fine-tuning of the wind description to become improved, if at all). The triplet N III 4634/4640/4641 is in emission, but even though we did not use these lines in our minimization, since the equivalent widths are difficult to estimate, they agree reasonably well with our best-fitting model. As pointed out (and discussed) in the main section, for hotter objects the oxygen abundance estimated from O III 5592 (mostly) agrees with the one derived from the other O III lines, as visible in the last panels. For this and similar objects, we have to rely on the calculated oxygen ionization balance, and have no means to check it, except for the fact that all O II lines should be absent in the theoretical spectra.

For HD 151515 (O7 II(f)) (#18), the number of suitable lines is even more restricted than for the hot dwarf described just above. From Fig. 4.14, we see that only few lines are detectable, whereas the majority is embedded in the noise. In this case, we could use C III 4186, 5696; C IV 5801, 5811; N III 4097, 4379, 4511, 4515, 4518, 4634, 4640; N IV 4058; O III 5508, 5592. In comparison to the observations, the synthetic C III 4647 profile is too strong, while C III 5696 is too weak. The C IV lines show a slight asymmetry, but even though we have a fair representation. The triplet N III 4634/4640/4641 is clearly in emission, and our theoretical emission lines are too weak (improved wind description required!), but all other nitrogen lines are well reproduced. Oxygen displays only few lines, but all of them as calculated from our best-fitting model, and including O III 5592, show a good agreement.

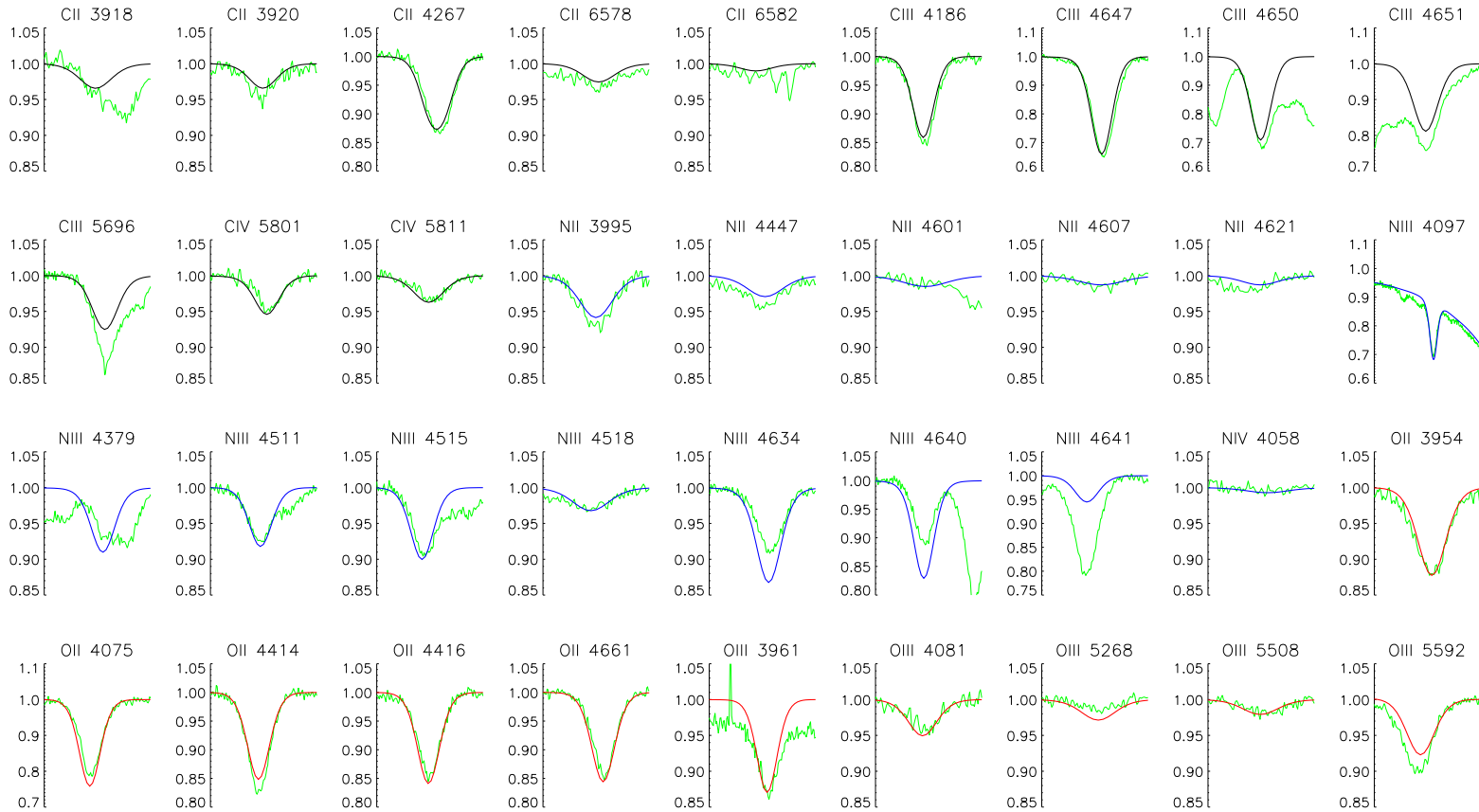


Figure 4.12: HD 36512 (O9.7 V) (#1). Comparison of observed (green) and synthetic line profiles: black – carbon; blue – nitrogen; red – oxygen. The lines N IV 6380, N V 4603, and NV 4619 are not visible (neither in the observations nor in the synthetic spectra), and are not displayed in this figure.

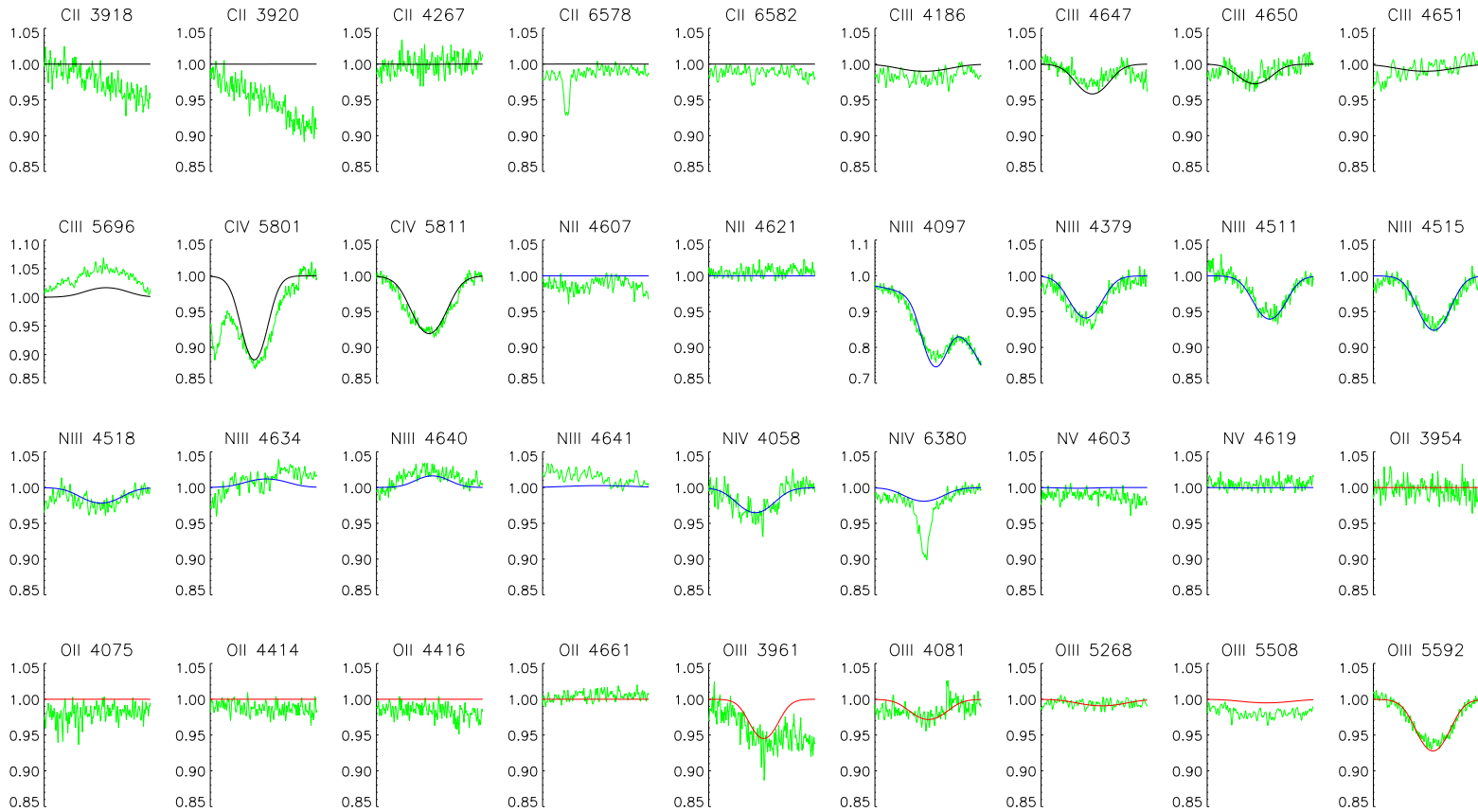


Figure 4.13: As Fig. 4.12, but for HD 12993 (O6.5 V(f) Nstr) (#8). N_{II} 3995, 4601, and the N_{V} lines are not visible (neither in the observations nor in the synthetic spectra), and have been skipped in this figure.

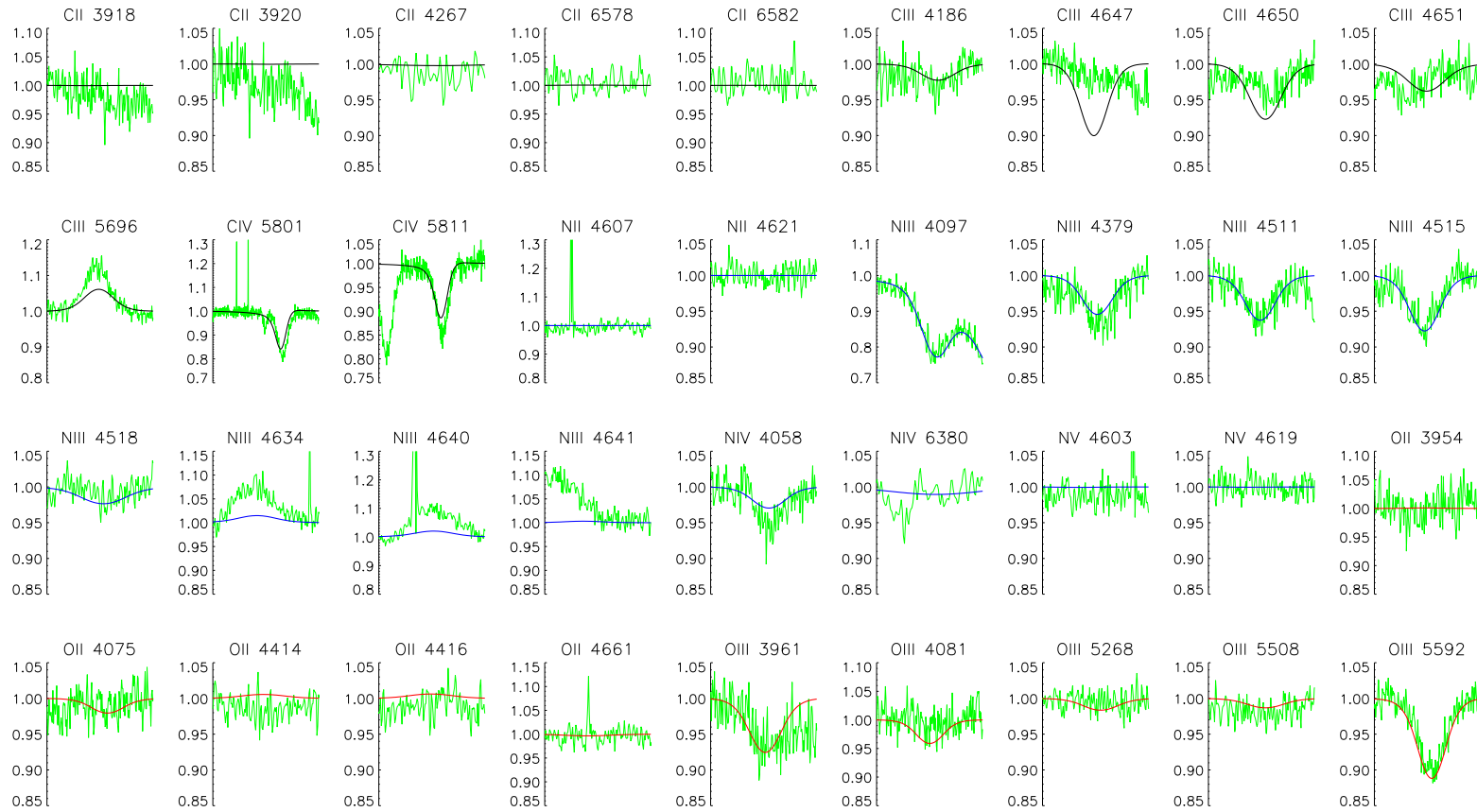


Figure 4.14: As Fig. 4.12, but for HD 151515 (O7 II(f)) (#18). As in the previous figure, the lines N Π 3995, 4601 and N ν 4447 are not visible and therefore not displayed.

Chapter 5

Summary and Conclusions

The complex physics governing the life of massive stars can be studied from many points of view. In this work, we detailed from the smallest impact of a single radiative transition to large structures as the shocks embedded in stellar winds. Independent of the particular relevance on the final results, both need to be precisely described in order to obtain a better reproduction of observations. By the end of this thesis, we are able to obtain CNO abundances with a robust and scalable method, ready to be applied to large samples, which produces results in agreement with theoretical expectations as well as with alternative studies.

Throughout this work, we presented various improvements of the `FASTWIND` code, and we can classify these in two categories: at first, the front-end developments where we implemented the possibility of including shock radiation in the calculation of atmospheric models, and secondly the back-end developments, where we improved the database used for the calculation of carbon collisional and radiative transitions. This last part is hidden from the user inputs, but essential for the realistic description of carbon ionization. In the end, we performed an extensive set of tests to reassure the quality of our results and tested if these were in agreement with theoretical assumptions.

In the first part of this work, we developed, implemented and tested a module to provide the inclusion of X-ray radiation in the calculation of stellar atmospheric models using the `FASTWIND` code. The setup is basically done by three (user-provided) input values, called the X-ray emission parameters: the filling factor, which gives an estimate of the volume fraction that actually emits high energy radiation; the maximum shock temperature, and the radial onset of the emitting plasma. Afterwards we investigated the most affected ions in different stellar conditions. Remarkably, we found that not only metals but also He can be affected by shock emission (Sect. 2.5.1). We also presented a detailed discussion regarding the usage of a radially constant mass absorption coefficient, and estimated under which conditions such approximation is plausible to be adopted (Sect. 2.5.4).

In the second part of this thesis, we improved the data describing the radiative and collisional transitions that control the carbon ionization and excitation stratification. Our new carbon atom was thoroughly tested, including a first spectrum synthesis where we estimated, through a by-eye fit, the carbon abundances of five stars. Another remarkable result was the indirect effect that X-rays can have on the shape of optical carbon (mainly C IV) lines, which is similar to a reduction of the abundance itself (depending on the strength of the X-ray emission, the effect may be similar to a reduction of

0.6 dex). At this point our group had a detailed description of carbon and nitrogen, the latter from the work done by Rivero González et al. (2012a,b). Therefore we were equipped with the tools for analyzing chemical-mixing evolution through the N/C ratio. In order to do a quantitative analysis and to increase the number of objects studied, our methodology had to be automatized.

In the last part we obtained CNO surface abundances for a sample of 18 O-type stars with a new and semi-automatized method, which, after our tests, can now be applied to larger samples. While developing and testing our pipeline for the data analysis at this point, we selected targets which should favor a straightforward abundance analysis: high quality spectra from presumably single and slowly rotating stars. Our method is based on a χ^2 -minimization of the (weighted) deviation between observed and theoretical equivalent widths. This technique allowed us to obtain the best fitting value of abundance and microturbulence in parallel. After obtaining the CNO abundances for all the stars in our sample, we presented an extensive investigation of the evolutionary stage of each target by analyzing their N/C and N/O ratios. The majority of our results were in accordance with the predicted theoretical evolution of massive stars considering chemical mixing, and agreed well with recent results obtained for the same targets by other groups. Briefly summarized, the early-type objects have abundances closer to the solar one, while the evolved targets present a nitrogen enrichment with a clear sign for chemical mixing (see Sect. 4.6.2 for details).

Now that we acquired a considerable knowledge regarding the quality and reliability of our tools (at least for the N/C ratio, see below), our chemical analysis may be extended to more complex objects as fast rotating stars, or using spectra with lower quality. We concentrated our study on spectra showing lines of different ionization stages of the same atomic species, which is limited by the effective temperature range of the selected targets. As we now trust the results produced by our semi-automatized method, we may also extend our analysis to cooler and hotter objects, for which only one ion has identifiable spectroscopic lines in the observations.

As for the science, also our code evolves continuously, and with this work we are in a position to provide state-of-the-art results with a particularly fast, stable and effective methodology. Considering the results and conclusions reached throughout this thesis, our research group has made a further step in the chemical analysis of massive stars, by providing a stable code, plus a semi-automatized methodology that can be used for large samples. In parallel, along the last chapters, we also discussed how our conclusions enable further evidences of many theoretical predictions, again contributing to the progress of our knowledge about O-stars.

However this is by no means a finished work. One of the main open questions is whether the abundances obtained from the UV and from the optical agree, and how well they do. This investigation itself requires many other studies, as for example, the development of a detailed model atom for oxygen (similar to the study presented in Chapter 3 for carbon), a study of the X-ray parameters scalability throughout the winds, and to understand the impact of clumping and porosity on the UV spectrum of massive stars. With the UV analysis, we finally will be able to determine the best fitting values of the X-ray parameters using the module described in Chapter 2. With the method presented in Chapter 4, we will be able to distinguish how well the optical metal lines still agree with observations after including the shock radiation. Summarizing, this work lays the basis for many relevant future studies, besides all the new results presented in the last chapters.

Any new investigation will produce newer versions of the `FASTWIND` code which then requires

the repetition of some of the tests presented in this thesis. This last point shows the necessity of continuous revision and enlargement of pipelines, not only to automatize tests, but also to calculate model grids and to understand the role of each parameter in the model description. Ultimately, the complete work presented in this thesis and all future steps taken from the results obtained here, will make our knowledge closer to our final objective: the precise reproduction of what is observed in nature and to obtain a precise virtual representation of objects (presently) impossible to be observed.

Bibliography

- Abbott, D. C. 1980: *The theory of radiatively driven stellar winds. I - A physical interpretation*, ApJ, 242, 1183
- Aggarwal, K. M. & Keenan, F. P. 2004: *Electron Impact Excitation of C IV*, Physica Scripta, 69, 385
- Allard, N., Artru, M.-C., Lanz, T., & Le Dourneuf, M. 1990: *Compilation of atomic oscillator strengths for carbon, nitrogen and oxygen ions - The beryllium isoelectronic sequence (C III, N IV, and O V)*, A&AS, 84, 563
- Allen, C. W. 1973, *Astrophysical quantities* (London: University of London, Athlone Press, 1973, 3rd ed.)
- Asplund, M., Grevesse, N., Sauval, A. J., & Scott, P. 2009: *The Chemical Composition of the Sun*, ARA&A, 47, 481
- Barbá, R. H., Gamen, R., Arias, J. I., Morrell, N., Maíz Apellániz, J., Alfaro, E., Walborn, N., & Sota, A. 2010: *Spectroscopic survey of galactic O and WN stars. OWN Survey: new binaries and trapezium-like systems*, in Revista Mexicana de Astronomía y Astrofísica, vol. 27, Vol. 38, Revista Mexicana de Astronomía y Astrofísica Conference Series, 30–32
- Barbá, R. H., Gamen, R., Arias, J. I., & Morrell, N. I. 2017: *OWN Survey: a spectroscopic monitoring of Southern Galactic O and WN-type stars*, in IAU Symposium, Vol. 329, The Lives and Death-Throes of Massive Stars, ed. J. J. Eldridge, J. C. Bray, L. A. S. McClelland, & L. Xiao, 89–96
- Behrend, R. & Maeder, A. 2001: *Formation of massive stars by growing accretion rate*, A&A, 373, 190
- Bernasconi, P. A. & Maeder, A. 1996: *About the absence of a proper zero age main sequence for massive stars.*, A&A, 307, 829
- Bièmont, E. 1977: *Theoretical oscillator strengths in the lithium isoelectronic sequence ($3 \leq Z \leq 22$)*, A&AS, 27, 489
- Bolton, C. T. & Rogers, G. L. 1978: *The binary frequency of the OBN and OBC stars*, ApJ, 222, 234
- Bouret, J.-C., Hillier, D. J., Lanz, T., & Fullerton, A. W. 2012: *Properties of Galactic early-type O-supergiants. A combined FUV-UV and optical analysis*, A&A, 544, A67

- Bouret, J.-C., Lanz, T., & Hillier, D. J. 2005: *Lower mass loss rates in O-type stars: Spectral signatures of dense clumps in the wind of two Galactic O4 stars*, A&A, 438, 301
- Bouret, J.-C., Lanz, T., Martins, F., Marcolino, W. L. F., Hillier, D. J., Depagne, E., & Hubeny, I. 2013: *Massive stars at low metallicity. Evolution and surface abundances of O dwarfs in the SMC*, A&A, 555, A1
- Boyajian, T. S., Beaulieu, T. D., Gies, D. R., Grundstrom, E., Huang, W., McSwain, M. V., Riddle, R. L., Wingert, D. W., & De Becker, M. 2005: *The Massive Runaway Stars HD 14633 and HD 15137*, ApJ, 621, 978
- Bresolin, F., Crowther, P. A., & Puls, J., eds. 2008, IAU Symposium, Vol. 250, IAU 250 Massive Stars as Cosmic Engines
- Bressan, A., Fagotto, F., Bertelli, G., & Chiosi, C. 1993: *Evolutionary sequences of stellar models with new radiative opacities. II - $Z = 0.02$* , A&AS, 100, 647
- Bromm, V., Kudritzki, R. P., & Loeb, A. 2001: *Generic Spectrum and Ionization Efficiency of a Heavy Initial Mass Function for the First Stars*, ApJ, 552, 464
- Brott, I., de Mink, S. E., Cantiello, M., Langer, N., de Koter, A., Evans, C. J., Hunter, I., Trundle, C., & Vink, J. S. 2011: *Rotating massive main-sequence stars. I. Grids of evolutionary models and isochrones*, A&A, 530, A115
- Bruccato, R. J. & Mihalas, D. 1971: *On the excitation mechanism of M emission in the Of stars*, MNRAS, 154, 491
- Butler, K. & Giddings, J. R. 1985: *notitle*, Newsl. Anal. Astron. Spectra, 9
- Cantiello, M., Langer, N., Brott, I., de Koter, A., Shore, S. N., Vink, J. S., Voegler, A., Lennon, D. J., & Yoon, S.-C. 2009: *Sub-surface convection zones in hot massive stars and their observable consequences*, A&A, 499, 279
- Carneiro, L. P., Puls, J., & Hoffmann, T. L. 2018: *Carbon line formation and spectroscopy in O-type stars*, A&A, 615, A4
- Carneiro, L. P., Puls, J., Sundqvist, J. O., & Hoffmann, T. L. 2016: *Atmospheric NLTE models for the spectroscopic analysis of blue stars with winds. III. X-ray emission from wind-embedded shocks*, A&A, 590, A88
- Cassinelli, J. & Olson, G. 1979: *The effects of coronal regions on the X-ray flux and ionization conditions in the winds of OB supergiants and Of stars*, ApJ, 229, 304
- Cassinelli, J. P., Cohen, D. H., Macfarlane, J. J., Drew, J. E., Lynas-Gray, A. E., Hoare, M. G., Vallerga, J. V., Welsh, B. Y., Vedder, P. W., Hubeny, I., & Lanz, T. 1995: *EUVE spectroscopy of epsilon Canis Majoris (B2 II) from 70 to 730 Å*, ApJ, 438, 932

- Cassinelli, J. P., Cohen, D. H., Macfarlane, J. J., Sanders, W. T., & Welsh, B. Y. 1994: *X-ray emission from near-main-sequence B stars*, ApJ, 421, 705
- Cassinelli, J. P. & Swank, J. H. 1983: *X-ray spectra of Orion OB supergiants*, ApJ, 271, 681
- Castor, J. I., Abbott, D. C., & Klein, R. I. 1975: *Radiation-driven winds in Of stars*, ApJ, 195, 157
- Castro, N., Fossati, L., Langer, N., Simón-Díaz, S., Schneider, F. R. N., & Izzard, R. G. 2014: *The spectroscopic Hertzsprung-Russell diagram of Galactic massive stars*, A&A, 570, L13
- Chiappini, C. 2001: *The Formation and Evolution of the Milky Way*, American Scientist, 89, 506
- Chiappini, C. 2002: *Abundance Gradients as a tool for understanding the Formation of the Milky Way*, Ap&SS, 281, 253
- Chlebowski, T., Harnden, F., & Sciortino, S. 1989: *The Einstein X-ray Observatory Catalog of O-type stars*, ApJ, 341, 427
- Cohen, D. H., Cassinelli, J. P., & MacFarlane, J. J. 1997: *ROSAT PSPC Observations of 27 Near-Main-Sequence B Stars*, ApJ, 487, 867
- Cohen, D. H., Cooper, R. G., Macfarlane, J. J., Owocki, S. P., Cassinelli, J. P., & Wang, P. 1996: *Evidence for Wind Attenuation and a Multitemperature Plasma in the Combined EUVE and ROSAT Observations of epsilon Canis Majoris (B2 II)*, ApJ, 460, 506
- Cohen, D. H., Gagné, M., Leutenegger, M. A., MacArthur, J. P., Wollman, E. E., Sundqvist, J. O., Fullerton, A. W., & Owocki, S. P. 2011: *Chandra X-ray spectroscopy of the very early O supergiant HD 93129A: constraints on wind shocks and the mass-loss rate*, MNRAS, 415, 3354
- Cohen, D. H., Kuhn, M. A., Gagné, M., Jensen, E. L. N., & Miller, N. A. 2008: *Chandra spectroscopy of the hot star β Crucis and the discovery of a pre-main-sequence companion*, MNRAS, 386, 1855
- Cohen, D. H., Leutenegger, M. A., Wollman, E. E., Zsargó, J., Hillier, D. J., Townsend, R. H. D., & Owocki, S. P. 2010: *A mass-loss rate determination for ζ Puppis from the quantitative analysis of X-ray emission-line profiles*, MNRAS, 405, 2391
- Cohen, D. H., Li, Z., Gayley, K. G., Owocki, S. P., Sundqvist, J. O., Petit, V., & Leutenegger, M. A. 2014a: *Measuring the shock-heating rate in the winds of O stars using X-ray line spectra*, MNRAS, 444, 3729
- Cohen, D. H., Wollman, E. E., Leutenegger, M. A., Sundqvist, J. O., Fullerton, A. W., Zsargó, J., & Owocki, S. P. 2014b: *Measuring mass-loss rates and constraining shock physics using X-ray line profiles of O stars from the Chandra archive*, MNRAS, 439, 908
- Cowley, C. R. 1971: *An approximate Stark broadening formula for use in spectrum synthesis*, The Observatory, 91, 139
- Crowther, P. 2007: *Physical properties of Wolf-Rayet stars*, ARA&A, 45, 177

- Crowther, P. A., Caballero-Nieves, S. M., Bostroem, K. A., Maíz Apellániz, J., Schneider, F. R. N., Walborn, N. R., Angus, C. R., Brott, I., Bonanos, A., de Koter, A., de Mink, S. E., et al. 2016: *The R136 star cluster dissected with Hubble Space Telescope/STIS. I. Far-ultraviolet spectroscopic census and the origin of He II $\lambda 1640$ in young star clusters*, MNRAS, 458, 624
- Crowther, P. A., Hillier, D. J., Evans, C. J., Fullerton, A. W., De Marco, O., & Willis, A. J. 2002: *Revised Stellar Temperatures for Magellanic Cloud O Supergiants from Far Ultraviolet Spectroscopic Explorer and Very Large Telescope UV-Visual Echelle Spectrograph Spectroscopy*, ApJ, 579, 774
- Cunto, W. & Mendoza, C. 1992: *The Opacity Project - the Topbase Atomic Database*, Revista Mexicana de Astronomia y Astrofisica, vol. 23, 23, 107
- Daflon, S. & Cunha, K. 2004: *Galactic Metallicity Gradients Derived from a Sample of OB Stars*, ApJ, 617, 1115
- Daflon, S., Cunha, K., & Becker, S. R. 1999: *Chemical Abundances of OB Stars in the Cepheus OB2 Association*, ApJ, 522, 950
- Daflon, S., Cunha, K., Becker, S. R., & Smith, V. V. 2001a: *Chemical Abundances of OB Stars in Five OB Associations*, ApJ, 552, 309
- Daflon, S., Cunha, K., & Butler, K. 2004: *Chemical Abundances for a Sample of Southern OB Stars*, ApJ, 604, 362
- Daflon, S., Cunha, K., Butler, K., & Smith, V. V. 2001b: *Chemical Abundances of OB Stars with High Projected Rotational Velocities*, ApJ, 563, 325
- Daltabuit, E. & Cox, D. 1972: *K-Shell Photoionization Cross-Sections*, ApJ, 177, 855
- de Mink, S. E., Langer, N., Izzard, R. G., Sana, H., & de Koter, A. 2013: *The Rotation Rates of Massive Stars: The Role of Binary Interaction through Tides, Mass Transfer, and Mergers*, ApJ, 764, 166
- Dessart, L. & Owocki, S. P. 2003: *Two-dimensional simulations of the line-driven instability in hot-star winds*, A&A, 406, L1
- Drout, M. R., Massey, P., & Meynet, G. 2012: *The Yellow and Red Supergiants of M33*, ApJ, 750, 97
- Dufton, P. L., Langer, N., Dunstall, P. R., Evans, C. J., Brott, I., de Mink, S. E., Howarth, I. D., Kennedy, M., McEvoy, C., Potter, A. T., Ramírez-Agudelo, O. H., et al. 2013: *The VLT-FLAMES Tarantula Survey. X. Evidence for a bimodal distribution of rotational velocities for the single early B-type stars*, A&A, 550, A109
- Duric, N. 2003, Advanced Astrophysics (Cambridge University Press)
- Eissner, W. 1991: *Superstructure - an atomic structure code*, J. Phys. IV (France), 1, C1

- Eissner, W. & Nussbaumer, H. 1969, in *Premiere Reunion de l'Association Europeene de Spectroscopie Atomique* No. No. 42 (Paris-Orsay: Faculte des Sciences)
- Ekström, S., Georgy, C., Eggenberger, P., Meynet, G., Mowlavi, N., Wyttenbach, A., Granada, A., Decressin, T., Hirschi, R., Frischknecht, U., Charbonnel, C., et al. 2012: *Grids of stellar models with rotation. I. Models from 0.8 to 120 M_{sun} at solar metallicity ($Z = 0.014$)*, A&A, 537, A146
- Evans, C., Hunter, I., Smartt, S., Lennon, D., de Koter, A., Mokiem, R., Trundle, C., Dufton, P., Ryans, R., Puls, J., Vink, J., et al. 2008: *The VLT-FLAMES Survey of Massive Stars*, The Messenger, 131, 25
- Evans, C. J., Lennon, D. J., Smartt, S. J., & Trundle, C. 2006: *The VLT-FLAMES survey of massive stars: observations centered on the Magellanic Cloud clusters NGC 330, NGC 346, NGC 2004, and the N11 region*, A&A, 456, 623
- Evans, C. J., Smartt, S. J., Lee, J.-K., & and 23 coauthors. 2005: *The VLT-FLAMES survey of massive stars: Observations in the Galactic clusters NGC 3293, NGC 4755 and NGC 6611*, A&A, 437, 467
- Evans, C. J., Taylor, W. D., Hénault-Brunet, V., Sana, H., de Koter, A., Simón-Díaz, S., Carraro, G., Bagnoli, T., Bastian, N., Bestenlehner, J. M., Bonanos, A. Z., et al. 2011: *The VLT-FLAMES Tarantula Survey. I. Introduction and observational overview*, A&A, 530, A108
- Fagotto, F., Bressan, A., Bertelli, G., & Chiosi, C. 1994a: *Evolutionary sequences of stellar models with new radiative opacities. III. $Z=0.0004$ and $Z=0.05$* , A&AS, 104, 365
- Fagotto, F., Bressan, A., Bertelli, G., & Chiosi, C. 1994b: *Evolutionary sequences of stellar models with new radiative opacities. IV. $Z=0.004$ and $Z=0.008$* , A&AS, 105, 29
- Fagotto, F., Bressan, A., Bertelli, G., & Chiosi, C. 1994c: *Evolutionary sequences of stellar models with very high metallicity. V. $Z=0.1$* , A&AS, 105, 39
- Feiveson, A. & Delaney, F. 1968, *The Distribution and Properties of a Weighted Sum of Chi Squares*, NASA technical note (National Aeronautics and Space Administration)
- Feldmeier, A. 1995: *Time-dependent structure and energy transfer in hot star winds.*, A&A, 299, 523
- Feldmeier, A., Kudritzki, R.-P., Palsa, R., Pauldrach, A. W. A., & Puls, J. 1997a: *The X-ray emission from shock cooling zones in O star winds.*, A&A, 320, 899
- Feldmeier, A., Puls, J., & Pauldrach, A. W. A. 1997b: *A possible origin for X-rays from O stars.*, A&A, 322, 878
- Fosbury, R. A. E., Villar-Martín, M., Humphrey, A., Lombardi, M., Rosati, P., Stern, D., Hook, R. N., Holden, B. P., Stanford, S. A., Squires, G. K., Rauch, M., et al. 2003: *Massive Star Formation in a Gravitationally Lensed H II Galaxy at $z = 3.357$* , ApJ, 596, 797
- Fullerton, A. W., Massa, D. L., & Prinja, R. K. 2006: *The Discordance of Mass-Loss Estimates for Galactic O-Type Stars*, ApJ, 637, 1025

- Gabler, R., Gabler, A., Kudritzki, R. P., Puls, J., & Pauldrach, A. 1989: *Unified NLTE model atmospheres including spherical extension and stellar winds - Method and first results*, A&A, 226, 162
- Garcia, M. 2005: *A Study of Massive Stars from High Resolution Spectroscopy in the Far-UV and UV*, PhD thesis, University of La Laguna (Teneriffe)
- Garmany, C. D., Conti, P. S., & Chiosi, C. 1982: *The initial mass function for massive stars*, ApJ, 263, 777
- Giddings, J. R. 1981 PhD thesis, University of London, (1981)
- Girardi, L., Bressan, A., Chiosi, C., Bertelli, G., & Nasi, E. 1996: *Evolutionary sequences of stellar models with new radiative opacities. VI. $Z=0.0001$* , A&AS, 117, 113
- Glass, R. 1983: *Electric Quadrupole Transitions in the Beryllium Isoelectronic Sequence*, Ap&SS, 92, 307
- Gräfener, G., Koesterke, L., & Hamann, W.-R. 2002: *Line-blanketed model atmospheres for WR stars*, A&A, 387, 244
- Grigsby, J. A., Morrison, N. D., & Anderson, L. S. 1992: *Non-LTE, line-blanketed model atmospheres for late O- and early B-type stars*, ApJS, 78, 205
- Grin, N. J., Ramírez-Agudelo, O. H., de Koter, A., Sana, H., Puls, J., Brott, I., Crowther, P. A., Dufton, P. L., Evans, C. J., Gräfener, G., Herrero, A., et al. 2017: *The VLT-FLAMES Tarantula Survey. XXV. Surface nitrogen abundances of O-type giants and supergiants*, A&A, 600, A82
- Groenewegen, M. A. T. & Lamers, H. J. G. L. M. 1989: *The winds of O-stars. I - an analysis of the UV line profiles with the SEI method*, A&AS, 79, 359
- Haemmerlé, L., Eggenberger, P., Meynet, G., Maeder, A., & Charbonnel, C. 2016: *Massive star formation by accretion. I. Disc accretion*, A&A, 585, A65
- Hamann, W.-R. & Oskinova, L. 2012: *Stellar Winds of Hot Stars - Diagnostics from UV spectra*, in COSPAR Meeting, Vol. 39, 39th COSPAR Scientific Assembly, 716
- Harnden, Jr., F. R., Branduardi, G., Gorenstein, P., Grindlay, J., Rosner, R., Topka, K., Elvis, M., Pye, J. P., & Vaiana, G. S. 1979: *Discovery of an X-ray star association in VI Cygni /Cyg OB2/*, ApJ, 234, L51
- Haser, S. M. 1995: *UV spectroscopy of hot stars in the Local Group (in German)*, PhD thesis, Ludwig-Maximilians-Universität München
- Hauschildt, P. H. 1992: *A fast operator perturbation method for the solution of the special relativistic equation of radiative transfer in spherical symmetry*, Journal of Quantitative Spectroscopy and Radiative Transfer, 47, 433

- Heger, A. & Langer, N. 2000: *Presupernova Evolution of Rotating Massive Stars. II. Evolution of the Surface Properties*, ApJ, 544, 1016
- Heger, A., Langer, N., & Woosley, S. E. 2000: *Presupernova Evolution of Rotating Massive Stars. I. Numerical Method and Evolution of the Internal Stellar Structure*, ApJ, 528, 368
- Herrero, A., Kudritzki, R. P., Vilchez, J. M., Kunze, D., Butler, K., & Haser, S. 1992: *Intrinsic parameters of galactic luminous OB stars*, A&A, 261, 209
- Herrero, A., Puls, J., & Villamariz, M. R. 2000: *Fundamental parameters of Galactic luminous OB stars. IV. The upper HR diagram*, A&A, 354, 193
- Herrero, A., Simon-Diaz, S., Najarro, F., & Ribas, I. 2007: *Single and Binary Massive Stars Close to the Zero Age Main Sequence*, in Astronomical Society of the Pacific Conference Series, Vol. 367, Massive Stars in Interactive Binaries, ed. N. St.-Louis & A. F. J. Moffat, 67
- Hertzsprung, E. 1911: *Ueber die Verwendung photographischer effektiver Wellenlaengen zur Bestimmung von Farbaequivalenten*, Publikationen des Astrophysikalischen Observatoriums zu Potsdam, 63
- Hervé, A., Rauw, G., & Nazé, Y. 2013: *A detailed X-ray investigation of ζ Puppis. III. Spectral analysis of the whole RGS spectrum*, A&A, 551, A83
- Hillier, D. J. 1991: *The effects of electron scattering and wind clumping for early emission line stars*, A&A, 247, 455
- Hillier, D. J., Kudritzki, R. P., Pauldrach, A. W., Baade, D., Cassinelli, J. P., Puls, J., & Schmitt, J. H. M. M. 1993: *The 0.1-2.5-KEV X-Ray Spectrum of the O4F-STAR Zeta-Puppis*, A&A, 276, 117
- Hillier, D. J. & Miller, D. L. 1998: *The Treatment of Non-LTE Line Blanketing in Spherically Expanding Outflows*, ApJ, 496, 407
- Holgado, G., Simón-Díaz, S., Barbá, R. H., Puls, J., Herrero, A., Castro, N., Garcia, M., Maíz Apellániz, J., Negueruela, I., & Sabín-Sanjulián, C. 2018: *The IACOB project. V. Spectroscopic parameters of the O-type stars in the modern grid of standards for spectral classification*, A&A, 613, A65
- Howarth, I. D., Siebert, K. W., Hussain, G. A. J., & Prinja, R. K. 1997: *Cross-correlation characteristics of OB stars from IUE spectroscopy*, MNRAS, 284, 265
- Hubeny, I. 1998: *Non-LTE line-blanketed model atmospheres of hot stars*, in Astronomical Society of the Pacific Conference Series, Vol. 138, 1997 Pacific Rim Conference on Stellar Astrophysics, ed. K. L. Chan, K. S. Cheng, & H. P. Singh, 139
- Huenemoerder, D. P., Oskinova, L. M., Ignace, R., Waldron, W. L., Todt, H., Hamaguchi, K., & Kitamoto, S. 2012: *On the Weak-wind Problem in Massive Stars: X-Ray Spectra Reveal a Massive Hot Wind in μ Columbae*, ApJ, 756, L34

- Hunter, I., Brott, I., Lennon, D. J., Langer, N., Dufton, P. L., Trundle, C., Smartt, S. J., de Koter, A., Evans, C. J., & Ryans, R. S. I. 2008: *The VLT FLAMES Survey of Massive Stars: Rotation and Nitrogen Enrichment as the Key to Understanding Massive Star Evolution*, ApJ, 676, L29
- Hunter, I., Dufton, P. L., Smartt, S. J., Ryans, R. S. I., Evans, C. J., Lennon, D. J., Trundle, C., Hubeny, I., & Lanz, T. 2007: *The VLT-FLAMES survey of massive stars: surface chemical compositions of B-type stars in the Magellanic Clouds*, A&A, 466, 277
- Kaastra, J. & Mewe, R. 1993: *X-ray emission from thin plasmas. I - Multiple Auger ionisation and fluorescence processes for Be to Zn*, A&A, 97, 443
- Kane, L., McKeith, C. D., & Dufton, P. L. 1980: *Carbon, nitrogen, and oxygen abundances in loose association and field B-type stars*, A&A, 84, 115
- Kaufer, A., Wolf, B., Andersen, J., & Pasquini, L. 1997: *FEROS, the fiber-fed extended range optical spectrograph for the ESO 1.52-m telescope.*, The Messenger, 89, 1
- Kelleher, D. E., Mohr, P. J., Martin, W. C., Wiese, W. L., Sugar, J., Fuhr, J. R., Olsen, K., Musgrove, A., Reader, J., Sansonetti, C. J., & Dalton, G. R. 1999: *New NIST Atomic Spectra Database*, in Society of Photo-Optical Instrumentation Engineers (SPIE) Conference Series, Vol. 3818, Society of Photo-Optical Instrumentation Engineers (SPIE) Conference Series, ed. G. R. Carruthers & K. F. Dymond, 170
- Keszthelyi, Z., Puls, J., & Wade, G. A. 2017: *Modeling the early evolution of massive OB stars with an experimental wind routine. The first bi-stability jump and the angular momentum loss problem*, A&A, 598, A4
- Köhler, K., Langer, N., de Koter, A., de Mink, S. E., Crowther, P. A., Evans, C. J., Gräfener, G., Sana, H., Sanyal, D., Schneider, F. R. N., & Vink, J. S. 2015: *The evolution of rotating very massive stars with LMC composition*, A&A, 573, A71
- Krolik, J. & Raymond, J. 1985: *Radiation pressure-driven shocks in winds from hot stars*, ApJ, 298, 660
- Krtićka, J. & Kubát, J. 2001: *Multicomponent radiatively driven stellar winds. I. Nonisothermal three-component wind of hot B stars*, A&A, 369, 222
- Krtićka, J. & Kubát, J. 2009: *NLTE models of line-driven stellar winds - III. Influence of X-ray radiation on wind structure of O stars*, MNRAS, 394, 2065
- Krtićka, J. & Kubát, J. 2012: *Influence of extreme ultraviolet radiation on the P V ionization fraction in hot star winds*, MNRAS, 427, 84
- Kubát, J., Puls, J., & Pauldrach, A. W. A. 1999: *Thermal balance of electrons in calculations of model stellar atmospheres*, A&A, 341, 587
- Kudritzki, R.-P. & Puls, J. 2000: *Winds from Hot Stars*, ARA&A, 38, 613

- Kuiper, G. P. 1938: *The Empirical Mass-Luminosity Relation.*, ApJ, 88, 472
- Kupka, F., Piskunov, N., Ryabchikova, T. A., Stempels, H. C., & Weiss, W. W. 1999: *VALD-2: Progress of the Vienna Atomic Line Data Base*, A&AS, 138, 119
- Kupka, F. G., Ryabchikova, T. A., Piskunov, N. E., Stempels, H. C., & Weiss, W. W. 2000: *VALD-2 – The New Vienna Atomic Line Database*, Baltic Astronomy, 9, 590
- Lamers, H. & Rogerson, J. 1978: *The expanding envelope of Tau SCO (B0 V)*, A&A, 66, 417
- Lamers, H. J. G. L. M., Cerruti-Sola, M., & Perinotto, M. 1987: *The 'SEI' method for accurate and efficient calculations of line profiles in spherically symmetric stellar winds*, ApJ, 314, 726
- Lamers, H. J. G. L. M. & Morton, D. C. 1976: *Mass ejection from the O4f star Zeta Puppis*, ApJS, 32, 715
- Langer, N. 2012: *Presupernova Evolution of Massive Single and Binary Stars*, ARA&A, 50, 107
- Langer, N., Cantiello, M., Yoon, S.-C., Hunter, I., Brott, I., Lennon, D., de Mink, S., & Verheijdt, M. 2008: *Rotation and Massive Close Binary Evolution*, in IAU Symposium, Vol. 250, Massive Stars as Cosmic Engines, ed. F. Bresolin, P. A. Crowther, & J. Puls, 167–178
- Langer, N., Heger, A., & Fliegner, J. 1997: *Rotation: a fundamental parameter of massive stars.*, in IAU Symposium, Vol. 189, IAU Symposium, ed. T. R. Bedding, A. J. Booth, & J. Davis, 343–348
- Langer, N. & Kudritzki, R. P. 2014: *The spectroscopic Hertzsprung-Russell diagram*, A&A, 564, A52
- Lefever, K. 2007: *Fundamental parameters of B-type stars - Application to a HIPPARCOS sample of B supergiants and a CoRoT sample of B dwarfs*, PhD thesis, Catholic University Leuven, Belgium
- Leutenegger, M. A., Cohen, D., Neely, J., Owocki, S., & Sundqvist, J. 2013a: *Benchmarking Abundance Determinations of Massive Stars with X-ray Spectroscopy*, in Massive Stars: From alpha to Omega, 42
- Leutenegger, M. A., Cohen, D. H., Sundqvist, J. O., & Owocki, S. P. 2013b: *Constraints on Porosity and Mass Loss in O-star Winds from the Modeling of X-Ray Emission Line Profile Shapes*, ApJ, 770, 80
- Leutenegger, M. A., Paerels, F. B. S., Kahn, S. M., & Cohen, D. H. 2006: *Measurements and Analysis of Helium-like Triplet Ratios in the X-Ray Spectra of O-Type Stars*, ApJ, 650, 1096
- Levesque, E. M. 2010: *The Physical Properties of Red Supergiants*, in Astronomical Society of the Pacific Conference Series, Vol. 425, Hot and Cool: Bridging Gaps in Massive Star Evolution, ed. C. Leitherer, P. D. Bennett, P. W. Morris, & J. T. Van Loon, 103
- Lindgård, A. & Nielsen, S. E. 1977: *Transition probabilities for the alkali isoelectronic sequences Li I, Na I, K I, Rb I, Cs I, Fr I*, Atomic Data and Nuclear Data Tables, 19, 533

- Lucy, L. B. 1982: *The formation of resonance lines in locally nonmonotonic winds*, ApJ, 255, 278
- Lucy, L. B. & Solomon, P. M. 1970: *Mass Loss by Hot Stars*, ApJ, 159, 879
- Lucy, L. B. & White, R. L. 1980: *X-ray emission from the winds of hot stars*, ApJ, 241, 300
- Macfarlane, J. J., Cohen, D. H., & Wang, P. 1994: *X-ray induced ionization in the winds of near-main-sequence O and B stars*, A&A, 437, 351
- Macfarlane, J. J., Waldron, W. L., Corcoran, M. F., Wolff, M. J., Wang, P., & Cassinelli, J. P. 1993: *Effects of Coronal and Shock-produced X-Rays on the Ionization Distribution in Hot Star Winds*, ApJ, 419, 813
- Maeder, A. 1999: *Comparisons of young clusters in the Galaxy, LMC, and SMC: the way to new stellar models.*, in Revista Mexicana de Astronomia y Astrofisica, vol. 27, Vol. 8, Revista Mexicana de Astronomia y Astrofisica Conference Series, ed. N. I. Morrell, V. S. Niemela, & R. H. Barbá, 83–88
- Maeder, A. 2009, Physics, Formation and Evolution of Rotating Stars
- Maeder, A. & Meynet, G. 1994: *New models of Wolf-Rayet stars and comparison with data in galaxies*, A&A, 287, 803
- Maeder, A. & Meynet, G. 2000a: *Stellar evolution with rotation. VI. The Eddington and Omega-limits, the rotational mass loss for OB and LBV stars*, A&A, 361, 159
- Maeder, A. & Meynet, G. 2000b: *The Evolution of Rotating Stars*, ARA&A, 38, 143
- Maeder, A. & Meynet, G. 2001: *Stellar evolution with rotation. VII. . Low metallicity models and the blue to red supergiant ratio in the SMC*, A&A, 373, 555
- Maeder, A. & Meynet, G. 2003: *Stellar evolution with rotation and magnetic fields. I. The relative importance of rotational and magnetic effects*, A&A, 411, 543
- Maeder, A. & Meynet, G. 2004: *Stellar evolution with rotation and magnetic fields. II. General equations for the transport by Tayler-Spruit dynamo*, A&A, 422, 225
- Maeder, A. & Meynet, G. 2005: *Stellar evolution with rotation and magnetic fields. III. The interplay of circulation and dynamo*, A&A, 440, 1041
- Maeder, A. & Meynet, G. 2010: *Evolution of massive stars with mass loss and rotation*, 54, 32
- Maeder, A., Meynet, G., Georgy, C., & Ekström, S. 2009: *The basic role of magnetic fields in stellar evolution*, in IAU Symposium, Vol. 259, IAU Symposium, 311–322
- Maeder, A., Przybilla, N., Nieva, M.-F., Georgy, C., Meynet, G., Ekström, S., & Eggenberger, P. 2014: *Evolution of surface CNO abundances in massive stars*, A&A, 565, A39

- Maíz Apellániz, J., Alfaro, E. J., Arias, J. I., Barbá, R. H., Gamen, R. C., Herrero, A., Leão, J. R. S., Marco, A., Negueruela, I., Simón-Díaz, S., Sota, A., et al. 2015: *MGB and the new Galactic O-Star Spectroscopic Survey spectral classification standard grid*, in Highlights of Spanish Astrophysics VIII, ed. A. J. Cenarro, F. Figueras, C. Hernández-Monteagudo, J. Trujillo Bueno, & L. Valdivielso, 603–603
- Markova, N. & Puls, J. 2008: *Bright OB stars in the Galaxy. IV. Stellar and wind parameters of early to late B supergiants*, A&A, 478, 823
- Markova, N., Puls, J., & Langer, N. 2018: *Spectroscopic and physical parameters of Galactic O-type stars. III. Mass discrepancy and rotational mixing*, A&A, 613, A12
- Martins, F., Escolano, C., Wade, G. A., Donati, J. F., Bouret, J. C., & Mimes Collaboration. 2012: *Observational effects of magnetism in O stars: surface nitrogen abundances*, A&A, 538, A29
- Martins, F., Foschino, S., Bouret, J.-C., Barbá, R., & Howarth, I. 2016: *Surface abundances of OC supergiants*, A&A, 588, A64
- Martins, F., Hervé, A., Bouret, J.-C., Marcolino, W., Wade, G. A., Neiner, C., Alecian, E., Grunhut, J., & Petit, V. 2015a: *The MiMeS survey of magnetism in massive stars: CNO surface abundances of Galactic O stars*, A&A, 575, A34
- Martins, F. & Hillier, D. J. 2012: *On the formation of C iii 4647-50-51 and C iii 5696 in O star atmospheres*, A&A, 545, A95
- Martins, F., Schaerer, D., & Hillier, D. J. 2005: *A new calibration of stellar parameters of Galactic O stars*, A&A, 436, 1049
- Martins, F., Simón-Díaz, S., Barbá, R. H., Gamen, R. C., & Ekström, S. 2017: *A study of the effect of rotational mixing on massive stars evolution: surface abundances of Galactic O7-8 giant stars*, A&A, 599, A30
- Martins, F., Simón-Díaz, S., Palacios, A., Howarth, I., Georgy, C., Walborn, N. R., Bouret, J.-C., & Barbá, R. 2015b: *Surface abundances of ON stars*, A&A, 578, A109
- Mason, B. D., Hartkopf, W. I., Gies, D. R., Henry, T. J., & Helsel, J. W. 2009: *The High Angular Resolution Multiplicity of Massive Stars*, AJ, 137, 3358
- Matteucci, F. & Calura, F. 2005: *Early chemical enrichment of the universe and the role of very massive population III stars*, MNRAS, 360, 447
- Meynet, G. & Maeder, A. 2000: *Stellar evolution with rotation. V. Changes in all the outputs of massive star models*, A&A, 361, 101
- Meynet, G., Maeder, A., Schaller, G., Schaerer, D., & Charbonnel, C. 1994: *Grids of massive stars with high mass loss rates. V. From 12 to 120 Msun at Z=0.001, 0.004, 0.008, 0.020 and 0.040*, A&AS, 103, 97

- Mihalas, D. & Hummer, D. G. 1973: *Analyses of light-ion spectra in stellar atmospheres.*, ApJ, 179, 827
- Mitnik, D. M., Griffin, D. C., Ballance, C. P., & Badnell, N. R. 2003: *An R -matrix with pseudo-states calculation of electron-impact excitation in C 2+*, Journal of Physics B: Atomic, Molecular and Optical Physics, 36, 717
- Mokiem, M. R., de Koter, A., Puls, J., Herrero, A., Najarro, F., & Villamariz, M. R. 2005: *Spectral analysis of early-type stars using a genetic algorithm based fitting method*, A&A, 441, 711
- Moore, C. E. 1993, *Tables of Spectra of Hydrogen, Carbon, Nitrogen, and Oxygen Atoms and Ions*
- Morales, M. F. & Wyithe, J. S. B. 2010: *Reionization and Cosmology with 21-cm Fluctuations*, ARA&A, 48, 127
- Morel, T., Hubrig, S., & Briquet, M. 2008: *Nitrogen enrichment, boron depletion and magnetic fields in slowly-rotating B-type dwarfs*, A&A, 481, 453
- Nahar, S. 2002: *Atomic Data and Nuclear Data Tables*, Atomic Data and Nuclear Data Tables, 80, issue 2, 205
- Nahar, S. N. & Pradhan, A. K. 1997: *Electron-Ion Recombination Rate Coefficients, Photoionization Cross Sections, and Ionization Fractions for Astrophysically Abundant Elements. I. Carbon and Nitrogen*, ApJS, 111, 339
- Najarro, F., Hanson, M. M., & Puls, J. 2011: *L-band spectroscopy of Galactic OB-stars*, A&A, 535, A32
- Najarro, F., Hillier, D. J., Puls, J., Lanz, T., & Martins, F. 2006: *On the sensitivity of He I singlet lines to the Fe IV model atom in O stars*, A&A, 456, 659
- Nazé, Y., Broos, P. S., Oskinova, L., Townsley, L. K., Cohen, D., Corcoran, M. F., Evans, N. R., Gagné, M., Moffat, A. F. J., Pittard, J. M., Rauw, G., et al. 2011: *Global X-ray Properties of the O and B Stars in Carina*, ApJS, 194, 7
- Nazé, Y., Flores, C. A., & Rauw, G. 2012: *A detailed X-ray investigation of ζ Puppis. I. The dataset and some preliminary results*, A&A, 538, A22
- Nazé, Y., Oskinova, L. M., & Gosset, E. 2013: *A Detailed X-Ray Investigation of ζ Puppis. II. The Variability on Short and Long Timescales*, ApJ, 763, 143
- Nieva, M. F. & Przybilla, N. 2006: *C II Abundances in Early-Type Stars: Solution to a Notorious Non-LTE Problem*, ApJ, 639, L39
- Nieva, M. F. & Przybilla, N. 2007: *Hydrogen and helium line formation in OB dwarfs and giants. A hybrid non-LTE approach*, A&A, 467, 295

- Nieva, M. F. & Przybilla, N. 2008: *Carbon abundances of early B-type stars in the solar vicinity. Non-LTE line-formation for C II/III/IV and self-consistent atmospheric parameters*, A&A, 481, 199
- Nieva, M.-F. & Simón-Díaz, S. 2011: *The chemical composition of the Orion star forming region. III. C, N, Ne, Mg, and Fe abundances in B-type stars revisited*, A&A, 532, A2
- Nussbaumer, H. & Storey, P. J. 1981: *C II two-electron transitions*, A&A, 96, 91
- Nussbaumer, H. & Storey, P. J. 1983: *Dielectronic recombination at low temperatures*, A&A, 126, 75
- Olson, G. & Castor, J. 1981: *Detailed empirical models for the winds of early-type stars*, ApJ, 244, 179
- Oskinova, L. M., Feldmeier, A., & Hamann, W.-R. 2006: *High-resolution X-ray spectroscopy of bright O-type stars*, MNRAS, 372, 313
- Oskinova, L. M., Hamann, W.-R., & Feldmeier, A. 2007: *Neglecting the porosity of hot-star winds can lead to underestimating mass-loss rates*, A&A, 476, 1331
- Owocki, S. P. 1994: *Theory review: Line-driven instability and other causes of structure and variability in hot-star winds*, Ap&SS, 221, 3
- Owocki, S. P. 2008: *Dynamical simulation of the velocity-porosity reduction in observed strength of stellar wind lines*, in Clumping in Hot-Star Winds, ed. W.-R. Hamann, L. M. Oskinova, & A. Feldmeier, 121–124
- Owocki, S. P., Castor, J. I., & Rybicki, G. B. 1988: *Time-dependent models of radiatively driven stellar winds. I - Nonlinear evolution of instabilities for a pure absorption model*, ApJ, 335, 914
- Owocki, S. P. & Cohen, D. H. 1999: *A Simple Scaling Analysis of X-Ray Emission and Absorption in Hot-Star Winds*, ApJ, 520, 833
- Owocki, S. P. & Cohen, D. H. 2006: *The Effect of Porosity on X-Ray Emission-Line Profiles from Hot-Star Winds*, ApJ, 648, 565
- Owocki, S. P. & Puls, J. 1999: *Line-driven Stellar Winds: The Dynamical Role of Diffuse Radiation Gradients and Limitations to the Sobolev Approach*, ApJ, 510, 355
- Owocki, S. P. & Rybicki, G. B. 1984: *Instabilities in line-driven stellar winds. I - Dependence on perturbation wavelength*, ApJ, 284, 337
- Owocki, S. P., Sundqvist, J. O., Cohen, D. H., & Gayley, K. G. 2013: *Thin-shell mixing in radiative wind-shocks and the $L_x \sim L_{bol}$ scaling of O-star X-rays*, MNRAS, 429, 3379
- Pauldrach, A. W. A., Hoffmann, T. L., & Lennon, M. 2001: *Radiation-driven winds of hot luminous stars. XIII. A description of NLTE line blocking and blanketing towards realistic models for expanding atmospheres*, A&A, 375, 161

- Pauldrach, A. W. A., Kudritzki, R. P., Puls, J., & Butler, K. 1990: *Radiation driven winds of hot luminous stars. VII - The evolution of massive stars and the morphology of stellar wind spectra*, A&A, 228, 125
- Pauldrach, A. W. A., Kudritzki, R. P., Puls, J., Butler, K., & Hunsinger, J. 1994: *Radiation-driven winds of hot luminous stars. 12: A first step towards detailed UV-line diagnostics of O-stars*, A&A, 283, 525
- Paxton, B., Cantiello, M., Arras, P., Bildsten, L., Brown, E. F., Dotter, A., Mankovich, C., Montgomery, M. H., Stello, D., Timmes, F. X., & Townsend, R. 2013: *Modules for Experiments in Stellar Astrophysics (MESA): Planets, Oscillations, Rotation, and Massive Stars*, ApJS, 208, 4
- Peach, G., Saraph, H. E., & Seaton, M. J. 1988: *Atomic data for opacity calculations. IX. The lithium isoelectronic sequence*, Journal of Physics B: Atomic, Molecular and Optical Physics, 21, 3669
- Piskunov, N. E., Kupka, F., Ryabchikova, T. A., Weiss, W. W., & Jeffery, C. S. 1995: *VALD: The Vienna Atomic Line Data Base.*, A&AS, 112, 525
- Przybilla, N., Farnsteiner, M., Nieva, M. F., Meynet, G., & Maeder, A. 2010: *Mixing of CNO-cycled matter in massive stars*, A&A, 517, A38
- Przybilla, N., Nieva, M., & Butler, K. 2008: *A Cosmic Abundance Standard: Chemical Homogeneity of the Solar Neighborhood and the ISM Dust-Phase Composition*, ApJ, 688, L103
- Puls, J. 1987: *Radiation-driven winds of hot luminous stars. IV - The influence of multi-line effects*, A&A, 184, 227
- Puls, J. 2009: *Modeling the atmospheres of massive stars*, Communications in Asteroseismology, 158, 113
- Puls, J., Kudritzki, R.-P., Herrero, A., Pauldrach, A. W. A., Haser, S. M., Lennon, D. J., Gabler, R., Voels, S. A., Vilchez, J. M., Wachter, S., & Feldmeier, A. 1996: *O-star mass-loss and wind momentum rates in the Galaxy and the Magellanic Clouds Observations and theoretical predictions.*, A&A, 305, 171
- Puls, J., Owocki, S. P., & Fullerton, A. W. 1993: *On the synthesis of resonance lines in dynamical models of structured hot-star winds*, A&A, 279, 457
- Puls, J., Urbaneja, M. A., Venero, R., Repolust, T., Springmann, U., Jokuthy, A., & Mokiem, M. R. 2005: *Atmospheric NLTE-models for the spectroscopic analysis of blue stars with winds. II. Line-blanketed models*, A&A, 435, 669
- Puls, J., Vink, J. S., & Najarro, F. 2008: *Mass loss from hot massive stars*, A&A Rev., 16, 209
- Ramírez-Agudelo, O. H., Simón-Díaz, S., Sana, H., de Koter, A., Sabín-Sanjulían, C., de Mink, S. E., Dufton, P. L., Gräfener, G., Evans, C. J., Herrero, A., Langer, N., et al. 2013: *The VLT-FLAMES Tarantula Survey. XII. Rotational velocities of the single O-type stars*, A&A, 560, A29

- Raskin, G., Van Winckel, H., & Davignon, G. 2004: *HERMES: a high-resolution spectrograph for the Mercator Telescope*, in Proc. SPIE, Vol. 5492, Ground-based Instrumentation for Astronomy, ed. A. F. M. Moorwood & M. Iye, 322–330
- Rauw, G., Hervé, A., Nazé, Y., González-Pérez, J. N., Hempelmann, A., Mittag, M., Schmitt, J. H. M. M., Schröder, K.-P., Gosset, E., Eenens, P., & Uuh-Sonda, J. M. 2015: *Simultaneous X-ray and optical spectroscopy of the Oef supergiant λ Cephei*, A&A, 580, A59
- Raymond, J. & Smith, B. 1977: *Soft X-ray spectrum of a hot plasma*, ApJS, 35, 419
- Repolust, T., Puls, J., & Herrero, A. 2004: *Stellar and wind parameters of Galactic O-stars. The influence of line-blocking/blanketing*, A&A, 415, 349
- Rivero González, J. G., Puls, J., & Najarro, F. 2011: *Nitrogen line spectroscopy of O-stars. I. Nitrogen III emission line formation revisited*, A&A, 536, A58
- Rivero González, J. G., Puls, J., Najarro, F., & Brott, I. 2012a: *Nitrogen line spectroscopy of O-stars. II. Surface nitrogen abundances for O-stars in the Large Magellanic Cloud*, A&A, 537, A79
- Rivero González, J. G., Puls, J., Najarro, F., & Massey, P. 2012b: *Nitrogen line spectroscopy of O-stars. III. The earliest O-stars*, A&A, 543, A95
- Russell, H. N. 1913: *"Giant" and "dwarf" stars*, The Observatory, 36, 324
- Ryabchikova, T., Piskunov, N., Kurucz, R. L., Stempels, H. C., Heiter, U., Pakhomov, Y., & Barklem, P. S. 2015: *A major upgrade of the VALD database*, Phys. Scr, 90, 054005
- Ryabchikova, T. A., Piskunov, N. E., Kupka, F., & Weiss, W. W. 1997: *The Vienna Atomic Line Database : Present State and Future Development*, Baltic Astronomy, 6, 244
- Sabín-Sanjulián, C., Simón-Díaz, S., Herrero, A., Puls, J., Schneider, F. R. N., Evans, C. J., Garcia, M., Najarro, F., Brott, I., Castro, N., Crowther, P. A., et al. 2017: *The VLT-FLAMES Tarantula Survey. XXVI. Properties of the O-dwarf population in 30 Doradus*, A&A, 601, A79
- Sana, H., Gosset, E., & Evans, C. J. 2009: *The massive star binary fraction in young open clusters - II. NGC6611 (Eagle Nebula)*, MNRAS, 400, 1479
- Sana, H., Gosset, E., Nazé, Y., Rauw, G., & Linder, N. 2008: *The massive star binary fraction in young open clusters - I. NGC 6231 revisited*, MNRAS, 386, 447
- Sana, H., James, G., & Gosset, E. 2011: *The massive star binary fraction in young open clusters - III. IC 2944 and the Cen OB2 association*, MNRAS, 416, 817
- Sana, H., Rauw, G., Naze, Y., Gosset, E., & Vreux, J.-M. 2006: *An XMM-Newton view of the young open cluster NGC 6231 - II. The OB star population*, MNRAS, 372, 661
- Santolaya-Rey, A. E., Puls, J., & Herrero, A. 1997: *Atmospheric NLTE-models for the spectroscopic analysis of luminous blue stars with winds.*, A&A, 323, 488

- Schaller, G., Schaerer, D., Meynet, G., & Maeder, A. 1992: *New grids of stellar models from 0.8 to 120 solar masses at $Z = 0.020$ and $Z = 0.001$* , A&AS, 96, 269
- Seaton, M. J. 1958: *The Quantum Defect Method*, MNRAS, 118, 504
- Seaton, M. J. 1962: *The Theory of Excitation and Ionization by Electron Impact*, in *Atomic and Molecular Processes*, ed. D. R. Bates (New York, Academic Press), 375
- Seaton, M. J. 1987: *Atomic data for opacity calculations. I - General description*, Journal of Physics B Atomic Molecular Physics, 20, 6363
- Seward, F. D., Forman, W. R., Giacconi, R., Griffiths, R. E., Harnden, Jr., F. R., Jones, C., & Pye, J. P. 1979: *X-rays from Eta Carinae and the surrounding nebula*, ApJ, 234, L55
- Shu, F. H., Adams, F. C., & Lizano, S. 1987: *Star formation in molecular clouds - Observation and theory*, ARA&A, 25, 23
- Simon, M. & Axford, W. 1966: *Shock Waves in the Interplanetary Medium*, Planet.Space Sci., 14, 901
- Simón-Díaz, S. 2010: *The chemical composition of the Orion star forming region. I. Homogeneity of O and Si abundances in B-type stars*, A&A, 510, A22
- Simón-Díaz, S., Castro, N., Garcia, M., & Herrero, A. 2011a: *The IACOB spectroscopic database of galactic OB stars*, in IAU Symposium, Vol. 272, IAU Symposium, ed. C. Neiner, G. Wade, G. Meynet, & G. Peters, 310–312
- Simón-Díaz, S., Castro, N., Herrero, A., Puls, J., Garcia, M., & Sabín-Sanjulián, C. 2011b: *The IACOB project: A grid-based automatic tool for the quantitative spectroscopic analysis of O-stars*, in Journal of Physics Conference Series, Vol. 328, Journal of Physics Conference Series, 012021
- Simón-Díaz, S. & Herrero, A. 2007: *Fourier method of determining the rotational velocities in OB stars*, A&A, 468, 1063
- Simón-Díaz, S. & Herrero, A. 2014: *The IACOB project. I. Rotational velocities in northern Galactic O- and early B-type stars revisited. The impact of other sources of line-broadening*, A&A, 562, A135
- Simón-Díaz, S., Herrero, A., Sabín-Sanjulián, C., Najarro, F., Garcia, M., Puls, J., Castro, N., & Evans, C. J. 2014: *The IACOB project. II. On the scatter of O-dwarf spectral type - effective temperature calibrations*, A&A, 570, L6
- Simón-Díaz, S., Negueruela, I., Maíz Apellániz, J., Castro, N., Herrero, A., Garcia, M., Pérez-Prieto, J. A., Caon, N., Alacid, J. M., Camacho, I., Dorda, R., et al. 2015: *The IACOB spectroscopic database: recent updates and first data release*, in Highlights of Spanish Astrophysics VIII, ed. A. J. Cenarro, F. Figueras, C. Hernández-Monteaigudo, J. Trujillo Bueno, & L. Valdivielso, 576–581

- Smith, N. 2014: *Mass Loss: Its Effect on the Evolution and Fate of High-Mass Stars*, ARA&A, 52, 487
- Smith, R. K., Brickhouse, N. S., Liedahl, D. A., & Raymond, J. C. 2001: *Collisional Plasma Models with APEC/APED: Emission-Line Diagnostics of Hydrogen-like and Helium-like Ions*, ApJ, 556, L91
- Snow, T. & Morton, D. 1976: *Copernicus ultraviolet observations of mass-loss effects in O and B stars*, ApJS, 32, 429
- Sota, A., Maíz Apellániz, J., Walborn, N. R., Alfaro, E. J., Barbá, R. H., Morrell, N. I., Gamen, R. C., & Arias, J. I. 2011: *The Galactic O-Star Spectroscopic Survey. I. Classification System and Bright Northern Stars in the Blue-violet at $R \sim 2500$* , ApJS, 193, 24
- Steidel, C. C., Giavalisco, M., Pettini, M., Dickinson, M., & Adelberger, K. L. 1996: *Spectroscopic Confirmation of a Population of Normal Star-forming Galaxies at Redshifts $Z > 3$* , ApJ, 462, L17
- Sundqvist, J. O. & Owocki, S. P. 2013: *Clumping in the inner winds of hot, massive stars from hydrodynamical line-driven instability simulations*, MNRAS, 428, 1837
- Sundqvist, J. O., Owocki, S. P., Cohen, D. H., Leutenegger, M. A., & Townsend, R. H. D. 2012a: *A generalized porosity formalism for isotropic and anisotropic effective opacity and its effects on X-ray line attenuation in clumped O star winds*, MNRAS, 420, 1553
- Sundqvist, J. O., Owocki, S. P., & Puls, J. 2012b: *The Nature and Consequences of Clumping in Hot, Massive Star Winds*, in *Astronomical Society of the Pacific Conference Series*, Vol. 465, Proceedings of a Scientific Meeting in Honor of Anthony F. J. Moffat, ed. L. Drissen, C. Robert, N. St-Louis, & A. F. J. Moffat, 119
- Sundqvist, J. O. & Puls, J. 2018: *Atmospheric NLTE-models for the spectroscopic analysis of blue stars with winds. IV. Porosity in physical and velocity space*, ArXiv e-prints
- Sundqvist, J. O., Puls, J., & Feldmeier, A. 2010: *Mass loss from inhomogeneous hot star winds. I. Resonance line formation in 2D models*, A&A, 510, A11+
- Sundqvist, J. O., Puls, J., Feldmeier, A., & Owocki, S. P. 2011: *Mass loss from inhomogeneous hot star winds. II. Constraints from a combined optical/UV study*, A&A, 528, A64
- Sundqvist, J. O., Puls, J., & Owocki, S. P. 2014: *Mass loss from inhomogeneous hot star winds. III. An effective-opacity formalism for line radiative transfer in accelerating, clumped two-component media, and first results on theory and diagnostics*, A&A, 568, A59
- Tachiev, G. & Fischer, C. F. 2000: *Breit-Pauli energy levels, lifetimes and transition data: boron-like spectra*, Journal of Physics B: Atomic, Molecular and Optical Physics, 33, 2419
- Telting, J. H., Avila, G., Buchhave, L., Frandsen, S., Gandolfi, D., Lindberg, B., Stempels, H. C., Prins, S., & NOT staff. 2014: *FIES: The high-resolution Fiber-fed Echelle Spectrograph at the Nordic Optical Telescope*, Astronomische Nachrichten, 335, 41

- Townsend, R. H. D., Oksala, M. E., Cohen, D. H., Owocki, S. P., & ud-Doula, A. 2010: *Discovery of Rotational Braking in the Magnetic Helium-strong Star Sigma Orionis E*, ApJ, 714, L318
- Trundle, C., Lennon, D. J., Puls, J., & Dufton, P. L. 2004: *Understanding B-type supergiants in the low metallicity environment of the SMC*, A&A, 417, 217
- Tully, J. A., Seaton, M. J., & Berrington, K. A. 1990: *Atomic data for opacity calculations. XIV. The beryllium sequence*, Journal of Physics B: Atomic, Molecular and Optical Physics, 23, 3811
- Unsöld, A. 1942: *Quantitative Analyse des B O-Sternes τ Scorpii. III. Teil. Theorie des kontinuierlichen Spektrums. Mit 4 Abbildungen.*, ZAp, 21, 229
- Urbaneja, M. 2004: *B Supergiants in the Milky Way and Nearby Galaxies: Models and Quantitative Spectroscopy*, PhD thesis, Universidad de la Laguna, La Laguna, Spain
- Šurlan, B., Hamann, W.-R., Aret, A., Kubát, J., Oskinova, L. M., & Torres, A. F. 2013: *Macroclumping as solution of the discrepancy between H α and P v mass loss diagnostics for O-type stars*, A&A, 559, A130
- van Regemorter, H. 1962: *Rate of Collisional Excitation in Stellar Atmospheres.*, ApJ, 136, 906
- Vanbeveren, D., De Loore, C., & Van Rensbergen, W. 1998: *Massive stars*, A&ARv, 9, 63
- Verner, D. A. & Yakovlev, D. G. 1995: *Analytic FITS for partial photoionization cross sections.*, A&AS, 109, 125
- Vink, J. S. 2009: *Eta Carinae and the Luminous Blue Variables*, in *Eta Carinae and the supernova imposters*, ed. R. Humphreys & K. Davidson
- Vink, J. S., Brott, I., Gräfener, G., Langer, N., de Koter, A., & Lennon, D. J. 2010: *The nature of B supergiants: clues from a steep drop in rotation rates at 22 000 K. The possibility of Bi-stability braking*, A&A, 512, L7
- Walborn, N. R. & Panek, R. J. 1984: *Ultraviolet spectral morphology of the O stars - The remarkable luminosity dependence of the SI IV stellar wind effect*, ApJ, 280, L27
- Waldron, W. L. & Cassinelli, J. P. 2007: *An Extensive Collection of Stellar Wind X-Ray Source Region Emission Line Parameters, Temperatures, Velocities, and Their Radial Distributions as Obtained from Chandra Observations of 17 OB Stars*, ApJ, 668, 456
- Waldron, W. L. & Cassinelli, J. P. 2010: *The Importance of XUV Radiation as a Solution to the P V Mass Loss Rate Discrepancy in O Stars*, A&A, 711, L30
- Waldron, W. L. & Cassinelli, J. P. 2001: *Chandra Discovers a Very High Density X-Ray Plasma on the O Star ζ Orionis*, ApJ, 548, L45
- Wilson, N. J., Bell, K. L., & Hudson, C. E. 2005: *Effective collision strengths for electron impact excitation of C II*, A&A, 432, 731

- Wilson, N. J., Bell, K. L., & Hudson, C. E. 2007: *Effective collision strengths for electron impact excitation of C II*, A&A, 461, 765
- Wolff, S. C., Edwards, S., & Preston, G. W. 1982: *The origin of stellar angular momentum*, ApJ, 252, 322
- Woosley, S. E. 1993: *Gamma-ray bursts from stellar mass accretion disks around black holes*, ApJ, 405, 273
- Yan, Y., Taylor, K. T., & Seaton, M. J. 1987: *Atomic data for opacity calculations. III. Oscillator strengths for C II*, Journal of Physics B: Atomic and Molecular Physics, 20, 6399
- Zhekov, S. A. & Palla, F. 2007: *X-rays from massive OB stars: thermal emission from radiative shocks*, MNRAS, 382, 1124
- Zsargó, J., Hillier, D. J., Bouret, J.-C., Lanz, T., Leutenegger, M. A., & Cohen, D. H. 2008: *On the Importance of the Interclump Medium for Superionization: O VI Formation in the Wind of ζ Puppis*, ApJ, 685, L149

Acknowledgements

Many people were important to make this work possible, but above all, I must thank my supervisor Joachim Puls for all his dedication to my development as a scientist. Joachim believed in me when we had not yet met in person, supported me when I experienced my first winter in Germany (I mean my first real winter), and encouraged me during all the difficulties of the last four years. Jo was most probably the toughest boss I will ever have and I will be always grateful for his straightforwardness to identify and explain my mistakes. I finish the Ph.D. not only with the skills Jo taught me but even more important, aware of the weak points I need to improve. I stress here that I will forever be thankful to have worked with him.

Between my collaborators, my special gratitude to Tadius Hoffmann who was always available (even in the weekends) to answer my questions and curiosities about Unix, physics or any other stuff. It was a big pleasure to collaborate with devoted colleagues as Jon Sundqvist, Johann Weber, Keith Butler, and Levin Hennicker. The quality of this work could only be reached due to their precise reviews, corrections, and experience. Last but of equal importance, thanks a lot to Sergio Simón-Díaz and Gonzalo Holgado that reviewed our results and made available the data we used for a large part of this work.

My respect for the USM employees, specially Uta Le Guay, Nicola Auer and Sabine Grötsch, that do an excellent work to provide good working conditions to the Ph.D. candidates. They helped me a lot, mainly during the time I could not speak a single word in German. Thanks also to Mustafa for the daily chat every morning.

My acknowledgments to my fellow students at USM: I would not have survived the Munich house market without the help of Christian Obermeier who basically found the house I live in since my first semester in Germany. Special thanks to my office mates Sebastian Bocquet, Raffaella Capasso and Nikhel Gupta for all the joy together. Thanks I-Non Chiu for all the discussions about TV series. The time in USM with Nathália Cibirka, Sebastian Grandis, Maria Paulus, and Matias Garate was short but well enjoyed and I appreciated their fellowship. Fortunately, I met many more nice people in USM and this paper is too short to mention every name, but know that I am very pleased with our time together.

Me, this work or anything related to me just exists because of Marta Carneiro, my mother. Someday I should write a book to tell all of our stories, but she is simply the reason of everything to me. I thank also my father for his friendship and love, and even though being distant, he often sends me messages with news from my soccer team. Even me being a single child I had the luck to grow up with cousins that are like brothers to me. Roberto and Pedro Carneiro are my biggest supporters and

the ones I miss the most every weekend. Videogames are way more boring nowadays that I cannot beat Luiz Cavalcanti and Lucas Carvalho. My whole family is huge and I know I will hear a lot if I do not cite some names, the reader may feel free to jump to the next paragraph. Thanks a lot Talita, Clara, Tia Ana, Karlany, Tio Carlos, Tia Jane, Tio Gilmar, Leticia, Lais, Gabriela, Beatriz, Tia Marcinha, Tia Gloria, Gustavo, Hiroce family, Mariana Séllos, Priscilla, Janaina, Dada ... and all the others from Oswaldo Cruz City. Soon we will be reunited.

Many thanks to my friends in Munich that coincidentally were always present in my best days in Munich. Thanks Johanna and Nathalia Eitel for all the laughs together. Thanks a lot Carolin Dagistan for being my first friend in Munich. Astrid Brunner and Marcelo Cardilo for all the partnership and Marie Kaiser for being the best person I could have met so far away from home.

Thank you for taking your time to read this work. This thesis describes approximately ten thousand hours of work and the dedication of many scientists.

Last, but not least, I also gratefully acknowledge the financial support from the Brazilian Coordination for the Improvement of Higher Education Personnel (CAPES).

Curriculum Vitae

Angaben zur Person:

Name: Carneiro Gama
Vorname: Luiz Paulo
Geburtsdatum: 23. März 1989
Geburtsort: Rio de Janeiro, Brasilien
Staatsangehörigkeit: Brasilianer
Kontakt: mail@luiz.pro

Aus- und Weiterbildung:

2017 - 2018 Zusammenarbeit mit Google (Udacity)
Mobile Web Specialist Nanodegree
Certificate & Code in <https://github.com/luizdotpro/mwsProjects>

2014 - 2018 Universitätssternwarte München, Fakultät für Physik -
Ludwig-Maximilians-Universität, Scheinerstraße 1, 81679 München
Promotionsstudium der Astronomie an der
LMU - Ludwig-Maximilians-Universität München

2011 - 2013 Brazilian National Observatory
Master Astronomie

2006 - 2010 Rio de Janeiro State University
Bachelor Physik